



HAL
open science

Synthesis of NIR Dyes and Nanoparticles for in vivo Bioimaging and Dicyanovinyl Dyes for Primary Amine Detection

Lulu Bu

► **To cite this version:**

Lulu Bu. Synthesis of NIR Dyes and Nanoparticles for in vivo Bioimaging and Dicyanovinyl Dyes for Primary Amine Detection. Other. Université de Lyon, 2020. English. NNT : 2020LYSEN086 . tel-03934684

HAL Id: tel-03934684

<https://theses.hal.science/tel-03934684>

Submitted on 11 Jan 2023

HAL is a multi-disciplinary open access archive for the deposit and dissemination of scientific research documents, whether they are published or not. The documents may come from teaching and research institutions in France or abroad, or from public or private research centers.

L'archive ouverte pluridisciplinaire **HAL**, est destinée au dépôt et à la diffusion de documents scientifiques de niveau recherche, publiés ou non, émanant des établissements d'enseignement et de recherche français ou étrangers, des laboratoires publics ou privés.



Numéro National de Thèse : 2020LYSEN086

THESE de DOCTORAT DE L'UNIVERSITE DE LYON

opérée par

l'Ecole Normale Supérieure de Lyon

Ecole Doctorale N° 206

École Doctorale de Chimie de Lyon

Discipline : CHIMIE

Soutenue publiquement le 17/12/2020, par :

Lulu BU

Synthesis of NIR Dyes and Nanoparticles for in vivo Bioimaging and Dicyanovinyl Dyes for Primary Amine Detection

Synthèse de colorants et nanoparticules NIR pour la bioimagerie in vivo et colorants dicyanovinyl pour la détection d'amines primaires

Devant le jury composé de :

Mme Florence MAHUTEAU-BETZER, Institut Curie

M. Frédéric BOLZE, Université de Strasbourg

M. Olivier SIRI, Université de Marseille

Mme Chantal ANDRAUD, ENS de Lyon

M. Yann BRETONNIERE, ENS de Lyon

Rapporteur

Rapporteur

Examinatrice

Directrice de thèse

Co-encadrant de thèse

Acknowledgements

The thesis is funded by the China Scholarship Council (CSC) and École Normale Supérieure de Lyon (ENS de Lyon), I would like to first of all express my gratitude to the CSC and ENS de Lyon.

During the three years PhD study in the chemistry laboratory of the ENS de Lyon, I have not only learned much professional knowledges and skills, but also received a lot of care and help from many people. Now, I would like to take the chance to thank them for living me so precious three-year experience.

Firstly, I would like to express my most sincere respect and thanks to my supervisors Dr. Chantal Andraud and Dr. Yann Bretonnière. I really appreciate Chantal Andraud for giving me a chance to work in her lab, and supporting my research and study. I wish you a happy and wonderful life in the future. I deeply thank Yann Bretonnière for guiding me three years in both my work and life. I really benefit a lot from his rigorous scientific attitude and professional knowledge. Thank you for encouraging all my ideas and leaving me a lot of constructive suggestions. I hope to be able to establish a cooperative relationship with you in the future if I continue research, and I wish you a happy life, happy work.

Besides my supervisors, I would like to warmly thank our collaborators Dr. Arnaud Favier from the Polymer Materials Engineering Laboratory of Lyon for their efforts in preparation of polymer nanoparticles; Dr. Olivier Hugon and Dr. Boudewin Van der Sanden at Liphy and TIMC-IMAG in Grenoble for photoacoustic imaging and two-photon fluorescence imaging. Then, I also want to thank many members from the laboratory: Frédéric Lerouge for giving me guidance on manipulating DLS and preparation of amine modified glass slides; Frédéric Chaput and Delphine Pitrat for helping me prepare sol-gel and PMMA films and synthesize intermediate products; Sandrine Denis-Quanquin and Laure Guy for training me NMR and mass; Christian Melkonian for fixing all kinds of computer problems; Maxime Rémond for his help during my first year. All the people outside ENS who have collaborated with us; and finally all the other colleagues and friends surrounding me: Tingting, Junchao, Qingyi, Shagor, Damien, Orsola, Caroline, Jean, Isis, Maher, Sylvain, Laura...

I really enjoy the four-year life in France. I will always keep this memory in mind. I wish everybody here a happy life. Finally, I would like to thank the understanding and support from my family, they are forever my strongest backing.

Table of Content

ACKNOWLEDGEMENTS.....	I
ABBREVIATIONS	V
GENERAL INTRODUCTION	VII
CHAPTER I. INTRODUCTION TO NIR DYES AND NANOPARTICLES (NPS) FOR <i>IN VIVO</i> OPTICAL IMAGING.....	1
1. BIOIMAGING TECHNOLOGIES	1
1.1. <i>Biological Transparency Window</i>	1
1.2. <i>Engineering of NIR-emitting Organic Dyes</i>	2
1.2.1. Rhodamine Dyes	4
1.2.2. BODIPY Dyes	7
1.2.3. Cyanine Dyes	10
1.2.4. Some Other Organic NIR-II-emitting Dyes.....	13
1.2.5. Push-pull Dipolar Dyes	15
1.3. <i>NIR Organic Dyes for in vivo PA Bioimaging</i>	21
1.3.1. PA Bioimaging	21
1.3.2. Dyes for PA Imaging.....	21
2. NIR DYE-LOADED NPS FOR FLUORESCENCE OR PA IMAGING	24
2.1. <i>Dye-loaded F127-SiO₂ NPs</i>	25
2.2. <i>Dye-loaded Polymer NPs</i>	28
3. OBJECTIVES	32
CHAPTER II. SYNTHESIS OF NIR DYES AND DYE-LOADED F127-SiO₂ NPS FOR <i>IN VIVO</i> FLUORESCENCE IMAGING	34
1. INTRODUCTION	34
1.1. <i>Previous Work</i>	34
1.2. <i>Objectives</i>	34
2. SYNTHESIS OF TCBZ DYES AND TCBZ@F127-SiO ₂ NPS FOR FLUORESCENCE IMAGING	35
2.1. <i>Synthetic Design</i>	35
2.2. <i>Synthesis and Photophysical Properties of TCBZ Dyes</i>	36
2.2.1. Synthesis of TCBZ Dyes.....	36
2.2.2. Photophysical Properties of TCBZ dyes.....	37
2.3. <i>Preparation and Characterization of TCBZ2@F127-SiO₂ and TCBZ5@F127-SiO₂ NPs</i>	46
2.4. <i>Preparation of Surface-functionalized TCBZ2@F127-SiO₂ and TCBZ5@F127-SiO₂ NPs for in vivo Fluorescence Imaging</i>	48

2.4.1.	Synthesis of F127-COOH and F127-N ₃	48
2.4.2.	Preparation of TCBZ2/5@F127-COOH-SiO ₂ , TCBZ2/5@F127-X-SiO ₂ and TCBZ5@F127-TPP-SiO ₂ NPs	49
2.4.3.	Characterization of Surface-functionalized TCBZ5@F127-SiO ₂ NPs	51
2.4.4.	TCBZ5@F127-SiO ₂ and TCBZ5@F127-X-SiO ₂ NPs for Biphotonic <i>in vivo</i> Fluorescence Imaging	52
3.	SYNTHESIS OF EBTN DYES AND EBTN@F127-SiO ₂ NPs FOR FLUORESCENCE IMAGING	55
3.1.	<i>Synthetic Design of EBTN Dyes</i>	55
3.2.	<i>Synthesis and Photophysical Properties of EBTN Dyes</i>	55
3.2.1.	Synthesis of EBTN Dyes	55
3.2.2.	Photophysical Properties of EBTN Dyes	57
3.3.	<i>Preparation of EBTN@F127-SiO₂ NPs for in vivo Fluorescence Imaging</i>	61
3.3.1.	Preparation of EBTN@F127-SiO ₂ NPs	61
3.3.2.	Characterization of EBTN F127-SiO ₂ NPs	62
4.	CONCLUSION	64
CHAPTER III. DESIGN OF NIR DYES AND NPS FOR <i>IN VIVO</i> PA IMAGING		66
1.	INTRODUCTION	66
1.1.	<i>Previous Work</i>	66
1.2.	<i>Objectives</i>	68
2.	PREPARATION OF CPO-SO ₃ PNPs FOR PA IMAGING	69
2.1.	<i>Synthetic Design of CPO-SO₃ Polymer</i>	69
2.2.	<i>Synthesis and Characterization of CPO-SO₃ PNPs</i>	70
2.2.1.	Synthesis of CPO-SO ₃	70
2.2.2.	Synthesis of CPO-SO ₃ Polymers and CPO-SO ₃ PNPs	70
2.2.3.	Characterization of CPO-SO ₃ PNPs	72
2.3.	<i>CPO-SO₃ PNPs for in vivo PA Imaging</i>	73
3.	PREPARATION OF CPOP PNPs FOR PA IMAGING	74
3.1.	<i>Synthetic Design of CPOP Polymers</i>	74
3.2.	<i>Synthesis of CPOP PNPs</i>	74
3.2.1.	Synthesis of CPOP1 and CPOP2 dyes	74
3.2.2.	Synthesis and Characterization of CPOP1 PNPs	75
3.2.3.	Synthesis and Characterization of CPOP2 PNPs	78
4.	PREPARATION OF F127-CPO-SO ₃ -SiO ₂ NPs FOR PA IMAGING	80
4.1.	<i>Synthetic Design of F127-CPO-SO₃-SiO₂ NPs</i>	80
4.2.	<i>Synthesis and Characterization of CPO-SO₃-F127-SiO₂ NPs</i>	80
4.2.1.	Synthesis of F127-CPO-SO ₃ -SiO ₂ NPs	80
4.2.2.	Synthesis of F127-CPO-SO ₃ -SiO ₂ NPs	81
4.2.3.	Characterization of CPO-SO ₃ -F127-SiO ₂ NPs	81
4.3.	<i>F127-CPO-SO₃-SiO₂ NPs for in vivo PA Imaging</i>	82

5. CONCLUSION	83
CHAPTER IV. DICYANOVINYL DYES FOR PRIMARY AMINE DETECTION	84
1. BACKGROUND	84
1.1. General Context	84
1.2. Why Primary Amine?	85
1.3. Preliminary Tests	86
2. PRIMARY AMINE SENSING: SOLUTION STUDIES	91
2.1. Synthesis of PTTCN.....	91
2.2. Solvent Test	91
2.3. Spectroscopic Response	93
2.4. Reversibility	96
2.5. Sensitivity and Selectivity.....	97
2.6. NMR Studies.....	98
3. PTTCN FILMS FOR PRIMARY AMINE VAPOR DETECTION	101
4. EBTN1-GLASS FOR PRIMARY AMINE VAPOR DETECTION	103
4.1. Objective	103
4.2. Preliminary Tests on EBTN1-glass	106
5. CONCLUSION	108
CHAPTER V. CONCLUSION AND PERSPECTIVES.....	109
CHAPTER VI. EXPERIMENTAL SECTION	112
1. SYNTHESIS	112
1.1. General Information.....	112
1.2. Synthesis and Characterization of Dyes.....	113
1.3. Synthesis and Characterization of Modified F127.....	133
2. PREPARATION OF DYE-LOADED F127-SiO ₂ NPS	137
3. <i>IN VIVO</i> MICROSCOPY	139
3.1. Two-Photon imaging.....	139
3.2. PA imaging.....	139
4. PREPARATION OF SOLID DEVICE FOR PRIMARY AMINE VAPOR DETECTION	141
5. OTHER EXPERIMENTS	141
6. X-RAY CRYSTALLOGRAPHY	142
REFERENCES.....	144

Abbreviations

A	Electron acceptor
ACQ	Aggregation caused quenching
AEM	4-(2-Aminoethyl)morpholine
AIBN	Azobisisobutyronitrile
AIE	Aggregation-induced emission
BBTD	Benzobisthiadiazole
C10	n-Decylamine
CMC	Critical micelle concentration
CV	Cresyl violet
D	Electron donor
DCC	<i>N,N'</i> -Dicyclohexylcarbodiimide
DCM	Dichloromethane
DEDMS	Diethoxydimethylsilane
DFT	Density functional theory
DIPEA	<i>N,N</i> -Diisopropylethylamine
DLS	Dynamic light scattering
DMF	<i>N,N</i> -Dimethylformamide
DMSO	Dimethylsulfoxide
EBTN	4 <i>H</i> -Dithieno[3,2- <i>b</i> :2',3'- <i>d</i>]pyrrole
EDC·HCl	<i>N</i> -(3-dimethylaminopropyl)- <i>N'</i> -ethylcarbodiimide hydrochloride
F127	Pluronic F127
FRET	Förster resonance energy transfer
HRMS	High-resolution mass spectrometry
HOMO	Highest Occupied Molecular Orbital
Hb	Hemoglobin
HOBt	1-Hydroxybenzotriazole
<i>I</i>	Light intensity
ICG	Indocyanine Green
ICT	Intramolecular charge transfer
ISC	Intersystem crossing
<i>J</i>	Scalar or J coupling constant
LUMO	Lowest Unoccupied Molecular Orbital

LDA	Lithium diisopropylamide
MHz	Millihertz
NIR	Near-infrared
NIR-I, NIR-II, NIR-III	First, second and third transparency window
NHS	<i>N</i> -Hydroxysuccinimide
NMR	Nuclear magnetic resonance
NLO	Non-linear optical
NPs	Nanoparticles
HbO ₂	Oxyhemoglobin
PA	Photoacoustic
PAM	Photoacoustic microscopy
PEG	Polyethylene glycol
PMMA	Poly(methyl methacrylate)
PNPs	Polymer nanoparticles
ppm	Parts per million (NMR data)
RAFT	Reversible addition-fragmentation chain transfer
TCBZ	3,6-Di- <i>tert</i> -butyl-9 <i>H</i> -carbazole or 4-[3,6-di- <i>tert</i> -butyl-9 <i>H</i> -carbazol-9-yl]-
TCF	(3-Cyano-4,5,5-trimethyl-2(5 <i>H</i>)-furanlylidene)malononitrile
TEM	Transmission electron microscopy
TEMPO	2,2,6,6-Tetramethylpiperidine-1-oxyl
TEOS	Tetraethyl orthosilicate
THF	Tetrahydrofuran
THPTA	Tris(3-hydroxypropyltriazolylmethyl)amine
TICT	Twisted intramolecular charge-transfer
TPP	Triphenylphosphine
UV	Ultraviolet
2P, 2PA	Two-photon, two-photon absorption
$\Delta\nu$	Stokes shift
ϵ	Molar absorption coefficient
λ_{em}	Maximum emission
λ_{max}	Maximum absorption
Φ	Fluorescence quantum yield
f_w	Water fraction

General Introduction

This thesis is mainly devoted to develop D- π -A dipolar dyes and nanoparticles for *in vivo* fluorescence or photoacoustic imaging. Dipolar dyes involve an intramolecular charge transfer between an electron-donating group D and an electron-withdrawing group A linked by a conjugated π bridge. Many advantages such as large Stokes shifts, high two-photon absorption cross sections and ease of modulation on dye absorption and emission by molecular engineering make dipolar dyes promising for fluorescence imaging. Micelle/silica nanoparticles originally developed for drug delivery present excellent potential as vehicles to load organic dyes for bioimaging thanks to their good biocompatibility, suitable size, and surface modifiable capability. Polymer nanoparticles are good candidates for improving dye concentration in photoacoustic imaging.

For this objective, this thesis is separated into two parts. The first part deals with the design and preparation of near infrared emitting dyes and micelle/silica nanoparticles for biphotonic *in vivo* fluorescence imaging, and the second part focuses on near infrared absorbing dyes and polymer nanoparticles for photoacoustic imaging.

In Chapter I, we will present the importance of near-infrared light for bioimaging, and give a detailed overview of dye engineering for red-shifting the optical properties to near-infrared, focusing on several dye families. Then we will detail the working mechanism of photoacoustic imaging technology and introduce the nanoparticles including micelle/silica nanoparticles and polymer nanoparticles for dye loading in fluorescence and photoacoustic imaging.

Chapter II concerns the synthesis of new dyes emitting in the far red/near infrared and the preparation of surface functionalized micelle/silica nanoparticles. In order to obtain a more red-shifted fluorescence as well as an enhanced molecular lipophilicity, we introduce bulky donor groups or strong acceptor groups on the dyes structure. The optical properties of the new dyes in solution and in the solid state will be presented and compared with those of dyes previously synthesized in our laboratory. For particles surface functionalization, we try to modify Pluronic F127 with different functions which enable the covalent linking with functional moieties. The preparation and characterization of the nanoparticles will be detailed. Finally, we will provide *in vivo* biphotonic imaging on living mice.

Chapter III will present our efforts on improving dye concentration for photoacoustic imaging, including the collaboration work on preparation of high-dye-loaded polymer nanoparticles and our try for loading

dyes on micelle/silica nanoparticles surface. The optical and physical properties of the new dyes and nanoparticles will be presented. The preliminary *in vivo* photoacoustic imaging will also be described in this chapter.

Finally, in Chapter IV we will apply our dipolar dyes for primary amine detection, focusing on two dyes bearing dicyanovinyl groups. The sensing behavior and mechanism both in solution and in solid films will be discussed, and a preliminary device for circle detection of primary amine vapor will also be presented.

This thesis will end up with a conclusion and perspective in Chapter V, followed by the experimental part in Chapter VI.

Chapter I. Introduction to NIR Dyes and Nanoparticles (NPs) for *in vivo* Optical Imaging

1. Bioimaging Technologies

Bioimaging technologies are power tools to obtain biological information in non-invasive ways. They can not only reflect the structural morphology of organisms, but also enable researchers to directly monitor different biological processes, such as proliferation and differentiation of cells,^[1] growth and metastasis of tumors,^[2] and even expression of specific genes.^[3] Hence, bioimaging technologies have recently attracted increasing interest in disease diagnosis and drug development fields.^[4-7] Based on different excitation or detection methods, they are mainly divided into ultrasonic, magnetic resonance and optical imaging. In this thesis, we will only focus on two optical imaging technologies: fluorescence and photoacoustic (PA) imaging.

1.1. Biological Transparency Window

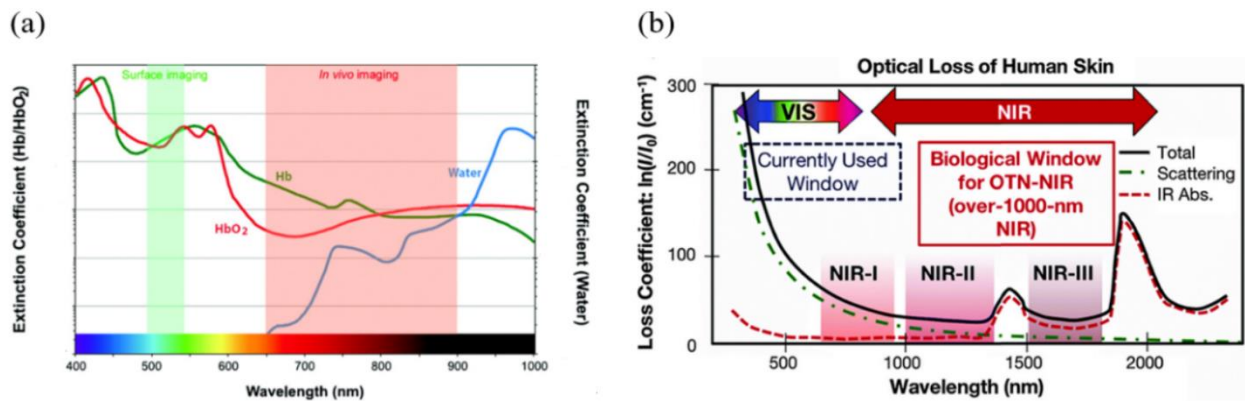


Figure 1 - 1. (a) Extinction coefficients of water and Hb/HbO₂ from 400 nm to 1000 nm;^[8] (b) Absorption spectra of human skin presenting the three different biological transparency windows in the far-red/NIR.^[9]

Imaging depth and spatial resolution are two significant indicators for *in vivo* optical imaging. The former closely relates to the penetration ability of photons in tissues, the latter is heavily affected by biological interference. Organisms are composed by various organic and inorganic components, which absorb and scatter light in varied degrees, leading to the transmission hindrance of photons and strong background noise. In this regard, light source is of vital importance for both fluorescence and PA imaging technologies.

On the one hand, light absorption in organisms derives from a sum of the light-absorbing components, including water, hemoglobin (Hb), oxyhemoglobin (HbO₂), protein and lipids, *etc.* From Figure 1 - 1, one can see that Hb and HbO₂ highly absorb the light in blue and visible range, limiting the photon penetration to a few millimeters.^[8] Thus, light from 245 to 550 nm is most used for surface imaging. Meanwhile, water has gradually increased absorption to light from 650 nm to 1000 nm, which permits a minimum whole extinction coefficient in wavelengths from 650 nm to 900 nm (NIR-I), this range is called the first biological transparency window. Given the greater transparency of biological tissues, wavelengths ranging from 1000 nm to 1300 nm (NIR-II) and from 1300 nm to 1700 nm (NIR-III) are called the second and the third biological windows, respectively (Figure 1 - 1, b).

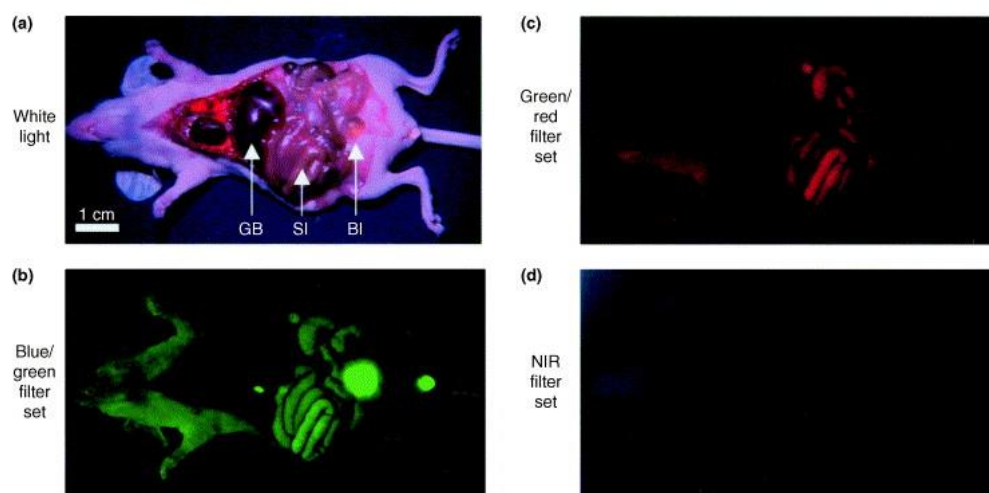


Figure 1 - 2. Auto-fluorescence images of a mice body. (a) Mice exposed under white light. Auto-fluorescence recorded by three different excitation/filter sets: (b) blue/green (460–500 nm/505–560 nm) filter set; (c) green/red (525–555 nm/590–650 nm) filter set and (d) NIR (725–775 nm/790–830 nm) filter set.^[10]

On the other hand, auto-fluorescence from organisms exerts strong background interference to fluorescence imaging. Figure 1 - 2 depicts the fluorescence variation of a mouse body by changing the excitation/emission filter sets. With a blue excitation, a strong green fluorescence appeared spreading all over the mouse skin, gallbladder, small intestine and bladder (Figure 1 - 2, b). The auto-fluorescence is greatly reduced using a green excitation (Figure 1 - 2, c), and is completely inhibited with a NIR filter set. This highlighted the low biological interference of NIR light for *in vivo* fluorescence imaging.

1.2. Engineering of NIR-emitting Organic Dyes

In vivo fluorescence imaging technology mainly relies on contrast agents that can transfer the light energy into fluorescence signals to form the images of the biological tissues, organs or cells by simulating the

distribution of the contrast agents. To fully exploit the potential of NIR light in *in vivo* imaging, extensive attention has been attracted to NIR contrast agents exhibiting spectroscopic properties in one of biological windows previously described. In the past decades, many NIR contrast agents have been developed, including biological molecules, inorganic materials and organic dyes, *etc.*^[11-14] Organic dyes are seen as good candidates for their merits of low cost, ease of preparation, moderate toxicity, high contrast and importantly, finely tunable optical properties by structural engineering.

Since the optical properties of organic dyes originate from the energy gap between the highest occupied and the lowest unoccupied molecular orbitals (HOMO and LUMO), any factors that can decrease the energy gap will shift the optical properties toward higher wavelengths. Generally, the modulations include the length of the π -conjugation, the molecule aromaticity and flatness, the introduction of electron-donating or/and electron-withdrawing substituents (Figure 1 - 3).^[15]

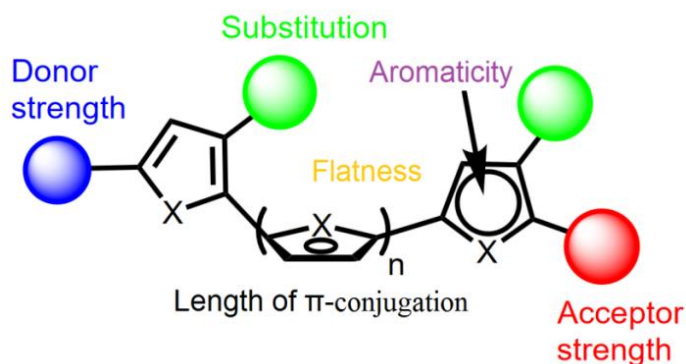


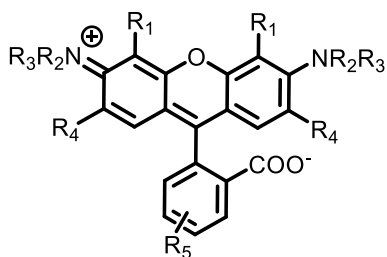
Figure 1 - 3. Possible modulations of fluorophores in order to red-shift the excitation and emission wavelengths.^[15]

Following these simple molecular engineering strategies, it is possible to tune the absorption of dyes up to NIR. However, this is often accompanied by a sacrifice on the fluorescence quantum yield. Indeed, the longer the fluorescence emission wavelength, the smaller the molecular bandgap, thus the stronger competition from non-radiative processes. For this reason, the development of novel NIR dyes has faced many challenges.

Extensive literature survey on the conception of NIR dyes for bio-imaging also makes us realize that the vast majority of studies and structures recently proposed are based on only few generic structures. The following section will therefore present a selection of molecular engineering strategies that have been developed over the recent years to obtain NIR dyes, focusing on three broad families of rhodamine, BODIPY and cyanine dyes. A paragraph will be dedicated to the rare and very recent examples of specific engineering of organic fluorophores emitting in the NIR-II window. Finally, we will end this presentation

by introducing dipolar fluorophores, which although much less studied than the previous examples, are a very interesting route to NIR fluorophores.

1.2.1. Rhodamine Dyes



Scheme 1 - 1. General structure of rhodamine.

Rhodamine (Scheme 1 - 1) is a generic name of an important family of synthetic cationic dyes characterized by a symmetrical π -electron system extending over a diaminoxanthene framework. Such structure confers interesting spectroscopic properties: high molar absorption coefficient, good photostability and, generally, high fluorescence quantum yield. These optical properties can be easily tuned by structural modification and since the 1990s, great efforts have been dedicated to improve the synthesis and to red-shift the optical properties of rhodamines to the far-red. This field has been extensively reviewed and rhodamine derivatives now offer a veritable palette of fluorophores that absorb and emit across the visible spectrum.^[16,17] Beside modification of the two amino group substituents, substitution of the O atom of the xanthene core for other elements, such as C, Si, P or its oxide, S and its oxide, is the most commonly described structural variation. It induces significant red-shifted optical properties that can be ascribed to the stabilization of the LUMO energy level of the fluorophore by σ^* - π^* conjugation between the X-C (X=C or Si) σ^* orbital and a π^* orbital, or by intramolecular charge transfer between the conjugated π -system and an acceptor moiety (P-oxide or SO₂). Thus, carbopyronine or Si-Rhodamines elicit a 50 nm to 90 nm bathochromic shift in comparison to simple rhodamines,^[18-21] whereas the fluorescence emission wavelength of phosphorous-substituted rhodamines (such as Nebraska Red) can reach about 750 nm with relative high fluorescence quantum yield (about 0.2 at 744 nm for NR744).^[22] As for sulfone rhodamines (SO₂R), strong σ^* - π^* interaction between the vacant σ^* orbital from the sulfur atom and the π^* system of the butadiene part (d^* - π^* conjugation) further lowers the LUMO energy level of the fluorophore, absorption can therefore reach about 700 nm, and the fluorescence emission wavelengths are over 740-750 nm (Figure 1 - 4).^[23] One can also find Se and Te replaced Rhodamines absorbing above 600 nm,^[24,25] and also one example of Bismuth rhodamine^[26] absorbing at 635 nm and emitting at 658 nm. However, restricted by heavy-atom effect, these compounds display very weak fluorescence quantum yields (about 0.01 for Se-rhodamine in Methanol,

below 0.001 for Te-rhodamine in water and less than 0.04 for Bi-rhodamine in methanol). However, oxidation diminishes the heavy-atom effect and therefore enhances the fluorescence of TeO or SeO-rhodamine.^[27] Note that all these dyes are efficient singlet oxygen photosensitizers.^[25,26]

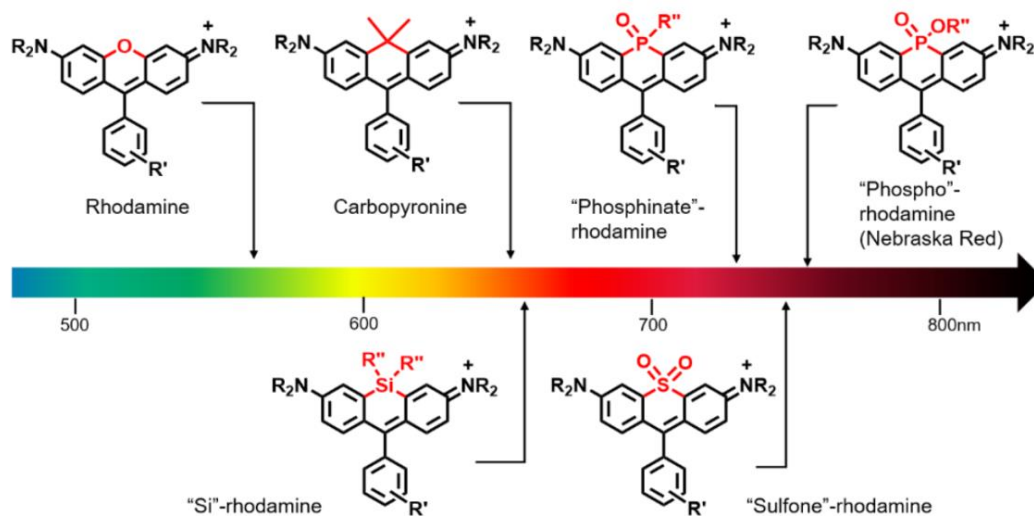


Figure 1 - 4. Tuning rhodamines to NIR by substitution of the xanthene core.^[23]

To give an example of practical application in imaging of such modified rhodamine, let's cite the work by Koide *et al.*, who synthesized a series of NIR-I-emitting Si-rhodamine dyes through extension of the xanthene ring (Figure 1 - 5). Then, **SiR 700** was modified with a NHS group to connect with the anti-tenascin-C antibody for *in vivo* targeted tumor imaging (Figure 1 - 5).^[19,20,28,29]

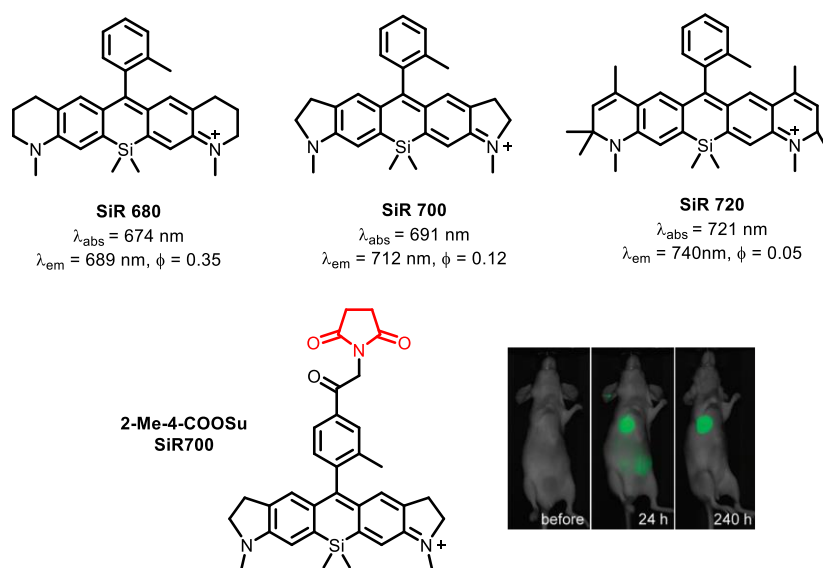


Figure 1 - 5. Chemical structures of SiR 680, SiR 700, SiR 720 dyes, and the *in vivo* tumor imaging of SiR700-labeled anti-tenascin-C antibody based on NHS modified SiR 700 (PBS at pH 7.4 as the solvent).^[28]

However, although these recent developments have improved the situation, higher wavelengths still seem out of reach with “simple” xanthene-like (i.e. 3-fused rings) structures without extension of the π -conjugated system. This is why some rectilinearly π -extended rhodamine dyes with up to 5 fused conjugated rings were reported, such as **TJ730** that displays emission peak at 730 nm or **ECX** that presents maximal absorbing and emitting wavelengths at around 880/915 nm (Figure 1 - 6).^[30,31]

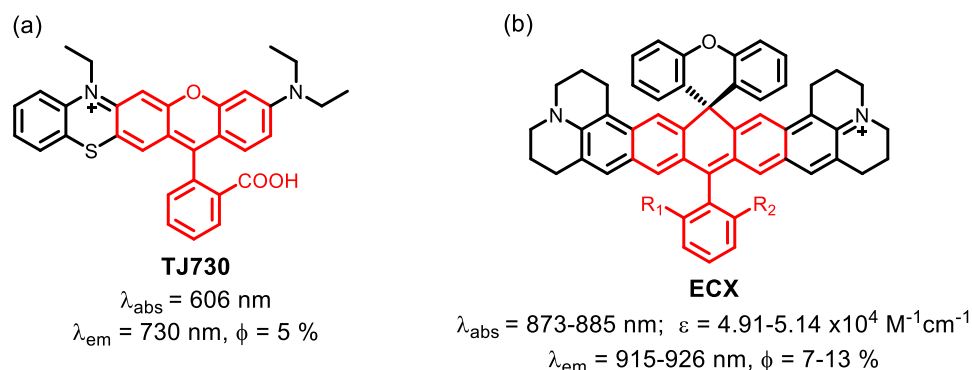


Figure 1 - 6. Chemical structures of **TJ730** and **ECX** (EtOH as the solvent).

Similarly, combining fragments of another chromophore (coumarin, cyanine, *etc*) with the xanthene ring is an efficient approach to increase the conjugation length. The terminology of "hybrid-rhodamine" dyes or hybridisation is sometimes used to describe this strategy (Figure 1 - 7). The first example (maximal absorption at around 700 nm) **Merocyanine A** obtained from the reaction of a chloroheptamethine cyanine with resorcinol in basic condition, was reported by Czerney in 1996,^[32] but fluorescence properties were not described at that time. The fluorophore has been taken over by Lin's group in 2012 who reported good far-red emission in methanol ($\lambda_{\text{em}} = 743 \text{ nm}, \Phi = 0.34$).^[33] Since, quite systematic structure modifications were performed on this class of fluorophores referred as **Changsha** dyes in order to improve their NIR optical properties.^[34-36] Worth noting that one example of **rhodamine-coumarin** hybrid show emission maxima up to 830 nm albeit low quantum yields (< 0.01).^[37]

To the best of my knowledge, there is only one example of a xanthene-based NIR-II fluorophore to date. **RhIndz Ethyl Ester** (Figure 1 - 7, d) was reported by the groups of Hammer, Delcamp and Scott in 2019.^[38] It is a Donor-Acceptor-Donor (D-A-D) fluorophore in which the 3 and 6 positions of the electron poor xanthene core are coupled with an electron rich indolizine ring (Pyrrolo[1,2-a]pyridine). **RhIndz Ethyl Ester** display outstanding long wavelength emission ($\lambda_{\text{abs}} = 920 \text{ nm}/\lambda_{\text{em}} = 1092 \text{ nm}$) for such a small structure, albeit a very weak quantum yield ($\Phi \sim 0.03\%$).

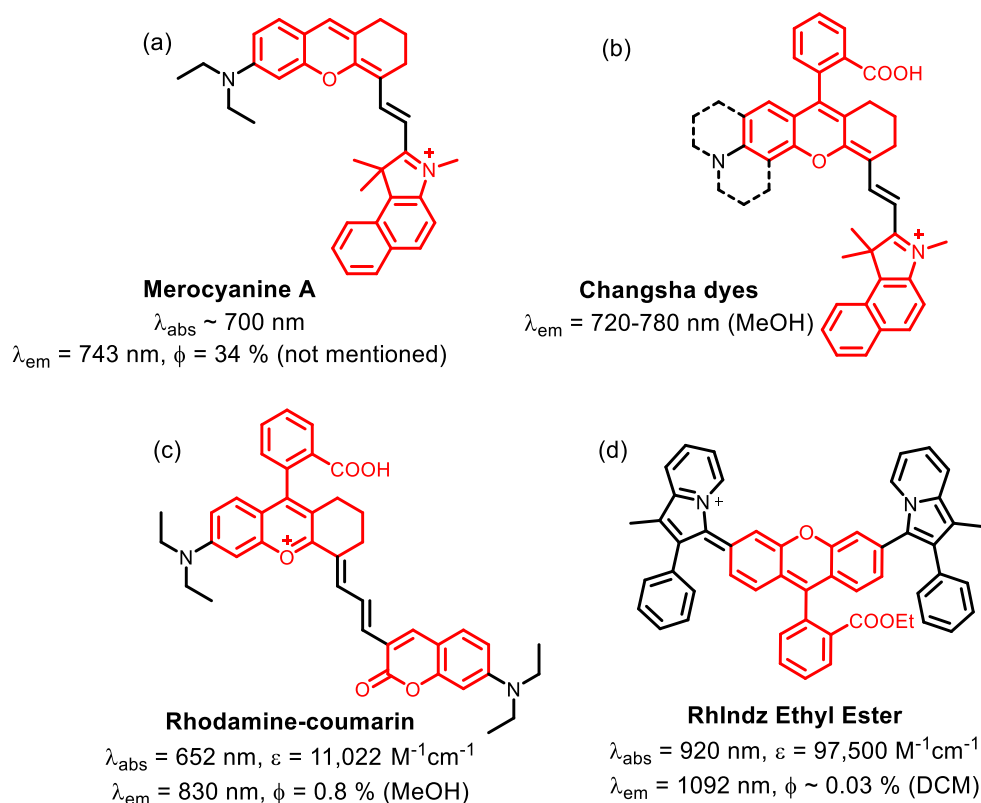
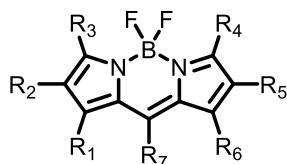


Figure 1 - 7. Chemical structures of *Merocyanine A*, *Changsha*, *Rhodamine-coumarin* and *RhIndz Ethyl Ester* dyes.

1.2.2. BODIPY Dyes



Scheme 1 - 2. General structure of *BODIPY*.

BODIPY (Scheme 1 - 2) is characterized by two pyrrole units that are connected by a methene bridge and both pyrrole-nitrogen atoms are coordinated by the same boron atom. The π -electrons fully delocalize over the framework. BODIPY dyes have many interesting properties such as high molar absorption coefficients (generally above $80,000 \text{ M}^{-1}\text{cm}^{-1}$), good fluorescence emission (Φ commonly above 0.5), as well as excellent photostability. However, parent BODIPY unit has absorption peak near 500 nm. The BODIPY dyes reported rarely emit over 650 nm by now. This limits drastically their potential usage for optical imaging. In this regard, great efforts are needed to tune the classical framework of BODIPY to the NIR.

As a matter of fact, recent reviews have shown growing interest in strategies that can improve the optical

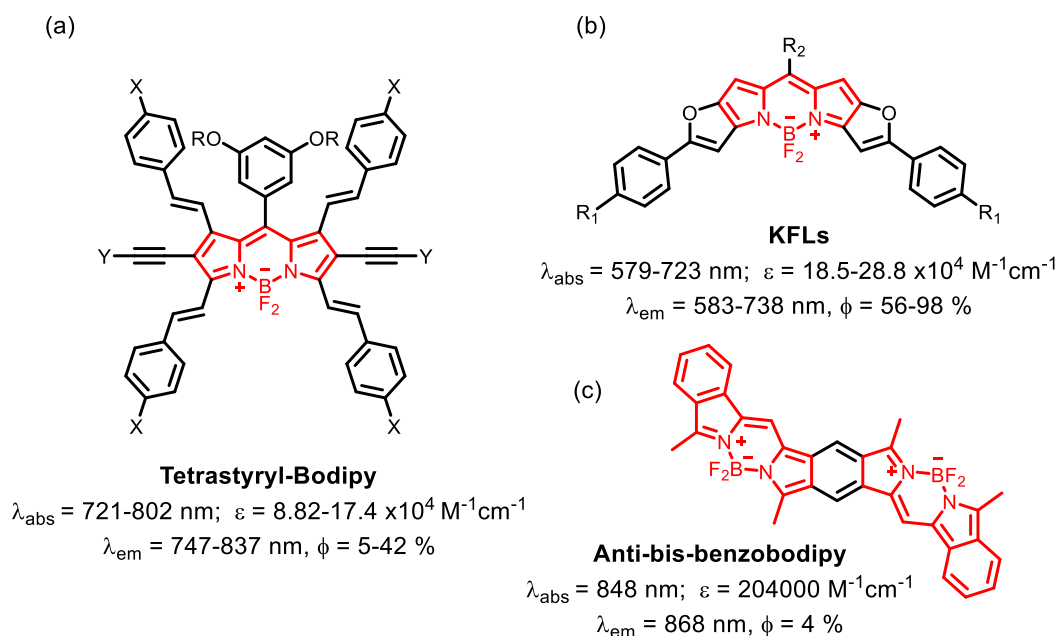


Figure 1 - 8. Chemical structures of **Tetrasteryl-Bodipy**, **KFLs** and **Anti-bis-benzobodipy** dyes (CHCl_3 as the solvent).

properties of BODIPY dyes to reach the biological transparency window.^[39-41] Firstly, for the readily modifiable property of BODIPY extension of the π -electron delocalization is an important manner to tune the absorption and emission of this family of dyes toward NIR. Introducing four styryl units by Knoevenagel-type condensation with aromatic aldehydes leads to **Tetrasteryl-Bodipy** (Figure 1 - 8, a).^[42] It has approximately 200-300 nm red-shifted absorption and emission as well as improved absorption coefficient (up to $173,900 \text{ M}^{-1}\text{cm}^{-1}$) compared with parent BODIPY. By the same idea of extending the π -system, fusion of BODIPY with two furan derivatives at both pyrrole units afforded Keio Fluors (**KFLs**), which have absorption and emission reached the far-red (738 nm) when the *meso* position is substituted by a trifluoromethyl group. Moreover, a BODIPY dimer **Anti-bis-benzobodipy**, reported by Nakamurain 2012,^[43] presented emission reached 868 nm beneficial from its further extended π -delocalization system, albeit much decreased quantum yield (0.04) was observed.

Substitution of the carbon atom in *meso* position by a nitrogen atom results in aza-BODIPY (Figure 1 - 9). In comparison to the normal BODIPY dyes, aza-BODIPY dyes have generally 100 nm red-shifts in both absorption and emission along with improved fluorescence quantum yields. Koch *et al.*^[44] reported last year a monofunctionalized dye **Tetra aryl-azaBODIPY**, in which a BODIPY core acting as a donor unit was linked to an aza-BODIPY as an acceptor unit, the formed cyanine-like structure with a push-pull framework achieved the emission peak at 708 nm with a high quantum yield of 0.46. On the same fashion, **Phenanthrene-fused azaBODIPY**^[45] obtained from phenanthrene fusion by a palladium-catalyzed intramolecular C-H activation show outstanding absorption ($\lambda_{\text{abs}} = 797 \text{ nm}$, $\epsilon > 160,000 \text{ M}^{-1}\text{cm}^{-1}$) and

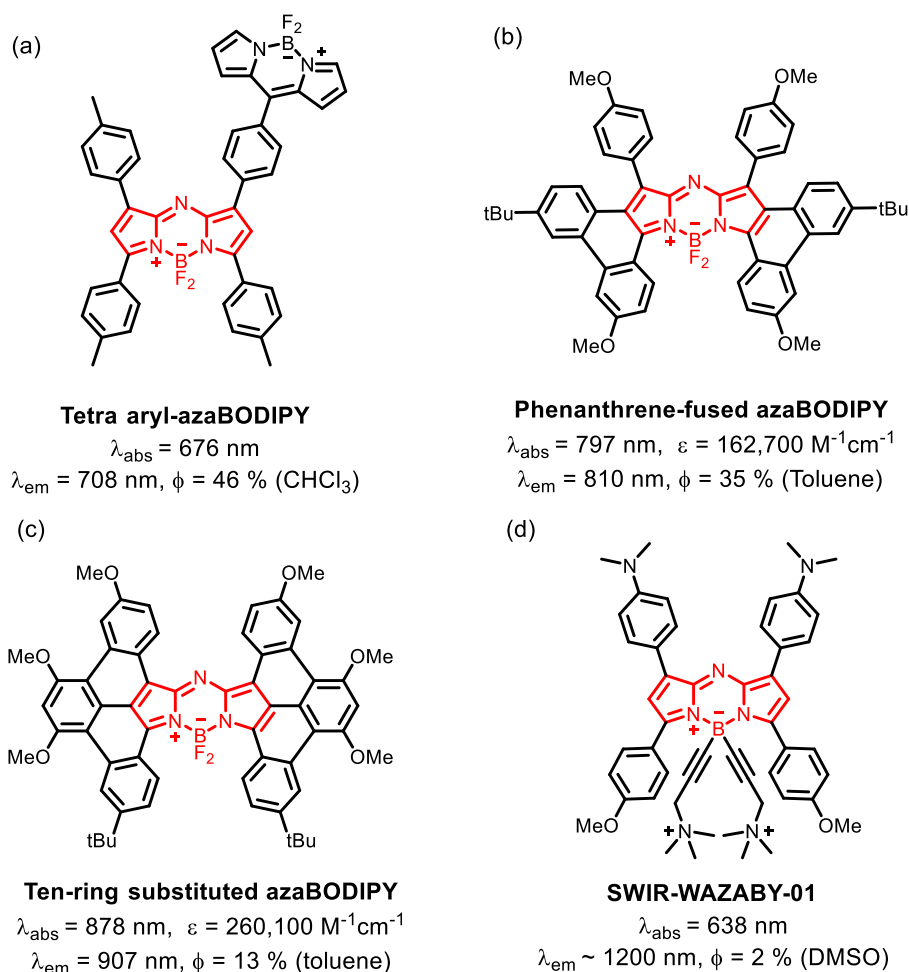
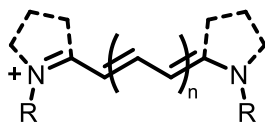


Figure 1 - 9. Chemical structures of **Tetra aryl-azaBODIPY**, **Phenanthrene-fused azaBODIPY**, **Ten-ring substituted azaBODIPY** and **SWIR-WAZABY-01** dyes.

emission ($\lambda_{\text{em}} = 810 \text{ nm}$, $\Phi = 0.35$) properties. In 2018, the same group further synthesized a **Ten-ring substituted azaBODIPY** core by Suzuki coupling between aza-BODIPY and two meta-methoxy phenyl, followed by regioselective oxidative ring-fusion.^[46] The fully annulated structure exhibited nearly planar conformation and excellent optical properties (absorption and emission in toluene: $\lambda_{\text{abs}}/\lambda_{\text{em}} = 878/907 \text{ nm}$, $\Phi = 0.13$), large extinction coefficient ($260,100 \text{ M}^{-1}\text{cm}^{-1}$) and excellent photostability.

Given the improved optical properties of aza-BODIPY compared to BODIPY, more attention to red-shift the optical properties of BODIPY dyes toward NIR have been attracted to functionalization of the aza-BODIPY core. Godard *et al.*^[47] synthesized recently a water-soluble dye **SWIR-WAZABY-01** (Figure 1 - 9, d) by substitution of the boron on aza-BODIPY with ammonium groups. It has emission peak in the NIR-II at approximately 1200 nm in plasma but with quantum yield that needs to be optimized.

1.2.3. Cyanine Dyes



Scheme 1 - 3. General structure of cyanines.

Cyanines (Scheme 1 - 3) can be represented as a D- π -D⁺ cationic structure consisting in an odd number of carbon atoms and two nitrogen-containing heterocycles terminated both ends. The fully delocalized charges give a perfectly symmetric electron delocalization system with no significant bond alternation. Therefore, cyanine dyes are characterized by narrow absorptions with high absorption coefficients ($\log \epsilon > 5 \text{ M}^{-1}\text{cm}^{-1}$). As a rule of thumb, every addition of vinylene unit (CH=CH) on the π -conjugated bridge induces an approximate 100 nm bathochromic shift, to a limit length of 9 to 11 as further extension of the chain cause severe distortion (Peierls-type) resulting in a loss of molecular symmetry.^[48] Consequently, the most published NIR cyanine dyes are heptamethine cyanines (7 CH units in the π -bridge).

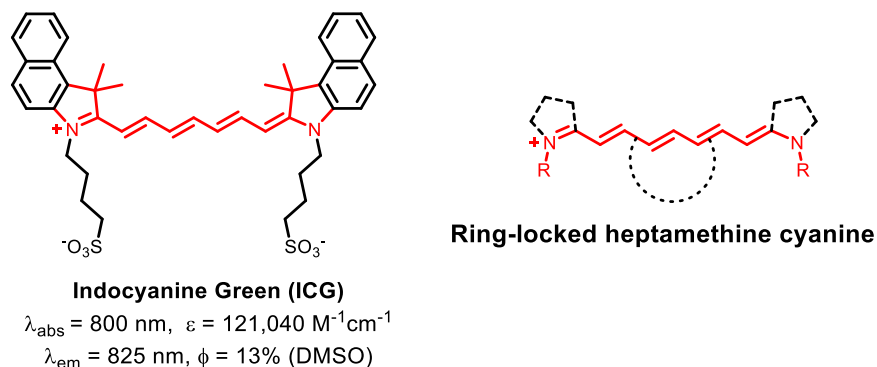


Figure 1 - 10. Chemical structure of ICG and general structure of Ring-locked heptamethine cyanine.

Notably, the huge majority of the Cy7 dyes were developed based on Indocyanine Green (ICG), a dye authorized by the US "food & drug administration" (FDA) agency as a clinical agent in 1954 (Figure 1 - 10). Consequently, ICG has been widely applied in biological researches, including sentinel lymph node mapping,^[49,50] assessment of lymphatic vascular structure and function,^[51,52] vascular repair^[53-55] and oncology imaging,^[56,57] despite its limited quantum yield in aqueous solution, poor photo-stability and high tendency to combine with biological components.

By molecular engineering strategies, many ICG derivatives were developed with improved optical properties for bioimaging. Fixing the heptamethyne chain with a cyclopentyl or cyclohexyl ring can not

only stabilize the π -bridge for an improved photostability, but also provide a reduced torsional movement that otherwise causes non-radiative decay. Hence, lots of researches are currently under development to further red-shift the optical properties of ring-locked heptamethyne-cyanines. Functionalization in the central C4' position offers another possibility for tuning the optical properties by modification of the charge delocalization along the π -framework.^[58] Heptamethyne-cyanines with alkyl-amino or aryl-amino group exhibit larger Stokes shift (> 140 nm) and enhanced fluorescence, while creation of a C-C(Ar) bond at the same position enhanced the stability. Attachment of C4'-O-aryl or C4'-S-alkyl linkers is by far the most commonly used approach for bioconjugation or introduction of various sophisticated groups for the design of stimuli responsive probes (pH, metal ion, anions, uncaging, and so on...),^[59,60] Such as dye **IR800-CW** (Figure 1 - 11, a), it has been widely used to label numerous of biomolecules after functionalization with a NHS (**IR800-CW-NHS Ester**) or a maleimide reactive group (**IRDye® 800CW Maleimide**) (Figure 1 - 11, b and c).^[61-63]

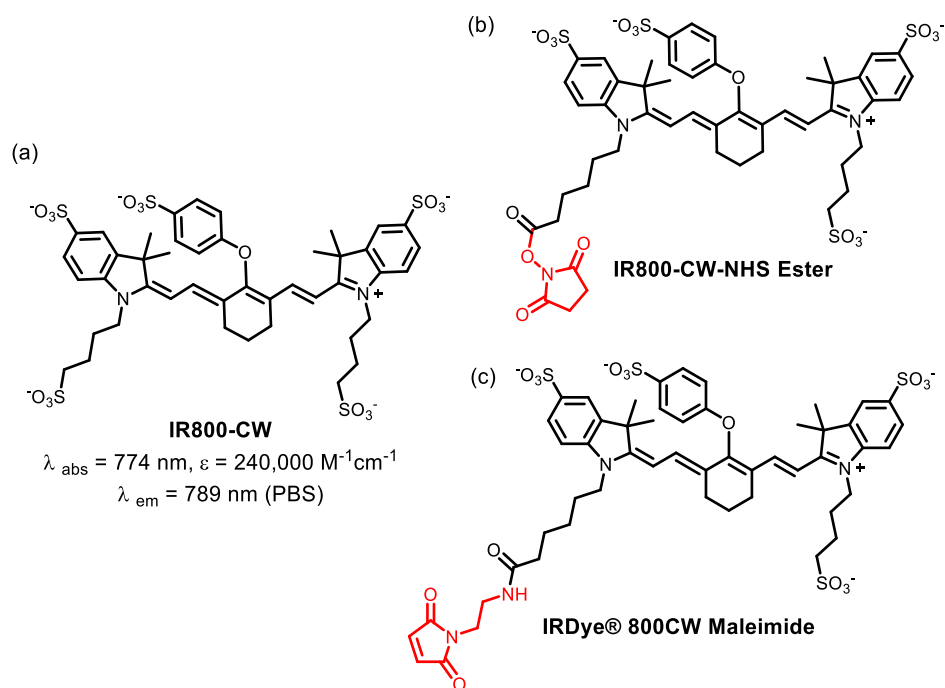


Figure 1 - 11. Chemical structures of **IR800-CW**, **IR800-CW-NHS Ester** and **IRDye® 800CW Maleimide**.

Extension of the π -conjugation system remains the main approach for further red-shift, but few examples of higher length cyanines are reported.^[64] **ONITCP** and **ODNITCP** (Figure 1 - 12, a and b) are the rare examples of nonamethyne cyanine dyes, reported by Ukrainian chemists in the 1984. The optical properties and in particular fluorescence quantum yield in the NIR were studied by Rurack *et al.* in 2011.^[65] Owing to the longer π -conjugated systems, the dyes showed red-shifted emissions up to 900 nm. However, their

fluorescence quantum yields are low, for an enhanced internal conversion and a narrowed HOMO-LUMO energy gap.

π -extension can also be achieved by ring fusion taking a benzo[cd]indole motive instead of a benzo[e]indole for instance, such as the commercially available dyes **IR1048**, **IR1050** and **IR1051**. In this way, Zhang *et al.* redesigned an old dye family by adding sulphonic groups for water solubility. Compound **FD-1080** show a remarkable NIR-II emission ($\lambda_{\text{abs}}/\lambda_{\text{em}} = 1064/1080$ nm, $\Phi = 0.31\%$), together with excellent aqueous solubility. Though the quantum yield is low, it can be increased to 6% by forming the **FD-1080-FBS** complex with fetal bovine serum FBS.^[66]

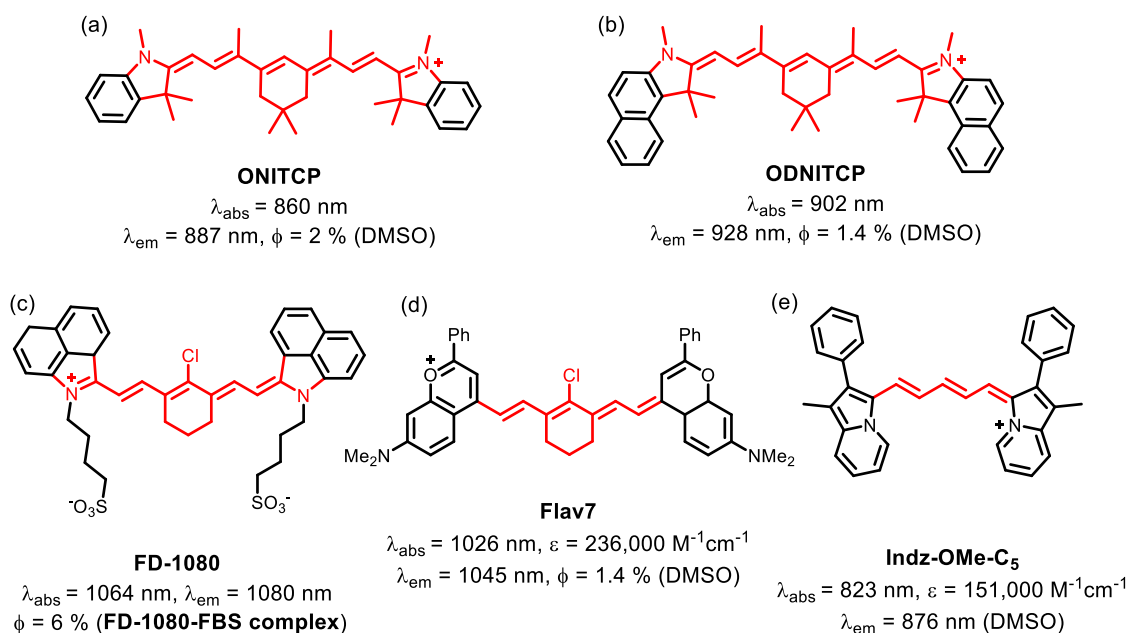
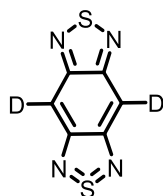


Figure 1 - 12. Chemical structures of **ONITCP**, **ODNITCP**, **FD-1080**, **Flav7** and **Indz-OMe-C₅** dyes.

Heterocycle modification is an alternate approach and represents a promising avenue toward stable NIR-emitting polymethine dyes. Extending heterocycle conjugation, varying the heteroatom from nitrogen to oxygen to other chalcogens, or adding electron-donating groups (or combination with other moieties) have been shown to bathochromically shift polymethine dyes. Thus, modified flavylum (with oxygen heterocycles) or thioflavylum (with sulfur heterocycle) polymethine fluorophores, inspired by older dyes **IR-26**, **IR-1048**, **IR-1051** or **IR-1061**,^[67] were recently reported for bio-imaging in the NIR-II window. **Flav7**, a dimethylamino flavylum anthocyanin dye displays fluorescence emission wavelength peaking at 1045 nm for a molar extinction coefficient of 236,000 L·mol⁻¹·cm⁻¹, and a remarkable 5% Φ in solution.^[68]

Finally, Delcamp's group reported recently the use of a novel donor group, pyrrolo[1,2-a]pyridine, to build new cyanine fluorophores of various bridge lengths, showing very red-shifted optical properties compared to the "classical" indo-cyanine.^[69] Indeed, a pentamethine cyanine (**Indz-OMe-C₅**), with an emission at around 900 nm is reported paving the way to a completely new molecular engineering.

1.2.4. Some Other Organic NIR-II-emitting Dyes



Scheme 1 - 4. General structure of BBTD.

Despite the high interest of emission in the NIR-II window for bioimaging, very few fluorophores have been designed meeting the study in this wavelength range. It is only very recently that the first specific dyes have appeared and, to date, they are almost all based on the benzobisthiadiazole core (**BBTD**) (Scheme 1 - 4) as conjugated π system and having a D-A-D structure. Such compounds were initially designed as NIR fluorophores for non-doped NIR OLEDs.^[70] Theoretical calculations have since shown that the existence of a hypervalent structure leads to a much lower LUMO level and plays a key role in the red-shift of fluorescence emission in the NIR-II region.^[71]

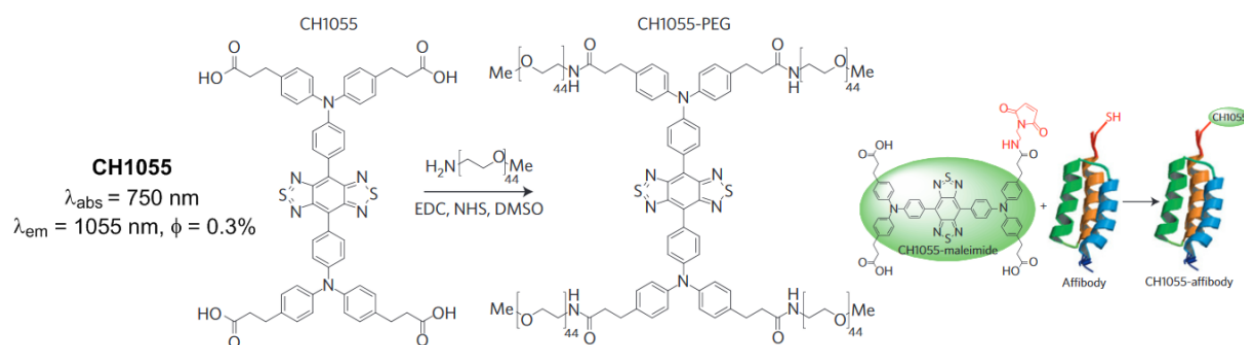


Figure 1 - 13. Chemical structures of **CH1055**, **CH1055-PEG** and synthesis of **CH1055-affibody** (water as the solvent).^[72]

Dai's group^[72] reported the NIR dye **CH1055** and substantially increased its water solubility by introducing four polyether glycol (PEG) chains (Figure 1 - 13). The formed **CH1055-PEG** presented high pharmacokinetics, fast renal clearance and good bioimaging properties. Meanwhile, the modification of the carboxylic acid group by a NHS makes it possible for **CH1055** to connect to affibody. The **CH1055-affibody** with a high biocompatibility as well as a good targetability was used for the image-guided surgery

in a mouse body. Additionally, another CH1055 based dye **CH1055-4Glu-AE105** designed by Kubegovic *et al.* (Figure 1 - 14) was successfully used for an image-guided brain surgery.

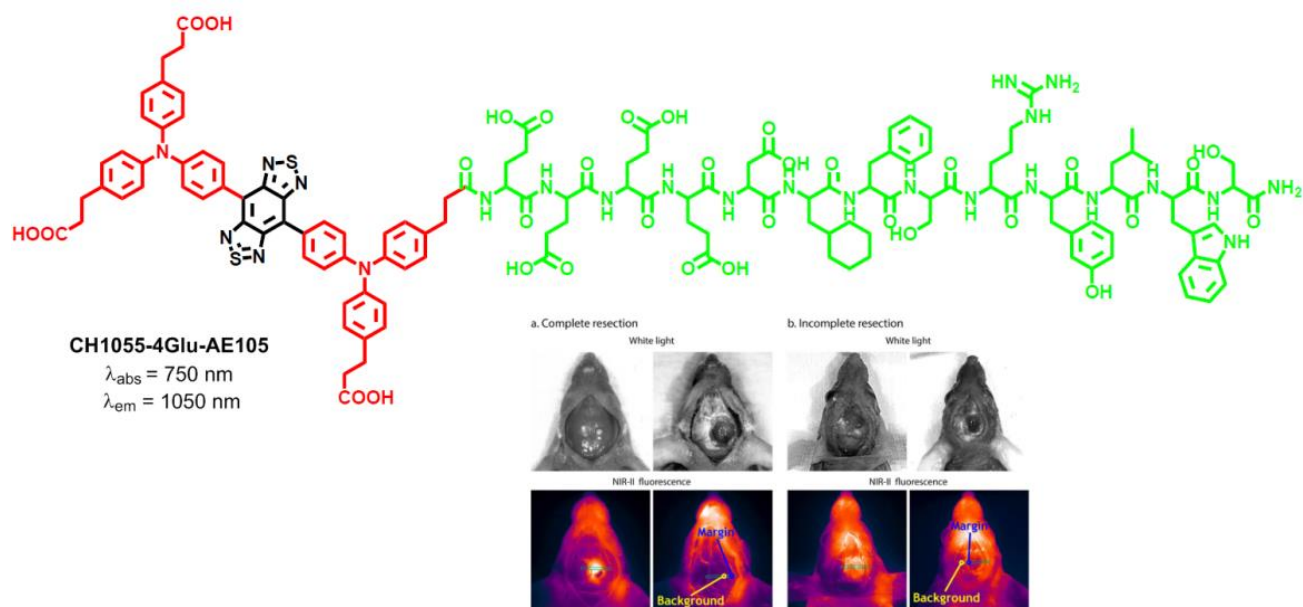


Figure 1 - 14. Chemical structure of dye **CH1055-4Glu-AE105** and its application on tumor surgery.^[72]

Further shifting to higher wavelength (up to 1100 nm) was achieved through extension of the π -conjugation system by adding an electron rich thiophene between the BBTD core and the nitrogen donor^[73] or using a fluorene to further substitute the N,N-diphenylamino group (Figure 1 - 15).^[74]

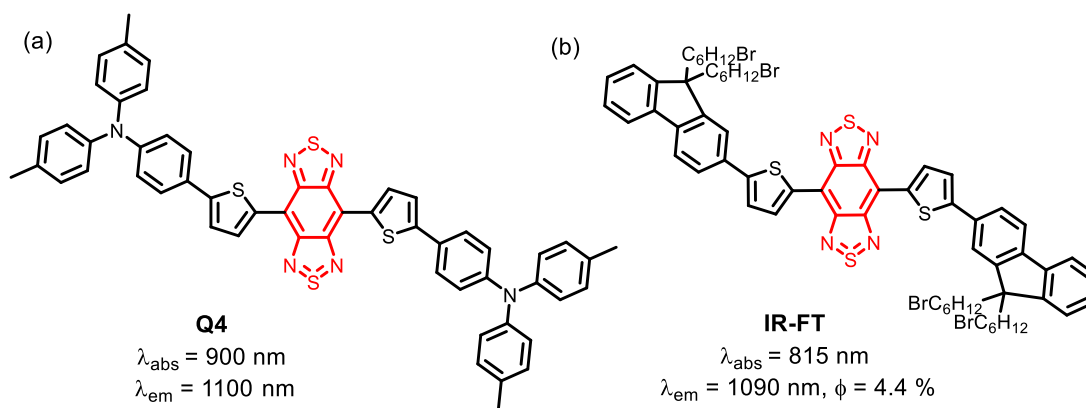
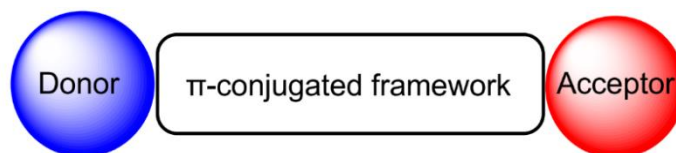


Figure 1 - 15. Chemical structures of **Q4** and **IR-FT** dyes (DMSO as the solvent).

Interestingly, theoretical calculations predicted that further red-shift would be possible provided larger ring-fused (up to 5 rings) systems are used, but still encompassing hypervalent BBTD. This opens the way to future screening out of potential candidates for excellent NIR-II molecular fluorophores. What the authors

do not mention, on the other hand, is the stability of these extended motives towards oxidation, which should not be very high.^[71]

1.2.5. Push-pull Dipolar Dyes



Scheme 1 - 5. General representation of a dipolar fluorophore pattern.

Push-pull dipolar dyes are characterized by a D- π -A scaffold (Scheme 1 - 5) in which an electron donor group (D) is linked to an electron acceptor group (A) by a π -conjugated framework. This kind of organic dyes have been widely used in material science such as optoelectronic,^[75] functional polymers^[76] and devices based on nonlinear optical effects,^[77] *etc.*

Dipolar dyes have a particular photophysical characteristic: the absorption of a photon by the chromophore is accompanied by a charge transfer from the donor to the acceptor, namely intramolecular charge transfer (ICT). Optical properties will therefore depend on the strength of the D/A pair, the length and the type of the conjugated bridge. Thus, spectroscopic modulation is quite easy to perform by changing the strength of the D/A pair or the conjugated bridge. Normally, increasing the strength of the D/A pair, or elongating the bridge will induce a red-shift in the optical properties.^[78-80]

Another characteristic of dipoles is their strong Stokes shift which results from the large difference between the ground state (neutral) and the excited state (zwitterionic). In addition, the Stokes shift is increased in polar solvents by solvatochromism. Comparatively to the other dyes families presented before, dipolar fluorophores often have moderate (molar absorption coefficient between 20,000 and 60,000 L·mol⁻¹·cm⁻¹) but broad absorptions, so it can in theory be difficult to obtain high brightness ($B = \Phi \cdot \epsilon$). However, a large Stokes shift avoids the reabsorption of higher energy photons emitted by neighboring fluorophores. The larger the Stokes shift, the easier it is to distinguish a photon from the excitation source from a photon emitted by the fluorophore and thus to collect the entire fluorescence spectrum. A large Stokes shift also means that the emission is considerably shifted into the red or even the near-infrared for an absorption in the visible.

Finally, owing to the strong ICT dipolar dyes generally possess good two-photon absorption (2PA) properties. The most characteristic feature in the 2PA properties in non-centrosymmetric D- π -A molecules is that excited states that are one-photon allowed states are also two-photon allowed. Consequently, the

maximum 2P occurs at wavelengths exactly twice the maximum absorption wavelength, so NIR (800-1200 nm) for an absorption in the visible (400-600 nm), making it possible to use far-red/NIR for excitation by 2PA.

Dipolar fluorophores are ideal structures to design environment sensitive fluorescent probes because they show strong solvatochromic properties. Indeed, most of fluorescent polarity probes or viscosity probes used in bioimaging, membranes staining probes that show fluorescence in the rigid environment of cell membranes, fluorescent probes for cell membrane tension, are dipolar fluorophores.[81-84] In the years 1990-2000s, a great deal of work has been dedicated to the design of efficient fluorescent fast-response voltage-sensitive optical probes showing good affinity for cell membrane. These works focused on charged dipolar fluorophores incorporating nitrogen as electron donor groups (mostly dialkylamino groups) and phenyl- (or naphthyl-) styryl-pyridinium moiety has electron-acceptor part (Figure 1 - 16, a).^[85,86] The same fluorophores, because of their high non-linear optical (NLO) properties, were later used for fast-response voltage-sensitive second-harmonic generation microscopy combined to 2P microscopy (Figure 1 - 16, b).^[87,88] In order to improve the fluorophore NLO properties, but also to red shift absorption and emission maxima to the NIR, considerable molecular engineering has been performed, naturally by playing on the nature and extent of the system-conjugated, incorporating groups such as amino-oligothiophene or porphyrine cycles.^[89]

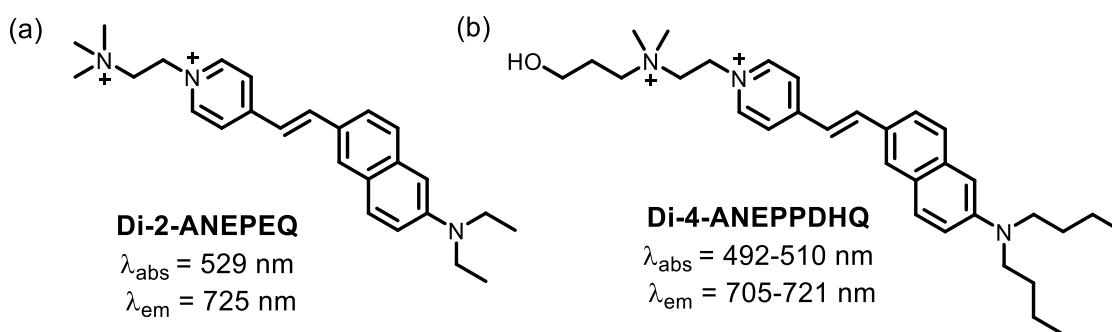


Figure 1 - 16. Chemical structures of **Di-2-ANEPEQ** and **Di-4-ANEPDHQ** dyes (EtOH as the solvent).

In the group, we designed amphiphilic far-red emissive dipolar fluorophore based on the strong electron-acceptor group dicyanoisophorone (Figure 1 - 17) for cell membrane imaging. Using copper(I) catalyzed alkyne-azide cycloaddition, we introduced saccharide moieties as water solubilizing groups to create the amphiphilicity. The position and the number (di- or trisaccharide) of saccharide structures were varied and very interesting fluorophores results were obtained with emission up to 694 nm in water.^[90]

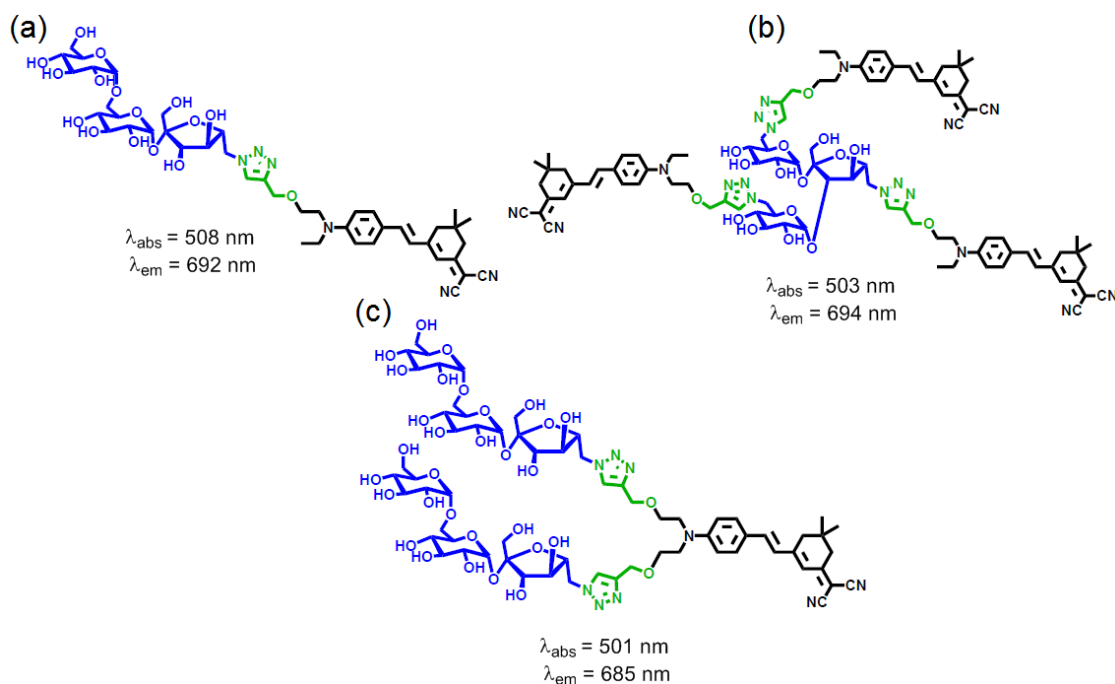


Figure 1 - 17. Chemical structures of the amphiphilic far-red emissive dipolar fluorophore dyes reported by our group (water as the solvent).^[90]

Moerner and Twieg used the strong 2-dicyanomethylene-3-cyano-2,5-dihydrofuran (TCF) acceptor group in small push-pull structures (**DCDHF**), in which it is separated from the donor (a dialkylamino group) by different π -rich conjugated networks. Like this, they design different series of far-red emitting compounds for single-molecule imaging in cells, amongst which some photo-activable probes were used for super-resolution microscopy.^[91,92] Recently, using a 2-(4-methoxyaryl)-indolizine unit as the electron donor, the TCF group as the electron acceptor and a alkene-thiophene spacer as the conjugated π -bridge, Delcamp *et al.*^[93] synthesized a push-pull dye **AH25** (Figure 1 - 18, b) with an unprecedented strong ICT. For this reason, **AH25** has an absorption peak at 925 nm and emission in the NIR-II ($\lambda_{\text{em}} = 1050 \text{ nm}$) with a Stokes shift of 180 nm.

The dipolar structure is also particularly interesting for the design of solid-state emitting fluorophores and for fluorophores displaying aggregation-induced emission (AIE) properties. Indeed, interactions between permanent dipoles can force particular aggregation patterns necessary to observe a solid-state emission. Also, the large Stokes shift characterizing most often the fluorescence of these compounds means that the spectral overlap between absorption and emission is minimal, which is an advantage for solid-state emission because it limits reabsorption phenomena and de-excitations by Förster-type energy transfer. Ben Zong Tang's group is more and more interested in dipolar fluorophores presenting an interesting fluorescence in aggregates, especially for applications in biology and imaging.^[94-97] Most of the fluorophores they reported

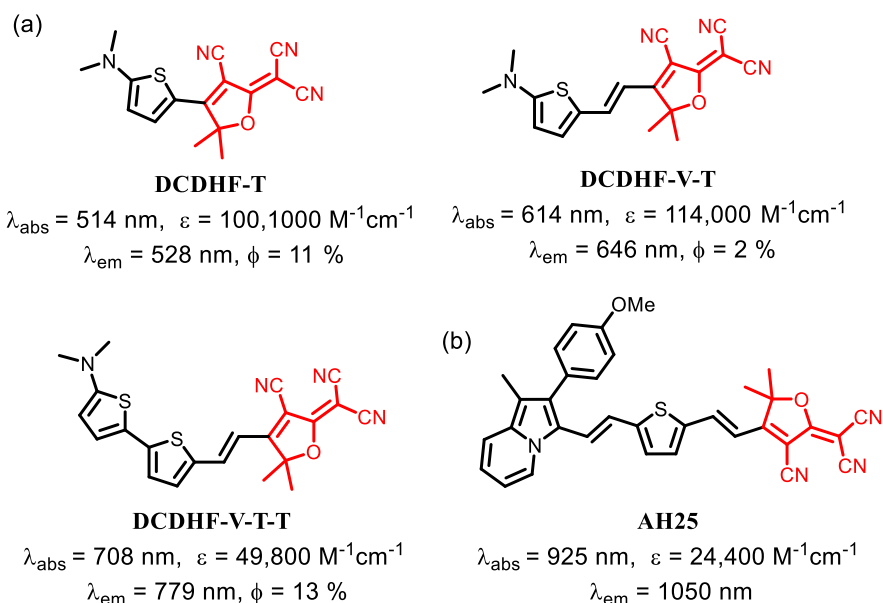


Figure 1 - 18. General structures of **DCDHF** dyes and **AH25** (toluene as the solvent).

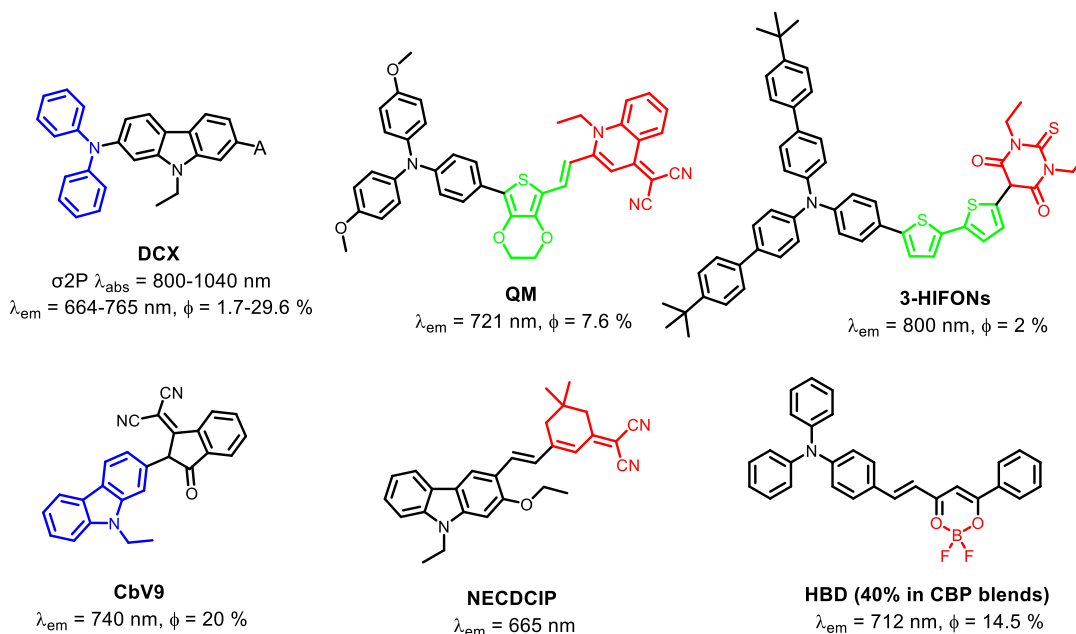


Figure 1 - 19. Chemical structures of **DCX**, **QM**, **3-HIFONs**, **CbV9**, **NECDCIP** and **HBD** dyes (in aggregates in water except for **HBD**).

are based on the *N,N*-diphenylamino- group as electron-donor part. Such group is called by the authors AIE-gen, i.e. inducing AIE properties. Various electron-acceptor part and π -bridge were introduced affording fluorophores having emission up to 700 nm in solution and in the aggregate-state, and also increased 2PA cross-section between 800 and 1000 nm (**DCX**, Figure 1 - 19, a). Similarly, Guo, Zhu and co-workers obtained small dipole **QM** emitting in the solid up to 721 nm using a quinoline-malononitrile electron-

acceptor motive and a thiophene bridge.^[98] Before Ben Zong Tang, Blanchard-Desce's group reported very similar fluorophores encompassing a bis-thiophene or thienothiophene units in the π -conjugated bridge and thiobarbiturate or dicyanovinylidene end pull group. Emission up to 800 nm in NPs (**3-HIFONs**) was obtained which is very interesting for *in vivo* imaging despite a low quantum-yield ($\Phi = 2\%$).^[98-100]

Besides triphenylamine, other donor groups include dimethylamine or *N*-ethylcarbazole. Singh *et al.* synthesized charge-transfer fluorophores with these two groups and various electron-acceptors.^[101] These chromophores showed intense fluorescence in aggregates reaching a 20% efficiency at 740 nm (**CbV9**). Sekar and Lanke also use the *N*-ethylcarbazole group in association with the dicyanoisophrone (**NECDCIP**).^[102] Finally, some dipolar boron complexes of 2'-hydroxychalcones and hemicurcuminoids (**HBD**) were described by D'Aléo *et al.* (the -OBF₂O- unit is a strong electron-acceptor group).^[103] Emission wavelengths beyond 700 nm and even up to 855 nm have been observed in the solid-state for some of these remarkable compounds, although quantum yields are not very high ($\Phi = 1-3\%$).

Following its initial work on dicyanoisophorone chromophores, our group has been working on the development of different series of small push-pull dipolar dyes displaying emission properties in solution, but also in the solid state (crystal and aggregates due to aggregation-induced properties). So far, several families of far-red- to NIR-emitting dyes have been developed.^[104-106] In particular, we focused on the investigation of new electron-withdrawing groups.

During the course of his PhD, Zheng Zheng designed and synthesized two series of NIR dyes (**a1-a11**, Figure 1 - 20) with 9,9-diethyl-9*H*-fluorene or fluorene as the conjugated π bridge, which was connected to either a diphenylamine or a carbazole donor group. Varying the electron acceptor part allows us to reach emission up to 800 nm in solution in apolar solvent and in the solid state ($\lambda_{em} = 595\sim 807$ nm, Φ from <0.01 to 0.2). Significantly, all these dyes showed good 2PA properties between 900 and 1200 nm, thus are able to be excited by light in the NIR-II.^[107-109] Zheng Zheng also encapsulated the most promising fluorophore **a10** in silica-pluronic NPs (*vide infra* part Dye-loaded F127-SiO₂ NPs). He showed that the emission properties in this kind of NPs were the same as those obtained in apolar solvent. So, NPs with very brightness ($\Phi = 39\%$ at 650 nm) were obtained and *in vivo* 2P microscopy performed.^[108] For the solid-state emissive fluorophores, Zheng Zheng obtained nanoaggregates NPs of roughly 80-100 nm by solvent shifting re-precipitation and stabilization by pluronic F127. The preparation method was later optimized by Maxime Rémond during his PhD.^[110,111]

By replacing the fluorene unit for a bithienopyrrole moiety, and using a triphenylamine group as the electron donor, Maxime Rémond obtained another series of NIR-emitting dyes (**BTN-based dyes**) with

more red-shifted absorption and emission, as well as much higher quantum yields compared to the fluorene-based dyes (Figure 1 - 21). Nevertheless, all the **BTN** dyes are prone to form non-emissive aggregates in both aqueous and organic solvents due to the poor solubility, as a consequence, they could hardly be incorporated efficiently into NPs.^[110]

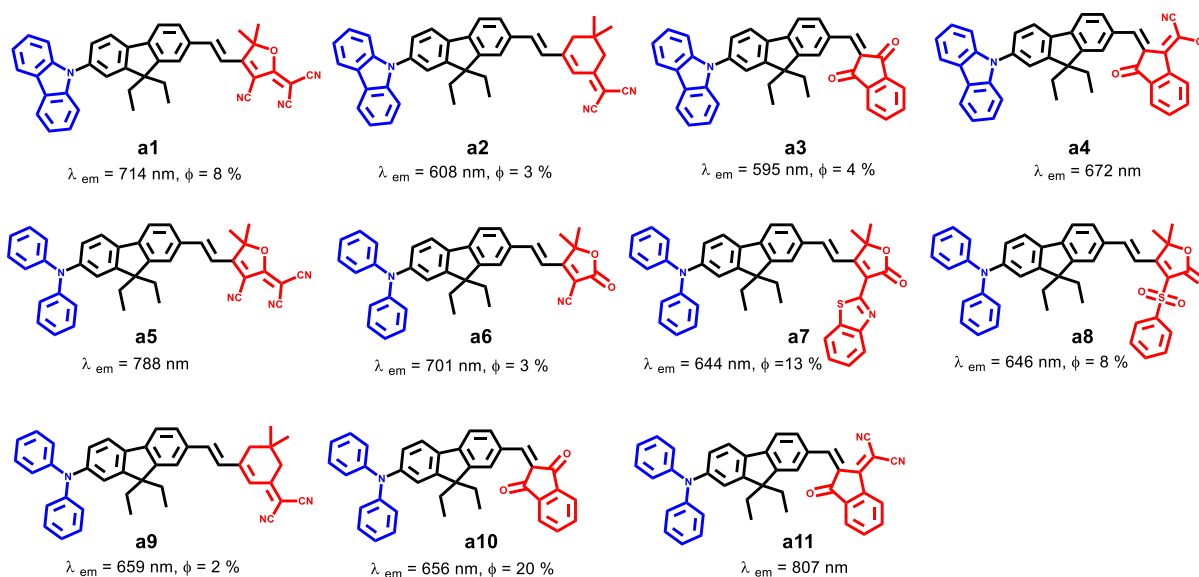


Figure 1 - 20. Chemical structures of **fluorene-based** dyes previously synthesized in our laboratory (in solid state).

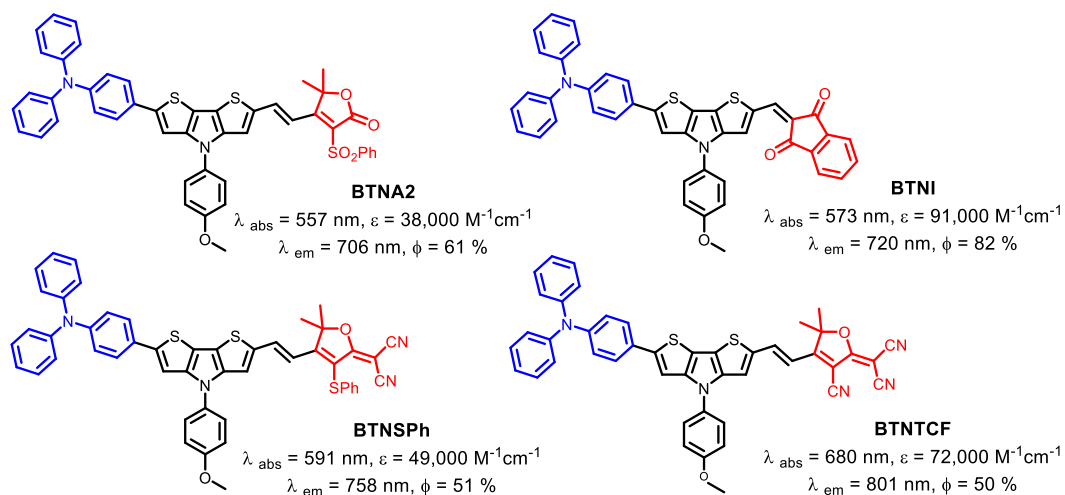


Figure 1 - 21. Chemical structures of **BTN-based** dyes previously synthesized in our laboratory (CHCl_3 as the solvent).

1.3. NIR Organic Dyes for *in vivo* PA Bioimaging

1.3.1. PA Bioimaging

Different from fluorescence bio-imaging, PA imaging is a technology based on optical excitation but acoustic detection. The imaging process is illustrated in Figure 1 - 22. By a laser excitation, the PA contrast agents in tissue convert the light energy into heat, leading to a local temperature rise and a thermo-elastic expansion of the tissue. With a pulsed laser beam, an alternation of tissue expansion and retraction is achieved, leading to the pressure waves propagating through the tissue. Finally, the ultrasonic transducers receive the pressure waves and transfer them into the pictorial information. In addition, the formed tissue image has a one-to-one correspondence with the contrast agent distribution on the premise of a uniform excitation.

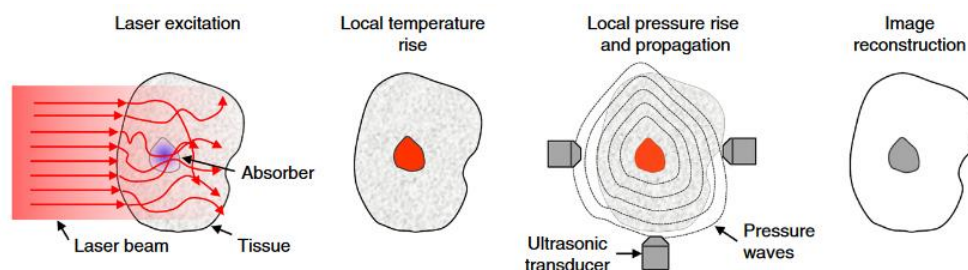


Figure 1 - 22. Principle of PA imaging.^[112]

PA imaging technology based on optical excitation and acoustic detection is of merits from both fluorescence imaging and ultrasonic imaging technologies. On the one hand, the acoustic signal scattering in biological tissues is two to three orders of magnitude lower than that of optical signal, the PA imaging depth is thus only limited by the penetration depth of the excitation. A 5-6 cm of depth can be reached while keeping the laser power harmless. Consequently, PA imaging technology possesses a greater imaging depth in comparison to fluorescence imaging.^[113,114] On the other hand, the variation in the form of the input and output signals allow a minimized background interference, which is beneficial for higher contrast than pure ultrasonic imaging.

1.3.2. Dyes for PA Imaging

Innovation of the PA imaging instrument is by no means easy; this makes optimization of the PA contrast agents more significant in PA imaging. Hemoglobin as a biogenic component has played an essential role in development of PA imaging technic. However, it is restricted by short absorption wavelength and discontinuity of blood vessels.^[115-119] Accordingly, various exogenous contrast agents with strong absorption

in NIR region have been used in PA imaging over the past decades, including small NIR organic dyes, gold and polymer nanostructures, *etc.* (Figure 1 - 23). As far as organic dyes are concerned, most of them that have been successfully used for PA imaging are old known compounds, such as **ICG** and Evans blue (**BE**).^{[111, [120]} Indeed, to our best of knowledge, no specific dye engineering for PA has been done yet as the link between molecular structure and PA signal generation remains quite opaque. In light of the following examples, we can just say that dyes with strong absorption in NIR and weak fluorescence emission may be promising for PA imaging.

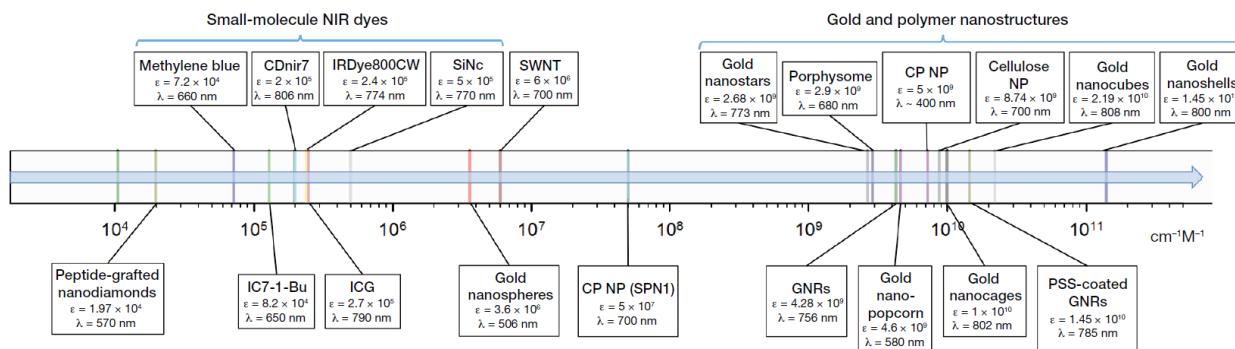


Figure 1 - 23. Extinction coefficients of different PA contrast agents.^[116] Abbreviations: SWNT (single-layer carbon nanotubes), CP NP (conductive nanoparticles) and GNR (gold nanorods).

The relationship between the absorption and PA signal of **ICG** revealed its good PA response to NIR excitation (Figure 1 - 24, a).^[121] However, **ICG** can hardly be directly used for *in vivo* PA imaging due to its short blood half-life of a few minutes and high tendency to bind with many proteins in plasma.^[122] This promoted the generation of many **ICG**-labelled polypeptides^[123,124] and antibodies.^[125-128] Furthermore, the fluorescent and PA properties make the use of **ICG** possible for bimodal imaging. Wang *et al.* imaged the sentinel nodes of a mouse through both fluorescence and PA imaging (Figure 1 - 24, b and c).^[120] Particularly, by comparison of the lateral resolution of the two imaging techniques as a function of the imaging depth, PA image presented more than ten times higher resolution than fluorescence image at a depth of a few millimeters.

BE is a biological dye with high affinity to albumin (Figure 1 - 25). The **BE**-albumin complex as a PA contrast agent in serum presented higher sensitivity than hemoglobin without the issue of blood discontinuity.^[120] Specifically, by tracing the diffusion of the free **BE** molecules in vascular system after injection, it is possible to monitor blood-brain barrier, assess potential leaks caused by head trauma as well as measure drug transfer efficiency.^[129]

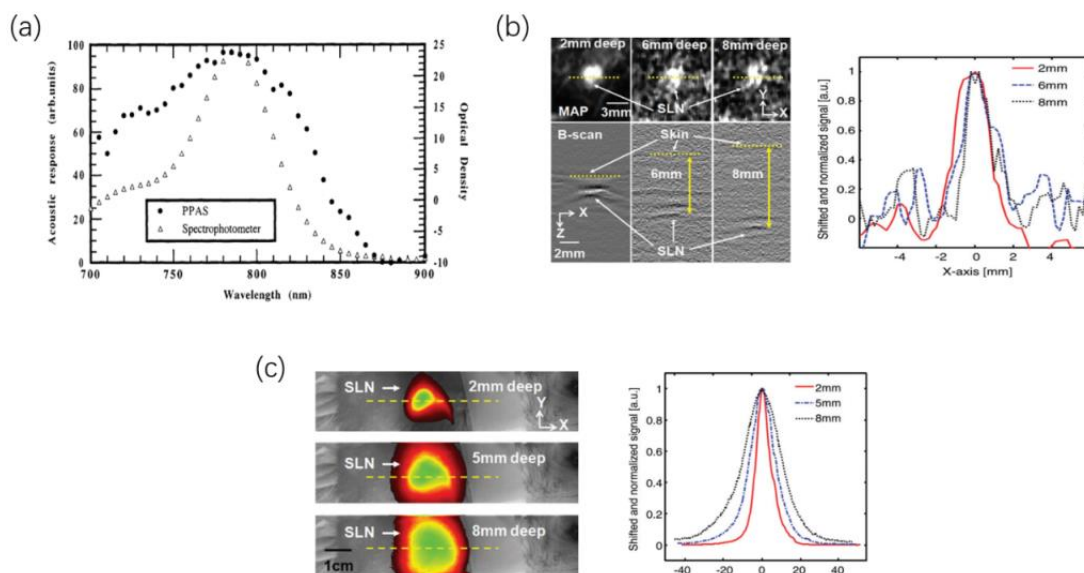


Figure 1 - 24. (a) optical (triangles) and acoustic (rounds) absorption of $ICG^{[121]}$; (b) depth-dependent bimodal imaging of sentinel nodes (SLNs) using ICG as contrast agents and PA images and the corresponding three 1D profiles taken from along the dotted lines in the maximum amplitude projection (MAP) images; (c) fluorescence images and the corresponding three 1D profiles taken from along the dashed lines.^[130]

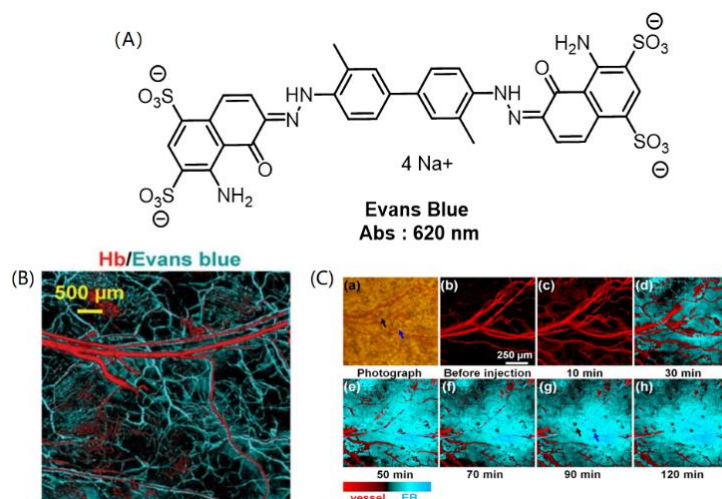


Figure 1 - 25. (A) Chemical structure of *Evans blue*; (B) Combined PA imaging of hemoglobin (in red, excitation 570 nm) and *Evans blue* (in blue, excitation 610 nm) immediately after injection;^[131] (C) PA imaging following diffusion of *Evans blue* into the extravascular system after injection.^[120]

Cyanine dyes with strong absorptions in NIR region are considered promising for PA imaging. Onoe *et al.*^[132] reported a symmetric cyanine **IC7-1-Bu** and compared it to **ICG** in terms of *in vivo* fluorescence imaging and *in vitro* PA imaging (Figure 1 - 26). From the fluorescence imaging following the duration of **IC7-1-Bu** or **ICG** in mice body after injection and the PA intensity of **IC7-1-Bu** or **ICG** in aqueous solution, **IC7-1-Bu** showed a much longer biological half-life and 2.3-fold higher PA signal than **ICG**. Finally, **IC7-1-Bu** provided a PA image of a mouse tumor with the ratio of approximately 2.5 of tumor to background.

Based on this study, the same group further developed a series of asymmetric cyanines **IC-n-T**.^[133] A 4-nitrobenzyl alcohol derivative as a triplet-state quencher (TSQ) was connected to **IC7-1-Bu**, leading to the enhanced photostability of **IC-n-T** dyes since the production of singlet-oxygen was inhibited. Additionally, neither the introduction of the 4-nitrobenzyl alcohol derivative nor the increase of the alkyl chain length exerted significant influence on other optical properties of the dyes. With the highest affinity to albumin, which helps improve the solubility and targeting ability of dyes in *in vivo* imaging, **IC-5-T** presented efficiently the mouse tumor by PA imaging.

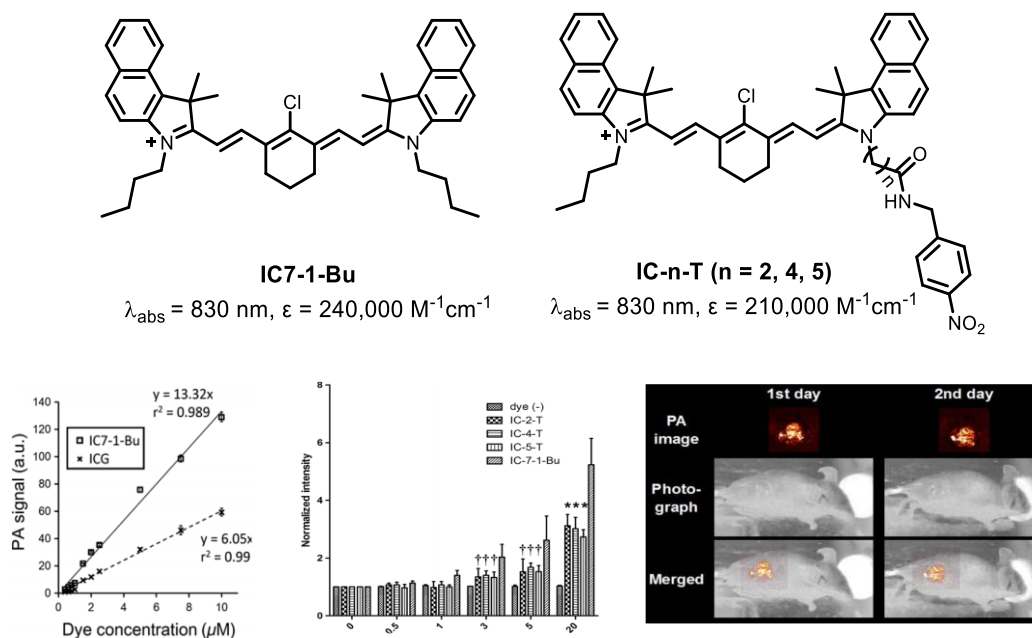


Figure 1 - 26. Chemical structures of **IC7-1-Bu**, **IC-n-T** and their using for PA imaging.^[133]

2. NIR dye-loaded NPs for fluorescence or PA imaging

NIR organic dyes are promising candidates for preparation of optical contrast agents, however, they are restricted by poor water solubility in the real applications.^[28] Structural modifications are widely used methods to overcome this issue, for example, one can introduce water-soluble groups such as ionic groups (anionic or cationic),^[134,135] polar segments (polyether chain or polyethylene ethanol)^[136,137] and water-soluble peptides,^[138,139] or functionalize them with biomolecules especially when a specific targeting is required.^[140] Nevertheless, these approaches often face difficulties in dye purification and functionalization processes.

Inspired by the drug-loaded vehicles for drug delivery, dye-loaded NPs have been developed to improve the water solubility of organic dyes, particularly for *in vivo* optical imaging.^[141,142] Normally, NPs are

Indeed, the F127 micelles were widely used as drug delivery carriers for their long lifespan in blood due to the stealth given by the highly biocompatible PEGs surface, as well as the ease of dissociation under critical micelle concentration (CMC). But for fluorescence imaging, the dissociation of the NPs would cause dye leakage and bring tremendous negative impact on the imaging process, thus a rigid silica shell is needed. By addition of tetraethyl orthosilicate (TEOS), the formed Si-O-Si network can not only fix the NPs to prevent the dye from leakage, but also improve the photostability of the dyes by protecting them from possible quenchers, such as molecular dioxygen.

In addition, covalent linking of the organic dyes to the NPs can completely block the leakage of the dyes from NPs. Rampazzo *et al.* functionalized rhodamine with a triethoxysilane group that allows the dye **R** to covalently bind with the micelle/silica NPs through Si-O-Si bonds, consequently, no dyes leakage was observed in the process of NPs purification (dialysis and ultrafiltration) (Figure 1 - 28). By Förster resonance energy transfer (FRET) strategy, they estimated an approximate number of dye molecule per NPs to be around 10^[145] and a NPs concentration in the suspension before dialysis of 67 μ M.^[146]

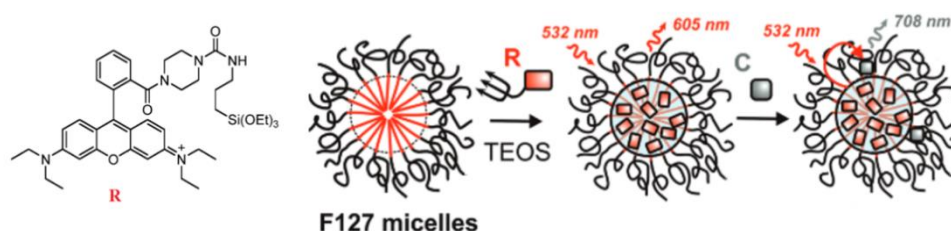


Figure 1 - 28. Depict of Rampazzo's study: energy transfer on F127-SiO₂ NPs based on the covalently linked dye **R**.^[145]

At last, the PO segment of the Pluronic counts for the dyes encapsulation and the core size of the NP (by TEM), the EO segment has influence on the whole size of the NP (by DLS), thus it is possible to optimize the NP size and dye loading capacity by changing the units of the PO and EO segments of Pluronic.

Biffi *et al.*^[147] prepared a F127-SiO₂ NPs based on **Cy5.5** (Figure 1 - 29). Triethoxysilane-modified **Cy5.5** was grafted onto the NPs during hydrolysis and condensation of the silica precursor TEOS. The NPs presented high stability and maximum absorption and emission at 700 nm and 750 nm, respectively. The NPs were successfully used for *in vivo* tumor imaging. Notably, with a neutral and hydrophilic surface formed by the external PEG chains, micelle/silica NPs can not only escape from the uptake of the mononuclear phagocyte system to have a long half-life in blood circulation, but also be grafted with some specific species or ligands for further applications.^[148] As shown in Figure 1 - 30, Soster *et al.*^[165] used the mixture of normal **F127** and carbonyl-modified F127 as encapsulation matrix prepared the micelle/silica NPs with carbonyl groups on their surface, then peptides were covalently linked with the NPs through condensation reaction. The formed NPs were able to visualize sub-millimetric metastases.

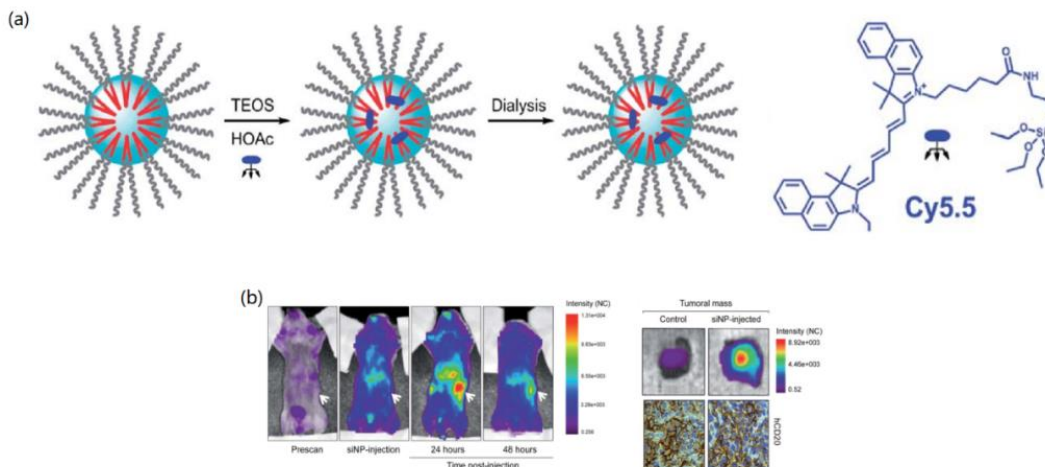


Figure 1 - 29. Fabrication of F127-SiO₂ NPs using triethoxysilane modified Cy5.5 and the in vivo fluorescence tumor imaging.^[147]

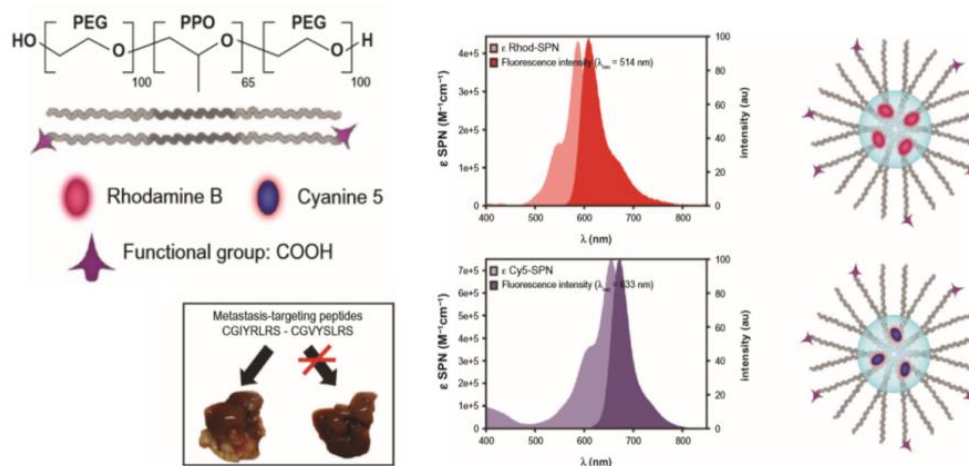


Figure 1 - 30. General structure of *CGIYRLRS* and *CGVYSLRS* peptides functionalized F127-SiO₂ NPs.^[148]

Our group previously prepared **a10@F127-SiO₂** NPs based on the fluorene dye **a10**, with high brightness ($\Phi = 39\%$ at 650 nm) and monodispersed size around 22 nm in saline. The NPs were successfully used for mouse tumor imagination by two-photon excitation (Figure 1 - 31).^[107,108] These NPs proved to be perfect blood-pool contrast agents staying in the vascular system for a long time, without leakage of the NPs near a tumor.

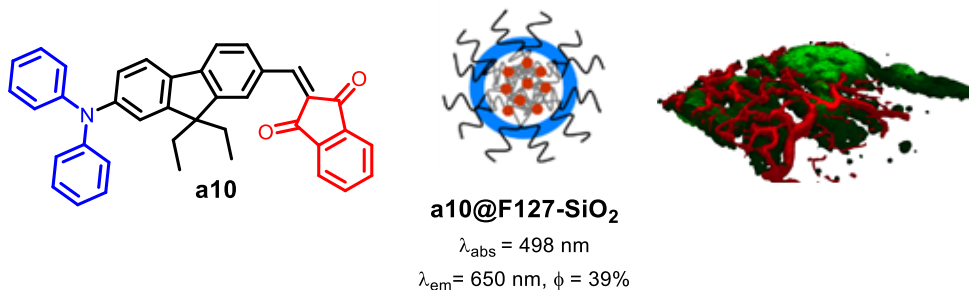


Figure 1 - 31. Two-photon vasculature imaging of **a10@F127-SiO₂** NPs.^[107,108]

2.2. Dye-loaded Polymer NPs

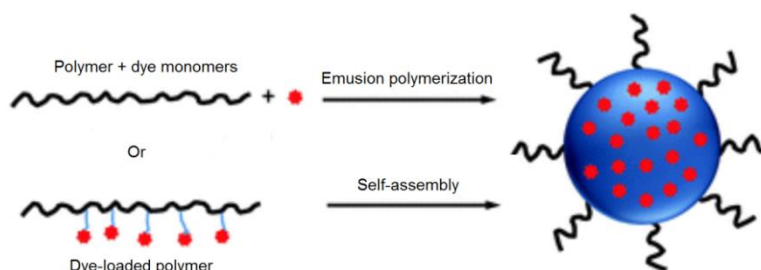


Figure 1 - 32. Schematic illustration of self-assembly NPs.^[149]

Dye-loaded polymer NPs characterized by high dye loading have attracted great interest in optical imaging. Basically, two main strategies are applied for their preparation: emulsion polymerization of dye monomers and self-assembly of preformed dye-loaded polymers (Figure 1 - 32).

In the general protocol of the first strategy, polymers and dye monomers are pre-dissolved in a water-miscible organic solvent (acetone, acetonitrile, *etc.*), followed addition of water to the mixture to induce the aggregation of the dye monomers through rapid diffusion of the organic solvent into the aqueous phase. Then the dye polymerization will give rise to a rigid dye-polymer core incorporated by the water-soluble polymers on its surface. By doing this, the polymer NPs formed are homogeneously dispersed in water, thus the particle suspension can be directly used for bio-imaging. The dye monomers are either small polymerizable segments, such as pyrrole, thiophene, or normal dyes which are modified by polymerizable groups (Figure 1 - 33). The polymers are usually various amphiphilic surfactants such as the PEG containing lipids, mPEG-DSPE, phosphoethanolamine-N-(polyethylene glycol) (**DSPE-PEG₂₀₀₀**), **DSPE-PEG₅₀₀₀-mal** and **DSPE-PEG₅₀₀₀-folate** (Figure 1 - 34).

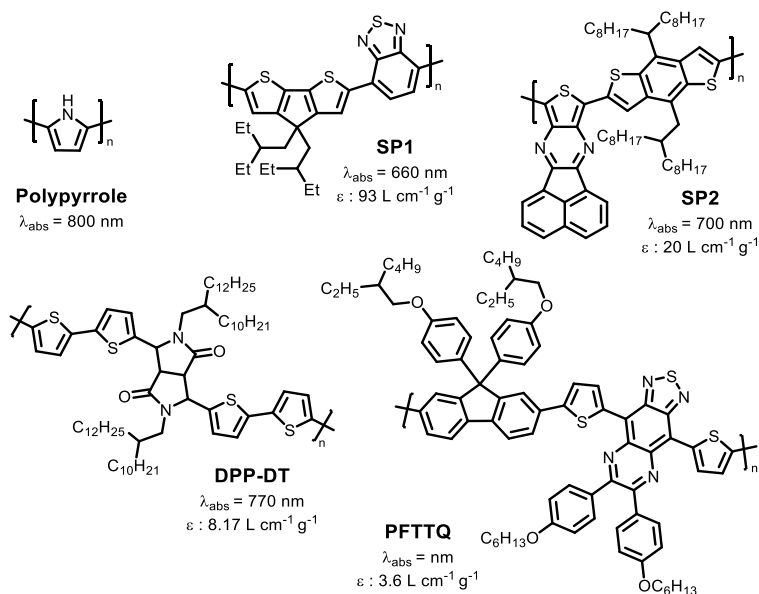


Figure 1 - 33. Chemical structures of several organic polymers used in PA studies.^[150-154]

Zha *et al.*^[150] obtained the **PPy** NPs with monodisperse size of about 46 nm through oxidation polymerization of pyrrole using FeCl_3 as an initiator and polyvinyl alcohol (PVA) as a stabilizer. The strong absorption around 800 nm made it possible for **PPy** NPs to visualize by PA microscopy the chicken breast muscles at depth up to 4.6 cm, as well as a higher clarity in a mice brain imaging in comparison to hemoglobin (Figure 1 - 35).

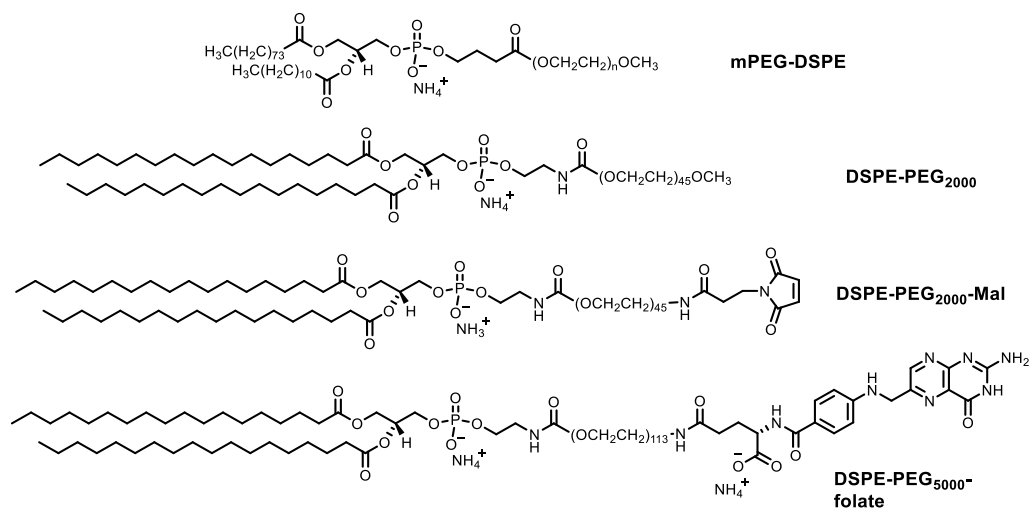


Figure 1 - 34. Chemical structures of normally used amphiphilic surfactants: *mPEG-DSPE*, *DSPE-PEG₂₀₀₀*, *DSPE-PEG₂₀₀₀-Mal* and *DSPE-PEG₅₀₀₀-folate*.

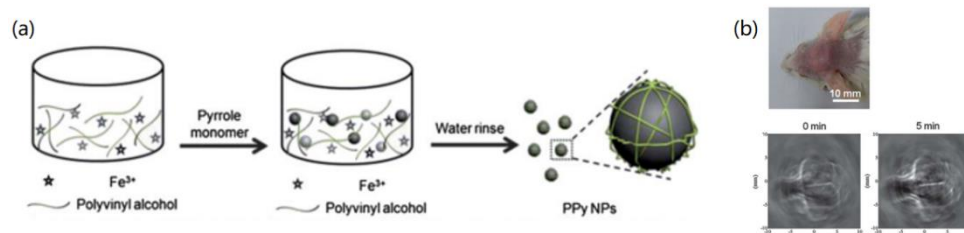


Figure 1 - 35. (a) fabrication and (b) PA imaging of PPy NPs.^[150]

SP1 and SP2 are well known semiconductor polymers in photovoltaics with strong absorptions in NIR region. Pu *et al.*^[131] mixed the ROS sensitive dye IR775S with SP1 to form the hybrid polymer NP that is able to detect *in vitro* the ROS by PA imaging (Figure 1 - 36, a and b). Liu *et al.*^[152] designed a non-radiative NPs with a wide absorption between 700 nm and 850 nm by synthesized the PFTTQ polymer and then co-precipitated it with DSPE-PEG2000. These NPs are found much more resistant to photobleaching than the gold nanobatoms under excitation at 800 nm with a fluence of 15 mJ/cm². The polymer DPP-DT with absorption around 770 nm was prepared by Chen *et al.*^[153] After co-precipitation with the PEGylated polystyrene, the stabilized NPs were successfully used in photothermal therapy to treat tumors (Figure 1 - 36, c).

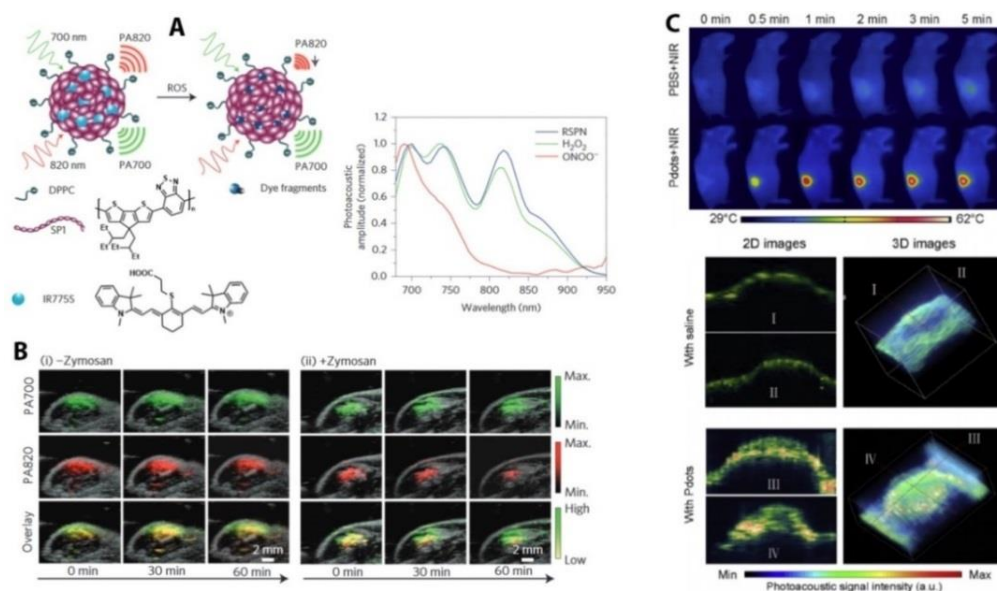


Figure 1 - 36. PA imaging with semiconductor polymers. (A) ROS ratiometric probe based on polymer SP1/IR775S and the PA spectra of the NPs alone or in the presence of ROS; (B) *in vivo* PA imaging without (left) and with (right) zymosan treatment to produce ROS;^[131] (C) Thermal and PA imaging of a tumor containing DPP-DT.^[153]

The second strategy relies on the preparation of dye-loaded polymers. Synthetic design of the polymers that bear functions to allow dye loading is the first step, then the correspondingly modified dyes will be

grafted to form the dye-loaded polymers. Generally, the dye-polymer conjugation is performed in organic solvent, thus the formed polymers have to be extracted and saved in form of a solid state. Finally, self-assembly of the polymers in water leads to the dye loaded polymer NPs. Additionally, the size of the NPs can be regulated from several nanometers to 100 nm by simply control of the length of polymer.^[155-166]

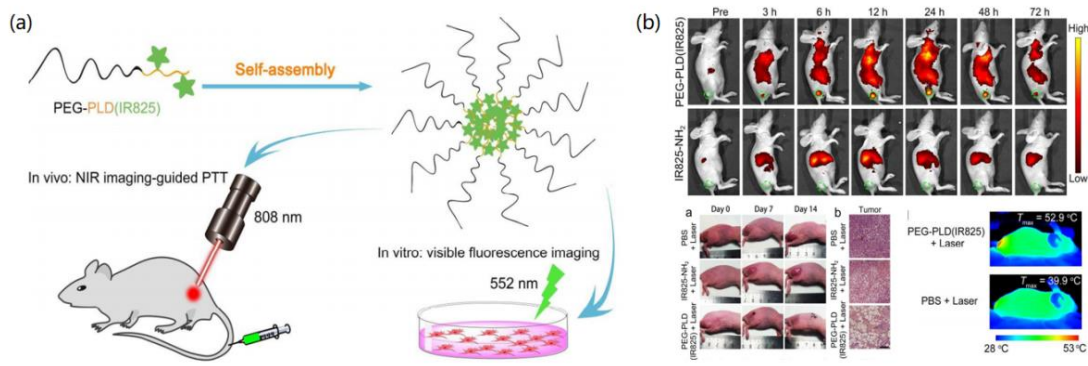


Figure 1 - 37. (a) Schematic illustration of fabrication of **PEG-PLD-IR825** NPs and (b) the in vivo optical imaging.^[167]

Pan *et al.*^[167] primarily prepared IR825 linked amphiphilic block copolymer **PEG-PLD-IR825** by conjugating the amine-functionalized IR825 to the double hydrophilic block copolymer PEG-PLD which containing 10 carboxyl groups in the PLD segment and then obtained the nanomicelles by self-assembly of **PEG-PLD-IR825** in aqueous solution. With **IR825** trapped in the NP core and the PEG segments distributed on the NP surface, the **PEG-PLD-IR825** NPs presented excellent biocompatibility, high tumor accumulation due to enhanced permeability and retention effect, and great promise for cancer theranostics (Figure 1 - 37).

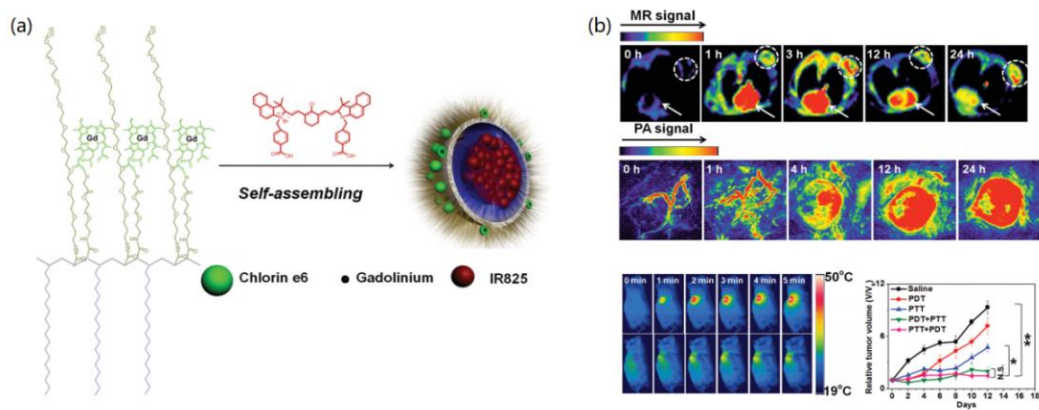


Figure 1 - 38. Schematic illustration of fabrication of **IR825@C18PMH-PEG-Ce6** and its in vivo fluorescence, PA and magnetic resonance MR imaging.^[168]

Through connection of the polymer poly(maleic anhydride-alt-1-octadecene) (**C18PMH**) with a long PEG-amine (5 kDa) and a short biamine-PEG (324 Da), Gong *et al.*^[168] obtained the amphiphilic block polymer C18PMH-PEG 5k/PEG 324-NH₂ modified with amine. Chlorin e6 (**Ce6**) were then conjugated to C18PMH-PEG 5k/PEG 324-NH₂ by amide groups, and the formed dye-linked polymer C18PMHPEG-Ce6 further encapsulated **IR825** to fabricate the **IR825@C18PMH-PEG-Ce6** by self-assembly. Finally, containing photothermal agents **IR825** photosensitive Gd³⁺chelating agents **Ce6**, the **IR825@C18PMH-PEG-Ce6** can be utilized for fluorescence, PA and magnetic resonance (MR) imaging and PTT and PDT of mice tumors (Figure 1 - 38).

Yuan *et al.*^[169] developed a doxorubicin (**DOX**) delivery system AIE-NPs/DOX with **DOX** encapsulated by an amphiphilic polymer **TPETP-TK-PEG** through self-assembly (Figure 1 - 39). Composed by a photosensitive and AIE active TPETP, a hydrophilic PEG chain and a reactive ROS cleavable thioketal linker (TK), the **TPETP-TK-PEG** polymer can encapsulate a high amount of DOX to form a strong fluorescence emitting NPs in water, and disassembly upon light irradiation to release the **DOX** molecules, as a result, the drug delivery and release process in MDA-MB-231/DOX cells was successfully followed by fluorescence imaging.

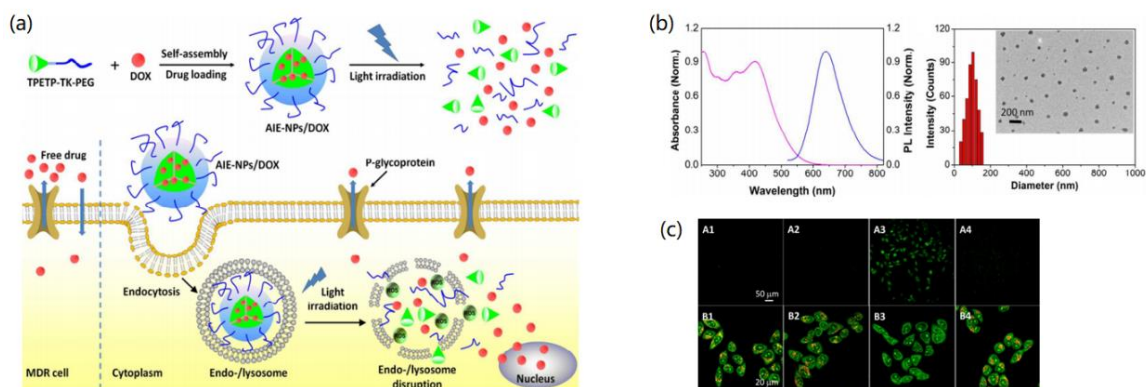


Figure 1 - 39. (a) schematic illustration of fabrication of AIE-NPs/DOX and its disassembly upon light irradiation to release Dox in cells; (b) characterization and (c) cell fluorescence imaging of AIE-NPs/DOX.^[169]

3. Objectives

As reviewed above, NIR light is promising for bio-imaging for merits of strong penetration in organisms that favors a deeper imaging, low interference from auto-fluorescence that benefits for a high special resolution, as well as low energy input to minimize bio-damage. Hence, NIR organic dyes as contrast agents

are extremely desired for fluorescence or PA imaging. In this regard, the main objective of this thesis is to synthesize high-performance NIR organic dyes.

Push-pull dipolar scaffold is an ideal candidate for design of NIR dyes, given its ease of HOMO-LUMO gap modulation by varying the D/A pairs or the conjugated π bridge. In this context, we will synthesize NIR dyes based on dipolars.

Meanwhile, the problem with water solubility of organic dyes for biological application can be overcome by forming water soluble NPs. On the one hand, F127-SiO₂ NPs encapsulating organic dyes within its **F127** micelle core can not only provide the dyes excellent water-solubility, but also allow a high brightness for improved bio-imaging sensitivity. Thus, the F127-SiO₂ NPs encapsulation strategy will be utilized on NIR emitting dyes for fluorescence bio-imaging. Furthermore, taking advantage of the modifiable surface of F127-SiO₂ NPs, we manage to further modify the dye-loaded F127-SiO₂ NPs with different moieties. On the other hand, in order to meet the requirement for high-dye-concentration of PA imaging, polymer NPs with organic dyes loaded by dye polymerization or dye grafting, and F127-SiO₂ NPs modified by organic dyes on their surface will be developed to maximize the concentration of the organic dyes for PA imaging.

Chapter II. Synthesis of NIR dyes and dye-loaded F127-SiO₂ NPs for *in vivo* fluorescence imaging

1. Introduction

1.1. Previous Work

Dye **a10** with good optical properties was previously chosen by our group for fluorescence imaging. Silica encapsulation strategy was developed to improve the water-solubility of the dye. Finally, the **a10@F127-SiO₂** NPs with monodispersed size around 22 nm in saline and great brightness successfully imaged a mouse tumor by two-photon excitation. Nevertheless, the same strategy failed for all BTN dyes for their high tendency of forming non-emissive dye aggregates during the F127 micellization process, while their more in red absorption and excellent brightness would be very promising for fluorescence imaging.

1.2. Objectives

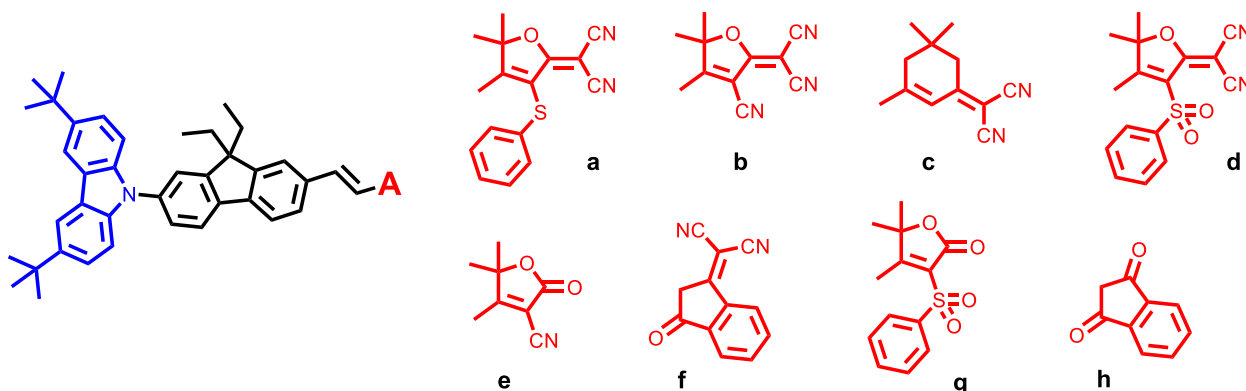
In light of these observations, we aim at further optimizing the dyes for *in vivo* fluorescence imaging. Given the great potential of fluorene dyes@F127-SiO₂ NPs for two-photon fluorescence imaging, we will use the molecular engineering strategies that we mentioned before to realize a more red-shifted emission for the fluorene dyes. Meanwhile, taking advantage of the modifiable surface of the F127-SiO₂ NPs, bioactive moieties will be grafted to endow the dye-loaded F127-SiO₂ NPs potential tumor targeting capability.

Besides, BTN dyes possessing high brightness in NIR region, however, are hardly to be encapsulated by F127 due to poor solubility. In this regard, we will improve their lipophilicity by molecular modification to enable them for preparation of dye-loaded F127-SiO₂ NPs for *in vivo* fluorescence imaging.

2. Synthesis of TCBZ dyes and TCBZ@F127-SiO₂ NPs for fluorescence imaging

2.1. Synthetic Design

Accordingly, four steps are needed to obtain a surface functionalized F127-SiO₂ NP with more red-shifted fluorene-dye loaded. Firstly, different electron-withdrawing groups will be introduced to modulate the ICT of the dyes for more red-shift emission. Then, normal F127 will be modified by different functions to allow a surface modified F127-SiO₂ NPs. After forming the surface modifiable F127-SiO₂ NPs with dye loaded, further conjugation with different functionalized moieties will give rise to the final surface-functionalized F127-SiO₂ NPs.

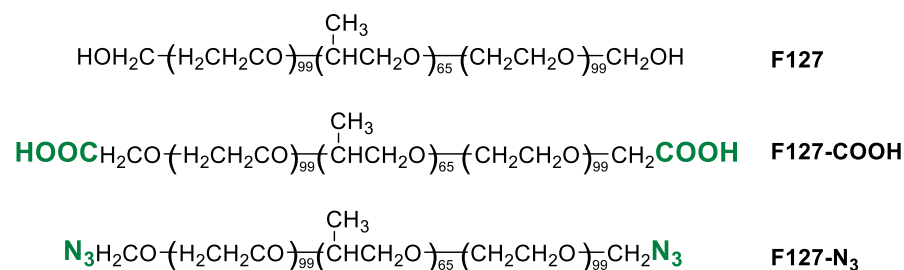


Scheme 2 - 1. Chemical structures of TCBZ dyes.

Through comparison of the fluorene dyes our laboratory synthesized before, it was found that substitution of the diphenylamine unit by the carbazole unit benefits a higher brightness. For this reason, carbazole was chosen by us for configuration of the new series of dyes. As shown in Scheme 2 - 1, different electron-withdrawing groups including the **b**, **c**, **d**, **g**, **f** previously applied in the fluorene dyes and the **a** and **c** recently developed in our laboratory were used as the acceptors of the new series of dyes. Additionally, the introduction of two *tert*-butyl groups to the carbazole units may increase the lipophilicity of the dyes, which favors the dye encapsulation process by F127.

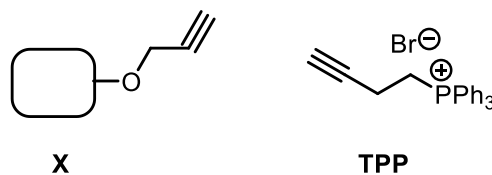
As shown in Scheme 2 - 2, F127 has two hydroxy groups at both ends of its polymer chain readily to be transformed into carboxyl or azido groups. Using the modified pluronic **F127-COOH** and **F127-N₃** as the encapsulation matrices, the formed F127-SiO₂ NPs will be modified by carboxyl or azido groups to be able to conjugate with moieties containing amine or alkynyl groups via amidation in presence of 1-ethyl-3-(3-

dimethyl aminopropyl) carbodiimide hydrochloride (EDC·HCl) and N-hydroxysuccinimide (NHS) or Cu(I) catalyzed alkyne-azide cycloaddition (“click”) reaction.



Scheme 2 - 2. Chemical structures of F127, F127-COOH and F127-N₃.

As shown in (Scheme 2 - 3), two different moieties encompassing an alkyne function were used for the preparation of the surface functionalized F127-SiO₂ NPs: a propargyl modified moiety **X** provided by Dr. S. Chambert from ICBMS / INSA Lyon (the structure of **X** will not be disclosed until a patent is issued) and triphylphosphine (**TPP**) bearing a positive charge.



Scheme 2 - 3. Chemical structures of alkyne modified X and TPP.

2.2. Synthesis and Photophysical Properties of TCBZ Dyes

2.2.1. Synthesis of TCBZ Dyes

The synthetic route to TCBZ dyes is depicted in Figure 2 - 1. Firstly, the 2-bromo-9,9-diethyl-7-iodo-9H-fluorene **3** and the *tert*-butyl modified carbazole derivative **4** were synthesized according to our previous protocol from carbazole and *tert*-butyl chloride with ZnCl₂ as the catalyst.^[107] In presence of CuI, 1,10-phenanthroline and K₂CO₃, **3** and **4** afforded compound **5**, in 41% yield. Lithiation by a stoichiometric amount of n-BuLi, followed by reaction with DMF, **5** transformed into the aldehyde precursor **6** in 82% yield. With a catalytic amount of piperidine, **6** afforded dyes **TCBZ1-TCBZ8** by Knoevenagel condensation with the acceptors **a-h** (presented in Scheme 2 - 1). All these dyes and intermediate products were carefully purified and fully characterized by NMR and mass spectrometry.

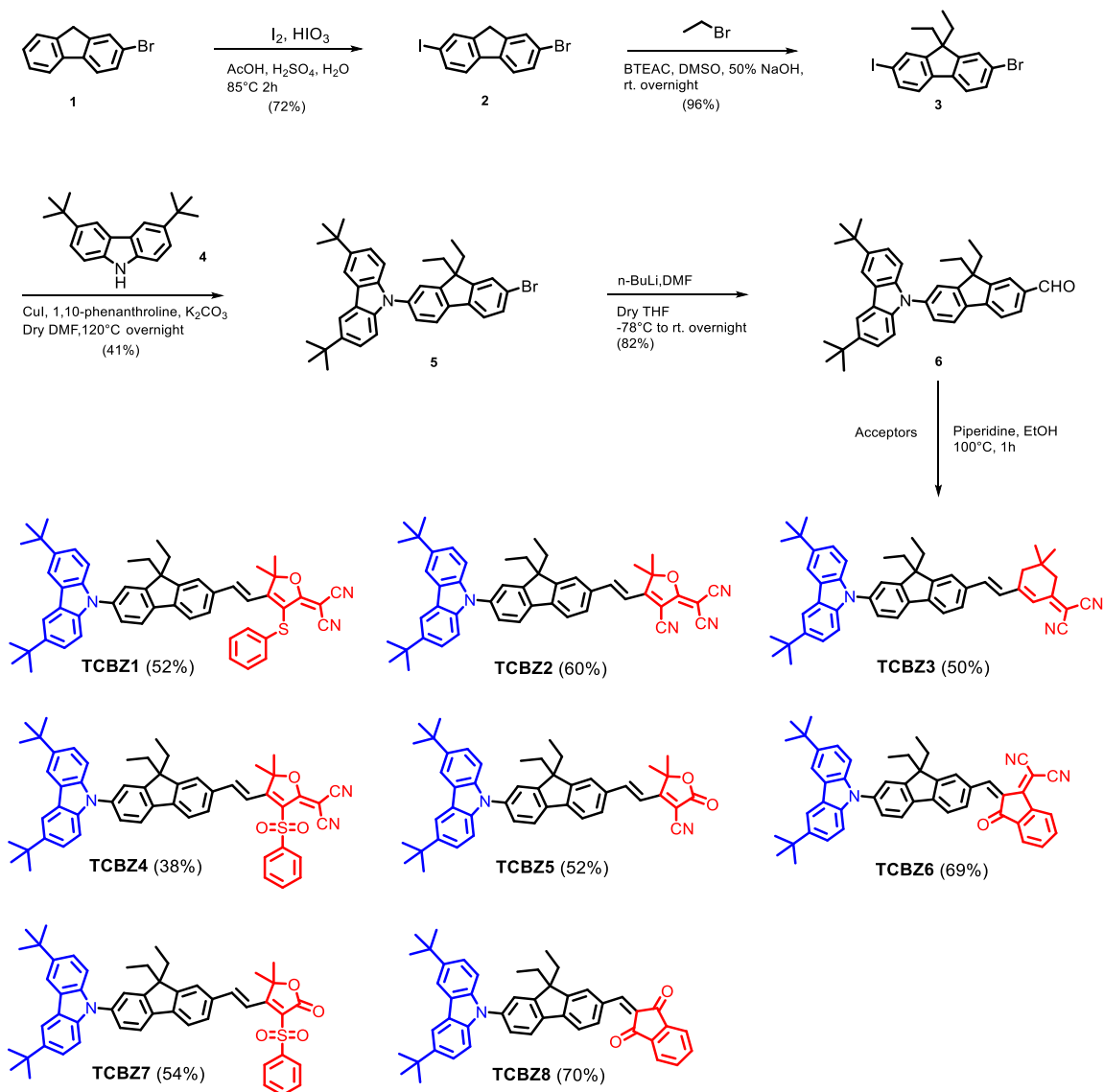


Figure 2 - 1. Synthetic routes of **TCBZ1-TCBZ8**.

2.2.2. Photophysical Properties of TCBZ dyes

2.2.2.1. Absorption and Emission

After obtaining the **TCBZ1-TCBZ8** dyes, we firstly studied their absorption and emission properties in chloroform, a solvent of intermediate polarity. All data are gathered in Table 2 - 1. The absorption spectra (Figure 2 - 2, a) show the characteristic ICT bands of **TCBZ1-TCBZ8** in visible range, from 433 nm for **TCBZ7** to 512 nm for **TCBZ6** according to their different electron-withdrawing acceptors thus distinguished ICT strengths. The extinction coefficients of **TCBZ1-TCBZ8** range from 24,000 mol⁻¹·L·cm⁻¹ for **TCBZ6** to 41,400 mol⁻¹·L·cm⁻¹ for **TCBZ2**.

Upon excitation in the main band, emissions were observed for all the dyes (Figure 2 - 2, b) except **TCBZ6**. The emissions are characterized by a large Stoke shifts from 6080 cm^{-1} for **TCBZ2** to 8060 cm^{-1} for **TCBZ7** ascribed to the ICT property, and the wavelengths ranging from 648 nm for **TCBZ8** to 745 nm for **TCBZ4** depending on different ICT strengths. With the most powerful electron-withdrawing acceptors, **TCBZ2** (acceptor **b**) and **TCBZ4** (acceptor **d**) presented the most red-shifted emissions at 735 nm and 745 nm, respectively. All the emissive dyes are of quantum yields around 2% (Rubrene in methanol ($\Phi = 27\%$) as a standard).^[170]

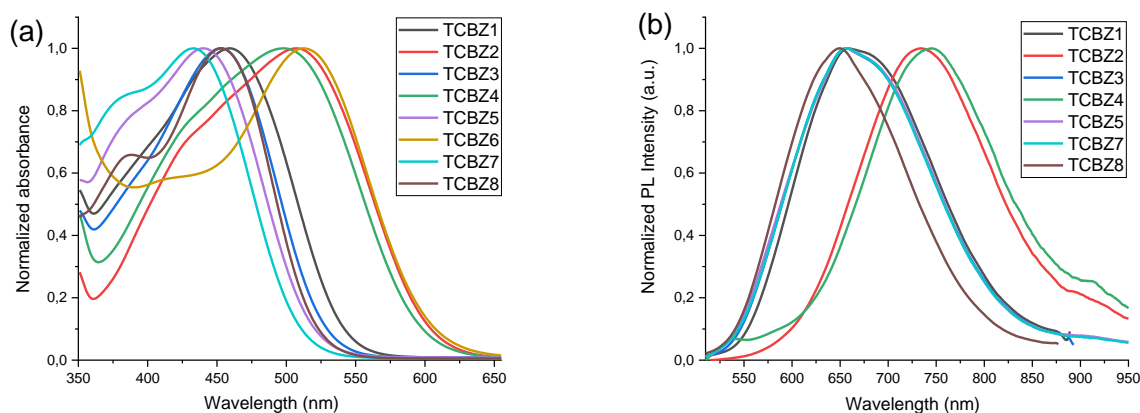


Figure 2 - 2. Normalized absorption (a) and emission (b) spectra of **TCBZ1-TCBZ8** in chloroform.

Sample	$\lambda_{\text{abs}}^{\text{[a]}}$	$\epsilon^{\text{[b]}}$	$\lambda_{\text{em}}^{\text{[c]}}$	$\Phi (\%)^{\text{[d]}}$	$\Delta\nu^{\text{[e]}}$
TCBZ1	460	3.46	670	2	6810
TCBZ2	508	4.14	735	2	6080
TCBZ3	453	3.84	666	2	7060
TCBZ4	498	2.96	745	3	6660
TCBZ5	440	2.47	667	3	7730
TCBZ6	512	2.40	--	--	--
TCBZ7	433	3.06	665	3	8060
TCBZ8	453	3.56	648	1	6640
a1	485	2.41	689	2	6230
a2	443	3.48	623	3	6392
a3	439	3.08	590	1	5829
a4	495	2.53	--	--	--

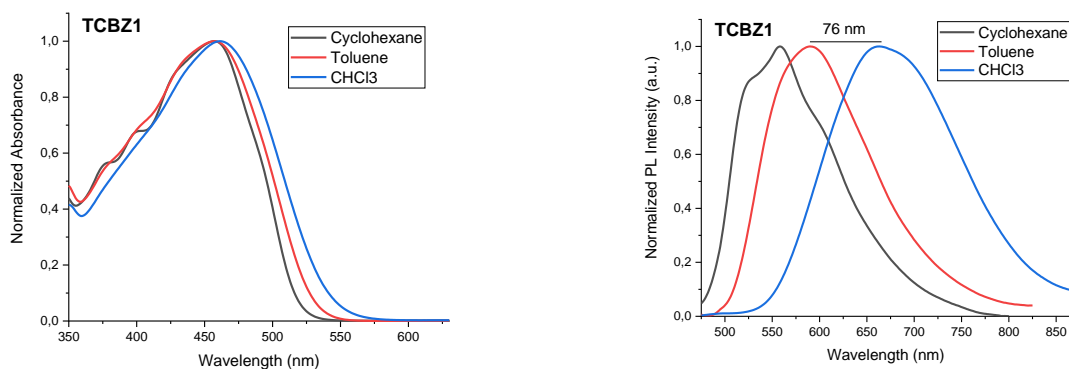
[a] Absorption maxima in nm. [b] Absorption coefficients in 10^{-4} L/mol/cm [c] Emission maxima in nm. [d] Quantum yields determined using rubrene in methanol ($\Phi = 27\%$) as the standard.^[170] [e] Stokes shifts in cm^{-1} .

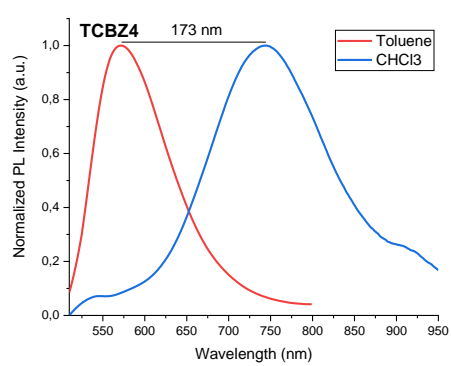
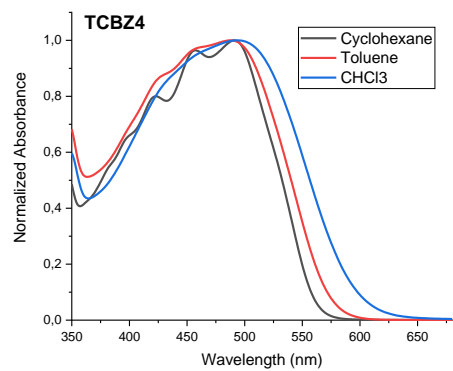
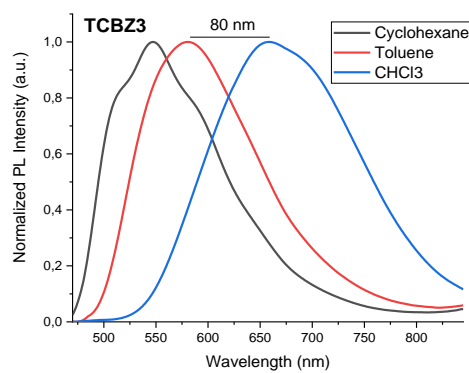
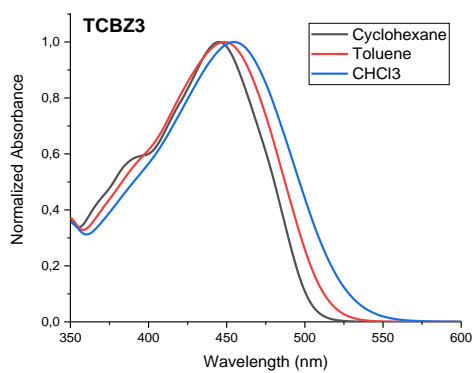
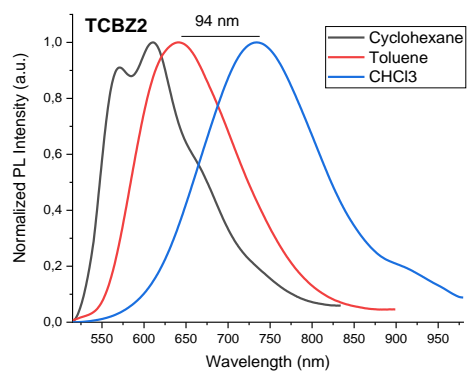
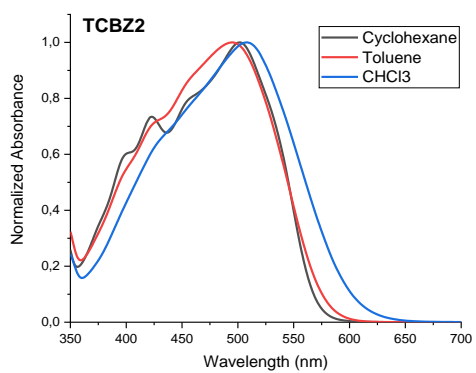
Table 2 - 1. Photophysical properties of **TCBZ1-TCBZ8** in chloroform.

By comparison of the TCBZ dyes with the corresponding fluorene dyes bearing the same acceptors (**TCBZ2-a1**, **TCBZ3-a2**, **TCBZ6-a4** and **TCBZ8-a3**), showed in Table 2 - 1 using the same color to emphasize, one can notice that the TCBZ dyes have more red-shifted absorptions (around 20 nm) and emissions (around 50 nm), while keeping the very similar extinction coefficients (ϵ) and quantum yields (Φ). This result indicated our success in improving the optical properties of the dyes by molecular modification strategy.

2.2.2.2. Solvatochromism

Then the optical properties of **TCBZ1-TCBZ8** in solvents of various polarities (cyclohexane, toluene, chloroform and DMSO) were measured. As these dyes are weakly emissive in polar solvent DMSO, the emission spectra are only shown for apolar cyclohexane and toluene in Figure 2 - 3. For each compounds of **TCBZ1-TCBZ8**, only a slight red-shift was observed in absorption with the increasing of the solvent polarity, which is in perfect agreement with previous observation on similar dyes.^[107] As shown in Figure 2 - 3, except **TCBZ6** which is not emissive in all the tested solvents, all the other dyes exhibited interesting solvatochromic effect in emissions. By varying the solvent from toluene to chloroform, the ICT effect produced distinctively bathochromic-shifted emissions from 76 nm (1880 cm^{-1}) for **TCBZ1** to 173 nm (4070 cm^{-1}) for **TCBZ4**.





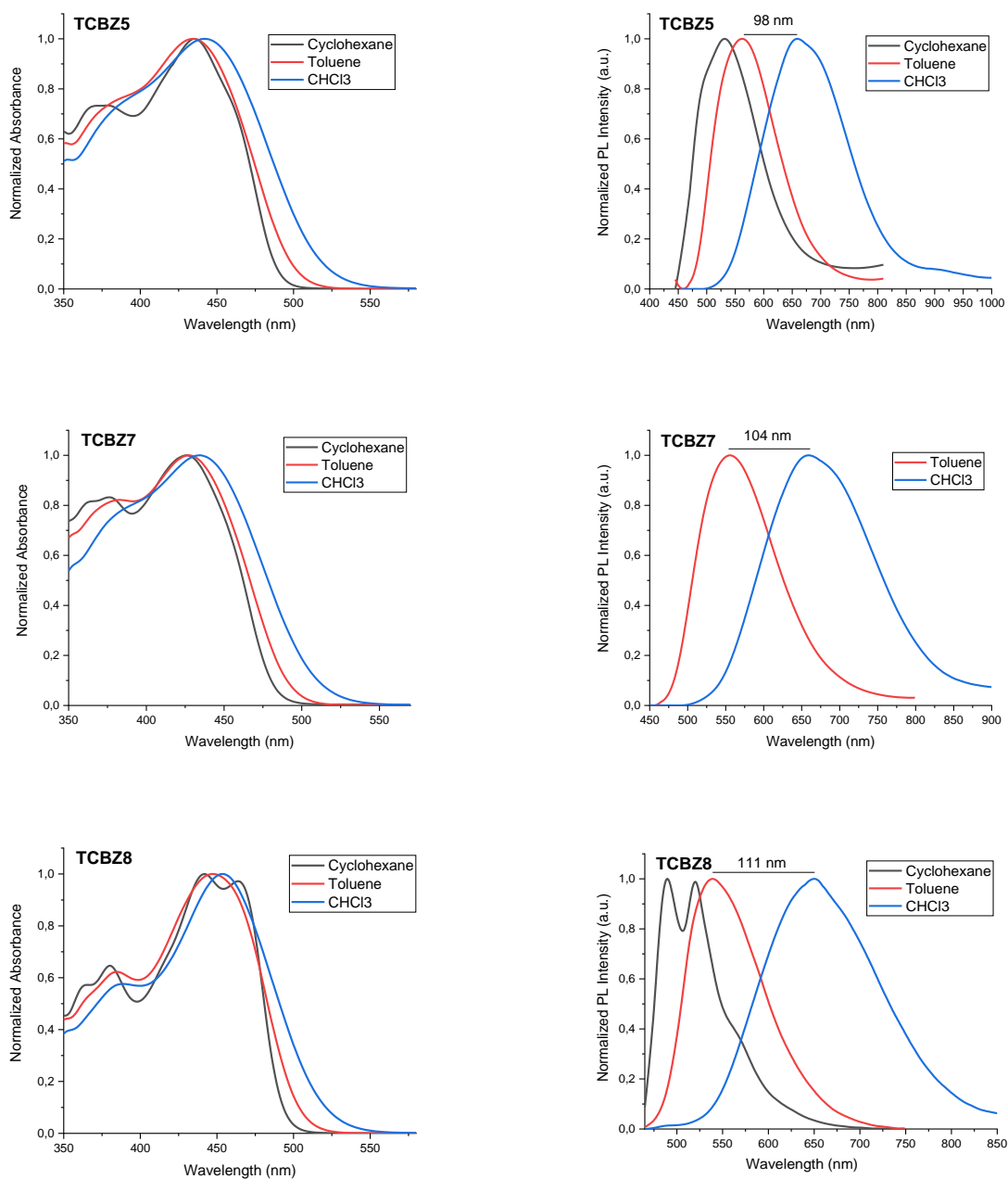


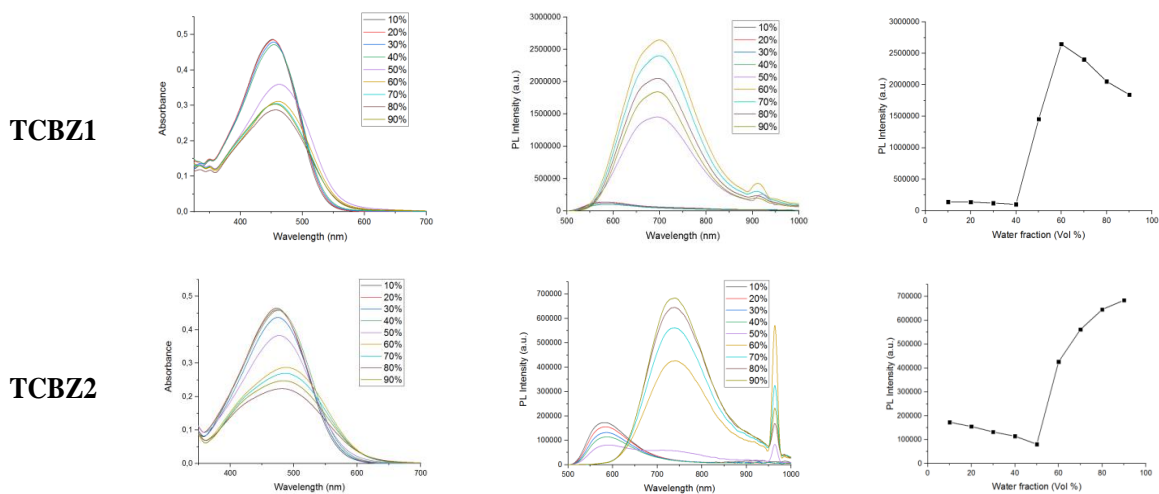
Figure 2 - 3. Normalized absorption (left) and normalized emission (right) spectra of *TCBZ1-TCBZ8* in different solvents.

2.2.2.3. AIE property

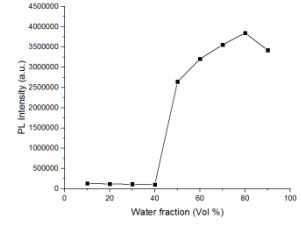
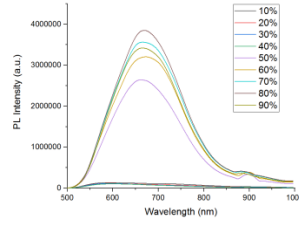
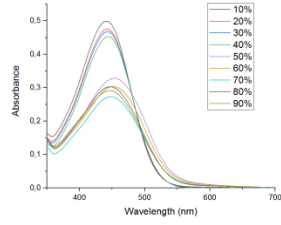
AIE refers to the phenomenon which leads a dye solution to become more fluorescent under the aggregation. Given the interesting AIE properties of the fluorene dyes **a1-a3**, we also studied our new dyes in this context.

AIE measurement is commonly carried out by monitoring the fluorescence variations of the dye solution with a continuous addition of a poor solvent to induce the aggregation of the dye. In our test, water as the poor solvent was added to the solution of TCBZ dyes in acetone, with dye concentration fixed at 5×10^{-5} mol.L⁻¹ and water fraction (f_w) increasing from 10% to 90%, the absorption and emission spectra of the mixtures were recorded at every f_w increase of 10%.

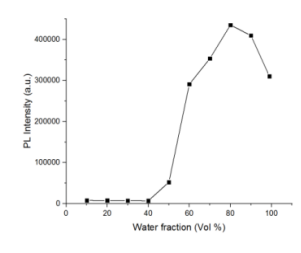
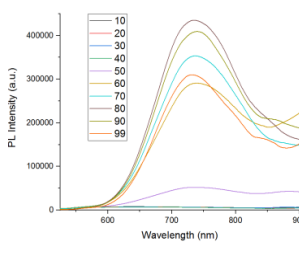
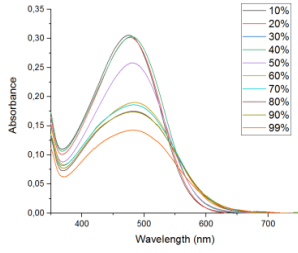
From the results of Figure 2 - 4, except **TCBZ6** which is weakly emissive in aggregated state, which is not surprising given dye **a4**, all the dyes showed interesting AIE behaviors in water/acetone mixtures. Taking dye **TCBZ1** as an example, initial addition of water induced a slightly decreased absorption and emission, which can be attributed to the increased solvent polarity by addition of water. Then a sudden decline of absorption was observed when the f_w reached 50%, indicating the formation of **TCBZ1**-nanoaggregates, which corresponds to a sharp fluorescence enhancement at 697 nm appeared. This demonstrated the AIE property of **TCBZ1**. The maximum fluorescence is obtained at f_w of 60%. Further addition of water caused a slight blue-shift in absorption and emission accompanied by a remarkably decreased fluorescence intensity. This is probably due to the irregular gathering of the **TCBZ1**-nanoaggregates.^[141] **TCBZ3-TCBZ5**, **TCBZ7** and **TCBZ8** all displayed periodical changes in absorption and emission with variations of f_w . It can be seen from the plot of fluorescence intensity versus f_w that the emission maxima of **TCBZ3-TCBZ5**, **TCBZ7** and **TCBZ8** were obtained for f_w values of 80%, 80%, 80%, 70% and 60%, respectively.



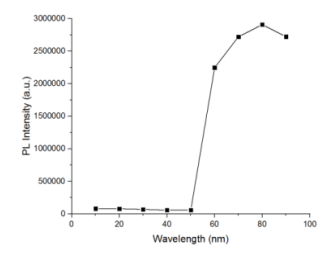
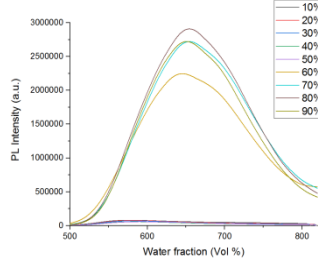
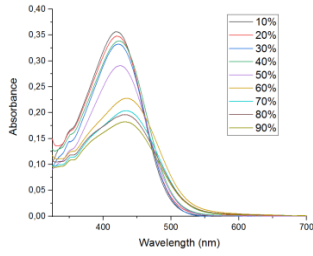
TCBZ3



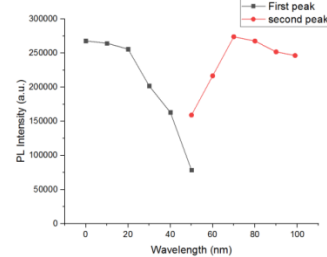
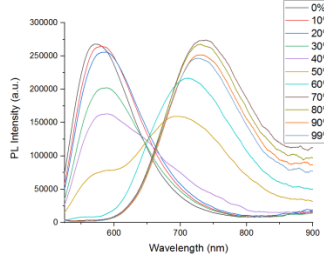
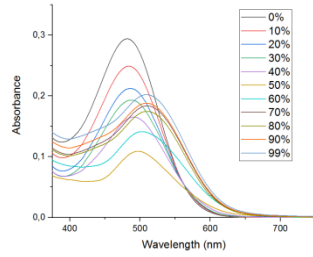
TCBZ4



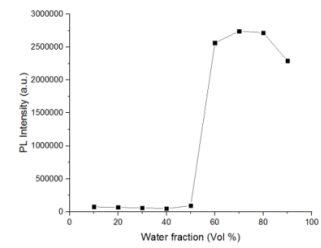
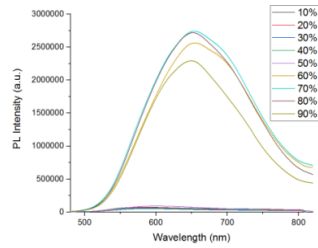
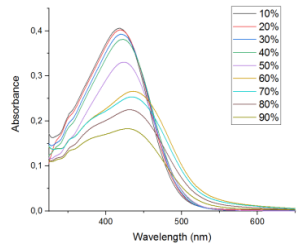
TCBZ5



TCBZ6



TCBZ7



TCBZ8

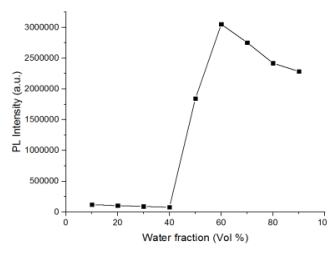
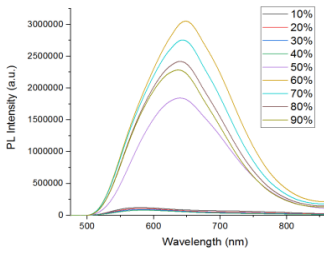
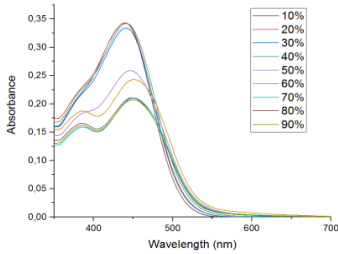


Figure 2 - 4. (Left) absorption and (middle) emission changes of **TCBZ1-TCBZ8** in acetone/water mixtures with increasing of water fraction; (Right) plot of fluorescence peaks intensity vs f_w .

To evaluate the AIE properties of **TCBZ1-TCBZ8**, we collected the photophysical properties of these nanoaggregates into Table 2 - 2. All the TCBZ-nanoaggregates showed emission peaks in NIR region with large Stokes shifts above 6000 cm^{-1} . The quantum yield Φ was determined to be 1%-19% using rubrene in methanol (27%) as the standard.^[170] As we expected, **TCBZ2**, **TCBZ3** and **TCBZ8** have more red-shifted absorptions and emissions with improved quantum yields compared with those of **a1-a3** aggregates. Additionally, the relatively lower f_w values (see $f_w(\%)^{[a]}$ in Table 2 - 2), at which the dyes start aggregation, illustrating the increased lipophilicity of our new dyes in comparison to **a1-a3**.

Sample	$f_w(\%)^{[a]}$	$f_w(\%)^{[b]}$	$\lambda_{\text{abs}}^{[c]}$	$\lambda_{\text{em}}^{[d]}$	$\Phi(\%)^{[e]}$	$\Delta\nu^{[f]}$
TCBZ1-aggregates	40	60	461	697	8	7340
TCBZ2-aggregates	50	90	485	737	9	7050
TCBZ3-aggregates	40	80	450	675	12	7400
TCBZ4-aggregates	40	80	484	732	1	7000
TCBZ5-aggregates	50	80	432	655	19	7880
TCBZ6-aggregates	50	70	515	650	--	4033
TCBZ7-aggregates	50	70	435	655	12	7720
TCBZ8-aggregates	40	60	452	650	9	6740
a1-aggregates	50	70	473	711	4	7077
a2-aggregates	40	60	440	637	11	7027
a3-aggregates	50	60	438	586	6	5766

[a] Water to acetone fractions starting inducing aggregation of the TCBZ dyes in solution [b] Water to acetone fractions at which the highest emissions of the TCBZ dyes in solution appeared. [c] Absorption maxima in nm. [d] Emission maxima in nm. [e] Quantum yields determined using rubrene in methanol ($\Phi = 27\%$) as the standard.^[170] [f] Stokes shifts in cm^{-1} .

Table 2 - 2. Photophysical properties of **TCBZ1-TCBZ8** aggregates in acetone/water mixtures ($5.0 \times 10^{-5}\text{ mol L}^{-1}$).

2.2.2.4. Solid state fluorescence

We also measured the emissions of **TCBZ1-TCBZ8** in powder. The fluorescence spectra are shown in Figure 2 - 5, the corresponding data are collected in Table 2 - 3. Firstly, all the dyes were found emissive in solid state. Among them, **TCBZ2** and **TCBZ4** showed the most red-shifted emissions, which is consistent with their performances both in solution and in nanoaggregates. **TCBZ7** possessing Φ up to 42% is promising for preparation of NIR solid luminescent materials. Furthermore, our new dyes are of more red-shifted emissions and relatively higher Φ compared with **a1-a3**, thanks to the introduction of two *tert*-butyl groups that may exerted impact on the dye aggregation in solid.

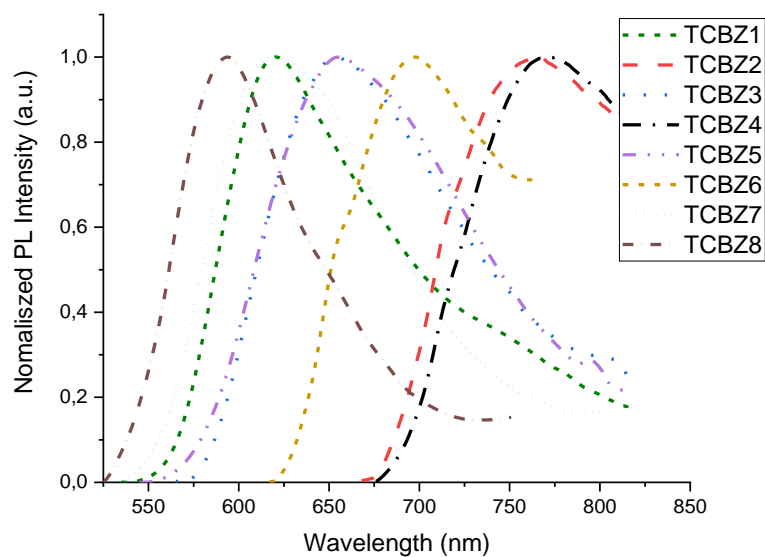


Figure 2 - 5. Emission spectra of TCBZ1-TCBZ8 in solid state.

Sample	λ_{em}	Φ (%) ^[a]
TCBZ1	618	7
TCBZ2	754	3
TCBZ3	656	15
TCBZ4	776	6
TCBZ5	653	18
TCBZ6	701	2
TCBZ7	608	42
TCBZ8	593	1
a1	714	8
a2	608	3
a3	595	4
a4	672	--

[a] Quantum yields measured by using an integrating sphere.

Table 2 - 3. Photophysical properties of TCBZ1-TCBZ8 in solid state.

2.3. Preparation and Characterization of TCBZ2@F127-SiO₂ and TCBZ5@F127-SiO₂ NPs

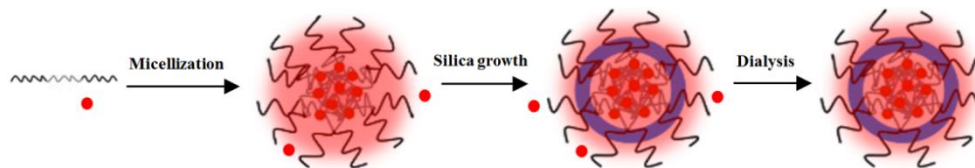
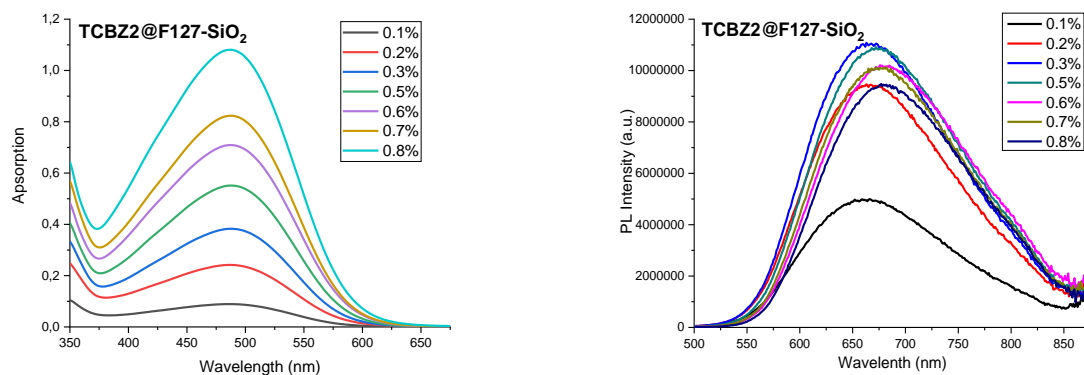


Figure 2 - 6. General procedure of preparation of dye-loaded F127-SiO₂ NPs.

Wavelength and brightness are both important factors for F127-SiO₂ NPs in *in vivo* fluorescence imaging, thus **TCBZ2** and **TCBZ5** with either the most red-shifted emission or a relatively high quantum yield in far-red region among the TCBZ series were chosen for preparation of the dye-loaded F127-SiO₂ NPs. In consideration of the possible fluorescence quenching caused by π - π stacking of dyes in high-dye-loaded F127-SiO₂ NPs, and to optimize the dye loading, we firstly investigated the relationship of the F127-SiO₂ NPs brightness with the dye loading amount (from 0.1 to 0.8% weight ratio).

The general procedure for preparation of F127-SiO₂ NPs is depicted in Figure 2 - 6. F127 and the appropriate amount of dyes are pre-dissolved in dichloromethane, followed by argon blow to form a thin film. 0.85 N hydrochloric acid is then added to induce the micellization of **F127** along with the encapsulation of the dyes within the F127-micelles. TEOS as the silica precursor is added to the suspension to start the silicate cross-linking on the micelles, which is terminated by further addition of diethoxydimethylsilane (DEDMS) to form a silica shell. The hydrochloric acid and impurities are lastly removed by dialysis.

Figure 2 - 7 showed the absorption of **TCBZ2@F127-SiO₂** and **TCBZ5@F127-SiO₂** NPs steadily increase as the dye-loading, the optimal brightness is reached at dye loading of 0.3% and 0.5%, respectively.



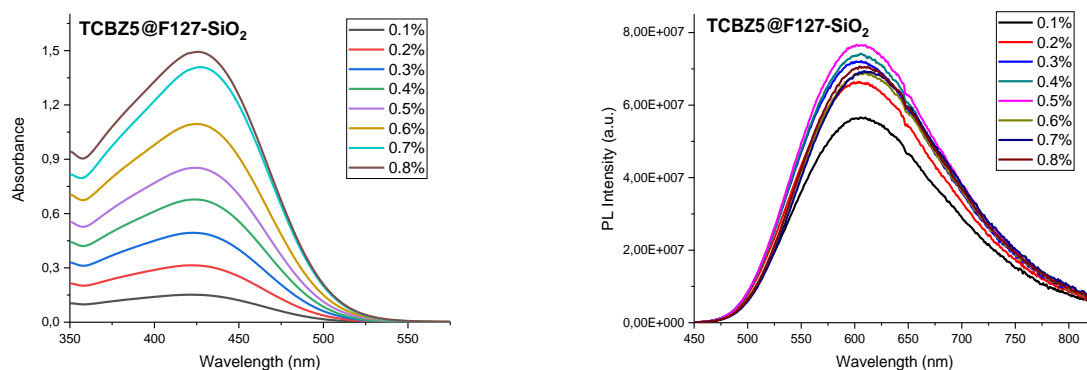


Figure 2 - 7. (Left) absorption and (right) emission changes of **TCBZ2@F127-SiO₂** (up) and **TCBZ5@F127-SiO₂** (down) by varying the dye to F127 mass ratio from 0.1 % to 0.8 %.

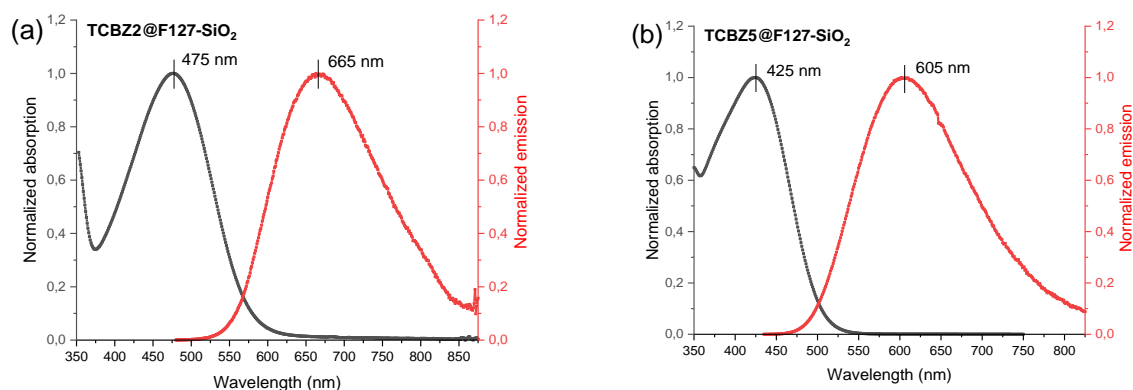


Figure 2 - 8. (a) normalized absorption and (b) emission spectra of **TCBZ2@F127-SiO₂** and **TCBZ5@F127-SiO₂**.

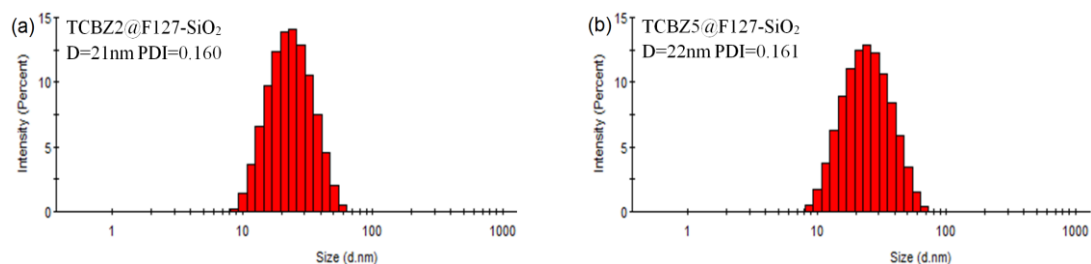


Figure 2 - 9. Particle size distributions of **TCBZ2@F127-SiO₂** (a) and **TCBZ5@F127-SiO₂** (b) in water, measured by DLS.

Then we investigated the properties of the dye-loading optimized **TCBZ2@F127-SiO₂** and **TCBZ5@F127-SiO₂** NPs (0.3% for **TCBZ2** and 0.5% for **TCBZ5**). As shown in Figure 2 - 8, **TCBZ2@F127-SiO₂** NPs showed absorption peak at 475 nm and emission peak at 665 nm with Φ of 8%. **TCBZ5@F127-SiO₂** NPs presented absorption and emission maxima at 428 nm and 605 nm, respectively,

with Φ of 27%. In dynamic light scattering (DLS) measurements, both **TCBZ2@F127-SiO₂** and **TCBZ5@F127-SiO₂** NPs exhibited monodispersed sizes around 22 nm in water and saline (Figure 2 - 9). According to the particle concentration of 67 μM before dialysis from literature^[146] and the dye concentration of 242 μM for **TCBZ2** and 432 μM for **TCBZ5**, the average dye numbers for each **TCBZ2@F127-SiO₂** and **TCBZ5@F127-SiO₂** NPs are 3 and 6, respectively (Table 2 - 4).

Sample	wt% ^[a]	λ_{abs} ^[b]	λ_{em} ^[c]	Φ (%) ^[d]	$\Delta\nu$ ^[e]	Size ^[f]	Dye/NP
TCBZ2@F127-SiO₂	0.3	475	665	8	6120	21	3
TCBZ5@F127-SiO₂	0.5	428	605	27	6830	22	6

[a] Weight percent of dyes to F127. [b] Absorption maxima in nm. [c] Emission maxima in nm. [d] Quantum yields determined using rubrene in methanol ($\Phi = 27\%$) as the standard.^[170] [e] Stokes shifts in cm^{-1} . [f] Diameters measured by DLS in nm.

Table 2 - 4. Photophysical properties of **TCBZ2@F127-SiO₂** and **TCBZ5@F127-SiO₂** NPs in water.

2.4. Preparation of Surface-functionalized **TCBZ2@F127-SiO₂** and **TCBZ5@F127-SiO₂** NPs for in vivo Fluorescence Imaging

2.4.1. Synthesis of F127-COOH and F127-N₃

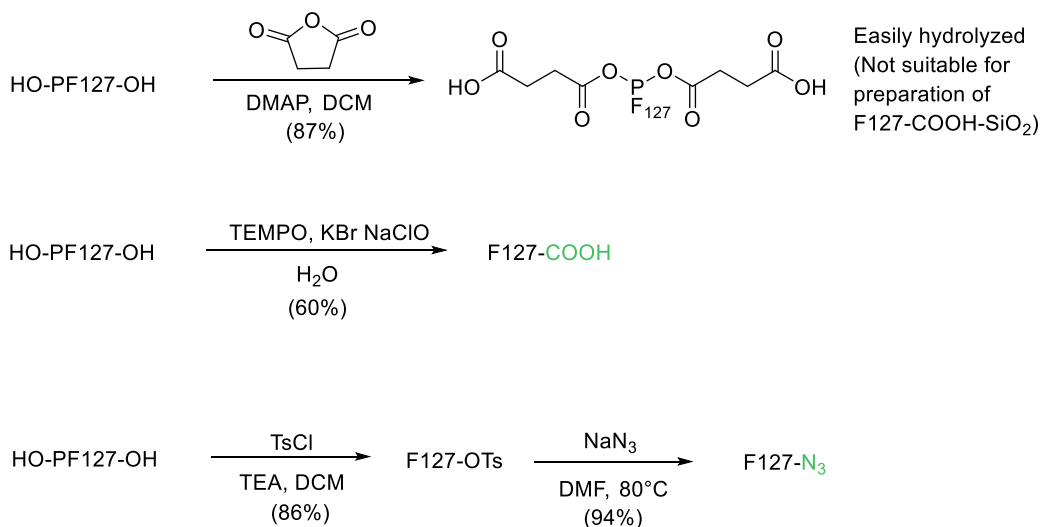


Figure 2 - 10. Synthetic route of **F127-COOH** and **F127-N₃**.

The synthetic routes of **F127-COOH** and **F127-N₃** are shown in Figure 2 - 10. In order to modify F127 with carboxyl, we firstly introduced a succinic acid moiety by opening succinic anhydride. However, the formed ester groups suffered hydrolysis in the silicate cross-linking process as it is done in acidic condition,

so we changed to the second way. Still using commercially available F127, its hydroxyl groups were directly oxidized into carboxyl groups by the catalytic system of 2,2,6,6-Tetramethyl-1-piperidinyloxy (TEMPO), KBr and NaClO,^[171] **F127-COOH** was obtained in 60% yield.

Azido modified F127 (**F127-N₃**) was synthesized by substitution of F127-OTs in NaN₃ in yield of 94%. **F127-OTs** was prepared by substitution of F127 with TsCl in 86% yield. All the modified F127 polymers were carefully purified by precipitation and fully characterized by IR spectrometry and NMR.

2.4.2. Preparation of TCBZ2/5@F127-COOH-SiO₂, TCBZ2/5@F127-X-SiO₂ and TCBZ5@F127-TPP-SiO₂ NPs

By simply using the mixture of **F127-COOH** or **F127-N₃** with the normal **F127** as the dye encapsulation matrices, the formed F127-SiO₂ NPs will obtain carboxyl or azido groups on their surface. Followed conjugation with functional moieties will allow them to be further functionalized (Figure 2 - 11).

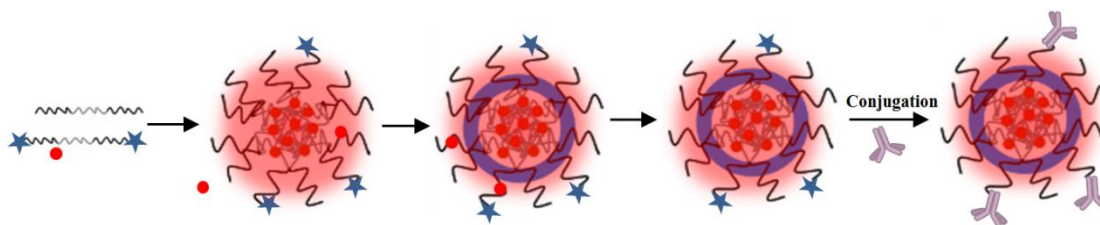


Figure 2 - 11. General procedure of preparation of surface functionalized F127-SiO₂ NPs.

It's well known that surface chemistry is critical to NPs properties, especially stability. Rampazzo and Prodi found that it is possible to use up to 50 wt% of F127-COOH to F127 for preparation of **F127-COOH-SiO₂** before having particle aggregation.^[172] We thus firstly studied the effects of surface modification on **F127-COOH-SiO₂** and **F127-N₃-SiO₂** NPs stabilities. The experiments were carried out on dye-absent NPs to exclude any possible interference from dye. The results are collected in **Table 2 - 5** and **Table 2 - 6**. As shown in **Table 2 - 5**, increasing the mass ratio of **F127-COOH** resulted in a more negative surface potential (ζ -potential) of the formed **F127-COOH-SiO₂**, which is consistent with more carboxyl groups on the particle surface. Meanwhile, no obvious size increase or particle aggregation problems happened during dialysis until the mass ratio of **F127-COOH** reached 15%, this value is much lower than 50% reported by Rampazzo and Prodi.^[172] It is probably due to the difference in the modification degree of **F127-COOH** we were using. Finally, 10% of **F127-COOH** was chosen for preparation of **TCBZ5@F127-COOH-SiO₂** NPs.

In the other hand, no obvious particle growth or aggregation was observed by varying the mass ratios of **F127-N₃** from 0% to 100% (Table 2 - 6). This demonstrated the negligible influence of azido groups on the particle stability. Therefore, 50% of **F127-N₃** was used for preparation of **TCBZ5@F127-N₃-SiO₂** NPs.

wt% ^[a]	Suspension	ζ-potential (mv)	Size ^[b]
0	Transparent	-2.2±0.4	22
5	Transparent	-3.6±1.0	26
10	Transparent	-4.2±0.6	30
15	Transparent	-4.4±0.4	29
30	Turbid	--	--
45	Big particles	--	--

[a] Weight percent of F127-COOH to total F127 polymers. [b] Diameters measured by DLS in nm.

Table 2 - 5. Properties of carboxyl modified F127-SiO₂ NPs with varied mass ratios of **F127-COOH** to F127.

wt% ^[a]	Suspension	Size (nm) ^[b]
0	Transparent	23
25	Transparent	24
50	Transparent	22
75	Transparent	22
100	Transparent	28

[a] Weight percent of F127-N₃ to total F127 polymers. [b] Diameters measured by DLS in nm.

Table 2 - 6. Properties of azido modified F127-SiO₂ NPs with varied mass ratios of **F127-N₃** to F127.

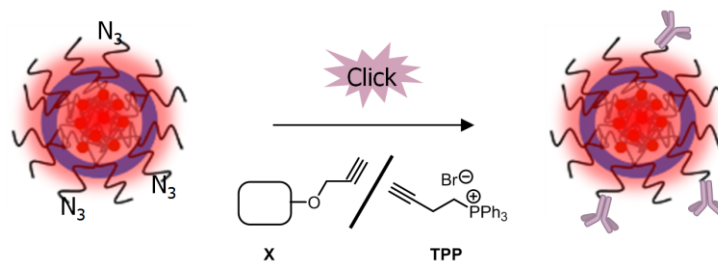


Figure 2 - 12. Preparation of **TCBZ5@F127-X-SiO₂** and **TCBZ5@F127-TPP-SiO₂** NPs from **TCBZ5@F127-N₃-SiO₂** NPs.

TCBZ5@F127-N₃-SiO₂ NPs with azido groups modified on the surface are ready to be grafted by functional moieties containing alkynyl groups by click reaction. Thus, by direct addition of the functional moieties (the alkynyl-**X** or alkynyl modified triphenylphosphine **TPP**) and the suitable “click” catalysts (CuSO₄, sodium ascorbate and the THPTA ligand) into the stock solution of **TCBZ5@F127-N₃-SiO₂** NPs (Figure 2 - 12), we obtained the target functionalized F127-SiO₂ NPs, **TCBZ5@F127-X-SiO₂** and **TCBZ5@F127-TPP-SiO₂** NPs. Dialysis was performed to remove the catalysts at the end.

2.4.3. Characterization of Surface-functionalized **TCBZ5@F127-SiO₂** NPs

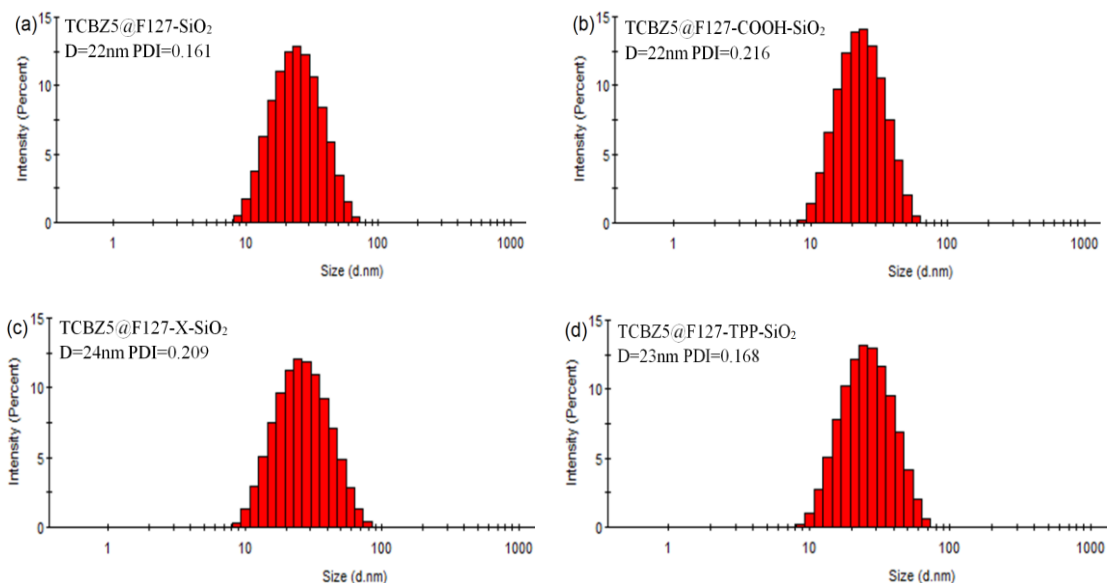


Figure 2 - 13. Particle size distributions of **TCBZ5@F127-SiO₂** (a), **TCBZ5@F127-COOH-SiO₂** (b), **TCBZ5@F127-X-SiO₂** (c) and **TCBZ5@F127-TPP-SiO₂** (d) NPs in water, measured by DLS.

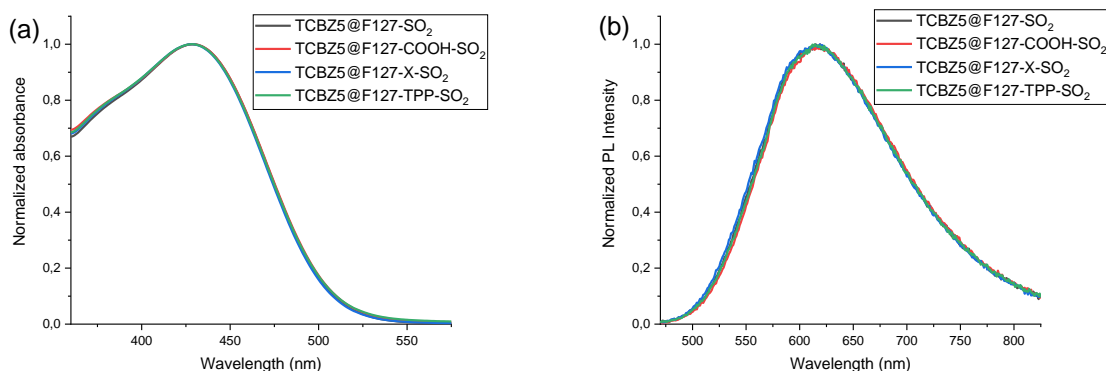


Figure 2 - 14 (a) absorption and (b) emission spectra of **TCBZ5@F127-SiO₂**, **TCBZ5@F127-COOH-SiO₂**, **TCBZ5@F127-X-SiO₂** and **TCBZ5@F127-TPP-SiO₂** NPs in water

Sample	$\lambda_{\text{abs}}^{[a]}$	$\lambda_{\text{em}}^{[b]}$	Φ (%) ^[c]	$\Delta\nu^{[d]}$	Size ^[e]	ζ -potential (mv)
TCBZ5@F127-SiO₂					23	-2.2 ± 0.4
TCBZ5@F127-COOH-SiO₂	428	605	27	6830	24	-4.2 ± 0.6
TCBZ5@F127-X-SiO₂					24	-0.7 ± 0.3
TCBZ5@F127-TPP-SiO₂					23	2.2 ± 0.6

[a] Absorption maxima in nm. [b] Emission maxima in nm. [c] Quantum yields determined using rubrene in methanol ($\Phi = 27\%$) as the standard.^[170] [d] Stokes shifts in cm^{-1} . [e] Diameters measured by DLS in nm.

Table 2 - 7. Properties of **TCBZ5@F127-SiO₂**, **TCBZ5@F127-COOH-SiO₂**, **TCBZ5@F127-X-SiO₂** and **TCBZ5@F127-TPP-SiO₂** NPs in water.

We then studied and compared the optical and physical properties of the surface functionalized NPs, **TCBZ5@F127-SiO₂**, **TCBZ5@F127-COOH-SiO₂**, **TCBZ5@F127-X-SiO₂** and **TCBZ5@F127-TPP-SiO₂**. From Figure 2 - 13, all the F127-SiO₂ NPs presented monodispersed sizes around 22 nm, which are in good agreement with the size previously measured in our laboratory, indicating neither the loading of **TCBZ5** nor the modifications of the NPs surface has significant influence on the particle size. Besides, the changes in ζ -potential proved us the successful conjugation of the functional moieties to the particle surface. As we expected, the modifications of the NPs surface did not alter the optical properties of the **TCBZ5@F127-SiO₂** NPs, either (Figure 2 - 14). Finally, all the four **TCBZ5@F127-SiO₂** NPs displayed absorption peaks at 428 nm and emission peaks at 605 nm with quantum yields around 27% (Table 2 - 7).

2.4.4. **TCBZ5@F127-SiO₂** and **TCBZ5@F127-X-SiO₂** NPs for Biphotonic *in vivo* Fluorescence Imaging

We thus performed biphotonic *in vivo* fluorescence imaging using **TCBZ5@F127-SiO₂** and **TCBZ5@F127-X-SiO₂** NPs. The NPs suspensions were diluted 3 times by distilled water after dialysis (dye concentration ~ 140 μM) and then sodium chloride was added (0.9 wt%) to form the target solutions for imaging.

Two white CD-1 IGS mice (Écully, France) were sacrificed for this experiment. They were anesthetized by a gas mixture of 1% isoflurane in air with body temperature maintained at 36-37°C using an electric heating pad. 0.1 mL of NPs solution was injected through the caudal vein using a catheter (BD Neoflon™, 16GA 0.6 x 19mm, Becton Dickinson, Helsingborg Sweden). A commercially available blood pool agent **FITC-dextran** (70 kDa) (0.01 mL) was also used as reference for blood vessels visualization and preliminary clearance experiments. **FITC-dextran** is indeed rapidly excreted through the kidneys. **FITC-dextran** was injected either right after the NPs or 10 minutes before animal sacrifice.

A bright fluorescence showing the whole blood vasculature network of a mice ear is visible by a 900 nm excitation immediately after injection of **TCBZ5@F127-SiO₂** NPs ('red' channel without emission filter other than the dichroic mirror, collecting all wavelengths > 560 nm) and **FITC-dextran** (green channel, band pass filter 522 ± 50 nm). The fluorescence persists for a long time, as shown in Figure 2 -15 (a and b), taken 1 h after injection. Even after 2 h of circulation, the bright fluorescence can still be seen in the blood vasculature network, which indicated a long circulation of the NPs in mice body. Imaging near the skin reveals sebaceous glands (auto-fluorescence in the green channel). The shadows beneath the sebaceous glands (Figure 2 – 15 a and b) indicated the absorption of NPs fluorescence by the biological tissue, and indicted that the imaging depth is less than 100 μm. It's worth noting that the yellow color of the blood vasculature came from the overlap of the red from **TCBZ5@F127-SiO₂** NPs and the green from **FITC-dextran**. In the case of **TCBZ5@F127-X-SiO₂** NPs, as shown in Figure 2 -15 c and d, without injection of **FITC-dextran** only red was observed in the vasculature system.

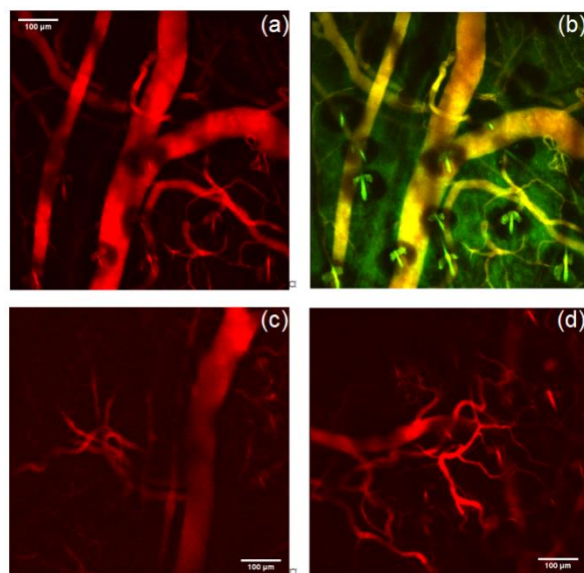


*Figure 2 - 15. Two-photon microscopic images of the circulation of **CBZ5@F127-SiO₂** (a, b) and **CBZ5@F127-X-SiO₂** (c, d) NPs in the mouse ear 1h after injection. The images are a z-projection of the standard deviations of fluorescence intensities: 50 slices, step-size 2 μm = thickness of 100 μm. $\lambda_{exc} = 900$ nm, green channel: 542 ± 50 nm, red channel: > 560 nm, yellow = red + green. The green channel shows endogenous fluorescence signals from sebaceous glands and **FITC-dextran**. These glands are at the surface of the skin, indicating that the imaging depth is less than 100 μm.*

From the two-photon microscopic images of the excised organs (Figure 2 - 16), the NPs clearance seems the same for both **TCBZ5@F127-SiO₂** and **TCBZ5@F127-X-SiO₂** NPs: the dye is mainly in the spleen and in lower concentration in the liver or kidney. This again explained a long circulation time (at least 2 hours and more) of the NPs in the blood. To further explain, we take the kidney as an example. As shown in pictures b and f, the green channel shows the fluorescence signals from **FITC-dextran** in the kidney tubules whereas fluorescence from NPs is still in the vascular system (red channel).

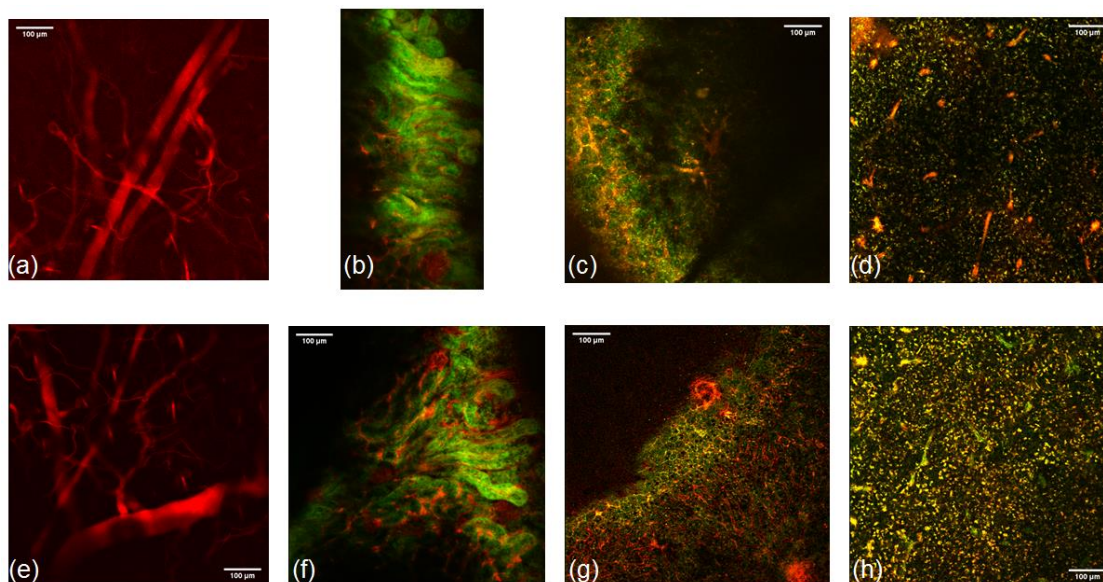


Figure 2 - 16. Two-photon microscopic images of ear vasculature system (a, e), kidneys (b, f), livers (c, g) and spleens (d, h) 2h after injection of **CBZ5@F127-SiO₂** (up) and **CBZ5@F127-X-SiO₂** (down) NPs. $\lambda_{exc} = 900 \text{ nm}$, green channel: $542 \pm 50 \text{ nm}$, red channel: $> 560 \text{ nm}$, yellow = red + green. 0.01 mL **FITC-dextran** was injected 30 min before dissection of the second mouse.

The only difference we observed between the two kinds of NPs in the imaging experiment is from the liver images. As shown in Figure 2 - 17 b, a zoomed picture of Figure g, **CBZ5@F127-X-SO₂** NPs seem stuck against the vasculature wall (endothelial cells), leading to a hollow lumen of the vessels. It is probably caused by the **X** moieties on the particle surface, but the specific mechanism is currently unknown.

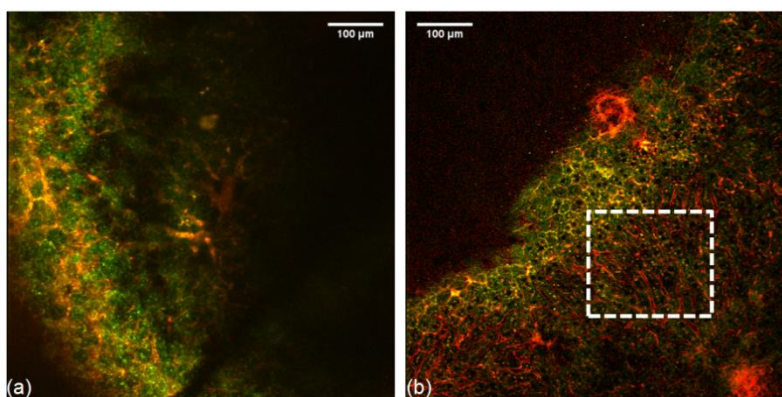
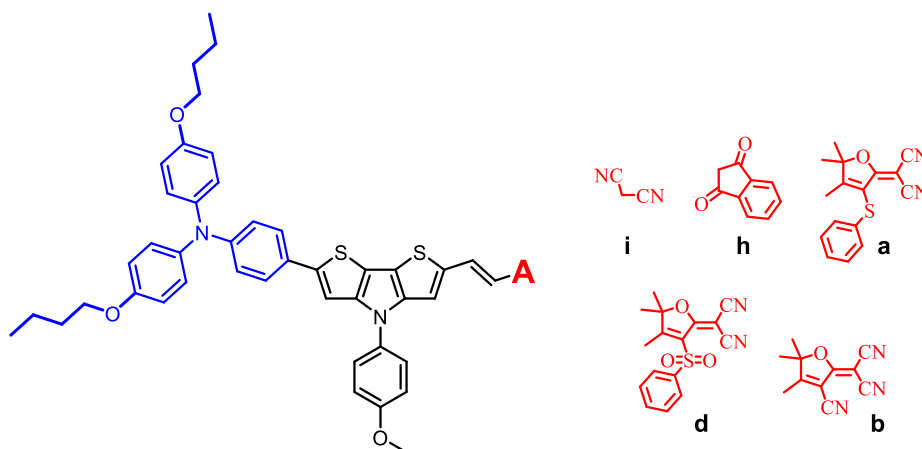


Figure 2 - 17. Two-photon microscopic images of excised livers 2h after injection of **CBZ5@F127-SiO₂** (a) and **CBZ5@F127-X-SiO₂** (b) NPs. $\lambda_{exc} = 900 \text{ nm}$, green channel: $542 \pm 50 \text{ nm}$, red channel: $> 560 \text{ nm}$, yellow = red + green. 0.01 mL **FITC-dextran** was injected 30 min before dissection of the second mouse. Red and yellow dots are probably NPs in Kupfer cells (macrophages).

3. Synthesis of EBTN dyes and EBTN@F127-SiO₂ NPs for Fluorescence Imaging

3.1. Synthetic Design of EBTN Dyes



Scheme 2 - 4. Chemical structures of EBTN dyes.

To optimize the BTN unit, we intended to modify it by two butoxy groups, as it is shown in Scheme 2 - 4. On the one hand, the introduction of two alkyl chains can increase the lipophilicity of dyes to make them easier to be wrapped by F127. On the other hand, alkoxy groups on the triphenylamine can strengthen its electron-donating ability and further push the spectra of the dyes forward longer wavelength. Furthermore, in order to retain the great photophysical properties of the previous BTN-based dyes, the same acceptors **h**, **a**, and **b** were chosen by us for the construction of the new series of dyes. At the same time, acceptor **i** with relatively weak electron-withdrawing ability, and **d** which was recently developed in our laboratory were used to enlarge the new dye system.

3.2. Synthesis and Photophysical Properties of EBTN Dyes

3.2.1. Synthesis of EBTN Dyes

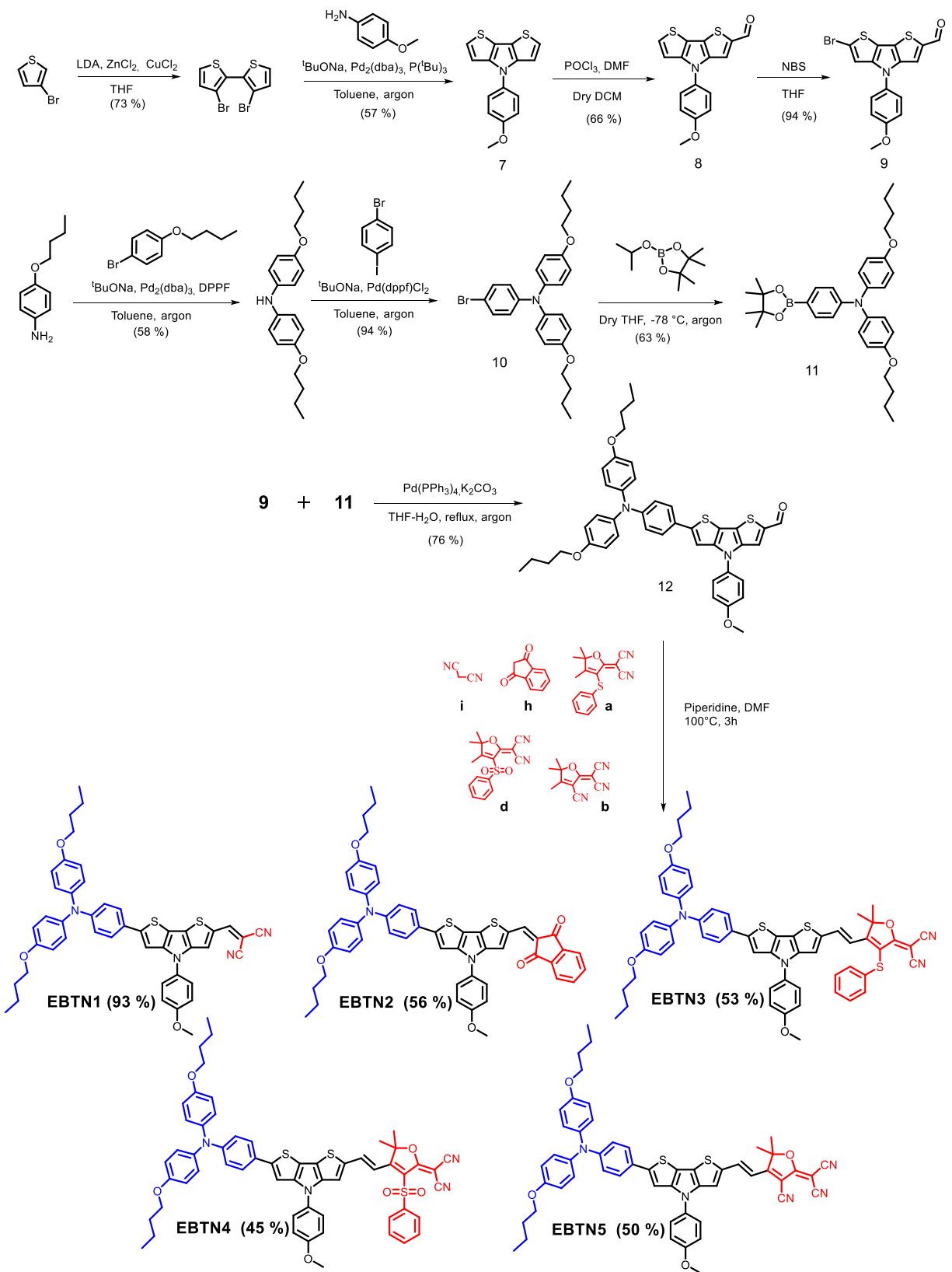


Figure 2 - 18. Synthetic routes of **EBTN1-EBTN5**.

The synthetic routes of **EBTN1-EBTN5** started from the dimerization of 3-bromothiophene to form 3,3'-dibromo-2,2'-dithiophene using lithium diisopropylamide (LDA) to selectively remove the hydrogen at position 2. Then, Buchwald-Hartwig coupling with p-anisidine provided **7** in yield of 57%. Through formylation by POCl₃ and DMF, **7** was transformed into **8** in 66% yield. Reaction with NBS afforded the bromo-derivative **9** in 94% yield. The active butoxy modified triphenylamine derivative **11** was obtained by boronation of **10** in 63% yield, **10** was synthesized by two steps of Buchwald-Hartwig coupling in presence of ^tBuONa and Pd catalysts from 4-butoxyaniline. Then, **9** and **11** formed the EBTN aldehyde **12** via Suzuki cross-coupling, in 76% yield. Condensation of **12** with acceptors (**i**, **h**, **a**, **d** and **b**) afford final dyes **EBTN1-EBTN5** (Figure 2 - 18). All the dyes and intermediate products were carefully purified and fully characterized by NMR and mass spectrometry.

3.2.2. Photophysical Properties of EBTN Dyes

3.2.2.1. Absorption and Emission

The absorption and emission spectra of **EBTN1-EBTN5** were recorded in chloroform (Figure 2 - 19). The relevant data are collected in Table 2 - 8.

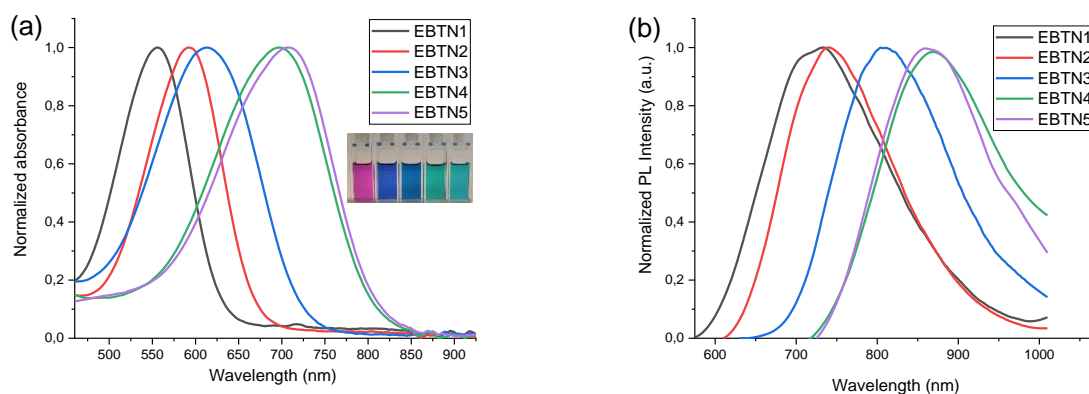


Figure 2 - 19. (a) Normalized absorption and (b) emission spectra of **EBTN1-EBTN5** in chloroform.

From the absorption spectra, **EBTN1-EBTN5** with different acceptors showed their characteristic ICT bands from visible to NIR region (Figure 2 - 19, left). Among them, **EBTN4** and **EBTN5** possessing relatively stronger acceptors thus more forceful ICT presented more red-shifted absorptions and emissions ($\lambda_{\text{abs}}/\lambda_{\text{em}} > 700/850$ nm). In Table 2 - 8, by variation of the acceptors from the weakest **i** to the strongest **b**, the corresponding **EBTN1** and **EBTN4** showed absorption maxima red-shifted from 555 nm to 710 nm, accompanied by the emission maxima red-shifted from 725 nm to 885 nm. All the dyes are characterized by large Stokes shifts from 2520 cm⁻¹ for **EBTN5** to 4220 cm⁻¹ for **EBTN1** thanks to

their ICT properties. In addition, all the EBTN dyes exhibited moderate to good quantum yield (Φ) in chloroform from $\Phi = 1\%$ for **EBTN4** to $\Phi = 11\%$ for **EBTN2**, which is much higher in toluene from $\Phi = 17\%$ for **EBTN3** to $\Phi = 62\%$ for **EBTN2** (Table 2 - 9).

Notably, given the lack of reliable standards having large Stokes shifts in the deep red range, quantum yields for all dyes were determined by multiple confirmations. For instance, using styryl 9M ($\Phi = 24\%$ in CHCl_3)^[173] as a reference, the Φ of **EBTN3** in CHCl_3 was determined to be $\Phi = 8\%$. This value was confirmed by using **Rho 800** ($\Phi = 25\%$ in EtOH)^[174] and **EBTN1** ($\Phi = 10\%$ in CHCl_3 , in turn determined using cresyl violet, **CV**, $\Phi = 55\%$ in MeOH)^[175] as additional references. That's to say, we are relatively confident about the quantum yield values measured. To be more rigorous, we are planning to build a chain of standards to go to NIR, starting from well characterized **Rho 6G** ($\lambda_{\text{em}} = 552\text{ nm}$ in MeOH) and using compounds such as **LDS 698** ($\lambda_{\text{abs}}/\lambda_{\text{em}} = 508/677\text{ nm}$ in CHCl_3) and **LDS 798** ($\lambda_{\text{abs}}/\lambda_{\text{em}} = 596/753\text{ nm}$ in CHCl_3). This work would be done in the near future to support all the NIR dyes we have synthesized in the lab.

In comparison with the previous BTN dyes (the dyes with the same acceptors are shown in the same color in Table 2-1), our new EBTN dyes present 20-30 nm more red-shifted absorptions and 30-60 nm more red-shifted emissions, indicating their relatively stronger ICT due to the enhanced electron-donating ability of the butoxy modified triphenylamine unit.

Dyes in chloroform	λ_{abs} ^[a]	ϵ ^[b]	λ_{em} ^[c]	Φ (%) ^[d]	$\Delta\nu$ ^[e]
EBTN1	555	56200	725	10	4220
EBTN2	593	75100	740	11	3350
EBTN3	615	65200	810	8	3910
EBTN4	700	77100	885	1	2990
EBTN5	710	77900	865	2	2520
BTNI	573	91100	706	41	3300
BTNSPh	591	49000	758	26	3730
BTNTCF	680	71750	801	25	2220

[a] Absorption maxima in nm. [b] Absorption coefficients. [c] Emission maxima in nm. [d] Quantum yields of dyes in chloroform determined using CV in ethanol ($\Phi = 55\%$)^[175] as the standard for **EBT1**, styryl 9M in CHCl_3 ($\Phi = 24\%$)^[173] for **EBT2-EBTN5**. [e] Stokes shifts in cm^{-1} .

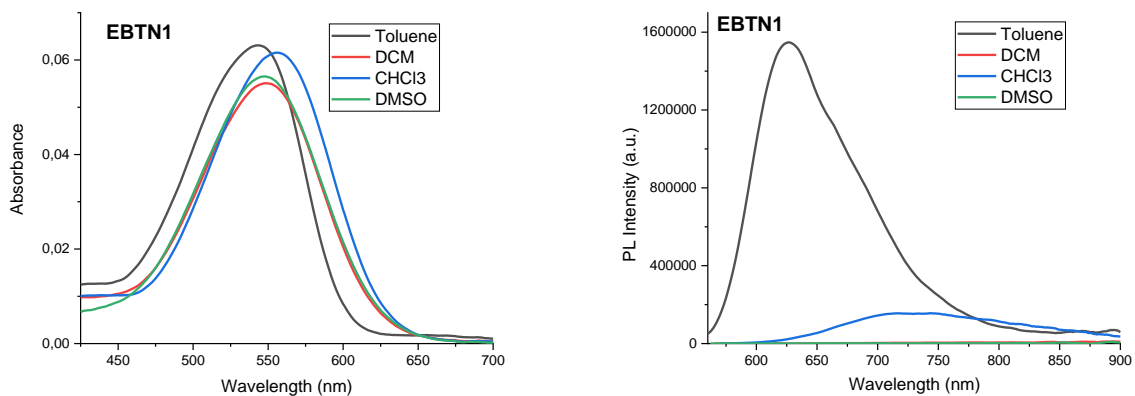
Table 2 - 8. Photophysical properties of **EBTNI-EBTN5** in chloroform.

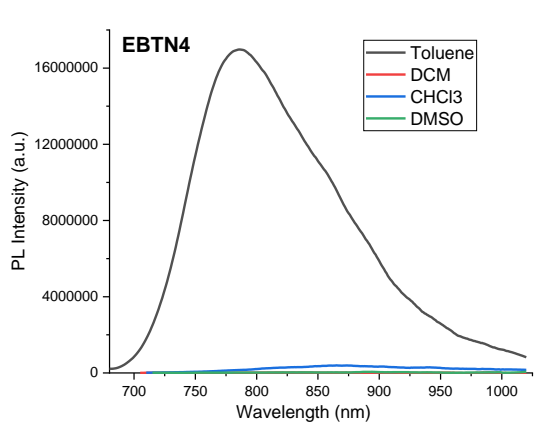
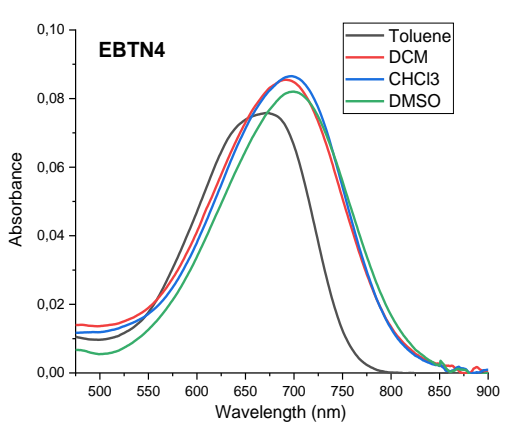
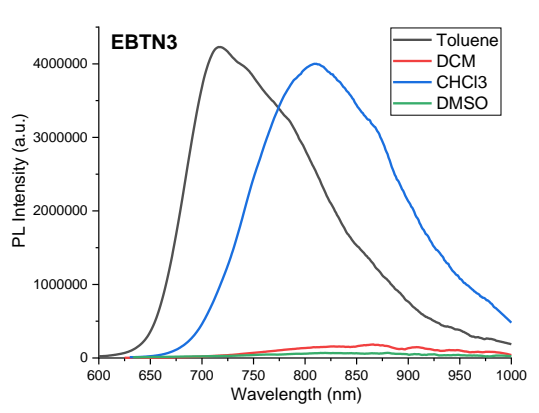
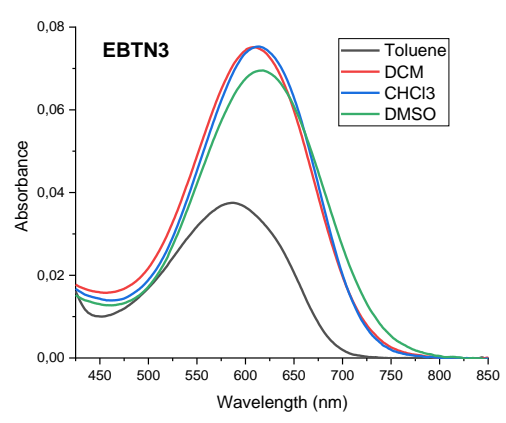
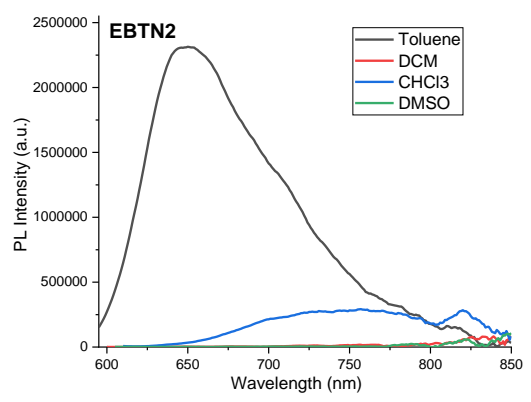
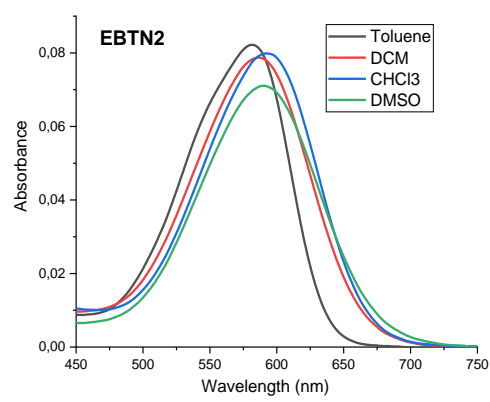
Dyes in toluene	$\lambda_{\text{abs}}^{[a]}$	$\lambda_{\text{em}}^{[c]}$	Φ (%) ^[d]	$\Delta\nu^{[e]}$
EBTN1	543	625	41	2416
EBTN2	581	650	62	1827
EBTN3	588	718	17	3079
EBTN4	664	786	33	2337
EBTN5	670	782	47	2137
BTNI	563	639	20	2110
BTNSPh	568	701	19	3340
BTNTCF	642	747	10	2190

[a] Absorption maxima in nm. [b] Absorption coefficients. [c] Emission maxima in nm. [d] Quantum yields of dyes in toluene determined using CV in ethanol ($\Phi = 55\%$)^[175] as the standard for **EBT1**, styryl 9M in CHCl_3 ($\Phi = 24\%$)^[173] for **EBT2-EBTN5**. [e] Stokes shifts in cm^{-1} .

Table 2 - 9. Photophysical properties of **EBTN1-EBTN5** in toluene.

3.2.2.2. Solvatochromism





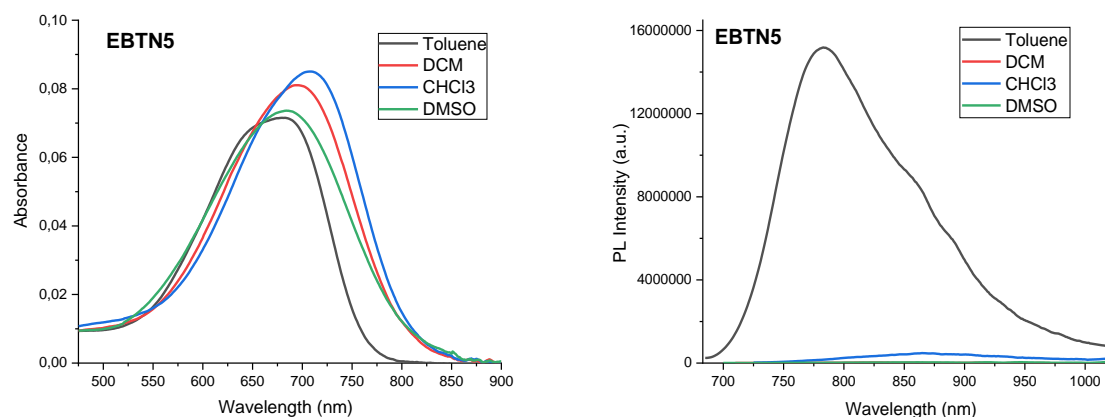


Figure 2 - 20. (Left) absorption and (right) emission spectra of **EBTN1-EBTN5** in different solvents. ($1.0 \times 10^{-6} \text{ mol L}^{-1}$).

Then we investigated the solvatochromic effects of **BTN1-BTN5** by recording their absorption and emission spectra in toluene, dichloromethane, chloroform and DMSO., solvent of increasing polarity

In the absorption spectra (Figure 2 - 20, left), all the dyes showed distinctive bathochromic-shifts with the increasing of the solvent polarity. Due to poor solubility, the absorption bands in toluene appeared severely broadened. Meanwhile, all the dyes also exhibited red-shifted emission bands as increasing of the solvent polarity. Except **EBTN3**, it presented comparative fluorescence intensities in toluene and dichloromethane due to the weak absorption in toluene caused by aggregation, all the other dyes showed significantly enhanced emissions in toluene than in other solvents (Figure 2 - 20, right).

Note that, consistently to what we already observed for the BTN dyes, EBTN dyes are not emissive in solid state.

3.3. Preparation of **EBTN@F127-SiO₂** NPs for *in vivo* Fluorescence Imaging

3.3.1. Preparation of **EBTN@F127-SiO₂** NPs

During the preparation of the dye solutions, all the EBTN dyes were found to be of higher solubility in organic solvents in comparison to the BTN dyes, which indicated their improved lipophilicity and high potential to be used for preparation of F127-SiO₂ NPs for *in vivo* fluorescence imaging.

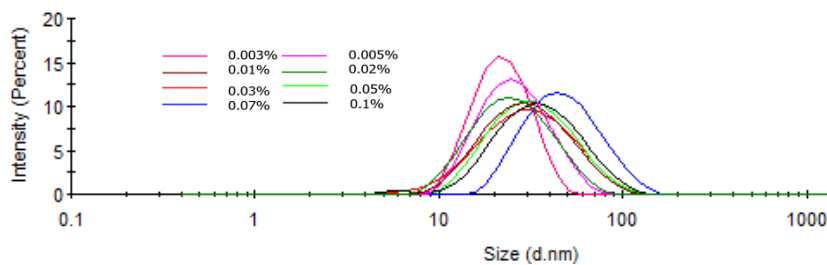


Figure 2 - 21. Particle size distributions of **EBTN5@F127-SiO₂** NPs in water with increasing of the mass ratio of **EBTN5** to **F127** from 0.1% to 0.8%, measured by DLS.

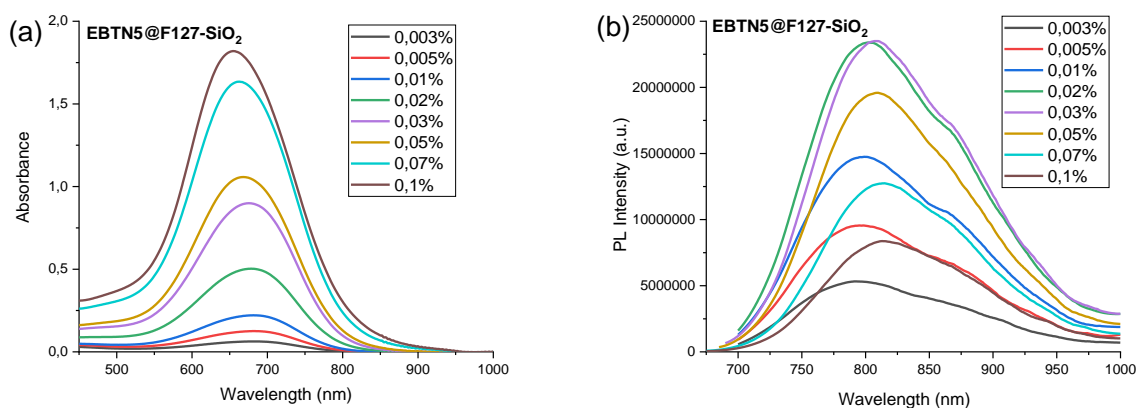


Figure 2 - 22. (a) absorption and (b) emission changes of **EBTN5@F127-SiO₂** NPs with varied mass ratio of **EBTN5** to **F127** (0.1% to 0.8%).

As we have already observed, the previous BTN dyes are prone to assemble into non-emissive aggregates, leading to heterogeneous NPs and fluorescence quenching in preparation of the **BTN@F127-SiO₂** NPs. Hence, we firstly took **EBTN5** as the representative to study the relationship between the dye loading and the NPs properties. From Figure 2 - 21, as increasing of the dye loading from 0.003% to 0.1%, the particle size slightly increased but no aggregates were observed. However, the absorption and emission spectra of **EBTN5@F127-SiO₂** NPs, as shown in Figure 2 - 22, showed the steadily increased absorption is accompanied by the emission declined after reaching the maximum at the dye loading of 0.03%. The gradually decreased emission was accompanied by a slight red-shift, indicating the aggregation and fluorescence quenching of **EBTN5** in **F127-SiO₂** NPs took place. All the EBTN dyes present an ACQ effect in the solid state, loading amount of 0.02% was thus chosen for preparation of the **EBTN@F127-SiO₂** NPs. Following the general procedure, we obtained **EBTN1-EBTN5@F127-SiO₂** NPs.

3.3.2. Characterization of EBTN F127-SiO₂ NPs

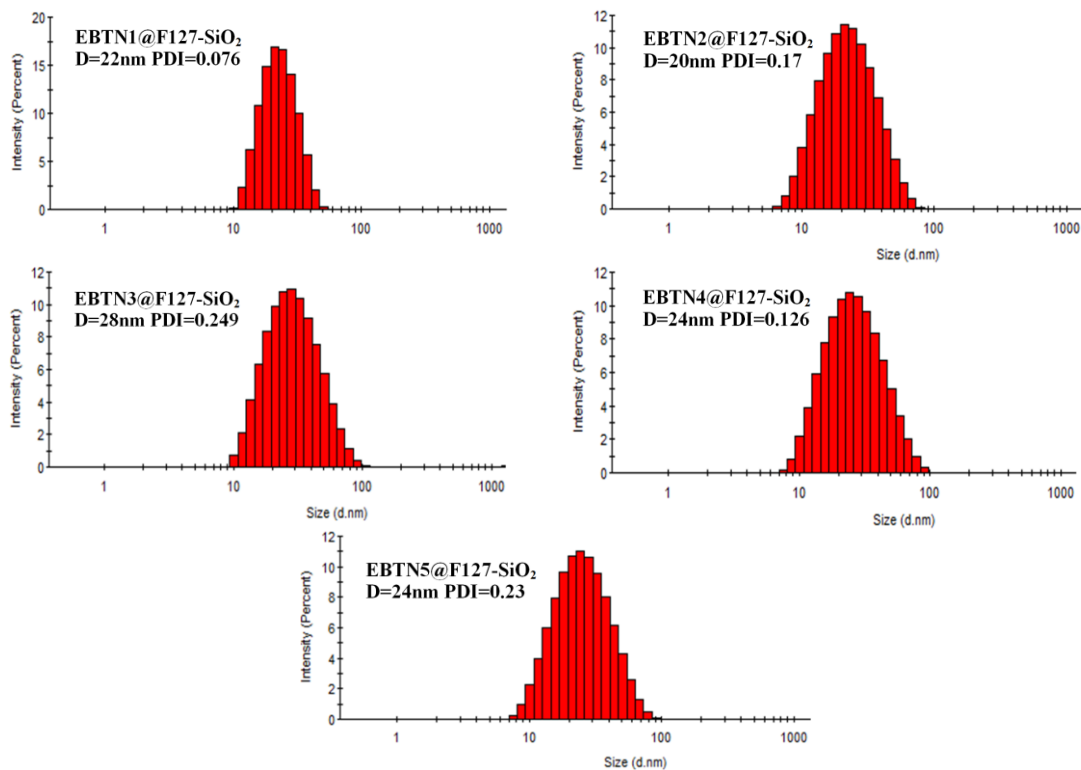


Figure 2 - 23. Particle size distributions of *EBTN1@F127-SiO₂* - *EBTN5@F127-SiO₂* NPs in water, measured by DLS.

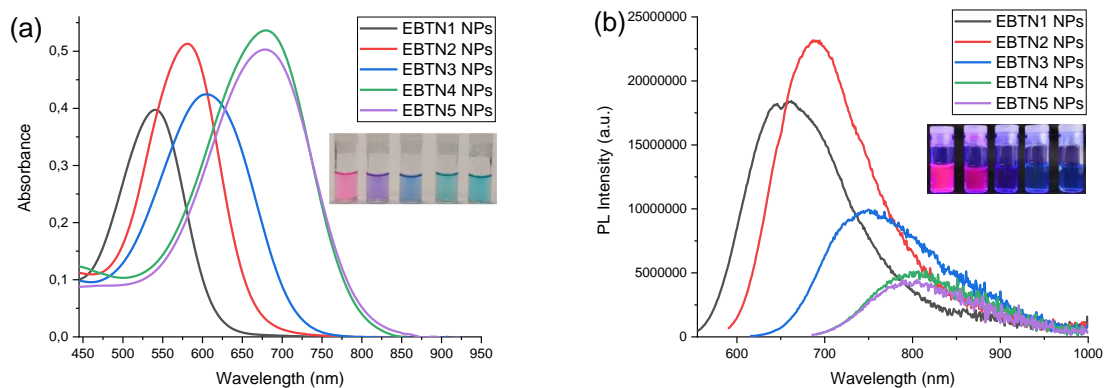


Figure 2 - 24. (a) absorption and (b) emission spectra of *EBTN1-EBTN5@F127-SiO₂* NPs in water.

Sample in water	$\lambda_{\text{abs}}^{\text{[a]}}$	$\lambda_{\text{em}}^{\text{[b]}}$	Φ (%) ^[c]	$\Delta\nu^{\text{[d]}}$	Size ^[e]
EBTN1 F127-SiO ₂	540	655	67	3250	22
EBTN2 F127-SiO ₂	580	690	59	2750	20
EBTN3 F127-SiO ₂	605	750	36	3200	28

EBTN4 F127-SiO₂	680	810	13	2360	24
EBTN5 F127-SiO₂	678	800	12	2250	24

[a] Absorption maxima in nm. [b] Emission maxima in nm. [c] Quantum yields of EBT@F127-SiO₂ NPs in water determined using CV in ethanol ($\Phi = 55\%$)^[175] as the standard for **EBT1**@F127-SiO₂ NPs, styryl 9M in CHCl₃ ($\Phi = 24\%$)^[173] for **EBT2-EBTN5**@F127-SiO₂. [d] Stokes shifts in cm⁻¹. [e] Diameters measured by DLS in nm

Table 2 - 10. Properties of **EBTN1-EBTN5**@F127-SiO₂ NPs in water.

Then, we investigated the general properties of the EBTN@F127-SiO₂ NPs. The size distributions are presented in Figure 2 - 23, the absorption and emission spectra are shown in Figure 2 - 24, and the relevant data are collected in Table 2 - 10.

From Figure 2 - 23, all the suspensions of the EBTN@F127-SiO₂ NPs showed monodispersed size of 22 nm by DLS, which is in good agreement with the F127-SiO₂ NPs we synthesized before. This proved the improved abilities of all the EBTN dyes to be encapsulated by F127 thus our success in BTN dyes modification. In Figure 2 - 24, all the EBTN@F127-SiO₂ NPs presented absorption and emission maxima between those in chloroform and in toluene, it is consistent with our previous finding that the environment of the dyes in F127-SiO₂ NPs is similar to the mixture of chloroform and toluene. As shown in Table 2 - 10, **EBTN1**@F127-SiO₂ and **EBTN2**@F127-SiO₂ NPs have Φ around 60%, which is much higher than those of the reported red/NIR NPs.^[172,176,177] Furthermore, even **EBTN4**@F127-SiO₂ and **EBTN5**@F127-SiO₂ NPs showed Φ falling to around 12%, this value is still considered great in the given wavelengths (above 800 nm). The NIR emissions along with the high Φ make all the EBTN@F127-SiO₂ NPs promising for *in vivo* fluorescence imaging. Nevertheless, it is at present impossible to test in *in vivo* microscopy the most red-shifted **EBTN3**@F127-SiO₂ - **EBTN5**@F127-SiO₂ NPs because the detectors mounted on the microscope in the *in vivo* microscopy platform in Grenoble do not allow to collect at such wavelengths. Current detectors cannot detect above at best 700 nm.

4. Conclusion

In this chapter, we synthesized two new series of push-pull dipolar dyes **TCBZ1-TCBZ8** and **EBTN1-EBTN5** based on the fluorene and BTN dyes previously synthesized in our laboratory. With improved optical and physical properties, they were allowed to be loaded by F127-SiO₂ NPs for two-photon fluorescence imaging.

TCBZ1-TCBZ8 are synthesized by introduction of two *tert*-butyl groups to the carbazole unit. With different acceptors thus different ICT, they presented emissions red-shifted from 648 to 745 nm as well as interesting solvatochromism and large stokes shifts. All the TCBZ dyes are emissive in solid states due to

AIE, particularly for **TCBZ7** whose Φ up to 42% makes it candidate for NIR solid luminescent materials. In addition, **TCBZ2** and **TCBZ5** with either the most red-shifted emission or relatively high Φ were chosen for preparation of F127-SiO₂ NPs. The optimal dye loading for **TCBZ2@F127-SiO₂** and **TCBZ5@F127-SiO₂** NPs was determined to be 0.3% and 0.5%, respectively.

For functionalization of the TCBZ@F127-SiO₂ NPs with functional moieties for active targeting, carboxyl and azido modified F127 were prepared. Then **TCBZ5@F127-COOH-SiO₂** and **TCBZ5@F127-N₃-SiO₂** NPs were afforded using 0.5% dye loading with 10% F127-COOH and 50% F127-N₃, respectively. Followed conjugation of the N₃ modified NPs with alkynyl modified **TPP** and **X**, the final **TCBZ5@F127-X-SiO₂** and **TCBZ5@F127-TPP-SiO₂** were obtained. The same size of around 22 nm and the similar optical properties of these surface functionalized F127-SiO₂ NPs indicated the negligible impacts of the surface functions to the particle optical and physical properties. In *in vivo* fluorescence imaging, **TCBZ5@F127-SiO₂** and **TCBZ5@F127-X-SiO₂** NPs successfully imaged the blood vessels and different organs of the mice by two-photon excitation, and they were demonstrated a slow clearance from the mice circulatory system.

New dyes **EBTN1-EBTN5** obtained by introducing two butoxy groups to the triethylamine unit of the BTN dyes maintain interesting solvatochromism and large stokes shifts due to ICT. Among them, **EBTN4** and **EBTN5** with relatively strong electron-withdrawing acceptors showed emissions above 850 nm. Moreover, thanks to the improved lipophilicity of EBTN dyes, they were successfully encapsulated by F127 to form the EBTN@F127-SiO₂ NPs. To achieve a highest brightness, **EBTN1-EBTN5@F127-SiO₂** NPs were prepared using 0.02% dye loading. Lastly, all these EBTN@F127-SiO₂ NPs are of high brightness in NIR region benefiting from the apolar environment and isolated environment provided by the particle core.

Complete measurement of the 2P cross-section is also missing. However, if cross-section measurements in the range 600-1000 nm is well described, this is not the case for higher wavelengths (> 1000 nm). At these wavelengths, solvent absorption has to be taken into account. Such measurements are not possible for the moment in the laboratory, but works are in progress in that direction.

Chapter III. Design of NIR Dyes and NPs for *in vivo* PA Imaging

1. Introduction

1.1. Previous Work

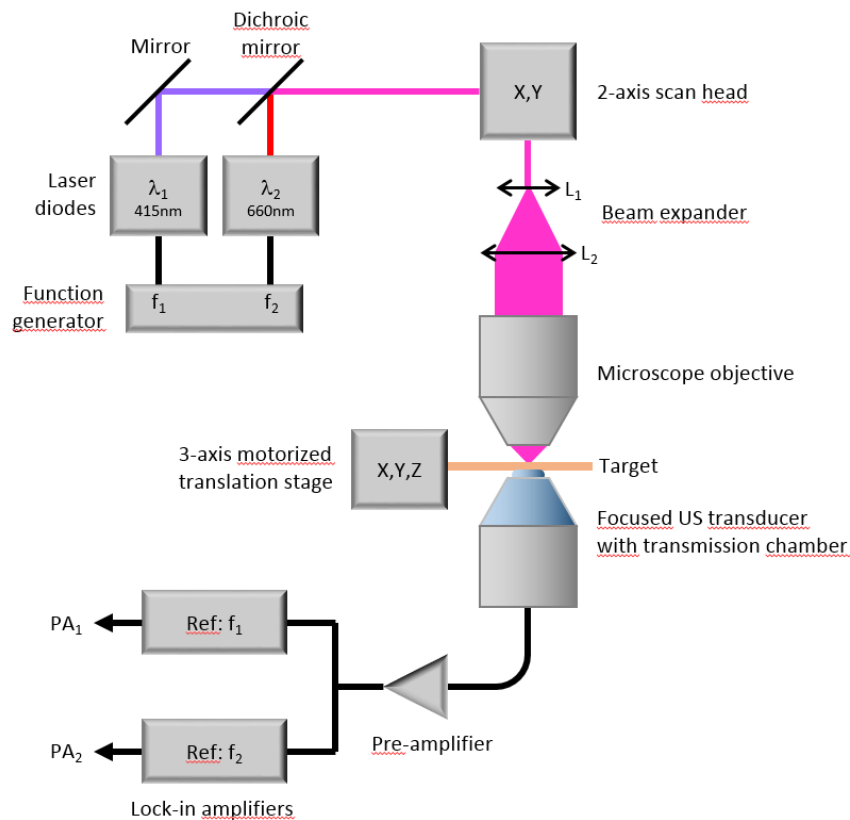


Figure 3 - 1. Photoacoustic microscope (PAM).^[110]

The photoacoustic microscope (PAM) available for us is a homemade device assembled by our collaborators Olivier Hugon and Boudewin Van der Sanden at Liphy in Grenoble. The working principle diagram is shown in Figure 3 - 1.

Four laser diodes (415 nm, 445 nm, 660 nm and 808 nm) are so far accessible, this means contrast agents with absorptions around these wavelengths are candidates for PA imaging. Indeed, modulation of the frequencies of the laser diodes through a sinusoidal function makes it possible to excite in a dual or multiple mode that facilitates the subsequent comparison of imaging generated by different contrast agents. For

example, if the 415 nm and 660 nm laser diodes work together, their frequency will be set differently at one of 5 MHz and another of 5.3 MHz. The two laser beams are firstly merged into one by the reflection of motorized mirrors. In the 2-axis scan head, the beam is then extended to cover the entire entrance of an x20 lens. The objective with an average power of a few milliwatts at the exit helps focus the light on the sample. After absorption of the light, the ultrasonic waves produced by the PA contrast agents are detected by an electric transducer. Finally, the electrical signal is amplified and demodulated to form the PA images of each wavelength. Therefore, with this combination it is possible to image the sample by two contrast agents with absorptions around 415 nm and 660 nm and compare their PA effects to each other.

Furthermore, two supports are used to pre-evaluate the PA effect of the contrast agents before *in vivo* imaging: a piece of paper on which the contrast agent is adsorbed, to simulate the PA signal, and a microfluidic circuit to simulate the microvasculature of mice.

Our laboratory recently tried two push-pull hemicyanine dyes **CPO1** and **CPO2** for *in vivo* PA imaging (Figure 3 - 2). They were previously synthesized in our laboratory for second order non-linear optics and electro-optical modulation, as well as optical limitation in telecommunication wavelengths utilities.^[178] With the indoline derivative as electron donor and TCF derivative as electron acceptor, these two dyes present good absorptions at 808 nm or 660 nm in chloroform, thus inspired us to try them for PA imaging. The first experiments performed on microfluidic circuits showed that a high dye concentration (at least 0.1 mM) is needed to visualize the PA signals. For the purpose of increasing the dye concentration in mice vessels, we tried to form dye nanoaggregates by nanoprecipitation. Each NPs indeed contains a high number of dyes. We also managed to obtain very concentrated nanoaggregates suspensions by further rotary evaporation of water. In the final imaging of the vasculature of a mouse, the concentrated nanoaggregates of **CPO1** and **CPO2** showed excellent PA response to 660 nm excitation. However, due to excessively high concentrations as well as low colloidal stability of the nanoaggregates in blood vessels, which was proved by the obvious size increases of the nanoaggregates in water over time, the blockage of the certain capillaries took place.

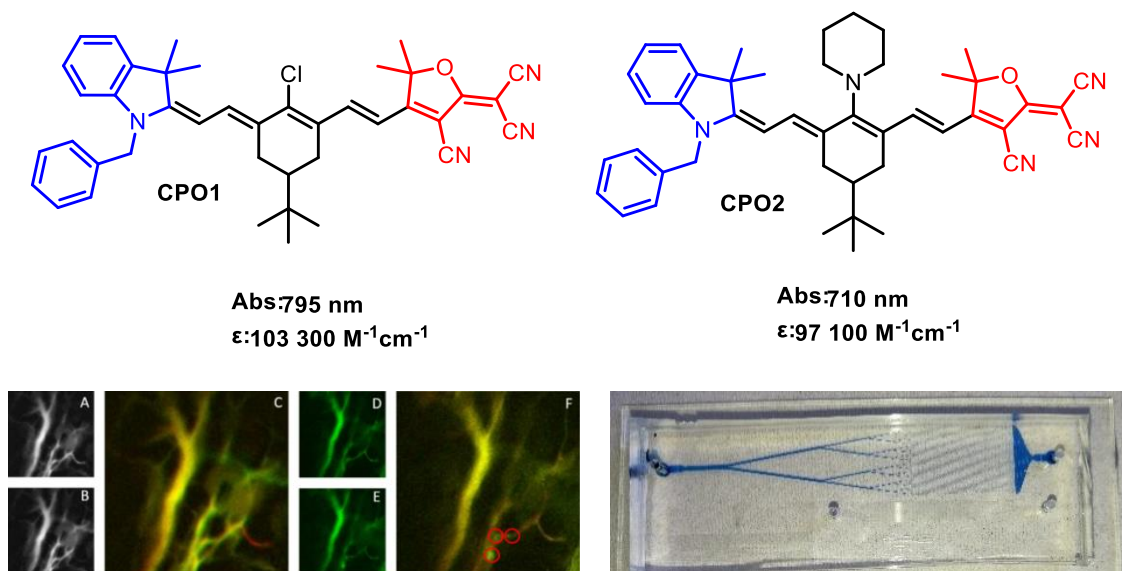


Figure 3 - 2. Chemical structures of CPO1 and CPO2 (up); (down) *in vivo* PA imaging of CPO1 (left) and the microfluidic circuit of CPO2 (right).^[110]

1.2. Objectives

While the hemicyanine dyes **CPO1** and **CPO2** presented great potential for PA imaging benefiting from their high absorptions at 660 nm or 808 nm, their nanoaggregates seemed far from ideal in *in vivo* application due to the blocking effect on the vascular system. Hence, our goal here was to find more stable and biocompatible nanoparticles to load our dyes for *in vivo* PA imaging.

Dye-loaded polymer NPs (PNPs), as we introduced in the first chapter, are good candidates for loading dyes for bioimaging. Therefore, we cooperated with Arnaud Favier from the Polymer Materials Engineering Laboratory of Lyon (IMP Lyon 1, UMR 5223), who has been working on developing polyacrylate polymers, to prepare the high dye-loaded PNPs for *in vivo* PA imaging.

Two strategies were envisaged:

- Grafting dyes on a pre-formed amphiphilic polymer through substitution, then forming the PNPs via self-assembly.
- Directly using dyes as monomer to form the polymer which can be stabilized by another water-soluble polymer.

Accordingly, we were mainly responsible for the modification of the hemicyanine dyes to allow them for the two strategies and Arnaud Favier helped us prepare the PNPs.

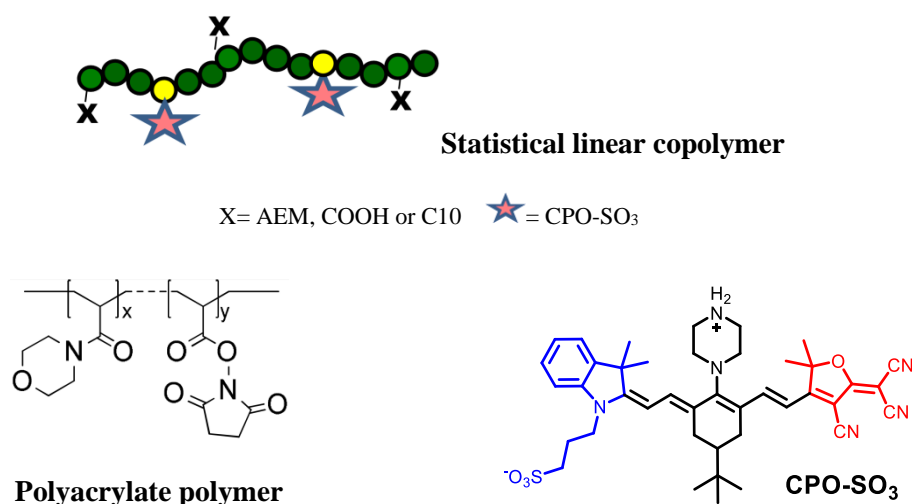
Besides, F127-SiO₂ NPs with limited dye encapsulation ability have been restricted in PA imaging. In this regard, we intended to take advantage of the modifiable surface of F127-SiO₂ NPs for dye conjugation to improve their dye loading.

This chapter presents the preliminary results we have obtained in this field, essentially the preparation and the beginning of the characterization of the different nanoparticles. If this work is far from being complete, this is due to the very particular situation we encountered in 2020 because of the Covid and the resulting lockdown. We hope to be able to continue and complete this work as soon as possible.

2. Preparation of CPO-SO₃ PNPs for PA Imaging

2.1. Synthetic Design of CPO-SO₃ Polymer

Arnaud Favier developed a polyacrylate polymer with multiple activated carboxylic acid functions (NHS ester) on its side chain (Scheme 3 - 1).^[179] Dyes containing amine groups are therefore easy to be grafted on the polymer via covalent linkage. Loading ratio can be varied by adjusting the stoichiometry. Hydrolysis or capping of the remaining acid functions with 4-(2-aminoethyl) morpholine (**AEM**) or various amines (we used decylamine, **C10**) make it possible to control the solubility or hydrophobicity of the formed dye-loaded polymer.



Scheme 3 - 1. Polymers developed at IMP and proposal for grafting CPO-SO₃ for PA imaging.^[179]

Hence, on dye synthesis, we planned to replace the piperidine unit of **CPO2** by a piperazine unit to obtain the amino group for dye grafting. Simultaneously, we will substitute the alkyl side chain carried by the 3,3-

dimethyl-2,3-dihydro-1*H*-indolizene group for a sulfonate functionalized chain to endow the dye with good aqueous solubility.

2.2. Synthesis and Characterization of CPO-SO₃ PNPs

2.2.1. Synthesis of CPO-SO₃

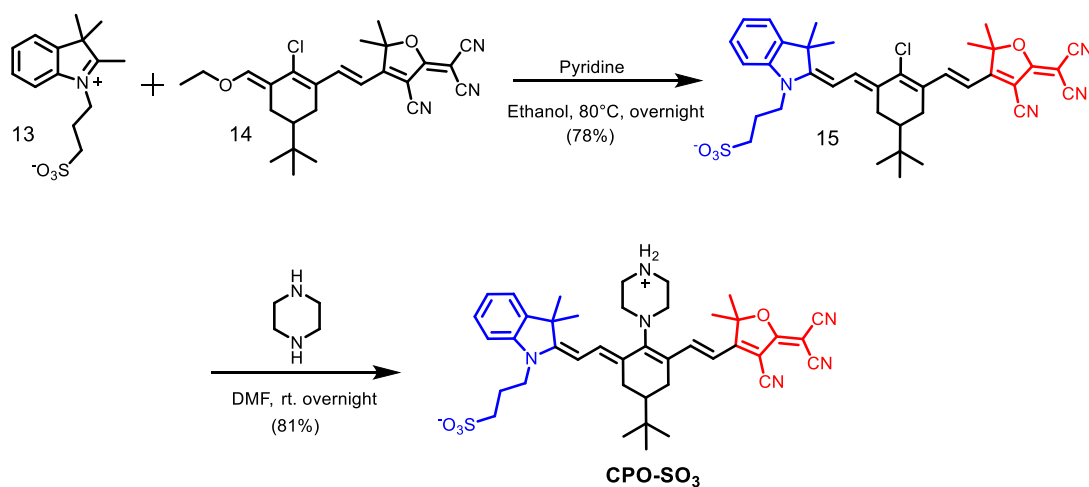


Figure 3 - 3. Synthetic route of CPO-SO₃.

The synthetic route of CPO-SO₃ is depicted in Figure 3 - 3. The sulfonate functionalized indolium derivative **13** and the hemicyanine precursor **14** were synthesized according to the literature.^[178,180] In presence of catalytic amount of pyridine they transformed into **15** in 78 % yield. Then, the chlorine atom is substituted for piperazine via a S_{NR1} reaction. This afforded CPO-SO₃ with a good yield of 81 %. The dye was carefully purified and fully characterized by mass spectrometry and NMR.

2.2.2. Synthesis of CPO-SO₃ Polymers and CPO-SO₃ PNPs

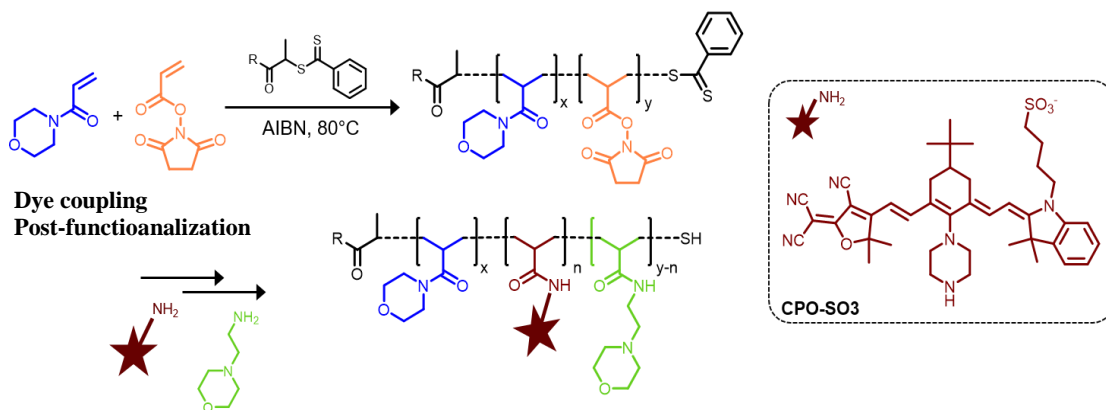


Figure 3 - 4. Preparation of CPO-SO₃ polymer.^[179]

As illustrated in Figure 3 - 4, the preparation of CPO-SO₃ polymer was started by reversible addition-fragmentation chain transfer (RAFT) polymerization to form the polyacrylate polymers, then **CPO-SO₃** was added into the polymer solution to be grafted by substitution of the NHS ester of the polymer. Followed by addition of excess of **AEM** or a borate buffer (pH = 9) into the mixture, the afforded **CPO-SO₃** polymer were modified by AEM or carboxylic acid groups on its side chain. The **CPO-SO₃@AEM** was purified by precipitation in ether and dried under a vane pump vacuum, and the **CPO-SO₃@COOH** was purified by dialysis against distilled water and then dried by freeze-drying.

Sample	M _n polymer (g/mol)	n _c [*]	X	solvent
1 CPO-SO ₃ @AEM	29600	1.7	AEM	Water
2 CPO-SO ₃ @COOH	29600	1.7	COOH	Water
3 CPO-SO ₃ @COOH	59900	5.8	COOH	Water
4 CPO-SO ₃ @COOH	59900	12.5	COOH	Water
5 CPO-SO ₃ @COOH	59900	14.5	COOH	Water

n_c^{*}: Estimated average number of CPO-SO₃ per polymer

Table 3 - 1. Properties of CPO-SO₃ polymers.

Two specifications of polyacrylate polymers with average molar mass of 29600 or 59900 were pre-obtained. Then, 5 different **CPO-SO₃** polymers were obtained with varied stoichiometry of **CPO-SO₃** and post functionalization (Table 3 - 1). Among them, **5 CPO-SO₃@COOH** with the highest dye density of 14 per polymer was tried for making **CPO-SO₃** PNPs. Actually, the redissolution of **5 CPO-SO₃@COOH** by

water was found not very easy. By a long-time ultrasonication, **5 CPO-SO₃@COOH** (1.0 mg) was finally dissolved in water (0.5 mL) to afford the **CPO-SO₃** PNPs suspension with the dye concentration calculated to be 0.4 mM (stock solution).

2.2.3. Characterization of CPO-SO₃ PNPs

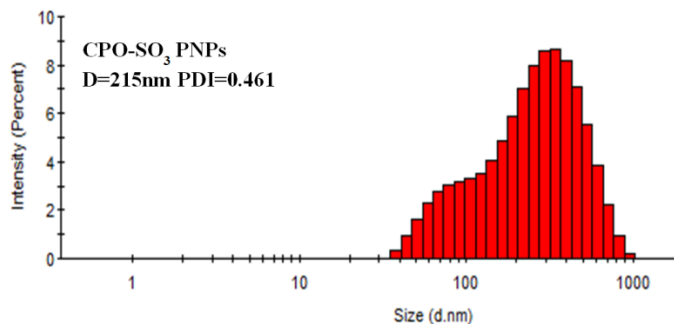


Figure 3 - 5. Size distribution of **CPO-SO₃** PNPs in water, measured by DLS.

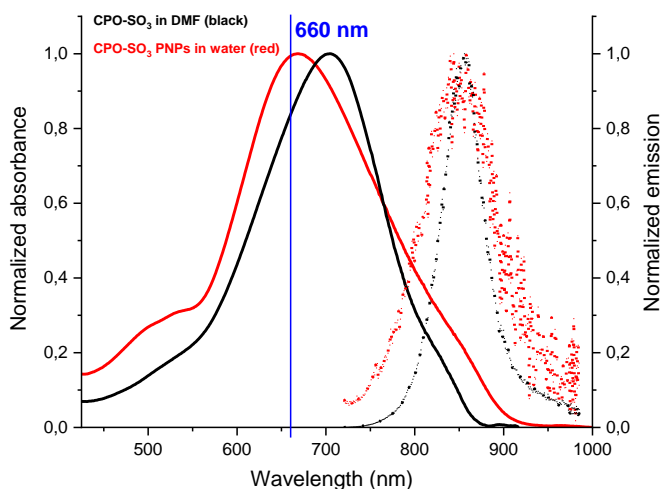


Figure 3 - 6. Absorption (solid) and emission (dot) spectra of **CPO-SO₃** in DMF (black) and **CPO-SO₃** PNPs in water.

The **CPO-SO₃** stock solution was diluted 5 times by addition of water for characterization. By DLS, two species of **CPO-SO₃** PNPs in water were observed with single size of 100 nm and 250 nm in average size of 215 nm (Figure 3 - 5).

Figure 3 - 6 presented the absorption and emission spectra of **CPO-SO₃** PNPs in water and **CPO-SO₃** in DMF. By comparison, **CPO-SO₃** PNPs showed absorption band slightly blue-shifted and widened as well as emission band greatly attenuated due to the aggregation of the **CPO-SO₃** dye molecules in the formed

PNPs. Additionally, with strong absorption at 660 nm **CPO-SO₃** PNPs were allowed to perform *in vivo* PA imaging with the 660 nm laser diode.

2.3. *CPO-SO₃ PNPs for in vivo PA Imaging*

To the **CPO-SO₃** PNPs stock solution was added salt to form the 0.9% saline for *in vivo* PA imaging.

The PA imaging was carried out on a CD-1 IGS mouse (Charles River, Écully, France). In the experiment, the mouse was anesthetized using the gas mixture of 1 % isoflurane in air followed by injection of 200 μ L of **CPO-SO₃** PNPs solution through its caudal vein. Then, the mouse ear was cleaned with a hair-removing cream and 70% ethanol, and was then positioned on the focal plane of the objective with an ultrasound gel painted. The PA signal was collected by a focused piezoelectric transducer (NDT System, IBMF054), then amplified and demodulated by two lock-in amplifiers. NIH ImageJ software was used to process the formed image.

Lastly, after injection of **CPO-SO₃** PNPs, the vasculature on the mouse ear (in red) was successfully imaged with the 660 nm excitation (Figure 3 - 7, a), which indicated the strong PA response of **CPO-SO₃** PNPs in the mouse blood vessels. And after 30minutes of circulation, strong PA signals appeared in the tissue sections of liver and kidney (Figure 3 - 7, b and c), which revealed the accumulation of **CPO-SO₃** PNPs in these organs and reflected their fast clearance from the mouse body.

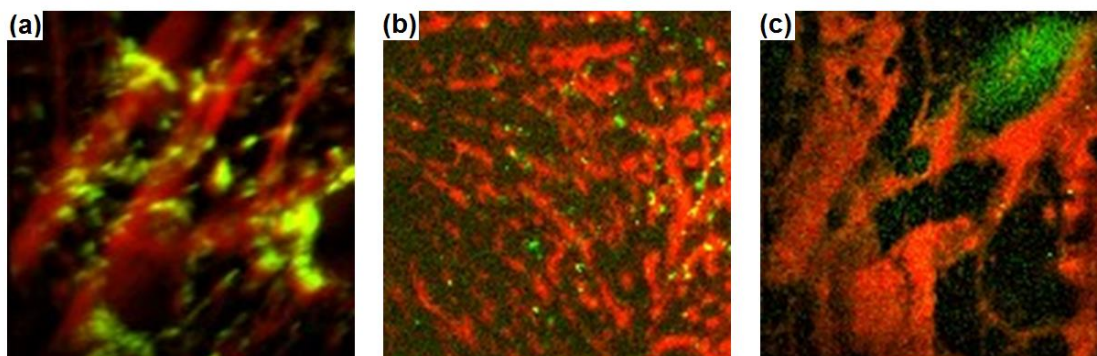
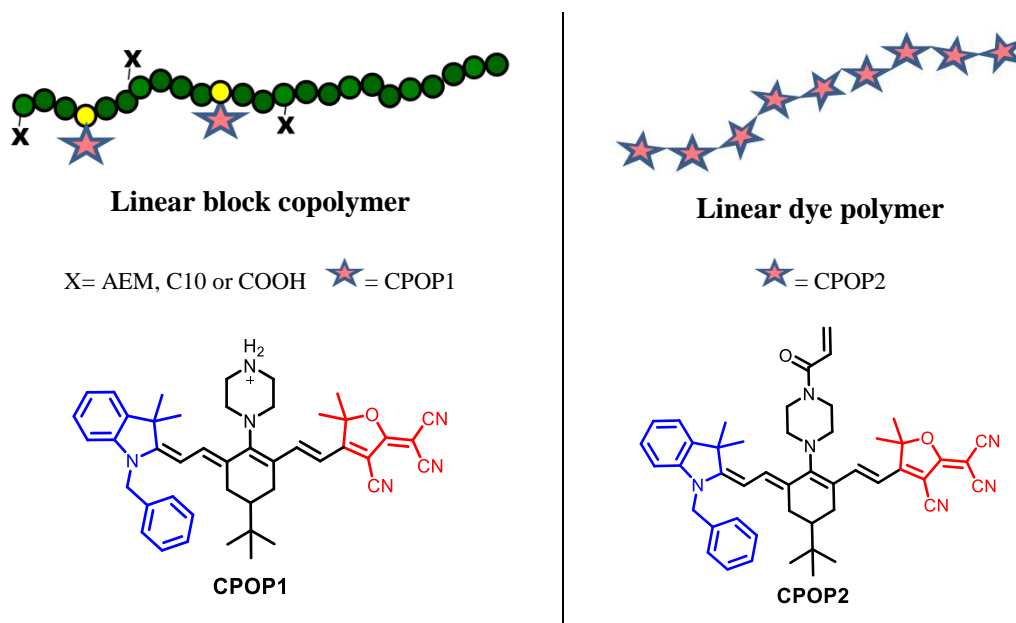


Figure 3 - 7. *In vivo* PA imaging of **CPO-SO₃** PNPs in a normal mouse ear (a) as soon as injection, liver (b) and kidney (c) after 30 min circulation. Red color comes from the PA signal generated by hemoglobin and melanin (415 nm) and green color by **CPO-SO₃** PNPs (660 nm).

3. Preparation of CPOP PNPs for PA Imaging

3.1. Synthetic Design of CPOP Polymers



Scheme 3 - 2. Polymers developed at IMP and proposal of CPOP polymers for PA imaging.

In order to obtain uniformly dispersed and easily re-dissolved PNPs, we designed another two dye-loaded polymers: the linear block copolymer (Scheme 3 - 2, left) and the linear dye polymer (Scheme 3 - 2, right). The former polymer composed by a polyacrylate segment for dye grafting and a hydrophilic block NAM chain for micellization in aqueous solution. The later one was designed with dye as polymerization monomer to achieve a high dye loading, and the water solubility can be obtained by wrapping with other water-soluble polymers.

Accordingly, **CPOP1** with a piperazine unit for covalent bonding with the polyacrylate polymer, **CPOP2** with an acrylamide that facile polymerization was designed.

3.2. Synthesis of CPOP PNPs

3.2.1. Synthesis of CPOP1 and CPOP2 dyes

Started from **CPO1** synthesized according to the literature,^[178] substitution of the chlorine atom by piperazine form **CPOP1** in 90 % yield. Further reaction with acryloyl chloride afforded **CPOP2** in yield of

77 % (Figure 3 - 8). **CPOP1** and **CPOP2** were carefully purified and fully characterized by mass spectrometry and NMR.

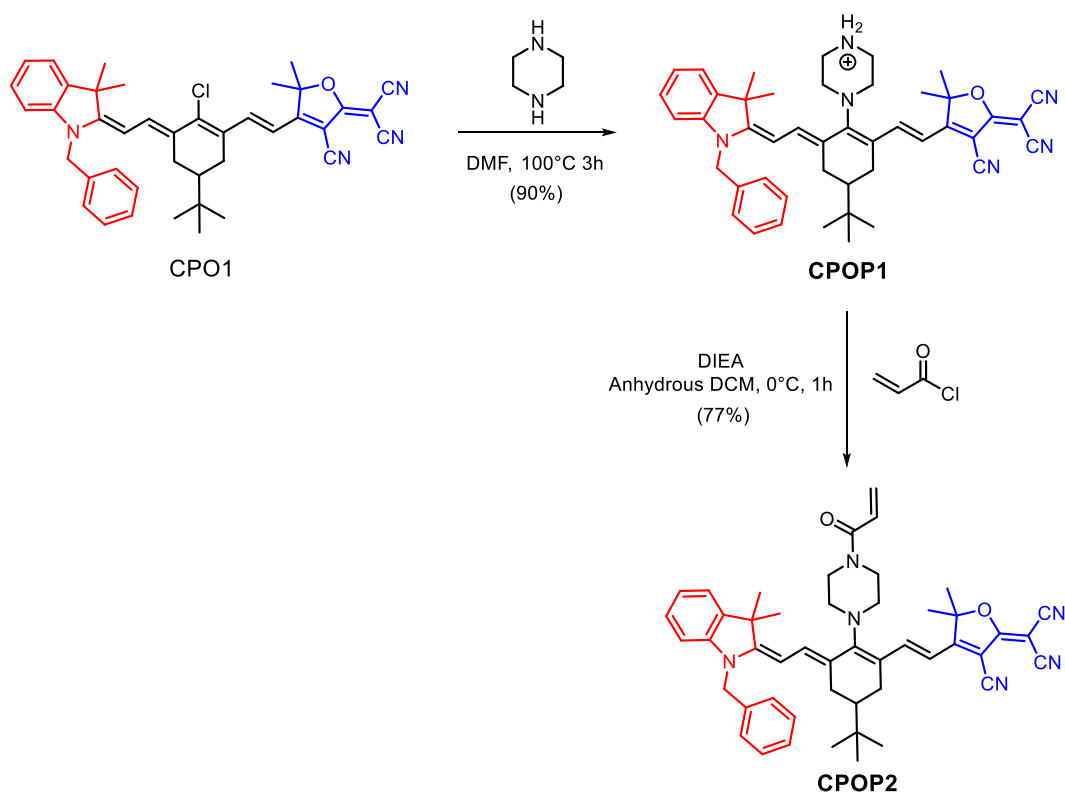


Figure 3 - 8. Synthetic routes of **CPOP1** and **CPOP2**.

3.2.2. Synthesis and Characterization of CPOP1 PNPs

3.2.2.1. Synthesis

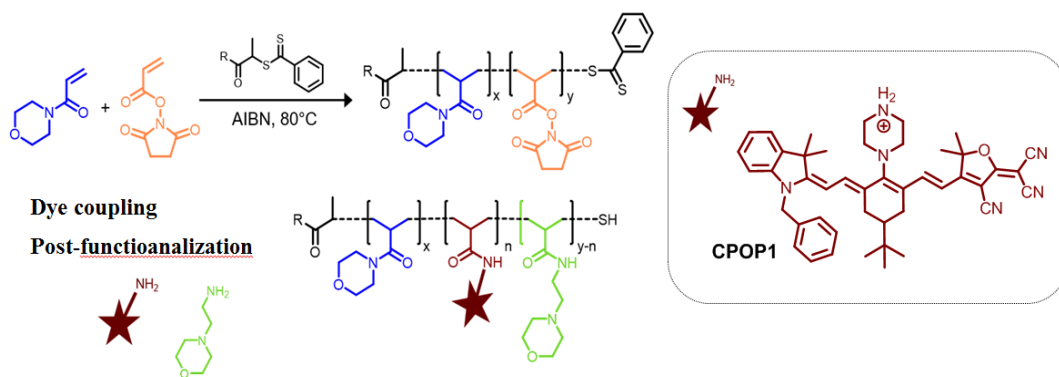


Figure 3 - 9. Preparation of **CPOP1** linear block copolymer.

As shown in Figure 3 - 9, still through RAFT polymerization, a linear block polyacrylate copolymer with one side of the statistical linear copolymer and the other side of a hydrophilic block NAM chain was pre-

obtained. Then in the presence of *N,N*-diisopropylethylamine (DIPEA), **CPOP1** was grafted onto the statistical linear copolymer side, leading to the formation of an amphiphilic **CPOP1** linear block copolymer. Different post-treatments of the activated esters were then applied, as they may alter the final morphology of the polymers or of the micelles in solution: i) (COOH) hydrolysis in borate buffer pH=9; ii) (AEM) coupling with excess aminoethylmorpholine; iii) (C10) coupling with excess decylamine. The hydrolyzed polymers (COOH) were purified by dialysis against distilled water and then dried by lyophilization. The AEM and C10 polymers were purified by precipitation in ether then dried by vacuum.

Sample	M _n polymer (g/mol)	M _n bloc NAM (g/mol)	n _c [*]	X
CPOP1@COOH	23000	12000	13.2	COOH
CPOP1@AEM	23000	12000	13.2	AEM
CPOP1@C10	23000	12000	13.2	C10

n_c^{*}: Estimated average number of **CPOP1** per polymer

Table 3 - 2. Properties of **CPOP1** polymers.

The amphiphilic **CPOP1** linear block copolymer with average molar mass of its hydrophobic segment of 23000 and its hydrophilic segment of 12000 was pre-synthesized. Then by three different post-treatments, the linear block copolymers **CPOP1@COOH**, **CPOP1@AEM** and **CPOP1@C10** loaded by **CPOP1** with average number of 13 were obtained (Table 3 - 2).

Since the direct redissolution of these polymers by water was found difficult, DMSO with relatively low biological toxicity was used as a co-solvent to re-solubilize these polymers before redispersion in aqueous medium. Among them, **CPOP1@COOH** showed the best solubility in water and is therefore more favored for preparation of **CPOP1** PNPs.

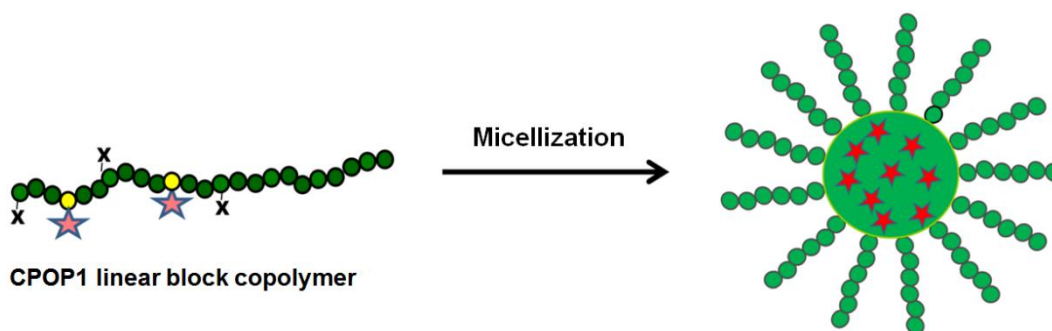


Figure 3 - 10. Formation of **CPOP1** PNPs.

By ultrasonication, **CPOP1@COOH** (0.5 mg) was re-dissolved in water (0.6 mL) to afford the **CPO-SO₃** PNPs solution. Micellization of **CPOP1@COOH** in water affords monodispersed **CPOP1** PNPs (Figure 3 - 10).

3.2.2.2. Characterization

DLS give the size of **CPOP1** PNPs as 71 nm in water (Figure 3 - 11). Coming along with the high absorption at 660 nm, they were promising to be excited by the 660 nm laser diode for *in vivo* PA imaging. Same as **CPO-SO₃** PNPs, the slightly widened and blue-shifted absorption band as well as the greatly attenuated emission band of **CPOP1** PNPs in comparison to that of **CPOP1** in DMF indicated the aggregation of **CPOP1** in the formed micelles (Figure 3 - 12).

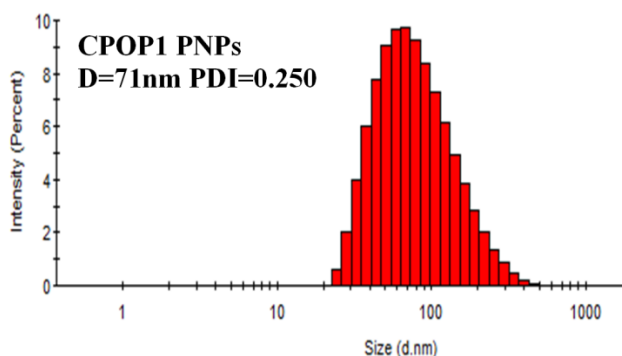


Figure 3 - 11. Size distribution of **CPOP1** PNPs in water, measured by DLS.

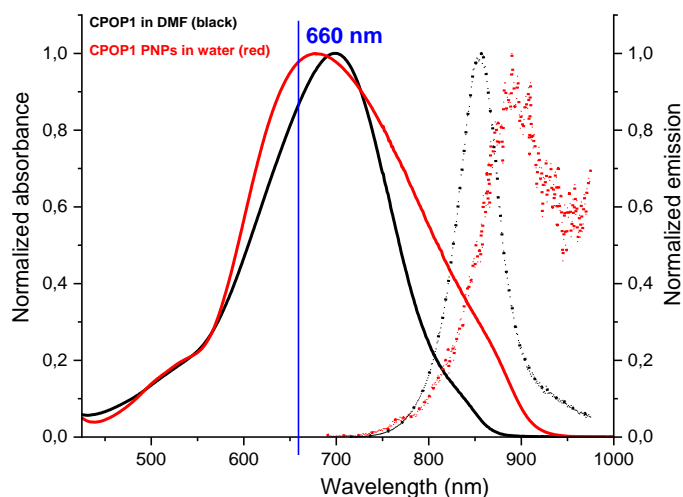


Figure 3 - 12. Absorption (solid) and emission (dot) spectra of **CPOP1** in DMF (black) and **CPOP1** PNPs in water.

3.2.3. Synthesis and Characterization of CPOP2 PNPs

3.2.3.1. Synthesis

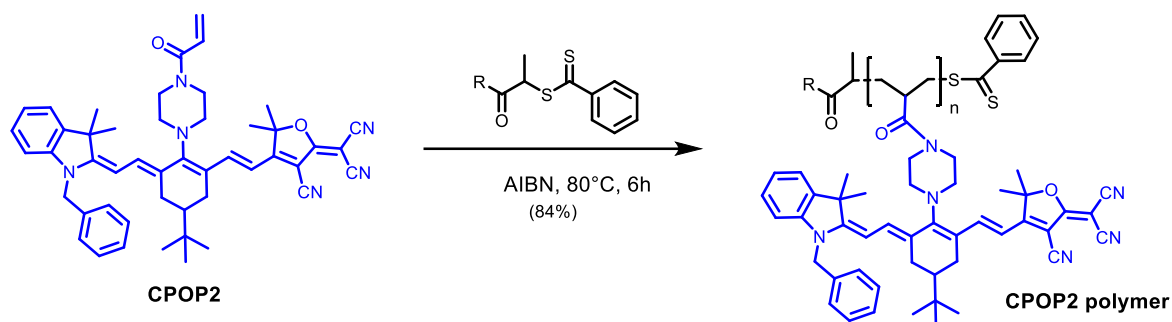


Figure 3 - 13. Preparation of CPOP2 polymers.

CPOP2 polymer was synthesized by directly using CPOP2 as monomer to perform the RAFT polymerization with n-butyl acrylate (AIBN) and chain transfer reagent SCS-R in 84% conversion (Figure 3 - 13).

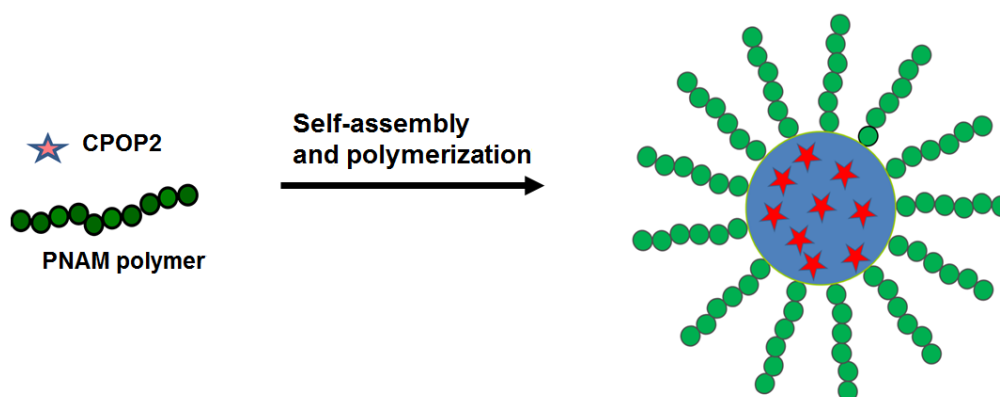


Figure 3 - 14. Formation of CPOP2 PNPs.

Different from the previous PNPs which were formed by redissolution of the dried dye-loaded polymers, CPOP2 NPs were generated by one-pot of polymerization and self-assembly. The aqueous solution of PNAM homopolymer pre-synthesized by RAFT was added to the solution of n-butyl acrylate, SCS-R and CPOP2, followed by degassing to start the self-assembly along with the polymerization. Then the afforded CPOP2 PNPs were filtered and further purified by dialysis (Figure 3 - 14).

Sample	M_n bloc PNAM (g/mol)	Dh (DLS) (nm)	n_c^*	solvent
CPOP2 PNPs	11000	60	≈ 260	Water

n_c^* : Estimated average number of CPOP2 per NP

Table 3 - 3. Properties of CPOP2 PNPs.

Finally, the **CPOP2** PNPs composed by a hydrophobic core (**CPOP2** copolymerized with AIBN) and a hydrophilic shell of PNAM were prepared. The hydrophilic PNAM polymer blocks of 11000 g/mol not only provided the **CPOP2** PNPs good water-solubility, but also made it possible to limit the non-specific biological interactions. And after purification, the PNPs size measured by DLS was 60 nm with approximately 260 **CPOP2** sequestered in the particle core (Table 3 - 3).

3.2.3.2. Characterization

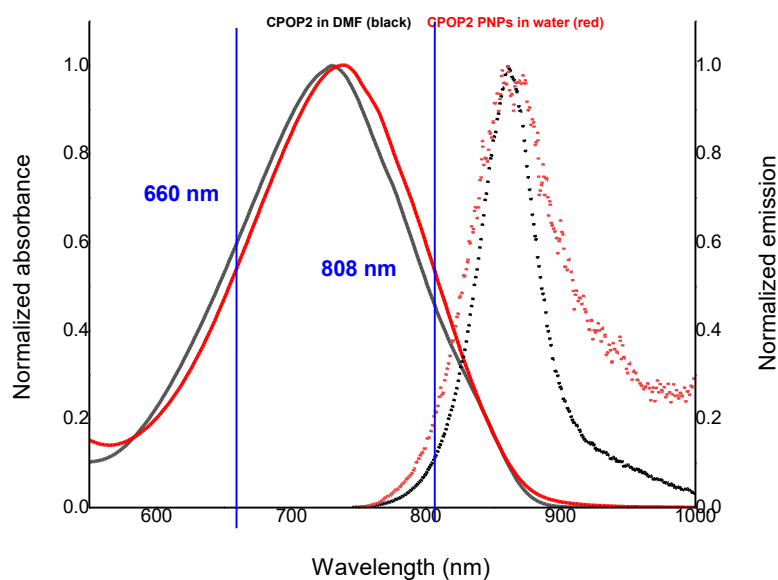


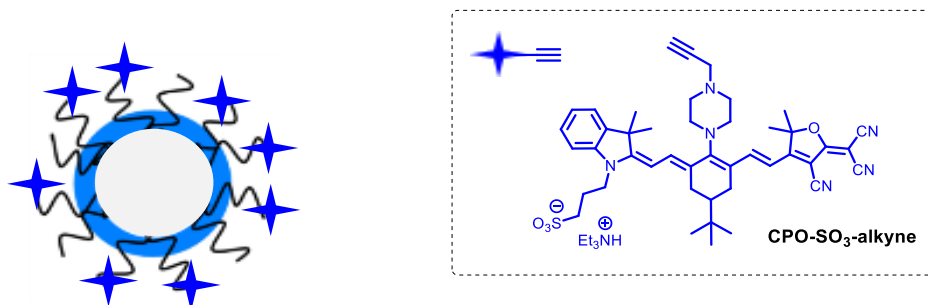
Figure 3 - 15. Absorption (solid) and emission (dot) spectra of **CPOP2** in DMF (black) and **CPOP2** PNPs in water.

As shown in Figure 3 - 15, **CPOP2** PNPs presented absorption and emission spectra very close to that of the separated **CPOP2** in DMF. This indicated the isolated state of the **CPOP2** dye molecules in the PNPs by the barrier effect of AIBN.

However, the **CPOP2** PNPs solution that Arnaud Favier gave us is not concentrated enough (judged by naked eye from the pale-blue color of the solution), the synthetic procedure needs to be developed.

4. Preparation of F127-CPO-SO₃-SiO₂ NPs for PA Imaging

4.1. Synthetic Design of F127-CPO-SO₃-SiO₂ NPs



Scheme 3 - 3. Proposal for grafting CPO-SO₃ on F127-SiO₂ NPs for PA imaging.

In the second chapter, surface-functionalized F127-SiO₂ NPs were successfully synthesized by conjugation of surface modified F127-N₃-SiO₂ by click reaction with the alkyne modified functional moieties. Such strategy can be applied here for preparation of the surface-dye-loaded F127-SiO₂ NPs (Scheme 3 - 3). Thanks to the big surface of the F127-SiO₂ NPs, the dye loading was expected to be boomed up to meet the requirement for PA imaging. To do this, we intended to modify **CPO-SO₃** with an alkyne group. The formed **CPO-SO₃-alkyne** can then react with the azido group by click thus be grafted on the particle surface.

4.2. Synthesis and Characterization of CPO-SO₃-F127-SiO₂ NPs

4.2.1. Synthesis of F127-CPO-SO₃-SiO₂ NPs

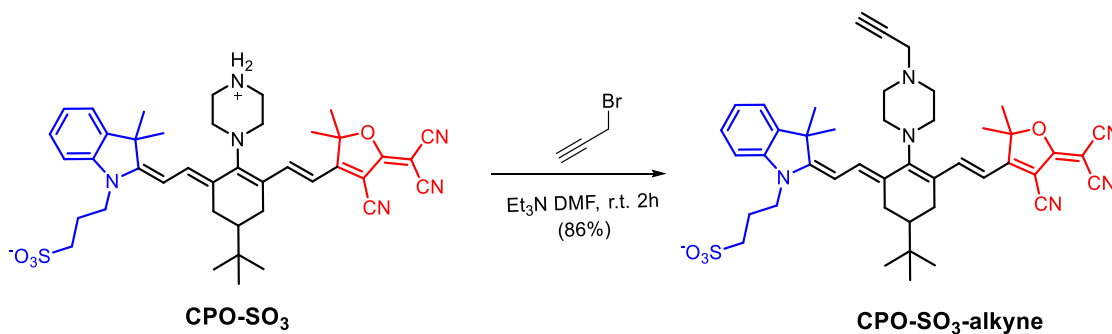


Figure 3 - 16. Synthetic route of CPO-SO₃-alkyne.

CPO-SO₃-alkyne was obtained in 86 % yield by a simple nucleophilic substitution of **CPO-SO₃** on propargylbromide (Figure 3 - 16).

4.2.2. Synthesis of F127-CPO-SO₃-SiO₂ NPs

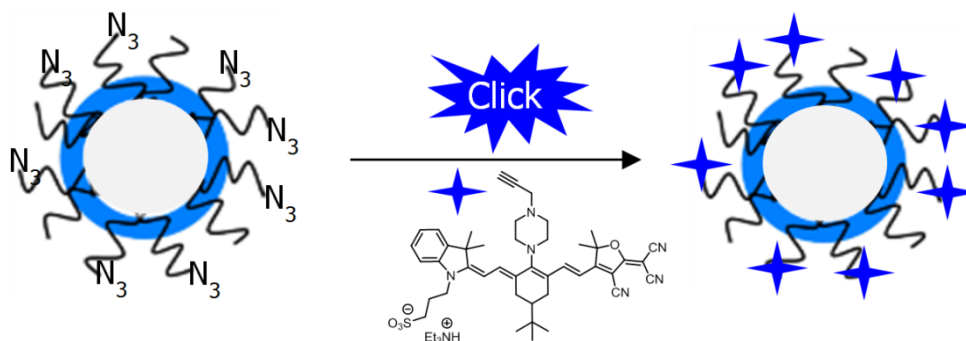


Figure 3 - 17. Preparation of F127-CPO-SO₃-SiO₂ NPs.

Same as the preparation of the surface functionalized F127-SiO₂ NPs in the last chapter, **F127-N₃-SiO₂** NPs were pre-formed by using **F127-N₃** as the only amphiphilic co-polymer. **F127-CPO-SO₃-SiO₂** NPs were obtained via click reaction by simply adding the alkyne modified dye **CPO-SO₃-alkyne** and the suitable Cu(I) catalyst into the stock solution (Figure 3 - 17). Finally, the catalysts and unreacted dyes were removed by dialysis.

For loading as much as possible the **CPO-SO₃** to the NPs surface, 100 % of **F127-N₃** was used to prepare the F127-N₃-SiO₂ NPs. The particles in this ratio were proved to be stable in the previous study. Then, by gradually increasing the concentration of **CPO-SO₃**, big nanoaggregates were observed after the loading (mass ratio of **CPO-SO₃** to the **F127-N₃-SiO₂** solution) above 0.05 %. This is probably due to the decreased stability of **F127-CPO-SO₃-SiO₂** NPs as increasing of the **CPO-SO₃** grafted.

4.2.3. Characterization of CPO-SO₃-F127-SiO₂ NPs

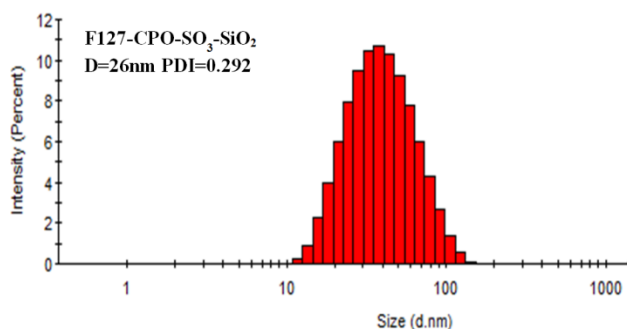


Figure 3 - 18. Size distribution of F127-CPO-SO₃-SiO₂ NPs in water, measured by DLS.

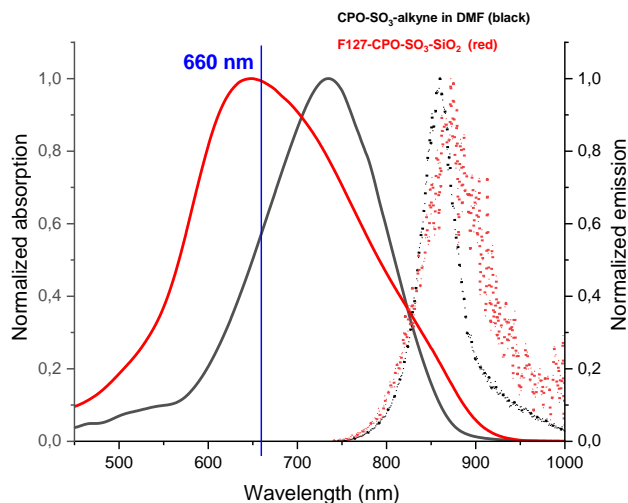


Figure 3 - 19. Absorption (solid) and emission (dot) spectra of **CPO-SO₃-alkyne** in DMF (black) and **F127-CPO-SO₃-SiO₂** NPs in water.

Sample in water	$\lambda_{\text{abs}}^{\text{[a]}}$	$\lambda_{\text{em}}^{\text{[b]}}$	$\Delta\nu^{\text{[c]}}$	Size ^[d]	Dye/NP
F127-CPO-SO ₃ -SiO ₂	646	875	4051	26	12

[a] Absorption maxima in nm. [b] Emission maxima in nm. [c] Stokes shifts in cm⁻¹. [d] Diameters measured by DLS.

Table 3 - 4. Collective information of **F127-CPO-SO₃-SiO₂** NPs in water.

F127-CPO-SO₃-SiO₂ NPs with mass ratio at 0.05 % presented monodispersed size of 26 nm and good stability in water (Figure 3 - 18). According to the **F127-N₃-SiO₂** NPs concentration (around 50 μM), **CPO-SO₃-alkyne** concentration (614 μM), the average number of dyes per particle was calculated to be 12. What's more, due to aggregation of **CPO-SO₃** molecules on the same particle, the dye absorption in water blue-shifted from 735 nm in isolated state to 646 nm, accompanied by the mostly quenched fluorescence emission. Lastly, the **CPO-SO₃F127-SiO₂** NPs with an absorption peak very close to 660 nm as well as a very weak emission were very promising for PA imaging (Figure 3 - 19 and Table 3 - 4).

4.3. **F127-CPO-SO₃-SiO₂** NPs for *in vivo* PA Imaging

However, in the pre-test of *in vivo* PA imaging, out of our expectation, **F127-CPO-SO₃-SiO₂** NPs did not show any PA signals on immersed paper fibers. Yet, the total dye concentration was estimated to be 0.55 mM, which is already higher than what is reported in the literature.^[132] As the dye we use is also very similar in structure to what is used in the literature, this is rather surprising. Moreover, dye loaded F127-

SiO₂ NPs have also been used in PA imaging. Therefore, the reason for lack of PA signal is still not clear to us.

5. Conclusion

In this chapter, for the purpose of obtaining high dye-loaded NPs for PA imaging, we cooperated with IMP to synthesize three kinds of dye-loaded polymers (**CPO-SO₃**, **CPOP1** and **CPOP2** polymers) by means of dye grafting or dye polymerization.

By adjusting the stoichiometry of the dyes and varying the post-processing of the remaining acid functions of the polymers, **CPO-SO₃** polymer and **CPOP1** polymer with different dye loadings and functionalization were firstly obtained. Redissolution of **CPO-SO₃@COOH** and **CPOP1@AEM**, which both containing the correspondingly highest dye densities in polymers afforded the **CPO-SO₃** PNPs and the **CPOP1** PNPs. The **CPO-SO₃** PNPs with dye concentration of 0.4 mM as well as maximum absorption at 668 nm successfully imaged a mouse vasculature system by the 660 nm laser diode. But due to their uneven size distribution the **CPO-SO₃** PNPs were fast cleared by the mouse liver and kidney. The **CPOP1** PNPs monodispersed in water with size of 71 nm, good absorption at 660 nm, as well as high dye concentration of 0.44 mM are very promising for long-time *in vivo* PA imaging.

Through one-pot dye polymerization, **CPOP2** PNPs were obtained with monodisperse size of 60 nm in water, and each PNP has approximately 260 molecules. Probably due to the blocking of AIBN to **CPOP2** in the particle core, the **CPOP2** PNPs presented similar absorptions to that of the dye in solution. With comparable absorptions at 660 nm and 808 nm, **CPOP2** PNPs are of potential to be excited by the 808 nm laser diode for *in vivo* PA imaging.

Besides, a surface-loading strategy was developed to break the dye-loading limitation of F127-SiO₂ NPs for PA imaging. By conjugation of the alkyne modified **CPO-SO₃** to the azido-modified F127-N₃-SiO₂ NPs developed in the second chapter via click reaction, **F127-CPO-SO₃-SiO₂** grafted NPs with dye concentration of 0.55 mM was prepared. Unfortunately, these NPs failed for PA imaging probably due to the low sensitive PAM we are using.

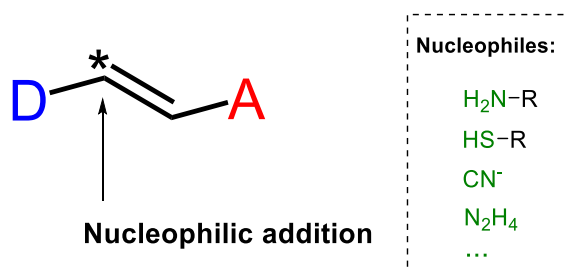
Chapter IV. Dicyanovinyl Dyes for Primary Amine Detection

In parallel with the work presented before, we studied the stability and reactivity of the dipolar dyes in the presence of nucleophiles, especially primary amines.

1. Background

1.1. General Context

The dipolar dyes that we developed in chapter 2 contain various strong π -acceptors, which, by definition, remove electron density from the adjacent π -systems, hence create partial positive charges in their vicinity. These electron deficient positions act as electrophiles and are prone to bonding with electron-rich nucleophiles. By the reaction that breaks the conjugation, the overall π -electron density of the chromophores will be heavily modified, resulting in consequent optical changes (absorption and/or emission). A recurrent and legitimate question when designing new chromophores bearing such electron-withdrawing groups is therefore their stability in presence of strong nucleophiles. As a matter of fact, given the huge optical changes induced of the reaction, nucleophilic addition to a chromophore electron deficient carbon center, and in particular to ICT chromophores, is a widely used approach to design optical (fluorescent) probes for nucleophiles, including primary amine,^[181-183] thiol,^[184,185] cyanide^[186-188] or else hydrazine (Scheme 4 - 1).^[189]

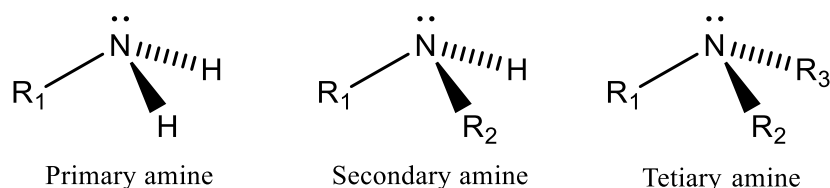


Scheme 4 - 1. Illustration of nucleophilic addition on electron deficient center of D- π -A structure.

This prompted us to test whether or not the push-pull dipolar dyes that we developed possessing a strong ICT and reactive sites for nucleophilic addition, are good candidates for nucleophile sensing, especially for primary amine.

1.2. Why Primary Amine?

Amines are derivatives of ammonia. With one or more hydrogen atoms substituted by alkyl or aryl groups, they are organized into three categories: primary amine, secondary amine and tertiary amine (Scheme 4 - 2). Amines play an important role in industry, agriculture and pharmaceutical, they are also the integral elements of organisms.



Scheme 4 - 2. Structures of primary, secondary and tertiary amines.

In addition, the structural differences allow them to be distinguished from each other by specific chemical reactions, i.e. the famous Hinsberg test.^[190] In recent years, much attention has been attracted to the selective recognition of trace amount of primary amine in environmental pollution,^[191] food quality inspection^[192] and health security^[193] fields. Till now, different methods including chromatography,^[194] electrochemistry^[195] and optical inspection (UV-Vis or fluorescence) have been developed with high detection accuracy. Since the first two manners often suffer from complicated manipulation and a long time sample-preparation, optical detection mainly relying on fluorescent organic dyes,^[196] supramolecular hydrogel^[197] or transition metal complexes^[198] have raised growing interest. With advantages of ease of preparation and application as well as superior sensitivity, many small fluorescent organic probes and solid devices were prepared for primary amine in solution and in vapor sensing.^[182,199]

As recently reviewed,^[200] many amine-response fluorescent probes were generated based on the basicity,^[199] metal coordination^[198] and nucleophilicity^[201] coming from the free lone pair on the nitrogen. Among these properties, the nucleophilicity is commonly used for differentiation of primary amines, i.e. addition of primary amine to aldehyde to form imine. It's worth noting that, the fluorescent probes based on nucleophilicity of analyst often have interaction with many kinds of nucleophiles such as cyanide or hydrazine, but primary amines are much less studied in comparison.

1.3. Preliminary Tests

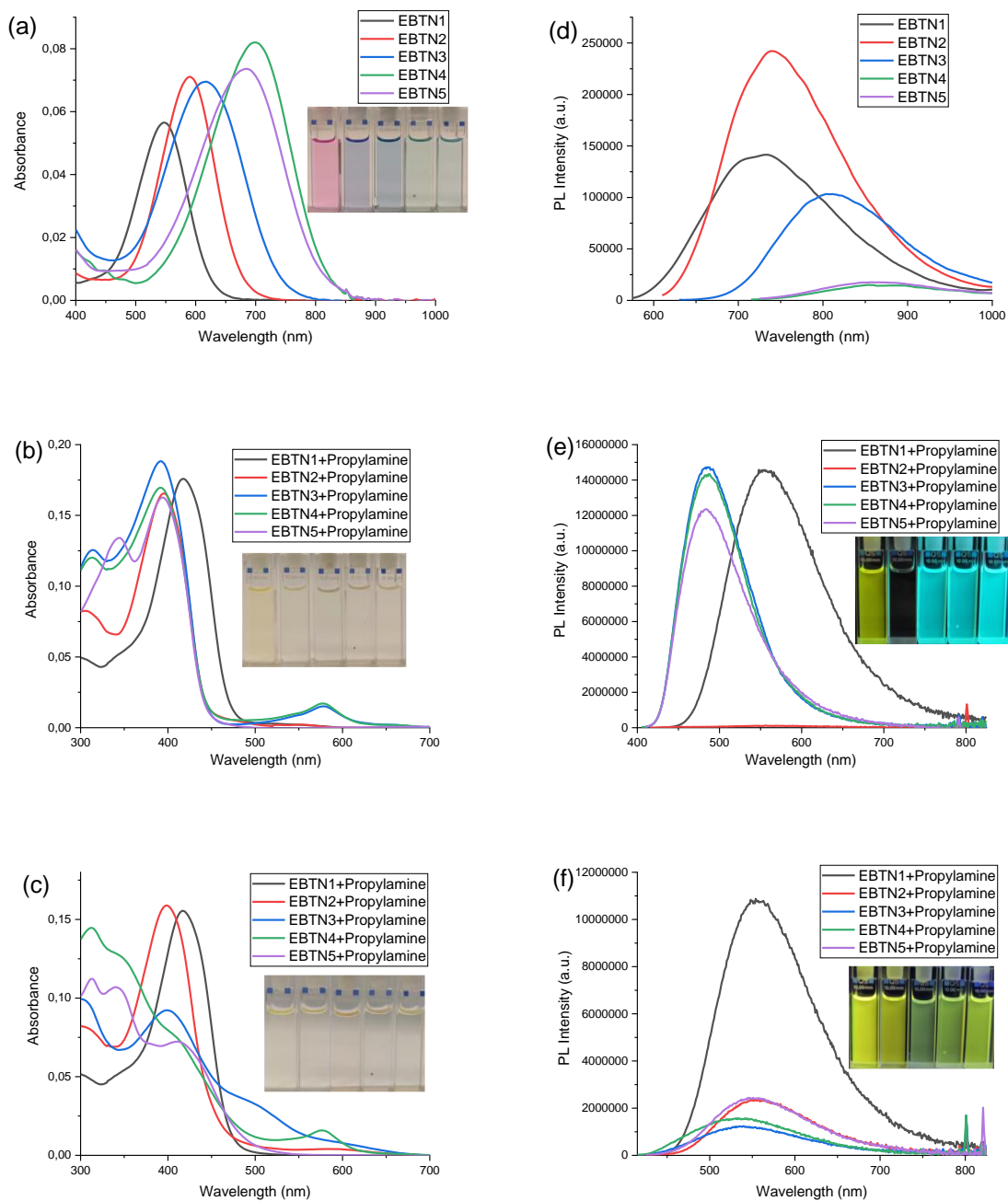


Figure 4- 1. (a) absorption and emission spectra of **EBTN1-EBTN5**; (b) after addition of excess of *n*-propylamine for few minutes; (c) after addition of excess of *n*-propylamine for several hours. ($6.0 \mu\text{M}$ in **DMSO**).

Started by the EBTN series, we simply tested their stability in presence of a large amount of a simple nucleophilic primary amine, n-propylamine, by monitoring the absorption and emission changes. The results are summarized in Figure 4 - 1.

As shown in Figure 4 - 1, a and b, addition of n-propylamine to **EBTN1-EBTN5** in DMSO induced considerable spectral changes. All the solutions had their colors (from red to deep blue) immediately faded away, becoming clear transparent (except **EBTN1** for which a slight yellow solution was observed). Absorption spectra show a complete disappearing of the ICT bands above 500 nm, which are substituted for new bands around 400 nm. This strong blue shift clearly implied the breaking of all the conjugated π -systems by n-propylamine.

Fluorescence spectra also showed considerable changes (Figure 4 - 1). Immediately after addition of n-propylamine, the far-red emission of **EBTEN2** completely vanished. In turn, the weak far-red emissions of **EBTN3-EBTN5** were completely replaced by the strong blue fluorescence (485 nm), whereas for **EBTN1** an intense yellow fluorescence (556 nm) was observed. Interestingly, after several hours, **EBTN2** started emitting the yellow fluorescence observed for **EBTN1**, while the fluorescence of **EBTN3-EBTN5** changed from blue to the same yellow (Figure 4 - 1, e and f) as well, albeit of lower intensity. This seems to indicate that at least one similar final (fluorescent) adduct was generated in all the mixtures.

As noted above, using a nucleophilic addition on the electrophilic position induced by the presence of an electron-withdrawing group in the dye is a commonly used approach to design optical probes. As far as

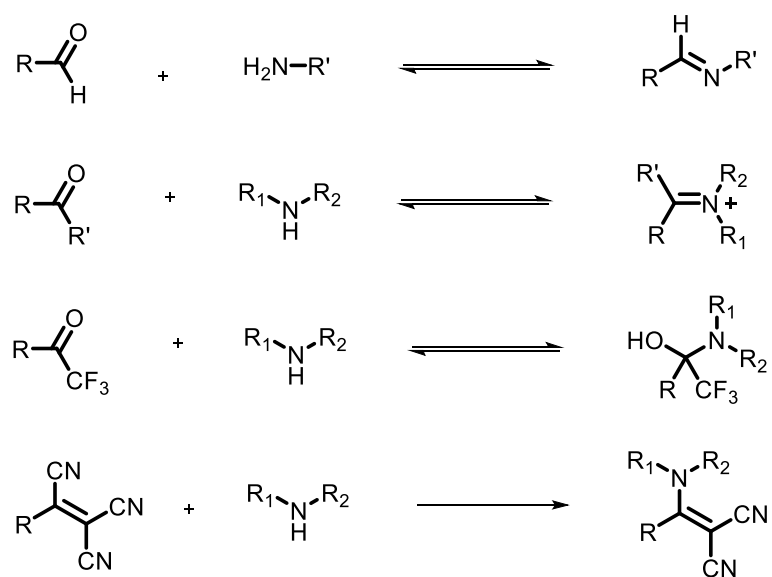


Figure 4 - 2. Illustration of interactions of aldehyde, ketone, trifluoroacetyl and tricyanovinyl with amines.

amines as concerned as nucleophile, the electrophilic functional groups mostly used are aldehyde,^[202-206] or ketone,^[207] but also trifluoroacetyl^[208,209] or tricyanovinyl.^[210] The end product of the reaction between the amine and the sensor is an imine or an iminium in the case of aldehyde or ketones, or a direct adduct in the electron-withdrawing group in the case of trifluoroacetyl and a 1,2 adduct in the case of tricyanovinyl. Note that for trifluoroacetyl the reaction is reversible but for tricyanovinyl (Figure 4 - 2).

To the best of our knowledge, for the electron-withdrawing groups that we have used in our EBTN dyes, only TCF and dicyanovinyl are reported to have response to primary amine and the others have not been really studied till now.

For TCF, Jen *et al.* described the reversible addition of an amine on the β carbon of the double bond (Michael addition) in a constraint polymer. The author pointed out that the product obtained was thermodynamic unstable so that a reversible elimination of the nucleophile by a low level mechanical force takes place to switch back to the starting dye, at least in the very specific system of the constraint polymer.^[181]

On the other hand, Yang *et al.* who used the very same chromophores in solution for fluorescent and colorimetric (di)amine sensing, did not mention reversibility. The end product described just result from a Michael addition on the β carbon of the double bond. Surprisingly, a strong fluorescence at 600 nm ($\Phi = 0.32$) is observed which is clearly in contradiction with the proposed structure. However, a closer on the

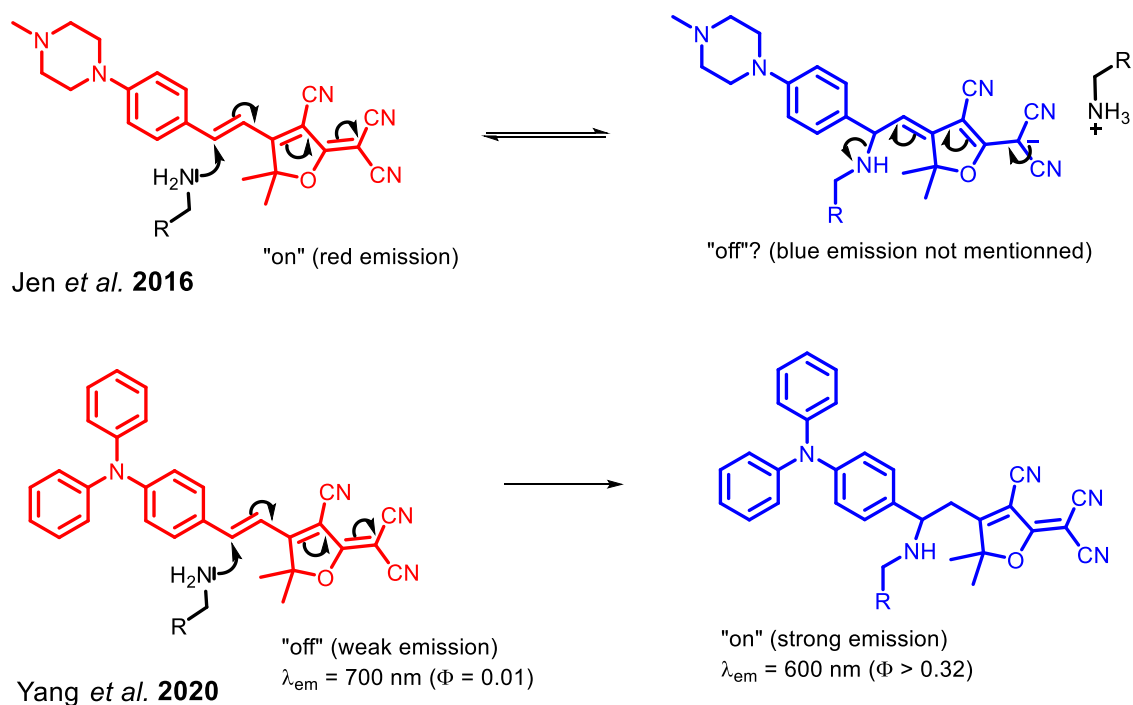


Figure 4 - 3. Illustration of Michael addition of amine on the β carbon of the double bond.

NMR spectra in the SI of this article show the presence of at least another unidentified compound beside the Michael adduct (Figure 4 - 3).^[211]

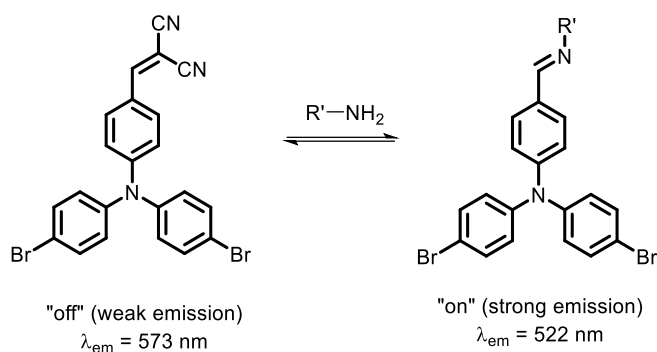


Figure 4 - 4. Mechanism of forming an imine from a dicyanovinyl group.

For the dicyanovinyl group, Shi *et al* proposed in 2014 that reaction with a primary amine form an imine resulting from the nucleophilic addition of the primary amine to the dicyanovinyl group followed by loss of a malononitrile molecule (Figure 4 - 4).^[182] The imine being much more emissive than the starting dye, they used that to design “turn on” amine vapor sensor of very sensitivity.

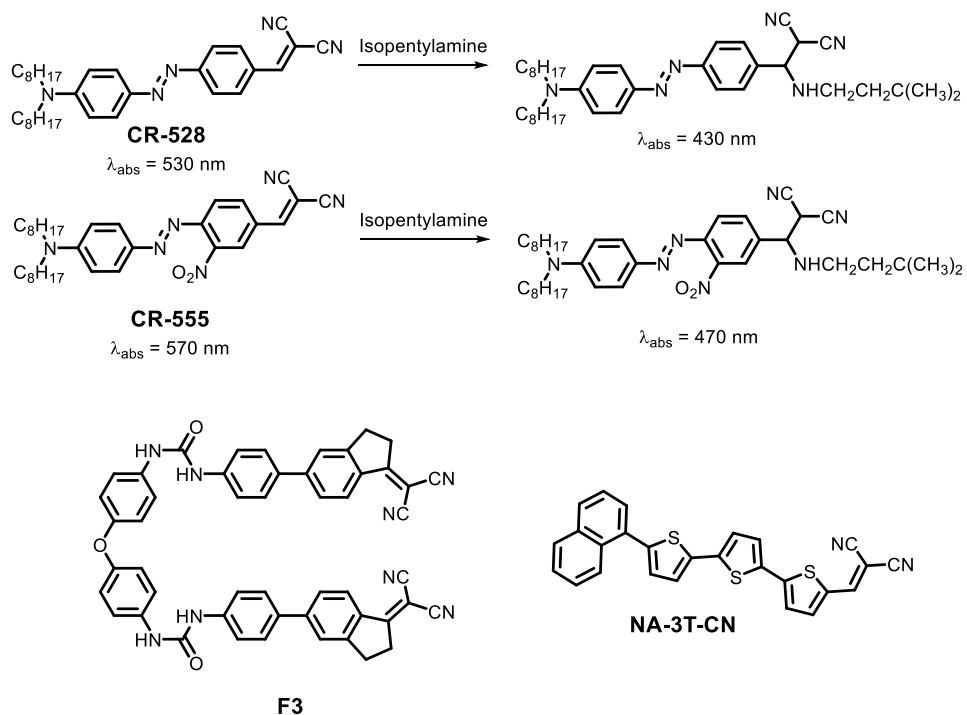


Figure 4 - 5. Several dicyanovinyl dyes for amine detection.

Previously, Mohr *et al.* described a colorimetric read-out sensor based on push-pull azo dye and therefore working at wavelengths compatible with low-cost light sources and detectors.^[212,213] A turn-on fluorogenic probe **F3** (Figure 4 - 5) for detecting 3,4-Methylenedioxymethamphetamine (MDMA) from ecstasy tablets^[214] and probe **NA-3T-CN** for dual-mode detection of aliphatic amines and hydrazine by fluorescence^[215] were also reported built upon a bis-diarylurea-dicyanovinyl push-pull fluorophore and a dicyanovinyl-substituted oligothiophene derivative associated with zinc tetraphenylporphyrin, respectively.

However in all these works, the end product was not characterized or simply postulated as being the 1,2 adduct.^[213] Finally, Sathiyarayanan *et al.* reported the design of a ratiometric fluorescence sensor for primary amine based on a dicyanovinyl substituted phenanthridine derivatives and they clearly identified the end product as being an imine resulting from the nucleophilic addition of the primary amine to the dicyanovinyl group followed by loss of a malononitrile molecule (Figure 4 - 6).^[183]

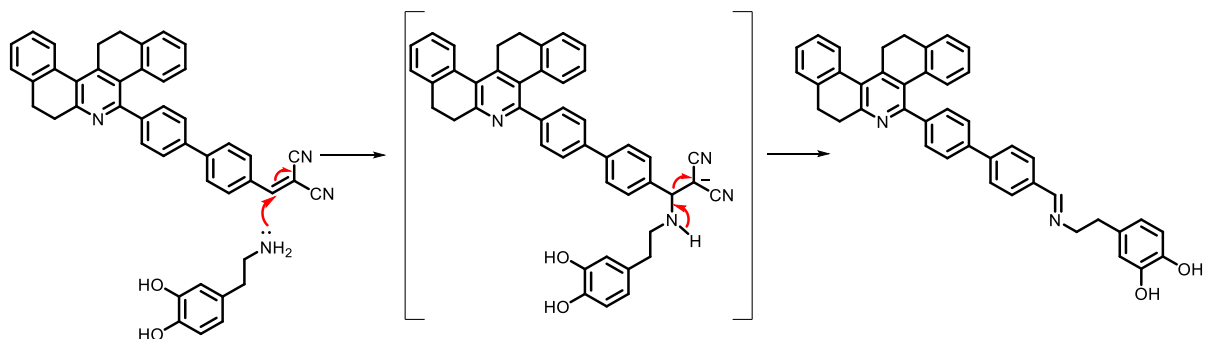
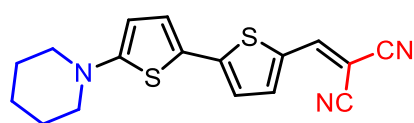


Figure 4 - 6. Mechanism for imine formation from dicyanovinyl provided recently.^[213]

The formation of an imine makes sense. The reaction of hydrazine on dicyanovinyl indeed yield hydrazone, a much weaker electron-withdrawing group and is well documented.^[216] This results in a decreased intramolecular charge transfer between the donor and the acceptor end of the chromophore and significant spectral changes (blue shift and generally fluorescence enhancement) exploited for hydrazine probes design.

So, given the relatively fast response of **EBTN1** to n-propylamine, the dicyanovinyl group was considered more reactive than the other electron-withdrawing groups in the EBTN dyes. Therefore, we decided to start this work from the simplest dicyanovinyl group to deeply study its sensing mechanism to primary amine. To do so, in addition to our dicyanovinyl containing dye **EBTN1**, we also used another dicyanovinyl push-pull dipolar dye **PTTCN** (Figure 4 - 7) which was previously tested for NIR-PA bioimaging.



PTTCN
 $\lambda_{\text{abs}} = 565 \text{ nm}$
 $\lambda_{\text{emi}} = 653 \text{ nm}$
 $\phi = 22\% (\text{CHCl}_3)$

Figure 4 - 7. Chemical structure of **PTTCN**.

2. Primary Amine Sensing: Solution Studies

2.1. Synthesis of **PTTCN**

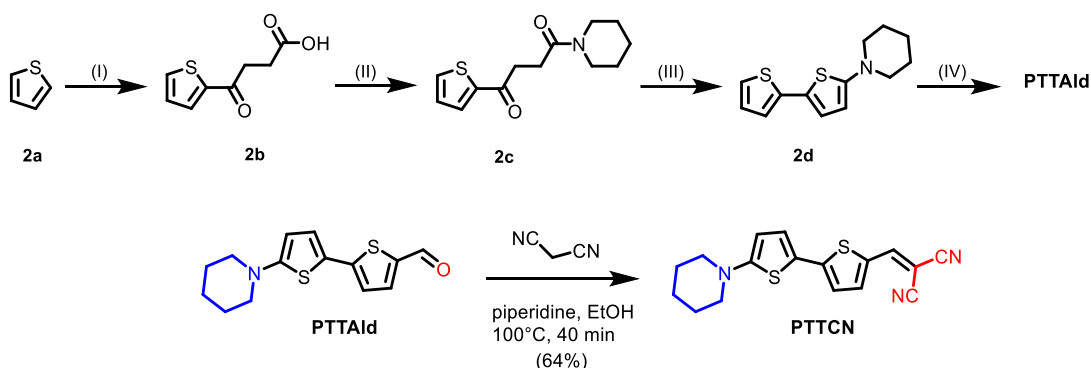


Figure 4 - 8. Preparation of **PTTCN**. Reaction conditions: (I) Succinic anhydride, AlCl_3 , DCM; (II) DCC, HOBT, piperidine, DCM; (III) Lawesson's reagent, toluene; (IV) *n*-BuLi, DMF, THF.

As shown in Figure 4 - 8, **PTTCN** was synthesized starting from thiophene. The piperidine unit was introduced by amide coupling on the acid unit of **2b** in presence of *N,N'*-dicyclohexylcarbodiimide (DCC) and hydroxybenzotriazole (HOBT). Then the cyclization reaction with Lawesson's reagent^[217] afforded **2d**, which was formylated by *n*-BuLi and DMF to form **PTTAld** in 78% yield. Finally, **PTTCN** was obtained by the Knoevenagel condensation of **PTTAld** and malononitrile in 64% yield.

2.2. Solvent Test

Firstly, we investigated the sensing behavior of **PTTCN** to *n*-propylamine in 11 different solvents mostly used in the laboratory. Due to solvatochromic effect, **PTTCN** presented red-shifted absorption and reduced emission with the increasing of the solvent polarity (Figure 4 - 9, a and Figure 4 - 10, a).

Immediately after addition of 50 equivalent (eq.) of *n*-propylamine, only the DMSO solution showed its violet color completely faded way (absorption peak at 575 nm disappears), which was accompanied by a brilliant yellow-green fluorescence emitted (Figure 4 - 9, b). It is only after standing overnight, that the color

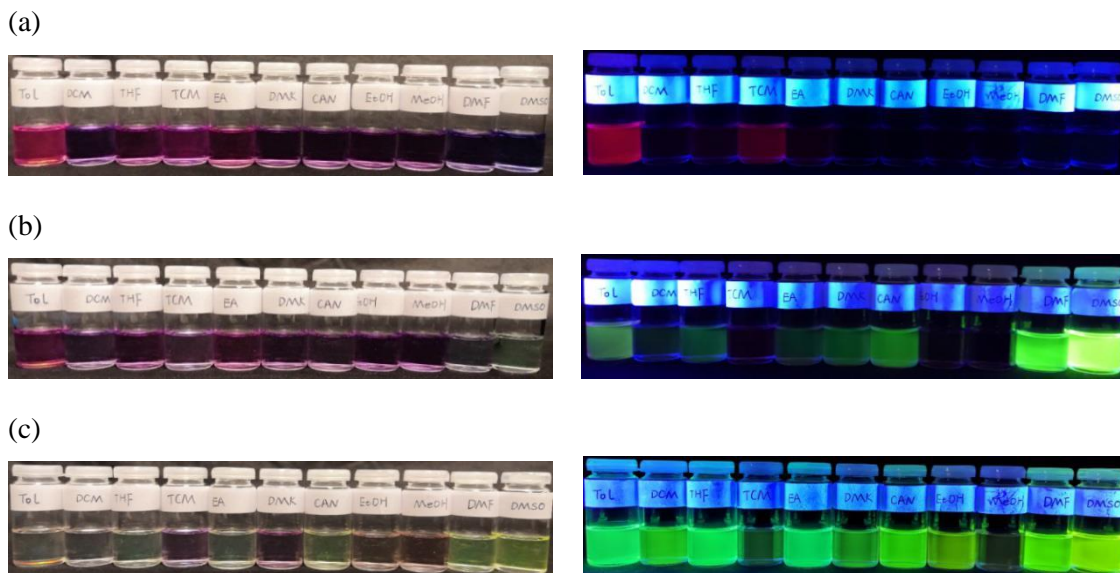
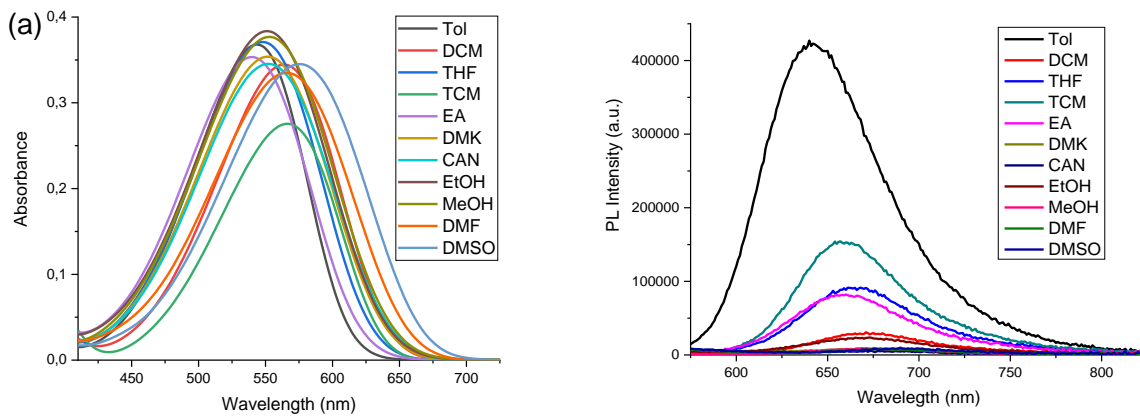


Figure 4 - 9. Photographs of *PTTCN* in different solvents (a) before, (b) after addition of 50 eq. of propylamine for 5 minutes, (c) overnight; (Left) under sun light, (Right) under UV lamp (365 nm). 10 μ M. toluene (Tol), dichloromethane (DCM), tetrahydrofuran (THF), chloroform (TCM), ethyl acetate(EA), acetone (DMC) acetonitrile (CAN), ethanol(EtOH), methanol (MeOH), dimethyl formamide (DMF), dimethyl sulfoxide(DMSO).



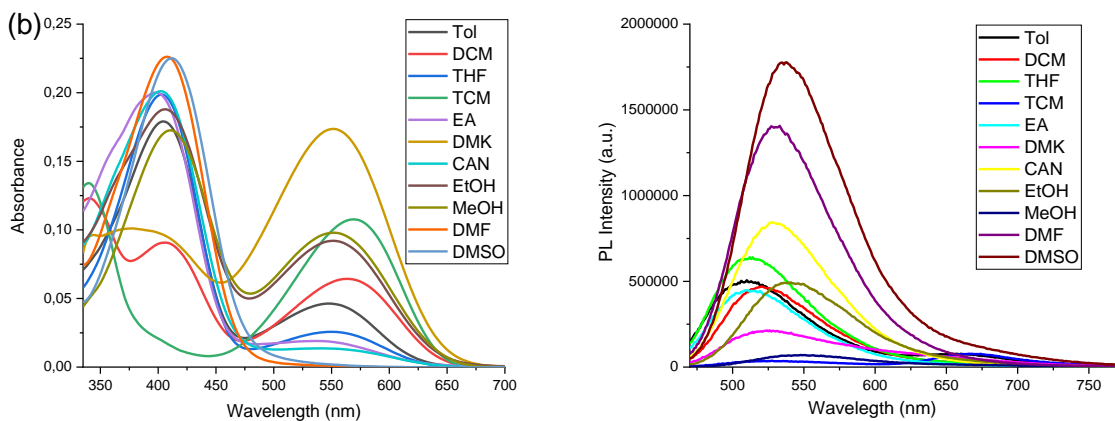


Figure 4 - 10. Absorption and emission spectra of **PTTCN** in different solvents (a) before and (b) after addition of 50 eq. of *n*-propylamine overnight (10 μ M).

fading and the yellow-green fluorescence were observed in most of the mixtures (Figure 4 - 9, c), demonstrating the kinetic of the reaction is solvent-dependent, or the reaction may be reversible.

Meanwhile, as can be seen in Figure 4 - 10 b showing the absorption and emission spectra of the mixtures after one night, it is only for the DMF and DMSO solutions that the absorption bands of **PTTCN** at 570 nm) completely disappeared, replaced by a blue-shifted band at 410 nm. In other solvents, two absorption bands at around 570 and 410 nm indicate the presence of at least one new compound along with starting **PTTCN**. Therefore, DMSO and DMF were considered more favorable for this reaction in comparison to other solvents, and DMSO was chosen for the following experiments.

2.3. Spectroscopic Response

Although addition of a large excess of *n*-propylamine to the solution of **PTTCN** or **EBTN1** in DMSO induced an immediate color change of the mixture from violet to yellow-green that comes along with the appearance of an intense yellow-green fluorescence, the reaction was found slow for low dye concentration. To allow enough time for the reaction to process, all the following spectra measurements were performed 14 h after addition of amines.

Upon stepwise addition of *n*-octylamine to **PTTCN**, the characteristic ICT band of **PTTCN** at 575 nm was gradually substituted by a new absorption peak at 412 nm, which left an isobestic point at 462 nm indicating that a single chemical reaction happened (Figure 4 - 11, a). The same was observed for **EBTN1**. Under stepwise addition of *n*-octylamine, the characteristic ICT band of **EBTN1** at 530 nm disappeared

while the violet colour of the dye solution faded away with the concomitant appearance of a new peak with a maximum absorbance at 410 nm and an isobestic point at 460 nm (Figure 4 - 11, c).

Accordingly, when exciting at the wavelength of the isobestic point (412 or 460 nm), the weak far-red emission of **PTTCN** ($\lambda_{em} = 685$ nm) and of **EBTN1** ($\lambda_{em} = 896$ nm) are steadily replaced by intense emission at 535 nm or 556 nm, respectively, with increasing addition of n-octylamine (Figure 4 - 11, b and d). The newly formed compounds are highly emissive with quantum yields values closed to unity ($\Phi = 1$ and 0.75, respectively). As **PTTCN** or **EBTN1** are barely emissive in DMSO, real “turn-on” fluorescence responses are observed, giving an almost 1160-fold emission fluorescence enhancement in the case of **PTTCN** and 112-fold for **EBTN1** (Figure 4 - 12, a and c).

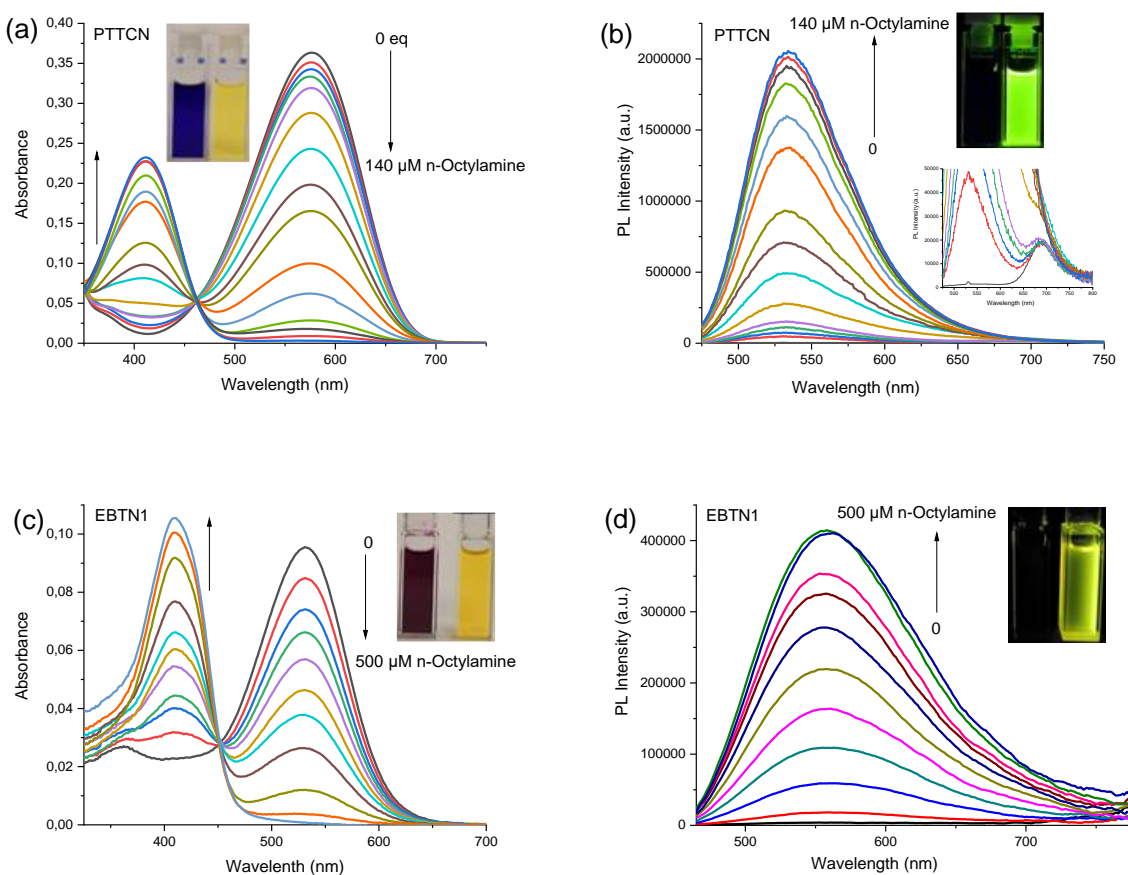


Figure 4 - 11. Absorption changes of **PTTCN** (a) and **EBTN1** (c) by increased addition of n-octylamine. Insert: photograph of **PTTCN** or **EBTN1** in the absence (left) and presence (right) of excess of n-octylamine under the ambient light. Fluorescence changes of **PTTCN** (b) and **EBTN1** (d) by increased addition of n-octylamine. Insert: photograph of **EBTN1** in the absence (left) and presence (right) of excess of n-octylamine under UV lamp (365 nm λ_{ex} : isobestic point. 10 μ M in DMSO).

The same experiments in low concentration of amines (below 100 μM) allow estimating the theoretical detection limits, as the increase of the fluorescence intensity at the maxima (λ_{ex} : isobestic point) are varying linearly with the quantity of amine added. So for both **PTTCN** and **EBTN1**, there is a linear variation (Figure 4 - 12, b and d) between the fluorescence intensity at 535 and 556 nm *vs* amine concentration, respectively. The slopes of the straight line κ give the limits of detection applying the formula $3\sigma/\kappa$,^[218] where σ refers to the standard deviation observed in the intensity of fluorescence measured at the wavelength of detection by 10-times continues scans. Theoretical detection limits of 32 nM for **PTTCN** and 0.16 μM for **EBTN1** were finally obtained. These figures are considered good in comparison with other amine probes published.^[219] For instance, Longstreet^[220] reported a primary amine probe with detection limit of 25 μM in 2014, Yang^[211] developed a probe tht possesses limit from 11.8 nM to 2.3 nM to different primary amines in 2020, and the most recently reported dicyanovinyl dye whose detection limit to n-butylamine is 15.8 nM.

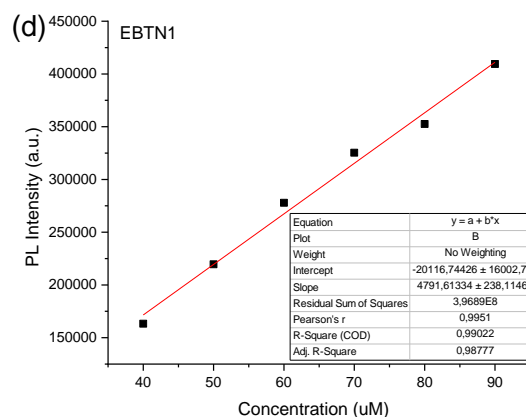
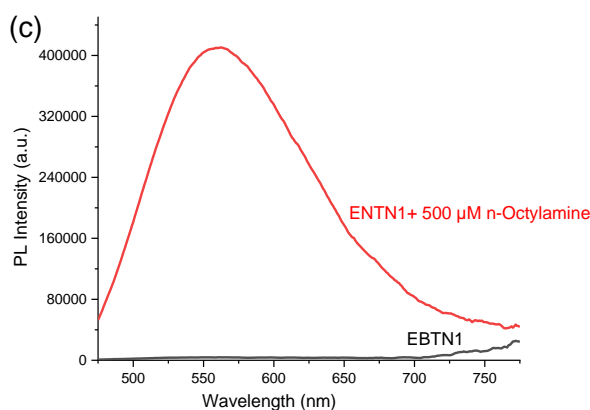
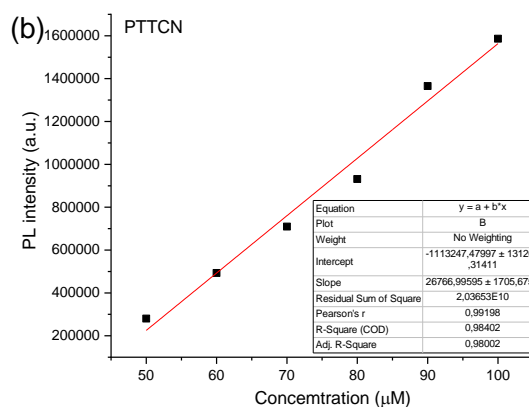
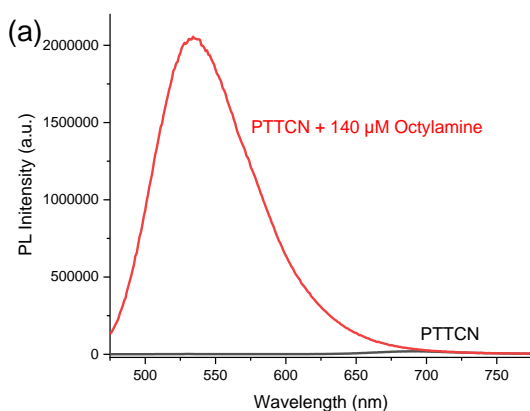


Figure 4 - 12. Fluorescence spectra comparison of **PTTCN** (a) or **EBTNI** (c) before (black) and after (red) addition of 140 or 500 μM of *n*-octylamine. (d) Plot of the fluorescence intensities of **PTTCN** (b) at 535 nm and **EBTNI** (d) at 556 nm as a function of concentration of *n*-octylamine added. λ_{ex} : isobestic point. 10 μM in DMSO.

2.4. Reversibility

We put in evidence the reversibility of the reaction. Indeed, for both dyes, further addition of malononitrile to the *n*-propylamine-dye adduct solution immediately induced another color change, with a smoke-like violet (**PTTCN**) or red (**EBTNI**) color spreading all over the solution (Figure 4 - 13, A). Homogenously violet solutions corresponding to the ones of the initial dyes (recovered) were obtained after a while.

More interestingly, the recovery of the starting dye was also observed when the excess *n*-propylamine from the end point of the titration experiments was removed by evaporation under vacuum (Figure 4 - 13, B), proving the total reversibility of the reaction.

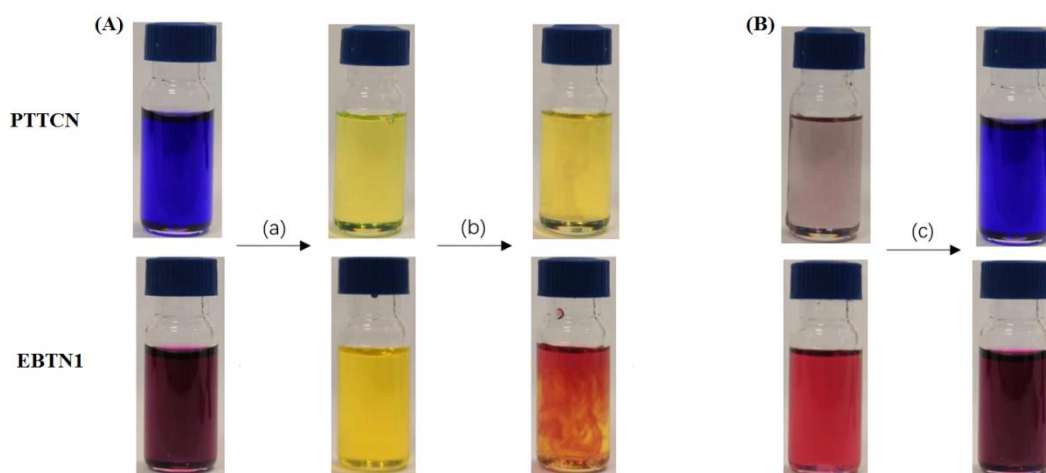


Figure 4 - 13. Photographs of **PTTCN** (up) and **EBTNI** (down) solutions. Treating processes: (a) addition of excess of *n*-propylamine, (b) addition of malononitrile, (c) vacuum.

2.5. Sensitivity and Selectivity

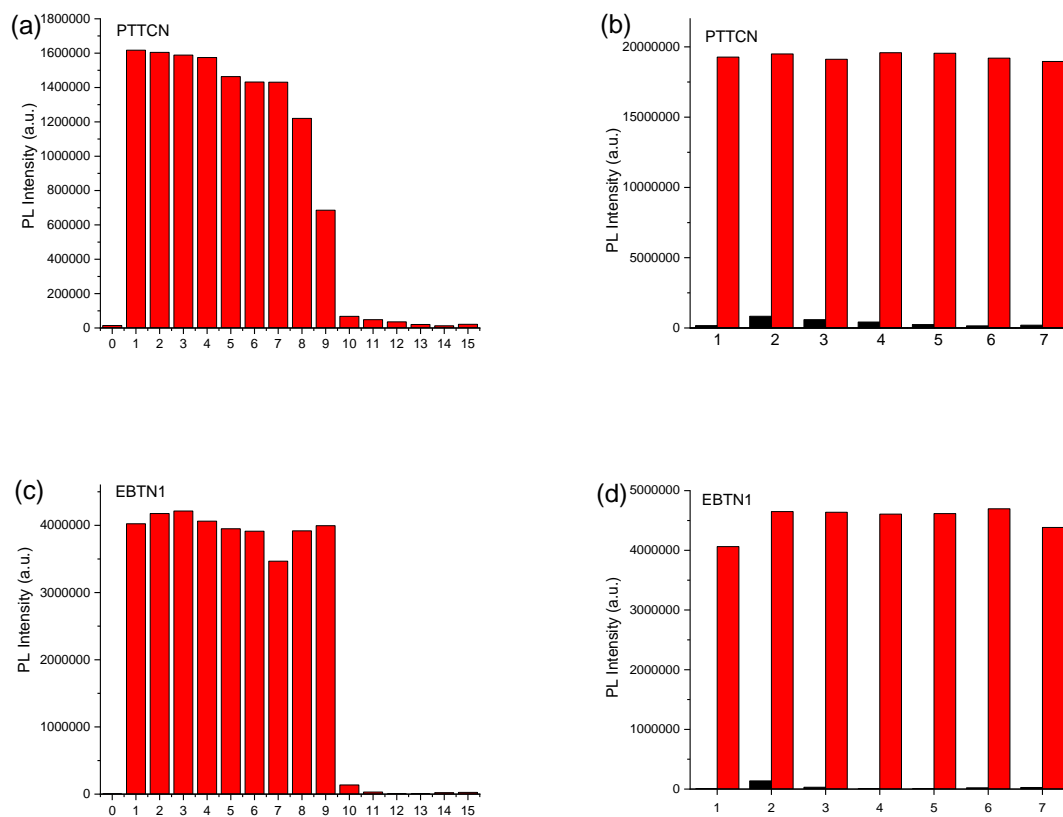


Figure 4 - 14. (a) Fluorescence intensity of **PTTCN** (at 535 nm) and **EBTN1** (at 556 nm) upon addition of various amines (0-blank, 1-putrescine, 2-tyramine, 3-cadaverine, 4-octylamine, 5-propylamine, 6-histamine, 7-tryptamine, 8-spermidine, 9-1,3-diamine, 10-diethylamine, 11-diisopropylamine, 12-trimethylamine, 13-pyridine, 14-aniline and 15-ethanethiol respectively, 50 eq). (b) Fluorescence intensity of **PTTCN** (at 535 nm) and **EBTN1** (at 556 nm) upon addition of various amines (black bars: 1-blank, 2-diethylamine, 3-diisopropylamine, 4-trimethylamine, 5-pyridine, 6-aniline, and 7-ethanethiol respectively, 50 eq). Red bars represented the corresponding fluorescence intensities with subsequent addition of *n*-octylamine (50 eq). λ_{ex} : isobestic point. 10 μ M in DMSO.

We then evaluated the sensitivity and selectivity of **PTTCN** and **EBTN1** to primary amine. Various nucleophiles including primary amines (putrescine, tyramine, cadaverine, octylamine, propylamine, histamine, tryptamine, spermidine, 1,3-diamine), secondary amines (diethylamine, diisopropylamine), tertiary amine (triethylamine), aromatic amine (pyridine, aniline), thiol (ethanethiol) and hydrazine (hydrazine and dimethylhydrazine) were tested in this study. As shown in Figure 4 - 14 a and c, strong fluorescence enhancements were observed for all the primary amines, but not for either the secondary, tertiary, aromatic amines or thiol under the given condition. More importantly, the followed addition of *n*-octylamine to these mixtures induced the characteristic yellow-emission (Figure 4 - 14, b and d). This

demonstrated the good sensitivity and selectivity of **PTTCN** and **EBTN1** to primary amine over the other kinds of amine or thiol we used here. Indeed, no fluorescence enhancement on **PTTCN** and **EBTN1** by addition of ethanethiol was out of our expectation, maybe it is a question of kinetics.

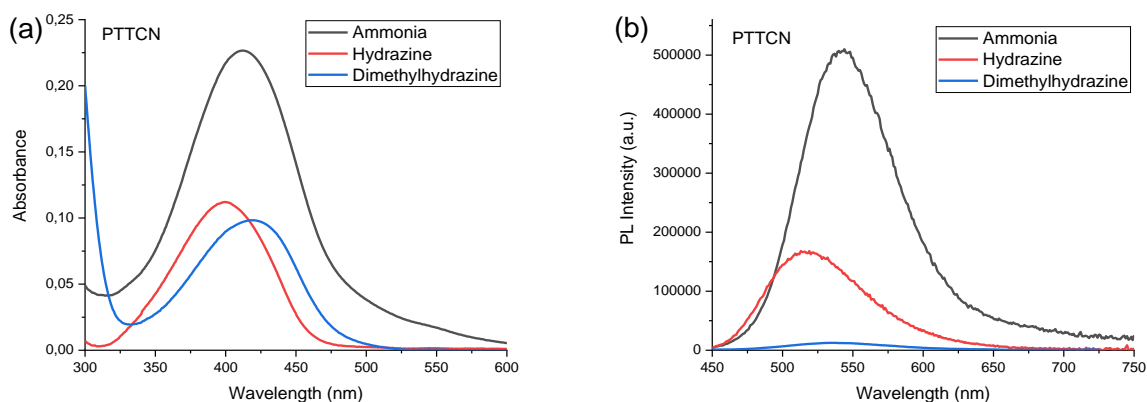


Figure 4 - 15. (a) absorption and (b) emission spectra of **PTTCN** upon addition of excess of ammonia, hydrazine or dimethylhydrazine. 10 μ M in DMSO.

On the other hands, it is worth noting that **PTTCN** also has fast fluorescence-response to ammonia and hydrazine compounds. From Figure 4 - 15, upon addition of ammonia, hydrazine or dimethylhydrazine to **PTTCN** solutions, the color violet immediately faded away (disappearing on the 575 nm absorption band) and a new absorption band around 400 nm appeared. The formed adducts are also emissive, but less fluorescent than the n-propylamine-**PTTCN** adduct: **PTTCN**/ammonia (543 nm, $\Phi = 0.6$), **PTTCN**/hydrazine (516 nm, $\Phi = 0.3$) **PTTCN**/dimethylhydrazine (535 nm, $\Phi = 0.05$). This would allow **PTTCN** to further distinguish hydrazine from other nucleophiles.

2.6. NMR Studies

To understand the sensing mechanism of **PTTCN** and **EBTN1** with primary amine, but also to clarify and confirm the structure of the final product, we then carried out the ^1H NMR analysis. In $[d_6]$ -DMSO, addition of n-propylamine immediately transformed **PTTCN** (resp. or n-octylamine to **EBTN1**) to only one another new compound. All the aromatic protons shifted upfield for both **PTTCN** and **EBTN1** (Figure 4 - 16). The vinylidene proton of both molecules also moved upfield, a new singlet integrating for one proton at 8.33 ppm for **PTTCN** and 8.43 ppm for **EBTN1** appeared (Figure 4 - 16). This is in perfect agreement with an imine structures (Figure 4 - 17 and Figure 4 - 20) in which the push-pull character is preserved, but a weaker electron-acceptor group is present. Indeed, a simple Michael addition of n-propylamine, as

observed with thiols^[212] or the cyanide anion^[188,221] would otherwise lead to a drastic upfield shift of the proton originally at the β -position as well as those of the closest thiophene ring due to a disruption of the π -conjugation from the donor to the acceptor end. The imine structures were further confirmed by mass spectrometry PTT-imine ($[M+H]^+$ calculated to be 319.1297, found at 319.1299), and EBTN-imine ($[M+H]^+$ calculated to be 812.3914, found at 812.3896).

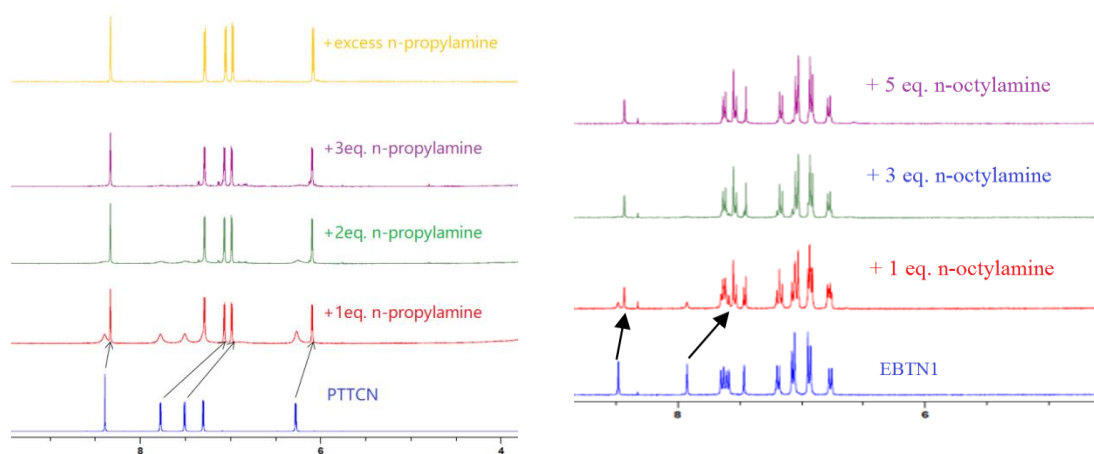


Figure 4 - 16. ^1H NMR changes upon addition of (left) *n*-propylamine to **PTTCN** or (right) *n*-octylamine to **EBTN1**.

To further confirm the Schiff-base structures, **PTT-imine** was independently synthesized from **PTTAld** and *n*-propylamine (Figure 4 - 17). By comparison of the ^1H and ^{13}C NMR spectra of the PTTCN/*n*-propylamine adduct to these of **PTT-imine** (Figure 4 - 18), the imine structure was unambiguously verified.

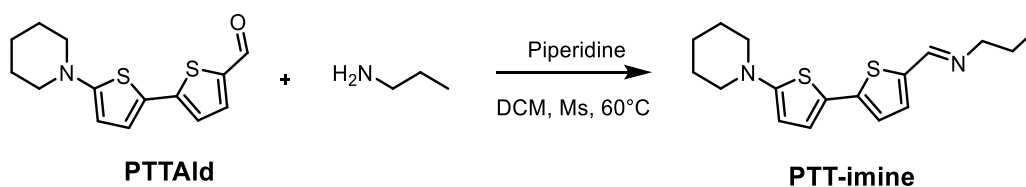


Figure 4 - 17. Synthesis of **PTT-imine**.

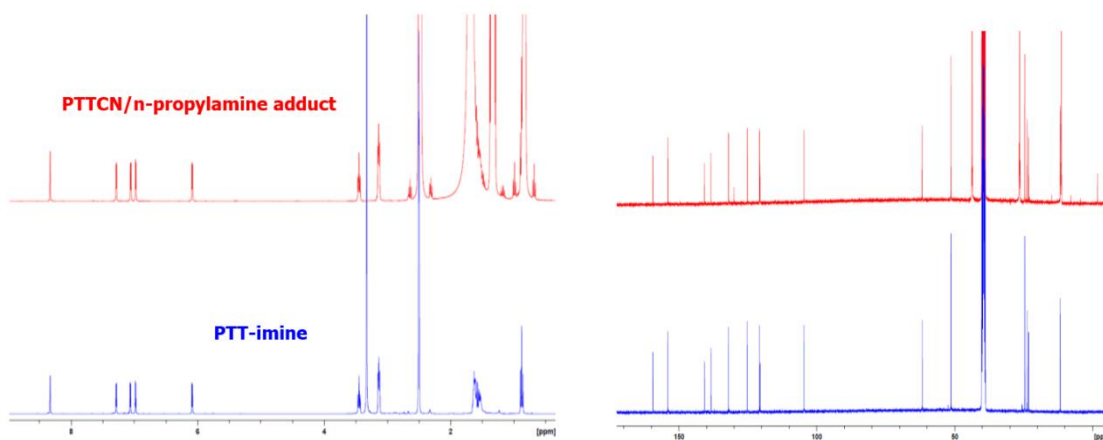


Figure 4 - 18. (Left) ^1H and (right) ^{13}C NMR spectral of **PTTCN/n-propylamine adduct** (red) and **PTT-imine** (blue).

The reversibility of the reaction was also clearly evidenced by ^1H NMR. As shown in Figure 4 - 19, when n-propylamine was removed by evaporation from the end point of the titration experiment, the ^1H NMR spectrum of **PTTCN** in $[d_6]$ -DMSO is again obtained.

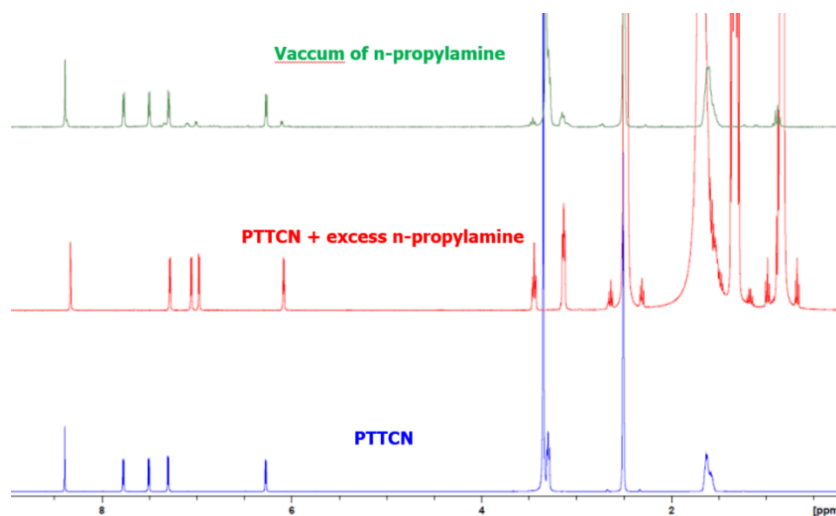


Figure 4 - 19. Reversibility of **PTTCN** to n-propylamine proved by ^1H NMR.

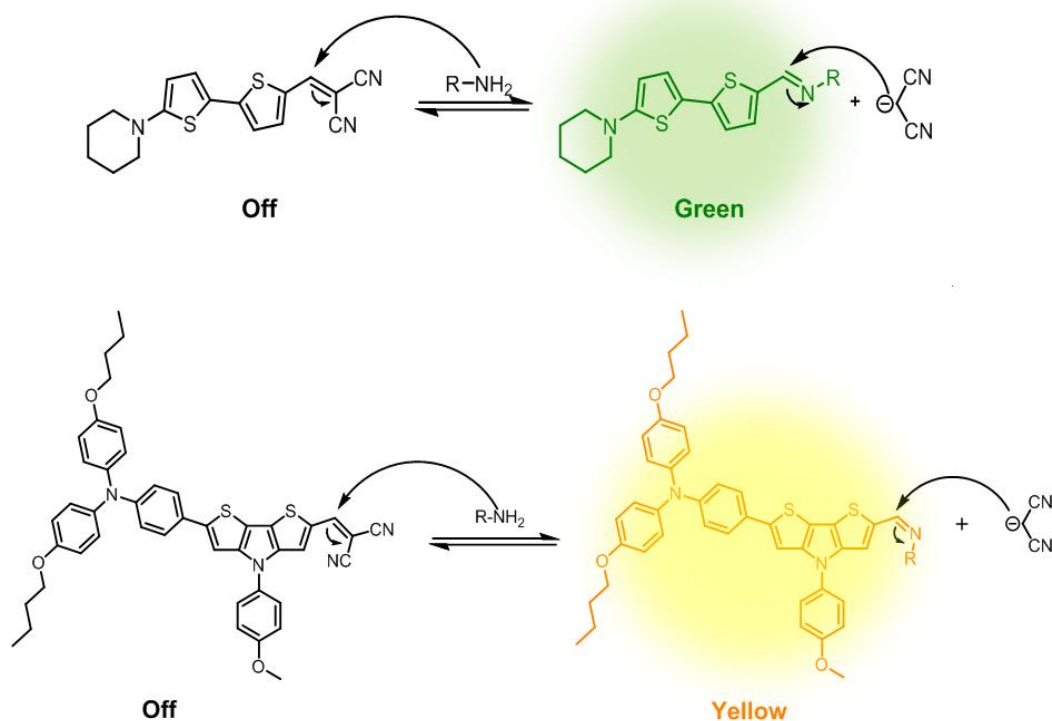


Figure 4 - 20. Sensing mechanism of **PTTCN** and **EBTNI** to primary amine.

3. **PTTCN** Films for Primary Amine Vapor Detection

In recent years, great efforts have been put to amine vapor detection, especially in food security field.^[222,223] Jia *et al.*^[199] prepared a cellulose-based ratiometric fluorescent material by covalently linking the amine-sensitive dye to the cellulose substrate, for detection of shrimp and crab freshness. In our case, having proved **PTTCN** as a high-performance primary amine sensor, we managed to use it for primary amine vapor detection.

By spin-coating of **PTTCN**/sol-gel or **PTTCN**/poly(methyl methacrylate) (PMMA) mixtures onto a glass slide, a homogeneous **PTTCN**/sol-gel or **PTTCN**/PMMA film was formed on the glass surface. To our surprised, although **PTTCN** is not emissive in solid state, both films show very strong red fluorescence (675 nm, $\Phi = 23\%$ for **PTTCN**/sol-gel and $\Phi = 13\%$ for **PTTCN**/PMMA). This is probably due to the rigidification as well as the isolation of **PTTCN** molecules within the films. More importantly, this property endows the films a ratiometric fluorescence response to primary amine vapor. As shown in Figure 4 - 21 a, upon exposure to a saturated n-propylamine vapor, the **PTTCN**/sol-gel film changes from violet to pale-green with absorption peak blue-shifted from 565 nm to 400 nm. Under UV 365 nm light, a significant

emission variation from red to green (500 nm, $\Phi = 43\%$) was observed by naked eye. **PTTCN**/PMMA film presented the same sensing behaviour to primary amine vapor with 57% quantum yield at the end. (Figure 4 - 21, b). Coming along with the quick response (in 10 seconds), **PTTCN** films are excellent for real-time primary amine vapor detection.

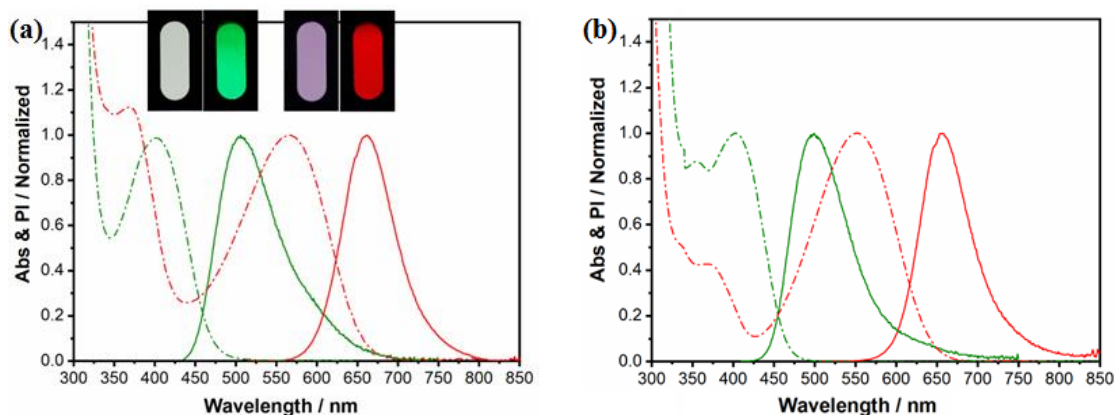


Figure 4 - 21. Absorption and fluorescence changes of (a) **PTTCN**/sol-gel and (b) **PTTCN**/PMMA films upon exposure to *n*-propylamine vapor. Insert: Photographs of **PTTCN** sol-gel film before (red) and after (green) exposure to *n*-propylamine vapor under ambient light and UV lamp (365 nm).

As the reaction of **PTTCN** with *n*-propylamine in DMSO is reversible, this feature can be used to prepare **PTTCN** film that is able to detect primary amine in a recyclable way. Nevertheless, the reacted films were failed to be recovered by vacuum, indicating the irreversibility of the reaction in the films. The reason could be attributed to the dilution of the imine and the malononitrile molecules by the films (Figure 4 - 22).

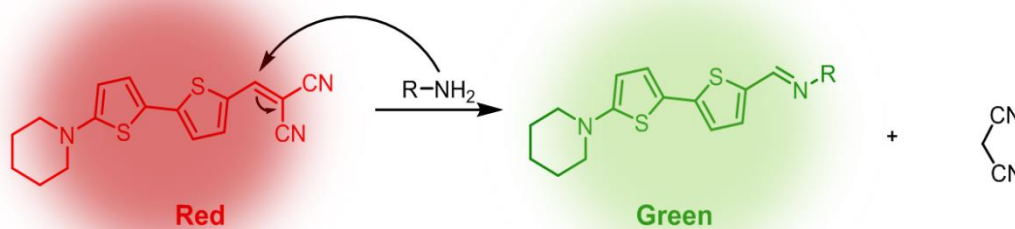
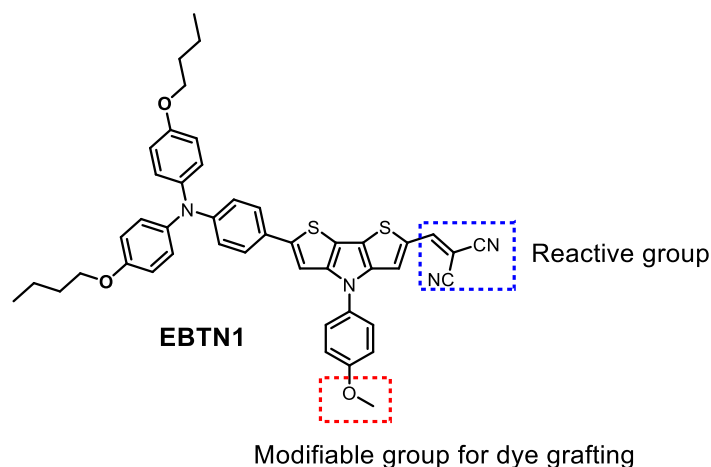


Figure 4 - 22. Sensing mechanism of **PTTCN** films to primary amine vapor.

4. EBTN1-glass for Primary Amine Vapor Detection

4.1. Objective

In spite of the excellent sensing behavior of **PTTCN** sol-gel film to primary amine vapor, the film cannot take advantage of the reversibility of the reaction in solution to be recycled by vacuum off the excess of amine. Therefore, we proposed to covalently link the dye to a device such as glass to enable the dye-modified device to be recovered by rinsing with malononitrile solution after exposing to amine vapor. However, as **PTTCN** has no modifiable site on its structure, **EBTN1** bearing a modifiable methoxy group would be allowed to be grafted onto a substrate for recycling detection of primary amine vapor (Scheme 4 - 3).



Scheme 4 - 3. Depict of reactive sites of **EBTN1** for preparation of recyclable amine vapor device.

Glass slide is a commonly used material in preparation of DNA and protein chips, due to its low cost, corrosion resistance, low fluorescence background and ease of surface modification. All these advantages promoted us to use it as the substrate for preparation of the dye-loaded device for primary amine vapor detection. As shown in Figure 4 - 23, **EBTNAld** functionalized by a NHS group is able to covalently link with the amine group modified on the glass surface via coupling. Followed treating with malononitrile, the **EBTNAld** molecules on the glass surface will transform into **EBTN1**, to form the **EBTN1**-loaded glass slide. It is worth noting that, the amine on the glass surface is a primary amine, which doesn't have reaction with **EBTNAld** in the absence of catalyst. Finally, upon exposure to primary amine vapor, the **EBTN1** molecules on the glass surface will transformed into **EBTN-imine** to present strong fluorescence, most importantly, which can be recovered by rinsing with malononitrile solution taking advantage of the reversibility of the reaction.

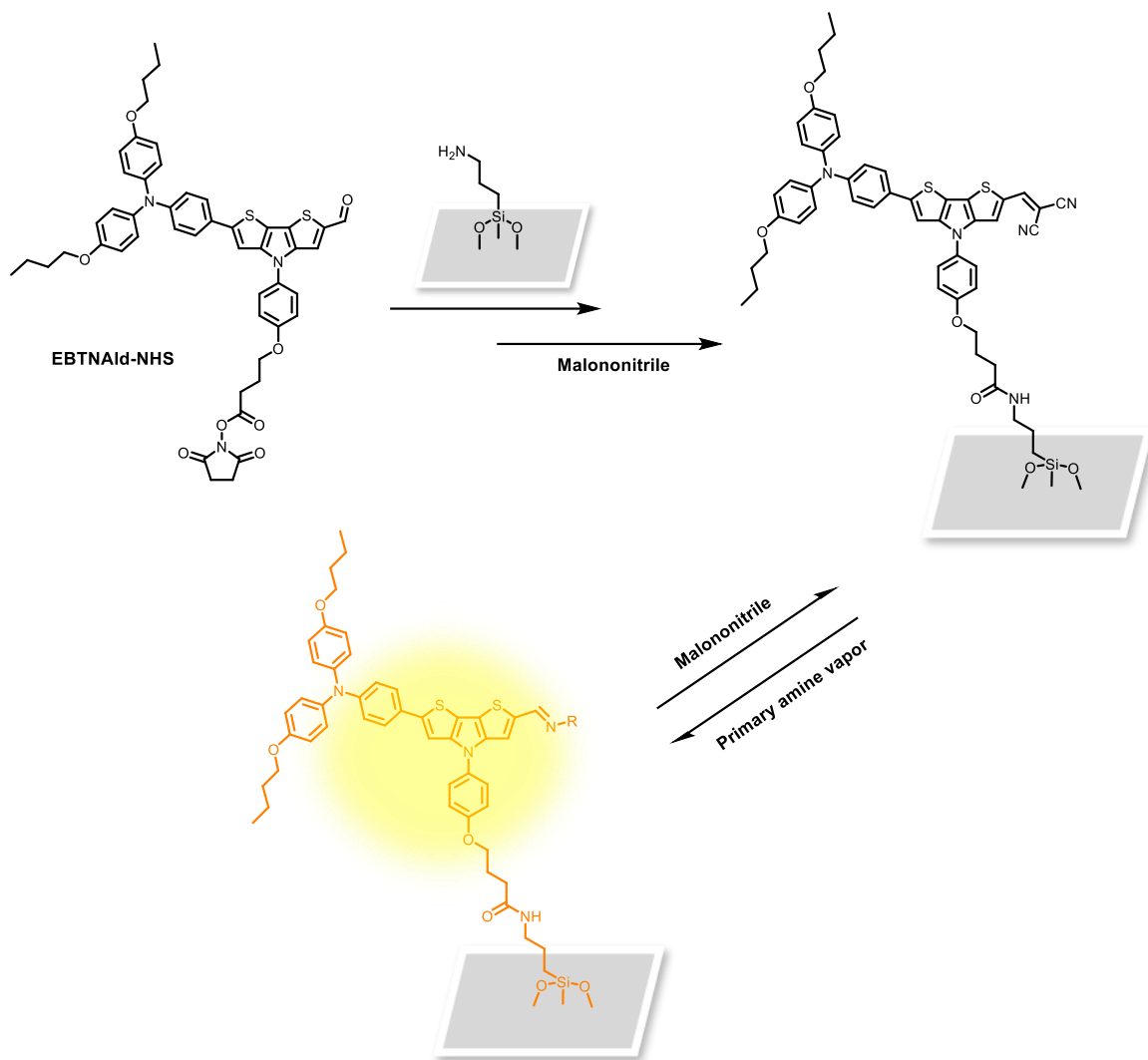


Figure 4 - 23. Synthetic design of *EBTNI-glass* for recyclable primary amine vapor detection.

4.1.1.1. Synthesis of EBTNAld-NHS

The synthesis of **EBTNAld-NHS** was depicted in Figure 4 - 24. Firstly, in the presence of BBr_3 , compound **9** transformed into **13** through demethylation in 93% yield. Then a functional lateral chain bearing an end ethyl ester group was introduced by nucleophilic substitution of **13** with ethyl 4-bromobutanoate. Followed by Suzuki cross-coupling, compound **15** was formed in 76% yield. The ethyl ester group of **15** was then hydrolyzed in acidic condition to afford compound **16**. Lastly, the **EBTNAld-NHS** was obtained by addition of 1-hydroxypyrrolidine-2,5-dione under the catalysis of EDC-HCl in yield of 82%.

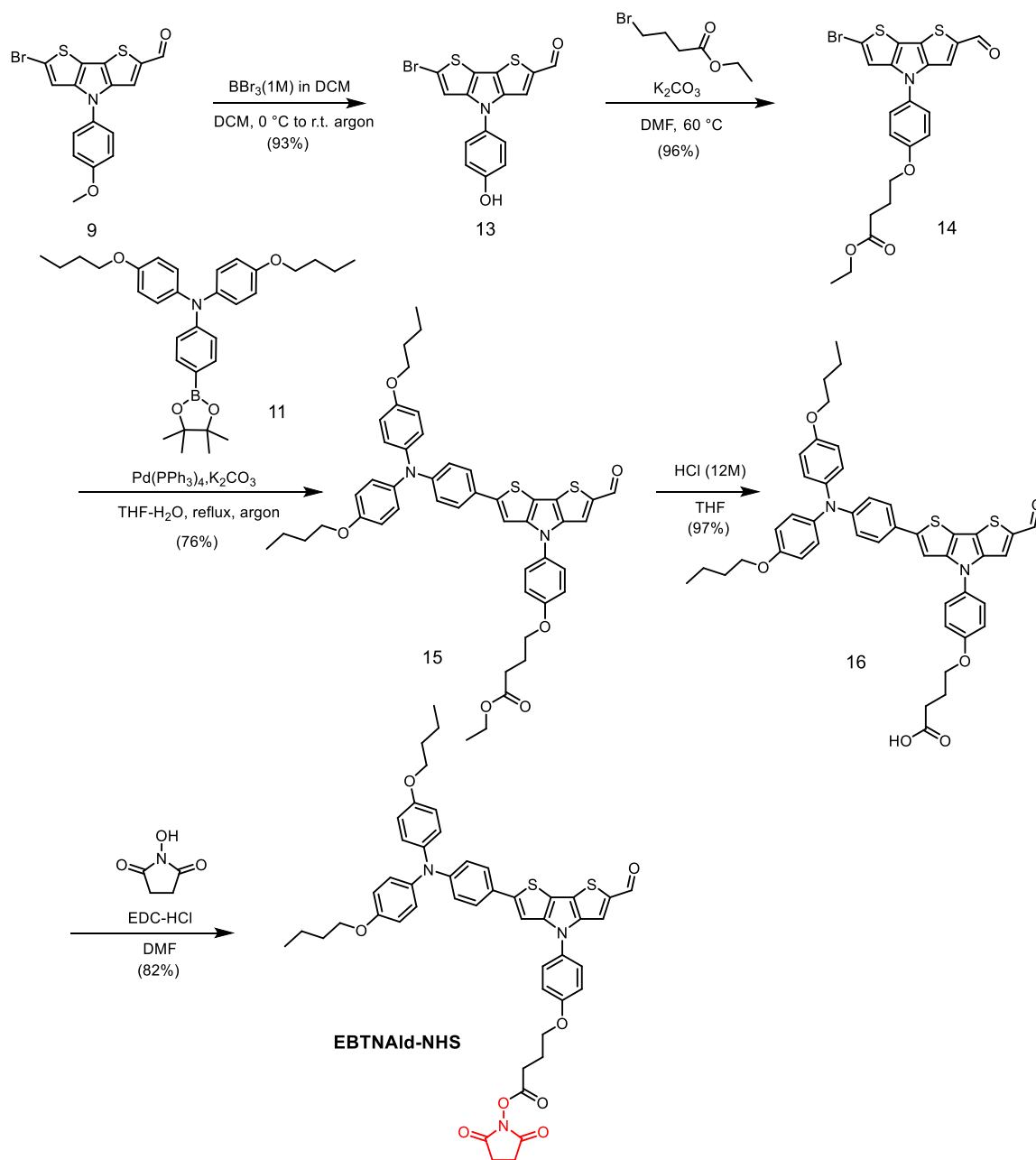


Figure 4 - 24. Synthetic route of *EBTNAld-NHS*.

4.1.1.2. Preparation of EBTN1-grafted Glass Slide

For preparation of the **EBTN1-grafted** glass slide, the first step was to prepare the amine modified glass slide. As shown in Figure 4 - 25, normal glass slide was carefully washed with detergent to expose the hydroxy groups on its surface, followed by silicate cross-linking with APTES, the amine groups were fixed on the glass surface. After wash and dry, the amine modified glass slide was immersed into the solution of the **EBTNAld-NHS** to allow the grafting of **EBTNAld** onto the glass surface. Then further immersing of

the **EBTNAld**-loaded glass in the malononitrile solution enabled the formation of the **EBTN1-grafted** glass slide.

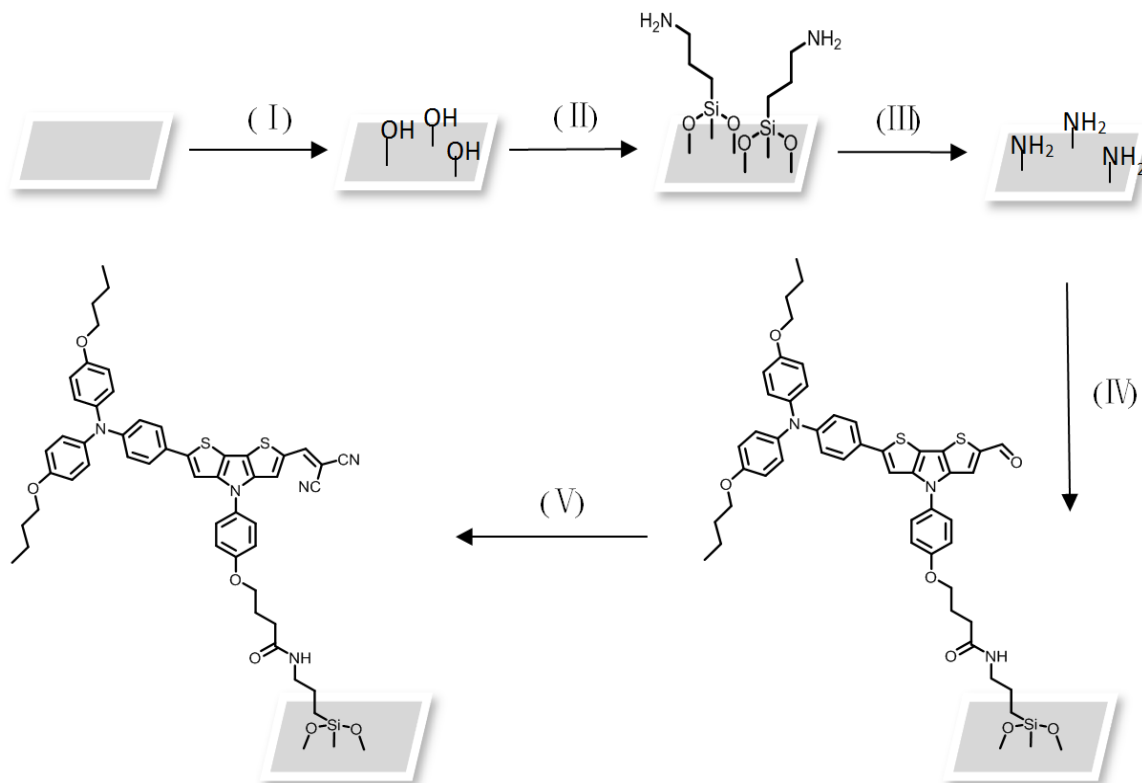


Figure 4 - 25. Procedure of preparation of **EBTN1** grafted glass. Conditions: (I) Detergent/water/acetone/methanol, ultrasonication; (II) APTES (5% in methanol), 45~60min; (III) Wash with methanol, dry for 30min at 120°C; (IV) Immerse in **EBTNAld** solution (100 μ M) overnight, rinse with methanol; (V) Immerse in malononitrile solution (10 mM) for 6h, rinse with DCM.

4.2. Preliminary Tests on **EBTN1**-glass

From the colored edges of the glass slides shown in Figure 4 - 26 a, it can be seen that **EBTNAld** and **EBTN1** were successfully grafted on the surface of the normal glass. However, given the single layer of **EBTN1** coated insufficiently reduced the glass transparency, it's by no means easy to follow the color or fluorescence changes of the glass with naked eye in its process of detection of primary amine vapor. Benefited by the strong emission property of **EBTN-imine**, **EBTN1-glass** slide in n-propylamine vapor atmosphere showed bright blue fluorescence (Figure 4 - 26, b).

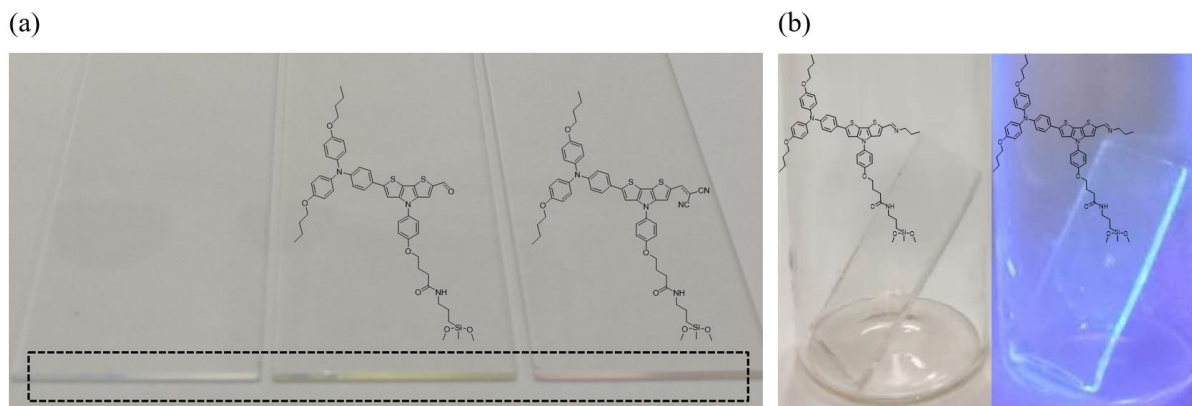


Figure 4 - 26. (a) Photographs of normal, **EBTNAld** and **EBTN1-glass** slides; (b) Photographs of **EBTN1-glass** slide in saturated propylamine vapor under ambient light (left) and UV lamp (365 nm, right).

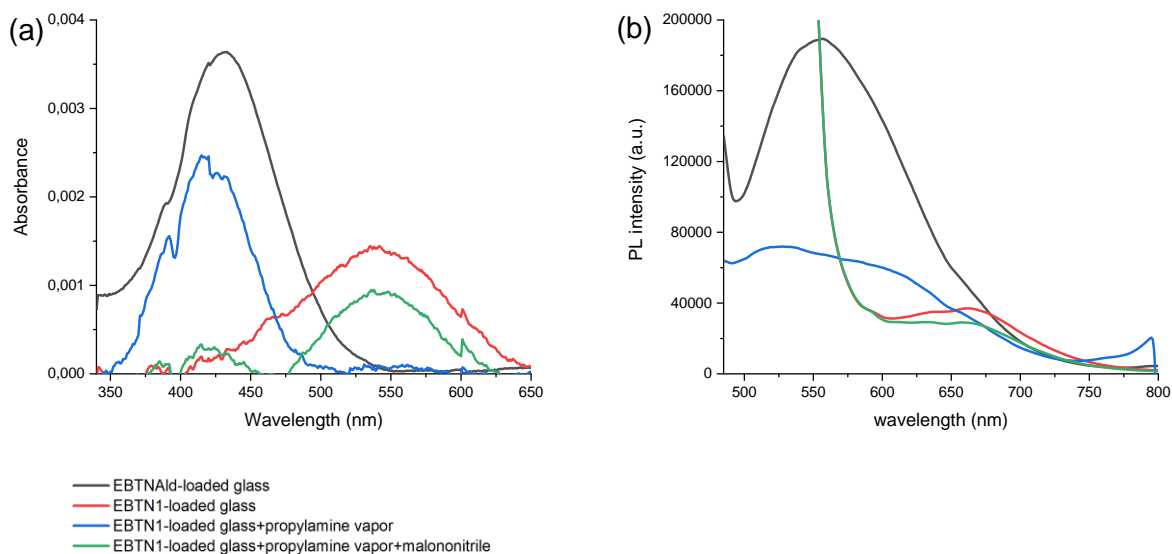


Figure 4 - 27. (a) absorption and (b) emission changes of **EBTN1-glass** slide in the cycle test of *n*-propylamine vapor.

Figure 4 - 27 showed the absorption and emission changes of **EBTN1-glass** slide in its cycle test of propylamine vapor. From the spectra, **EBTNAld** modified glass slide with absorption and emission peaks at 430 nm and 555 nm red-shifted to 542 nm and 666 nm, respectively after soaking in malononitrile solution overnight, which indicated the conversion of **EBTNAld** to **EBTN1** on the glass slide. It's worth noting that **EBTN1** on the glass slide presented similar absorption but enhanced fluorescence compared to itself in DMF, this can be attributed to the separation of **EBTN1** molecules on the glass surface. By placing the glass in saturated *n*-propylamine vapor for 5 min, its absorption band at 542 nm blue-shifted to 420 nm with a corresponding new fluorescence peak at 530 nm appearing, this demonstrated the colorimetric detection of **EBTN1-glass** slide for primary amine vapor. Then, immersing the glass slide into the malononitrile solution

again restored the initial absorption and emission spectra, proving the reversibility of the reaction on the glass surface and the potential recyclability of **EBTN1-glass** slide for primary amine vapor detection.

However, limited by the loading amount of **EBTN1** molecules on the glass surface, the slide was weakly absorptive and emissive. Hence, other substrates with higher dye-loading ability were expected to overcome this problem.

5. Conclusion

In this chapter, based on nucleophilic addition and ICT mechanism **PTTCN** and **EBTN1** were utilized for primary amine detection.

Addition of an excess of primary amine to the solution of **PTTCN/EBTN1** in DMSO induced an immediate color change from violet to yellow (575 to 412 nm/530 to 410 nm) coming along with the apparition of an intense yellow fluorescence (535 nm, $\Phi = 1/556$ nm, $\Phi = 0.75$), which left an isobestic point at 462 nm/460 nm and the 1160-fold/112-fold fluorescence intensity enhancement. In addition to the good sensitivity and selectivity to primary amine, the detection limit was calculated to be 32 nM/0.16 μ M for n-octylamine. Significantly, the reaction was found reversible by removing the n-propylamine added from the solution or by further addition of malononitrile. The imine structure of the sensing adducts were confirmed by NMR and mass spectrometry.

Furthermore, **PTTCN/sol-gel** and **PTTCN/PMMA** films were prepared to detect primary amine vapor. Thanks to the strong start emission of the films (675 nm, $\Phi = 23\%$ for **PTTCN/sol-gel** and $\Phi = 13\%$ for **PTTCN/PMMA**), they are able to detect primary amine vapor in a ratiometric way (emission blue-shifted to 500 nm, $\Phi = 43\%$ for **PTTCN/sol-gel** and $\Phi = 57\%$ for **PTTCN/PMMA**). Both films have quick response (in 10 seconds) to primary amine vapor, and the sensing process can be easily followed by naked eye.

In order to take advantage of the reversibility of the reaction between dicyanovinyl and primary amine to prepare a recyclable device for primary amine vapor detection, **EBTN1** functionalized glass slide was preliminarily designed. Upon exposure to primary amine vapor, the **EBTN1-glass** had absorption blue-shifted from 542 nm to 420 nm coming along with its fluorescence shifted from 666 nm to 530 nm. Dramatically, by immersing with malononitrile solution the glass was successfully restored, proving our objective of making recyclable primary amine sensing device is feasible.

Chapter V. Conclusion and Perspectives

To sum up, our main goal in this thesis was to synthesize novel organic contrast agents for *in vivo* fluorescence or PA imaging, focusing on small push-pull dipolar dyes and F127-SiO₂ or polymer NPs.

In the first part, we design and synthesized two series of NIR-emitting dyes **TCBZ1-TCBZ8** and **EBTN1-EBTN5** based on the fluorene and bishienopyrrole dyes previously synthesized in our group. TCBZ dyes have *tert*-butyl substituted carbazole as the electron donor, which was connected to different electron acceptors by a fluorene unit, presenting absorptions and emissions from 433 to 512 nm and 648 to 745 nm, respectively, as well as interesting solvatochromism and large Stokes shifts. In comparison to the previous carbazole-fluorene dyes, the new dyes showed more red-shifted optical properties while keeping good solid-state emissions. EBTN dyes were synthesized using butoxy modified triphenylamine as the electron donor, which was linked by the bishienopyrrole unit (BTN) to different electron-withdrawing groups. An increased ICT effect made it possible to further push the emissions of the dyes toward longer wavelengths. Especially for **EBTN4** and **EBTN5**, with relatively strong electron-withdrawing acceptors exhibited emission peaks above 850 nm in chloroform with excellent quantum yields, albeit low quantum yield (1 to 2 %). They, however, have a much higher quantum yield in toluene (30 and 47 % respectively) for an emission above 780 nm. More importantly, all the EBTN dyes presented much improved lipophilicities compared to the previous ones. This allows us to form F127-SiO₂ NPs by dye encapsulation by F127. These NPs display very high brightness in NIR region, thanks to the apolar environment of the F127-SiO₂ core that is similar to a toluene / chloroform mixture (1/1 v/v).

On the other hand, for the purpose of functionalization of the F127-SiO₂ NPs surface with different moieties, carboxyl and azido modified F127 were firstly prepared. Then, the maximum surface modification that permits a good particle-stability and the dye loading ratio that allows a highest particle-brightness were optimized. Using 10 % **F127-COOH** and 50 % **F127-N₃** with 0.5 % of **TCBZ5**, **TCBZ5@F127-COOH-SiO₂** and **TCBZ5@F127-N₃-SiO₂** NPs were obtained. Followed grafting of the NPs with alkynyl modified TPP or **X** via “click” reaction afforded other surface-functionnalized NPs: **TCBZ5@F127-X-SiO₂** or **TCBZ5@F127-TPP-SiO₂**. **TCBZ5@F127-SiO₂** and **TCBZ5@F127-X-SiO₂** NPs were then tested in *in vivo* biphotonic fluorescence imaging. They successfully imaged the vasculature system of the mice while presented a long circulation time within the mice vessels.

In the third chapter, different strategies were developed to increase the dye-loading of the NPs, aiming to overcome the problem of insufficient generation of PA signal in biological tissues. On the one hand, through collaboration with IMP we designed and synthesized three kinds of dye-loaded polymer NPs, involving dye-

polymer conjugation and dye polymerization methods. Polyacrylate polymer developed by Arnaud Favier with multiple NHS ester units was able to conjugate dyes containing amine groups, thus we synthesized **CPO-SO₃** and **CPOP1**. For polymerization, we introduced an acrylamide group to form the dye monomer **CPOP2**. Benefiting from the hemicyanine structures, all the dyes showed strong absorptions in NIR region with moderate fluorescence emissions. Among these polymer NPs, **CPO-SO₃** NPs was successfully used to image a mouse vasculature with a 660 nm excitation. However, the accumulated signals in liver and kidney indicated the fast clearance of the NPs from a mouse body. **CPOP1** NPs and **CPOP2** NPs with improved water solubility and homogeneity were expected for a long-time *in vivo* PA imaging.

On the other hand, based on the surface-functionalization of F127-SiO₂ NPs developed in the second chapter, a surface dye-grafting strategy was applied to improve the particle dye-loading capacity. Through “click” reaction in presence of CuSO₄, sodium ascorbate and the ligand tris(hydroxypropyltriazoly)methylamine and THPTA, **CPO-SO₃-alkyne** was covalently linked to the **F127-N₃-SiO₂** NPs. Limited by the particle stability, maximum dye loading was determined at 0.55 mM, about 10 dyes per particle according to the concentration of the particle provided by literatures. However, the concentration was still not enough for the PAM we are using.

The fourth chapter preliminarily investigated the response of EBTN dyes we obtained to primary amines. It was found that all the dyes with different acceptors can form a same structure but **EBTN1** with a dicyanovinyl acceptor presented the relatively fast kinetic. For this reason, **PTTCN** and **EBTN1** were used for primary amine detection. Based on ICT mechanism, **PTTCN** and **EBTN1** both showed drastic fluorescence “turn-on” response to primary amine in DMSO (1160-fold/112-fold fluorescence enhancement for **PTTCN/EBTN1**) with high sensitivity, selectivity as well as good detection limit (32 nM/0.16 μM for n-octylamine of **PTTCN/EBTN1**). The reaction was also found reversible by removing the amine or further addition of malononitrile from/to the adduct solution. **PTTCN** sol-gel and PMMA films were prepared for detection of primary amine vapor. In 10 seconds, the films in saturated n-propylamine changed color from violet to yellow-green with fluorescence changed from red to green. The quick response and the obvious color changing make it possible to follow the sensing process by naked eye. To take advantage of the reversibility of the reaction for circle detection of primary amine vapor, **EBTN1** was modified by a NHS group for preparation of a dye-grafted glass slide. However, limited by the loading ratio, it is hard to follow the detection process by naked eye. To tackle this issue, other substrates or grafting methods that can improve the dye loading is required.

For *in vivo* optical imaging, firstly, the two-photon cross-section of all the dyes will be measured once the instrument is accessible. At the same time, the biphotonic *in vivo* imaging experiments based on NPs (**TCBZ5@F127-COOH-SiO₂**) as well as PA (**CPOP1** NPs) will be performed in the near future.

For primary amine detection, in order to improve the dye loading of the substrates, we manage to further modify **EBTN1** with a triethoxysilane group which would allow the dye to be directly grafted onto various substrates. Additionally, preliminary work revealed that all the other EBTN dipolar dyes besides **EBTN1** have similar fluorescence responses to primary amine, but with more complicated two-stages sensing processes and slower kinetics. Thus, in the following study, we will study the mechanism of all the other acceptors.

Chapter VI. Experimental Section

1. Synthesis

1.1. General Information

All commercially available solvents and reagents were used without further purification. Anhydrous THF was obtained by distillation over sodium and benzophenone, toluene was dried over Al₂O₃ column. Anhydrous DMF, DCM and acetonitrile were purchased from Acros under AcroSeal™. Column chromatography was performed on Merck silica gel (40-63 μm). Microwave syntheses were conducted in 20 mL or 5 mL sealed tube on a Biotage Initiator 2.5 single-mode reactor using external IR temperature control. NMR spectra were recorded at ambient temperature on Bruker Advance 300 or 400 operating at 300.1 or 400.0 MHz for ¹H and 75.0 or 101.0 MHz for ¹³C, respectively. Chemical shifts are given in parts per million (ppm) with the residual solvent peaks as internal standard (7.26 ppm and 77.2 ppm for chloroform, 2.50 and 39.5 ppm for DMSO). ¹H NMR splitting patterns are described as singlet (s), doublet (d), triplet (t) or multiplet (m) and coupling constants are given in hertz (Hz). High-resolution mass spectrometry (HRMS) were measured by ESI-TOF (Bruker Daltonics Micro TOF-Q II) at the *Centre Commun de Spectrométrie de Masse* (UCBL, Villeurbanne, France).

All solvents used in optical measurements are of spectrophotometric grades. UV/Vis absorption spectra were measured using a dual beam Jasco 670 spectrometer. Fluorescence spectra in diluted solution and in solid were recorded on a Horiba Jobin-Yvon Fluorolog-3® spectrofluorimeter equipped with red-sensitive Hamamatsu R928 or water-cooled R2658 photomultiplier tubes. Spectra were reference corrected for both the excitation source light intensity variation (lamp and grating) and the emission spectral response (detector and grating). Quartz cuvettes with thickness of 1 cm or 1mm were used as sample cells. The quantum yield relative to the reference is given by equation (1):

$$\phi^S = \phi^{Ref} \frac{S^S}{S^{Ref}} \times \left(\frac{n_d^{Ref}}{n_d^S} \right)^2 \quad (1)$$

where S is the slope obtained by plotting the integrated area under the fluorescence emission spectrum vs the absorbance at λ_{exc} and n_d the refractive index of the solvents. Superscript *Ref* and *s* correspond to the reference and the sample respectively. For each experiment 5 points were recorded, all corresponding to an absorbance at λ_{exc} below 0.1. Fluorescence standards Rubrene, Cresyl violet perchlorate and Styryl 9M were

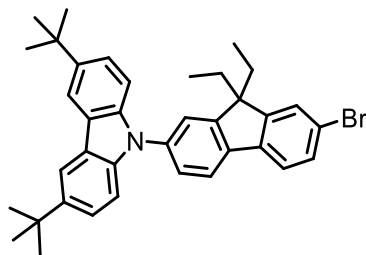
purchased respectively from Aldrich and Acros Organic. Absolute fluorescence quantum yields in solid Φ_s were measured using a calibrated integrative sphere collecting all the emission (2π steradians covered with spectralon®), model G8 from GMP (Renens, Swiss). For each sample, four measurements were made using the same excitation and emission monochromatic band pass (slits opening) to give four integrated intensities. Quantum yield are therefore given by equation (2):

$$\Phi_s = \frac{E_c - E_a}{ND \times (L_a - L_c)} \quad (2)$$

where E_c and E_a are the integrated fluorescence resulting of a direct excitation of the sample and the integrated fluorescence without any sample (the background of the sphere), L_a is the integrated excitation profile with the empty sphere, and L_c is the integrated excitation profile with the sample inside the sphere. For the determination of L_a and L_c , a neutral density filter (0.5 %) was used to reduce the intensity without changing the excitation profile. The ND value is wavelength dependent and is determined for λ_{exc} .

Precursors **a-h**, 2-iodo-7-bromo-9,9-diethyl-9H-fluorene **3**, 3,6-di-*tert*-butyl-9H-carbazole **4** and 4-(4-methoxyphenyl)-4H-dithieno[3,2-b:2',3'-d]pyrrole **7** were previously synthesized in our team.^[107,111] Compound 10 was prepared according to the literature.^[224,225] The alkynyl modified **X** was provided by our collaborator.

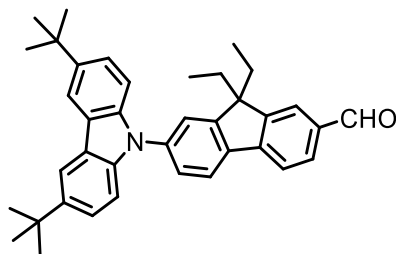
1.2. Synthesis and Characterization of Dyes



9-(7-bromo-9,9-diethyl-9H-fluoren-2-yl)-3,6-di-*tert*-butyl-9H-carbazole (**5**)

In a 100 mL round-bottom flask, 3,6-di-*tert*-butyl-9H-carbazole (**4**) (4.30 g, 15.38 mmol), copper iodide (0.21 g, 1.10 mmol), 1,10-phenanthroline (0.49 g, 2.72 mmol) and K_2CO_3 (5.00 g, 36.18 mmol) were added to a solution of 2-iodo-7-bromo-9,9-diethyl-9H-fluorene **3** (5.56 g, 13.02 mmol) in DMF (56 mL) under argon atmosphere. After stirring at 120°C overnight, DMF was removed by evaporation under reduced pressure. Then the crude oil was purified by column chromatography on silica using pentane as the eluent to afford **5** as a white solid (3.10 g, yield: 41 %). 1H NMR (400 MHz, $CDCl_3$, ppm): δ 8.18 (s, 2H), 7.88 (d, $J = 7.9$ Hz, 1H), 7.65 (d, $J = 8.8$ Hz, 1H), 7.59-7.48 (m, 6H), 7.38 (d, $J = 8.8$ Hz, 2H), 2.07 (q, $J = 7.4$ Hz,

4H), 1.50 (s, 18H), 0.45 (t, $J = 7.4$ Hz, 6H). ^{13}C NMR (101 MHz, CDCl_3 , ppm): δ 152.4, 151.3, 142.9, 140.0, 139.3 (2C), 137.4, 130.3, 126.4, 125.7, 123.7, 123.4, 121.5, 121.3, 121.1, 120.8, 116.3, 109.1, 56.7, 34.8, 32.7, 32.0, 8.6. HR-MS (ESI-QTOF): m/z $[\text{M}+\text{H}]^+$ calcd for $\text{C}_{37}\text{H}_{41}\text{BrN}$, 578.2422; found, 578.2417.

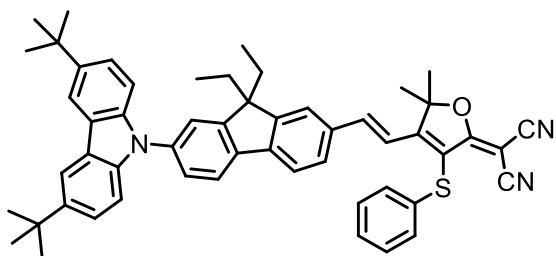


7-(3,6-di-*tert*-butyl-9H-carbazol-9-yl)-9,9-diethyl-9H-fluorene-2-carbaldehyde (**6**)

To a solution of **5** (1.00 g, 1.73 mmol) in anhydrous THF (10 mL), *n*-BuLi (2.25 mmol, 2.5 M in hexane) was added dropwise at -78°C under argon atmosphere. After stirring at -78°C for 1h, the mixture was allowed to warm up to room temperature for 5 min, then DMF (0.36 mL, 3.60 mmol) in anhydrous THF (2 mL) was added at -78°C . After stirring at room temperature overnight, the reaction was quenched by addition of water (2 mL). Then, the mixture was extracted by DCM and washed twice with water. The organic phases were collected, dried over MgSO_4 , and evaporated under reduced pressure. Further purification by column chromatography on silica (eluent: DCM:PE=1:1, v/v) afforded **6** as an orange solid (750 mg, yield: 82%). ^1H NMR (400 MHz, CDCl_3 , ppm): δ 10.12 (s, 1H), 8.19 (s, 2H), 8.01 (d, $J = 8.2$ Hz, 1H), 7.97-7.91 (m, 3H), 7.65-7.58 (m, 2H), 7.52 (d, $J = 8.2$ Hz, 2H), 7.44-7.38 (m, 2H) 2.26-2.03 (m, 4H), 1.51 (s, 18H), 0.45 (t, $J = 7.4$ Hz, 6H). ^{13}C NMR (101 MHz, CDCl_3 , ppm): δ 192.3, 153.2, 151.0, 147.2, 143.1, 139.1, 138.7, 138.6, 135.5, 130.8, 125.8, 123.8, 123.5, 123.3, 122.1, 121.5, 120.1, 116.4, 109.1, 56.6, 34.8, 32.6, 32.0, 8.6. HR-MS (ESI-QTOF): m/z $[\text{M}+\text{H}]^+$ calcd for $\text{C}_{38}\text{H}_{42}\text{NO}$, 528.3266; found, 528.3238.

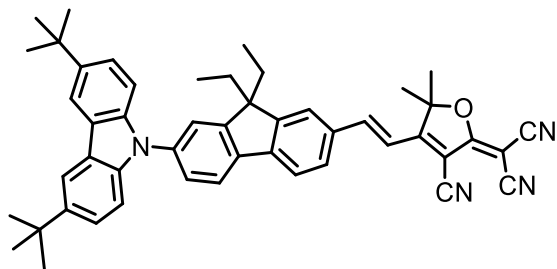
General procedure for Knoevenagel condensation. Synthesis of TCBZ1-TCBZ8.

In 5 mL microwave tubes, **6** (100 mg, 0.19 mmol) and the corresponding acceptors **a-h** (0.20 mmol) were dissolved in anhydrous EtOH (2 mL), followed by addition of one drop of piperidine. Then the tubes were sealed and heated at 90°C by microwave irradiation for 45 min. After cooling down to room temperature, the solids formed were filtrated and recrystallized from DCM/pentane to afford the pure products.



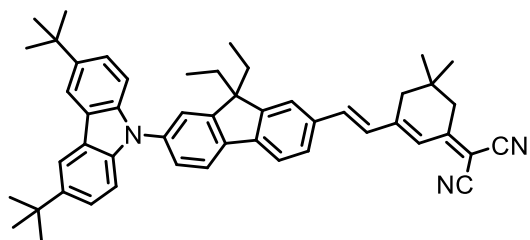
(E)-2-(4-(2-(7-(3,6-di-tert-butyl-9H-carbazol-9-yl)-9,9-diethyl-9H-fluoren-2-yl)vinyl)-5,5-dimethyl-3-phenylthiofuran-2(5H)-ylidene)malononitrile (TCBZ1)

Red solid (78 mg, yield: 52%) ^1H NMR (400 MHz, $\text{DMSO-}d_6$, ppm) δ 8.32 (s, 1H), 8.31 (s, 1H), 8.14 (d, $J = 8.2$ Hz, 1H), 8.00 (d, $J = 8.2$ Hz, 1H), 7.92-7.76 (m, 3H), 7.72 (s, 1H), 7.60 (d, $J = 8.2$ Hz, 1H), 7.51 (d, $J = 8.7$ Hz, 2H), 7.43-7.26 (m, 8H), 2.13-2.02 (m, 4H), 1.91 (s, 6H), 1.43 (s, 18H), 0.32 (t, $J = 7.4$ Hz, 6H). ^{13}C NMR (101 MHz, $\text{DMSO-}d_6$, ppm) δ 181.7, 172.2, 152.8, 151.1, 145.0, 144.0, 143.1, 139.4, 139.1, 137.6, 134.9, 134.6, 130.3, 128.9, 127.7, 127.3, 125.9, 124.3, 123.5, 123.3, 122.6, 121.8, 121.1, 118.2, 117.2, 116.3, 114.5, 113.3, 109.5, 98.0, 56.7, 54.0, 35.0, 32.3, 32.1, 28.5, 9.0. HR-MS (ESI-QTOF): m/z $[\text{M}+\text{H}]^+$ calcd for $\text{C}_{54}\text{H}_{54}\text{N}_3\text{OS}$, 792.3987; found, 792.3956.



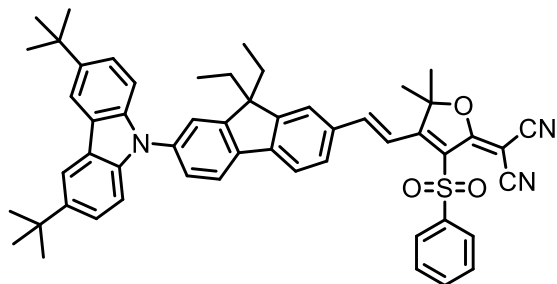
(E)-2-(3-cyano-4-(2-(7-(3,6-di-tert-butyl-9H-carbazol-9-yl)-9,9-diethyl-9H-fluoren-2-yl)vinyl)-5,5-dimethylfuran-2(5H)-ylidene)malononitrile (TCBZ2)

Red solid (42 mg, yield: 31 %) ^1H NMR (400 MHz, $\text{DMSO-}d_6$, ppm) δ 8.33 (s, 1H), 8.32 (s, 1H), 8.20 (d, $J = 8.0$ Hz, 1H), 8.14-7.98 (m, 4H), 7.76 (s, 1H), 7.64 (d, $J = 8.0$ Hz, 1H), 7.52 (d, $J = 8.0$ Hz, 2H), 7.41-7.31 (m, 3H), 2.27-2.12 (m, 4H), 1.86 (s, 6H), 1.44 (s, 18H), 0.35 (t, $J = 7.3$ Hz, 6H). ^{13}C NMR (101 MHz, $\text{DMSO-}d_6$, ppm) δ 177.7, 175.8, 153.0, 151.3, 148.6, 145.2, 143.1, 139.2, 139.0, 138.0, 134.1, 130.4, 126.0, 124.4, 123.4, 122.9, 121.8, 121.3, 117.2, 115.2, 113.3, 112.4, 111.5, 109.5, 99.8, 99.1, 56.8, 54.6, 35.0, 32.3, 32.1, 25.8, 9.0. HR-MS (ESI-QTOF): m/z $[\text{M}+\text{H}]^+$ calcd for $\text{C}_{49}\text{H}_{49}\text{N}_4\text{O}$, 709.3906; found, 709.3895.



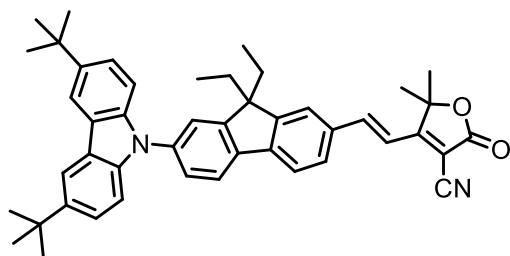
(E)-2-(3-(2-(7-(3,6-di-tert-butyl-9H-carbazol-9-yl)-9,9-diethyl-9H-fluoren-2-yl)vinyl)-5,5-dimethylcyclohex-2-en-1-ylidene)malononitrile (TCBZ3)

Yellow solid (66 mg, yield: 50%) ^1H NMR (400 MHz, $\text{DMSO-}d_6$, ppm) δ 8.31 (s, 2H), 8.12 (d, $J = 8.2$ Hz, 1H), 7.96 (d, $J = 8.2$ Hz, 1H), 7.93 (s, 1H), 7.73 (d, $J = 8.2$ Hz, 1H), 7.70 (s, 1H), 7.62-7.40 (m, 5H), 7.33 (d, $J = 8.8$ Hz, 2H), 6.94 (s, 1H), 2.65 (s, 2H), 2.61 (s, 2H), 2.21-2.08 (m, 4H), 1.43 (s, 18H), 1.05 (s, 6H), 0.34 (t, $J = 7.3$ Hz, 6H). ^{13}C NMR (101 MHz, $\text{DMSO-}d_6$, ppm) δ 170.7, 156.6, 152.5, 151.0, 143.0, 142.5, 139.8, 139.1, 138.8, 137.2, 135.8, 129.5, 128.7, 125.8, 124.3, 123.3, 123.0, 122.3, 122.2, 121.7, 121.0, 117.2, 113.7, 109.5, 76.4, 56.6, 55.4, 35.0, 32.3, 32.2, 27.9, 27.7, 25.4, 9.0. HR-MS (ESI-QTOF): m/z $[\text{M}+\text{H}]^+$ calcd for $\text{C}_{50}\text{H}_{54}\text{N}_3$, 696.4318; found, 696.4301.



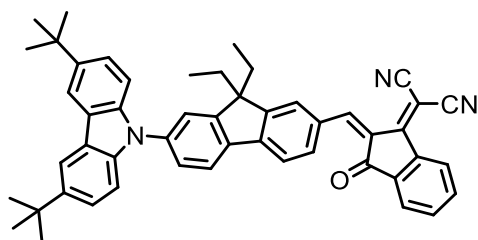
(E)-2-(4-(2-(7-(3,6-di-tert-butyl-9H-carbazol-9-yl)-9,9-diethyl-9H-fluoren-2-yl)vinyl)-5,5-dimethyl-3-(phenylsulfonyl)furan-2(5H)-ylidene)malononitrile (TCBZ4)

Red solid (60 mg, yield: 38%) ^1H NMR (400 MHz, $\text{DMSO-}d_6$, ppm) δ 8.32 (s, 1H), 8.31 (d, $J = 8.4$ Hz, 2H), 8.20 (d, $J = 8.0$ Hz, 1H), 8.15-8.05 (m, 3H), 8.03-7.87 (m, 3H), 7.86-7.68 (m, 4H), 7.65 (d, $J = 8.4$ Hz, 1H), 7.53 (d, $J = 8.8$ Hz, 2H), 7.35 (d, $J = 8.6$ Hz, 1H), 7.32 (d, $J = 8.6$ Hz, 1H), 3.02 (t, $J = 5.6$ Hz, 1H), 2.30-2.01 (m, 4H), 1.93 (s, 4H), 1.69-1.56 (m, 2H), 1.44 (s, 18H), 0.37 (t, $J = 7.3$ Hz, 6H). ^{13}C NMR (101 MHz, $\text{DMSO-}d_6$, ppm) δ 173.8, 170.8, 152.9, 151.6, 148.0, 145.9, 143.2, 140.0, 139.1, 138.7, 138.6, 134.5, 133.6, 129.7, 128.9, 127.7, 127.4, 125.8, 124.9, 123.8, 123.7, 123.6, 122.0, 121.4, 120.8, 116.4, 115.0, 113.3, 112.4, 109.1, 94.6, 56.7, 34.8, 32.7, 32.0, 27.9, 9.0. HR-MS (ESI-QTOF): m/z $[\text{M}+\text{H}]^+$ calcd for $\text{C}_{54}\text{H}_{54}\text{N}_3\text{O}_3\text{S}$, 824.3886; found, 824.3880.



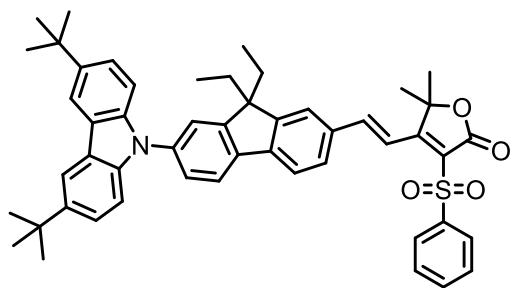
(E)-4-(2-(7-(3,6-di-tert-butyl-9H-carbazol-9-yl)-9,9-diethyl-9H-fluoren-2-yl)vinyl)-5,5-dimethyl-2-oxo-2,5-dihydrofuran-3-carbonitrile (TCBZ5)

Red solid (65 mg, yield 52%) ^1H NMR (400 MHz, $\text{DMSO-}d_6$, ppm) δ 8.32 (s, 2H), 8.18 (d, $J = 8.0$ Hz, 1H), 8.10-7.91 (m, 4H), 7.74 (s, 1H), 7.62 (d, $J = 8.4$ Hz, 1H), 7.52 (d, $J = 8.6$ Hz, 2H), 7.38-7.30 (m, 3H), 2.27-2.12 (m, 4H), 1.73 (s, 6H), 1.43 (s, 18H), 0.34 (t, $J = 7.3$ Hz, 6H). ^{13}C NMR (101 MHz, $\text{DMSO-}d_6$, ppm) δ 177.6, 166.9, 152.8, 151.2, 146.4, 144.4, 143.1, 139.4, 139.1, 137.8, 134.1, 129.7, 125.9, 124.3, 123.8, 123.4, 122.7, 121.8, 121.2, 177.2, 115.5, 113.4, 109.5, 97.2, 88.3, 56.8, 35.0, 32.3, 32.1, 25.8, 9.0. HR-MS (ESI-QTOF): m/z $[\text{M}+\text{H}]^+$ calcd for $\text{C}_{46}\text{H}_{49}\text{N}_2\text{O}_2$, 661.3794; found, 661.3767.



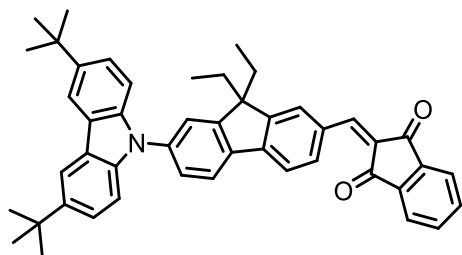
(Z)-2-(2-((7-(3,6-di-tert-butyl-9H-carbazol-9-yl)-9,9-diethyl-9H-fluoren-2-yl)methylene)-3-oxo-2,3-dihydro-1H-inden-1-ylidene)malononitrile (TCBZ6)

Red solid (92 mg, yield: 69%) ^1H NMR (400 MHz, $\text{DMSO-}d_6$, ppm) δ 8.77 (d, $J = 8.2$ Hz, 1H), 8.76 (s, 1H), 8.46 (s, 1H), 8.24-8.18 (m, 3H), 8.05-7.99 (m, 2H), 7.91 (d, $J = 8.2$ Hz, 1H), 7.89-7.79 (m, 2H), 7.67-7.61 (m, 2H), 7.53 (d, $J = 8.6$ Hz, 2H), 7.44 (d, $J = 8.6$ Hz, 2H), 2.30-2.07 (m, 4H), 1.57 (s, 6H), 1.51 (s, 18H), 0.53 (t, $J = 7.3$ Hz, 6H). ^{13}C NMR (101 MHz, $\text{DMSO-}d_6$, ppm) δ 186.5, 162.3, 153.7, 150.4, 148.5, 146.8, 143.2, 139.7, 139.1, 138.9, 138.7, 137.5, 135.5, 134.9, 131.6, 128.8 (2C), 125.7, 125.3, 124.4, 123.8, 123.6, 122.3, 121.4, 119.7, 116.4, 114.3, 114.1, 109.2, 71.8, 56.7, 34.8, 32.6, 32.0, 8.7. HR-MS (ESI-QTOF): m/z $[\text{M}+\text{H}]^+$ calcd for $\text{C}_{50}\text{H}_{44}\text{N}_3\text{O}$, 704.3641; found, 704.3629.



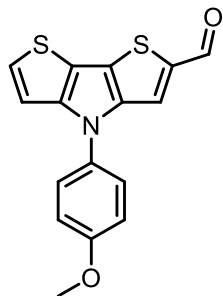
(*E*)-4-(2-(7-(3,6-di-*tert*-butyl-9*H*-carbazol-9-yl)-9,9-diethyl-9*H*-fluoren-2-yl)vinyl)-5,5-dimethyl-3-(phenylsulfonyl)furan-2(5*H*)-one (TCBZ7)

Red solid (80 mg, yield: 54%) ^1H NMR (400 MHz, $\text{DMSO-}d_6$, ppm) δ 8.33 (s, 2H), 8.28-8.05 (m, 5H), 7.95 (s, 1H), 7.94 (s, 1H), 7.89-7.60 (m, 6H), 7.53 (d, $J = 8.8$ Hz, 2H), 7.35 (d, $J = 8.8$ Hz, 2H), 2.31-2.05 (m, 4H), 1.77 (s, 6H), 1.43 (s, 18H), 0.38 (t, $J = 7.3$ Hz, 6H). ^{13}C NMR (101 MHz, $\text{DMSO-}d_6$, ppm) δ 172.3, 164.7, 152.8, 151.1, 146.8, 144.3, 143.1, 140.0, 139.3, 139.1, 137.8, 134.9, 134.8, 130.0, 128.4, 128.2, 126.0, 124.4, 124.3, 123.4, 122.7, 122.0, 121.8, 121.3, 117.7, 117.2, 109.5, 86.2, 56.7, 35.0, 32.3, 32.1, 27.0, 9.0. HR-MS (ESI-QTOF): m/z $[\text{M}+\text{H}]^+$ calcd for $\text{C}_{51}\text{H}_{54}\text{NO}_4\text{S}$, 776.3774; found, 776.3751.



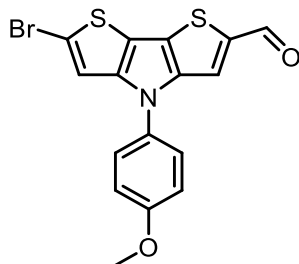
2-((7-(3,6-di-*tert*-butyl-9*H*-carbazol-9-yl)-9,9-diethyl-9*H*-fluoren-2-yl)methylene)-1*H*-indene-1,3(2*H*)-dione (TCBZ8)

Orange solid (87 mg, yield: 70%) ^1H NMR (400 MHz, CDCl_3 , ppm) δ 8.80 (s, 1H), 8.20 (d, $J = 8.2$ Hz, 1H), 8.20 (s, 2H), 8.11-7.98 (m, 4H), 7.93 (d, $J = 8.2$ Hz, 1H), 7.90-7.80 (m, 2H), 7.66-7.60 (m, 2H), 7.53 (d, $J = 8.6$ Hz, 2H), 7.44 (d, $J = 8.6$ Hz, 2H), 2.37-2.05 (m, 4H), 1.51 (s, 18H), 0.52 (t, $J = 7.3$ Hz, 6H). ^{13}C NMR (101 MHz, CDCl_3 , ppm) δ 190.7, 189.4, 153.6, 150.7, 147.6, 146.3, 143.1, 142.6, 140.1, 139.2, 138.9, 138.6, 135.3, 135.1, 134.9, 132.4, 128.7, 128.2, 125.7, 123.8, 123.5, 123.3, 122.1, 121.5, 120.0, 116.4, 109.2, 56.6, 34.8, 32.7, 32.0, 8.7. HR-MS (ESI-QTOF): m/z $[\text{M}+\text{H}]^+$ calcd for $\text{C}_{47}\text{H}_{45}\text{NO}_2$, 656.3529; found, 656.3512.



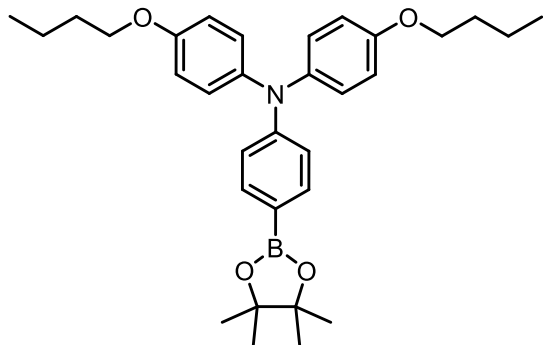
4-(4-methoxyphenyl)-4H-dithieno[3,2-b:2',3'-d]pyrrole-2-carbaldehyde (**8**)

To a solution of **7** (0.50 g, 1.75 mmol) in anhydrous DCM (20 mL) was added anhydrous DMF (280 μ L, 3.60 mmol) under argon atmosphere. After cooling down to 0°C using an ice-bath, POCl₃ (500 μ L, 5.10 mmol) was added dropwise to the mixture. After stirring at 0°C for 1h then at room temperature overnight, the reaction was quenched with 1M NaOH (5 mL). The organic phase was separated and washed with water and brine, then was dried over MgSO₄ and evaporated under reduced pressure. Followed column chromatography on silica gel with DCM as eluent to afford **8** as a yellowish solid (360 mg, yield: 66%). ¹H NMR (400 MHz, CDCl₃, ppm) δ 9.88 (s, 1H), 7.73 (s, 1H), 7.50 (d, *J* = 8.8 Hz, 2H), 7.42 (d, *J* = 5.4 Hz, 1H), 7.15-7.04 (m, 3H), 3.92 (s, 3H). ¹³C NMR (101 MHz, CDCl₃, ppm) δ 183.0, 158.6, 148.6, 144.0, 140.6, 131.8, 128.8, 124.7, 124.4, 120.6, 116.3, 115.2, 111.9, 55.7. HR-MS (ESI-QTOF) *m/z*: [M+H]⁺ Calcd for C₁₆H₁₂NO₂S₂, 314.0309; found, 314.0296.



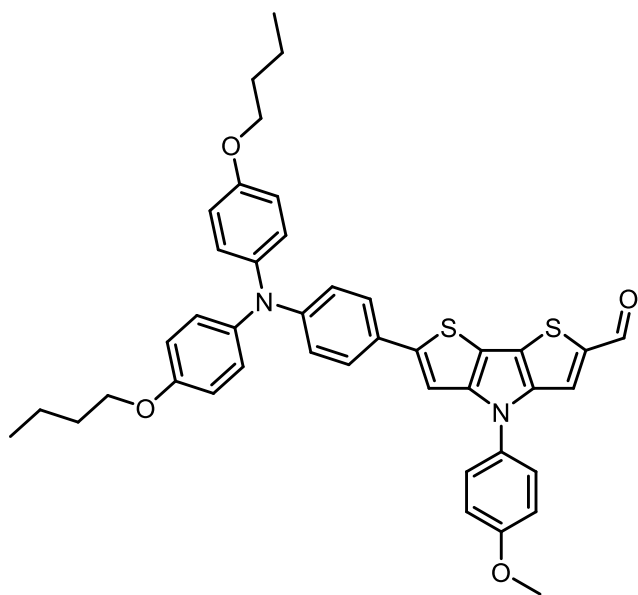
6-bromo-4-(4-methoxyphenyl)-4H-dithieno[3,2-b:2',3'-d]pyrrole-2-carbaldehyde (**9**)

To a solution of **8** (170 mg, 0.54 mmol) in THF (10 mL) was added NBS (103 mg, 0.58 mmol) at 0°C. The mixture was then stirred at room temperature for 3h. DCM and water were added to the mixture, followed by extraction of the aqueous phase separated using DCM. The combined organic phases were washed with saturated Na₂CO₃ and water. Finally, evaporation under reduced pressure gave **9** as an off-white solid (200 mg, yield: 94%). ¹H NMR (400 MHz, DMSO-*d*₆, ppm) δ 9.88 (s, 1H), 8.10 (s, 1H), 7.61 (d, *J* = 8.9 Hz, 2H), 7.47 (s, 1H), 7.16 (d, *J* = 8.9 Hz, 2H), 3.86 (s, 3H). ¹³C NMR (101 MHz, DMSO-*d*₆, ppm) δ 185.0, 158.7, 145.7, 142.7, 141.2, 131.1, 125.2, 123.6, 123.1, 116.6, 116.3, 116.2, 115.7, 56.0. HR-MS (ESI-QTOF) *m/z*: [M+H]⁺ Calcd for C₁₆H₁₁BrNO₂S₂, 391.9415; found, 391.9409.



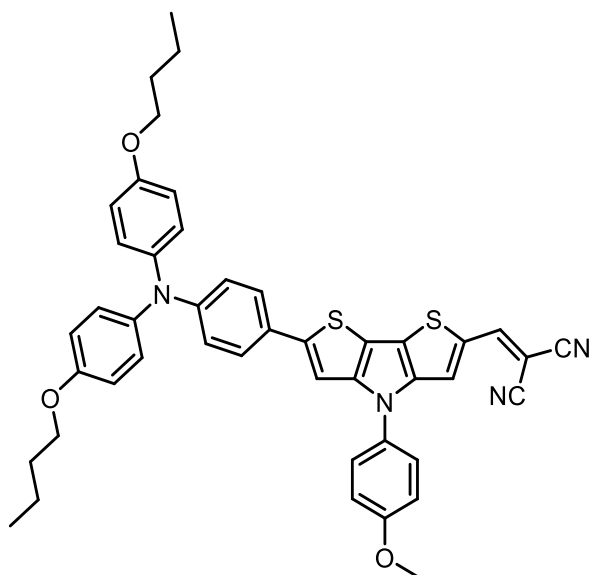
4-butoxy-N-(4-butoxyphenyl)-N-(4-(4,4,5,5-tetramethyl-1,3-dioxolan-2-yl)phenyl)aniline (11)

Under argon atmosphere, to a solution of **10** (1.00 g, 2.13 mmol) in anhydrous THF (10 mL) was added n-BuLi (2.3 mmol, 2.5 M in hexane) dropwise at -78°C . After stirring for 1h, bis(pinacolato)diboron (0.80 g, 4.26 mmol) was added and the mixture was allowed to warm up to room temperature. After stirring for 12h, water was added to quench the reaction. Ethyl acetate (15 mL \times 3) was used to extract the product from the aqueous phase. The combined organic phases were dried over MgSO_4 , and evaporated under reduced pressure. Further purification by column chromatography on silica (eluent: DCM:Hexane=2:1, v/v) afforded **11** as a pale violet solid (690 mg, yield: 63%). ^1H NMR (400 MHz, CDCl_3 , ppm) δ 7.62 (d, $J = 8.5$ Hz, 2H), 7.07 (d, $J = 8.9$ Hz, 4H), 6.89 (d, $J = 8.5$ Hz, 2H), 6.84 (d, $J = 8.9$ Hz, 4H), 3.96 (t, $J = 6.5$ Hz, 4H), 1.79 (m, 4H), 1.58-1.46 (m, 4H), 1.34 (s, 12H), 1.01 (t, $J = 7.4$ Hz, 6H). ^{13}C NMR (101 MHz, CDCl_3 , ppm): δ 151.1, 146.7, 135.5, 131.0, 122.4, 114.6, 113.8, 110.5, 78.6, 63.2, 26.7, 20.1, 14.5, 9.2. HR-MS (ESI-QTOF) m/z: $[\text{M}+\text{H}]^+$ Calcd for $\text{C}_{32}\text{H}_{43}\text{BNO}_4$, 516.3285; found, 582.3272.



6-(4-(bis(4-butoxyphenyl)amino)phenyl)-4-(4-methoxyphenyl)-4H-dithieno[3,2-b:2',3'-d]pyrrole-2-carbaldehyde (12**)**

To the solution of **9** (900 mg, 2.29 mmol) and **11** (1.42 g, 2.75 mmol) in THF (50 mL) were added Pd(PPh₃)₄ (132 mg, 0.12 mmol) and 1M NaCO₃ (15 mL) under argon atmosphere. After refluxing overnight, the mixture was allowed to cool down to room temperature and was diluted with DCM (20 mL). Filtration on celite was performed to remove the undissolved catalysts then, the organic phase was washed with water (150 mL×3). The combined organic phases were dried over MgSO₄ and evaporated under reduced pressure. The crude product was purified by column chromatography on silica (eluent: H₂Cl₂:EA=10:1, v/v) to afford **12** as an orange solid (960 mg, yield: 60 %). ¹H NMR (400 MHz, CDCl₃, ppm) δ 9.85 (s, 1H), 7.69 (s, 1H), 7.52 (d, *J* = 8.9 Hz, 2H), 7.44 (d, *J* = 8.7 Hz, 2H), 7.12 (m, 7H), 6.93 (d, *J* = 8.7 Hz, 2H), 6.86 (d, *J* = 8.9 Hz, 4H), 3.97 (t, *J* = 6.5 Hz, 4H), 3.93 (s, 3H), 1.86-1.72 (m, 4H), 1.60-1.43 (m, 4H), 1.01 (t, *J* = 7.4 Hz, 6H). ¹³C NMR (101 MHz, CDCl₃, ppm) δ 182.7, 158.6, 155.9, 149.2, 149.1, 148.5, 143.4, 140.1, 139.9, 131.8, 126.9, 126.4, 126.2, 125.0, 124.8, 120.2, 119.9, 115.4, 115.2, 114.4, 105.8, 68.0, 55.7, 31.4, 19.3, 13.9. HR-MS (ESI-QTOF) *m/z*: [M]⁺ Calcd for C₄₂H₄₁N₂O₄S₂, 701.2508; found, 701.2424.



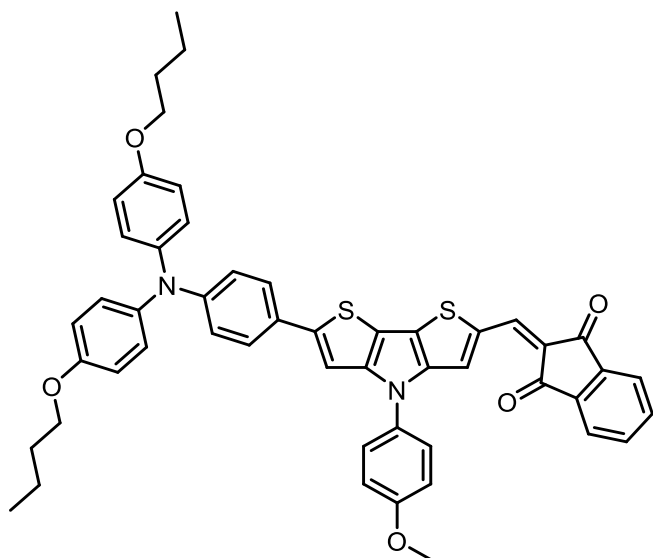
2-((6-(4-(bis(4-butoxyphenyl)amino)phenyl)-4-(4-methoxyphenyl)-4H-dithieno[3,2-b:2',3'-d]pyrrol-2-yl)methylene)malononitrile (EBTN1**)**

In a 25 mL round-bottom flask, **12** (100 mg, 0.14 mmol) and malononitrile (17 mg, 0.28 mmol) were dissolved in DMF (5 mL). After stirring at 100°C for 30 min, the mixture was evaporated under reduced pressure. Further purification by column chromatography on silica (eluent: DCM:PE=3:1, v/v) afforded **EBTN1** as a black solid (100 mg, yield: 93 %). ¹H NMR (400 MHz, CDCl₃, ppm) δ 7.67 (s, 1H), 7.62 (s, 1H), 7.47 (d, *J* = 8.9 Hz, 2H), 7.43 (d, *J* = 8.8 Hz, 2H), 7.17-7.06 (m, 7H), 6.92 (d, *J* = 8.8 Hz, 2H), 6.87 (d,

$J = 8.9$ Hz, 4H), 3.97 (t, $J = 6.5$ Hz, 4H), 3.92 (s, 3H), 1.85-1.74 (m, 4H), 1.53 (m, 4H), 1.01 (t, $J = 7.4$ Hz, 6H). ^{13}C NMR (101 MHz, CDCl_3 , ppm) δ 158.9, 156.1, 151.5, 151.4, 150.4, 149.6, 144.4, 139.8, 132.0, 131.1, 128.1, 127.1, 126.6, 125.5, 124.9, 119.5, 115.5, 115.4 (2C), 114.9, 114.4, 105.5, 71.0, 68.0, 55.7, 31.4, 19.3, 13.9. HR-MS (ESI-QTOF) m/z : $[\text{M}]^+$ Calcd for $\text{C}_{45}\text{H}_{40}\text{N}_4\text{O}_3\text{S}_2$, 748.2542; found, 748.2524.

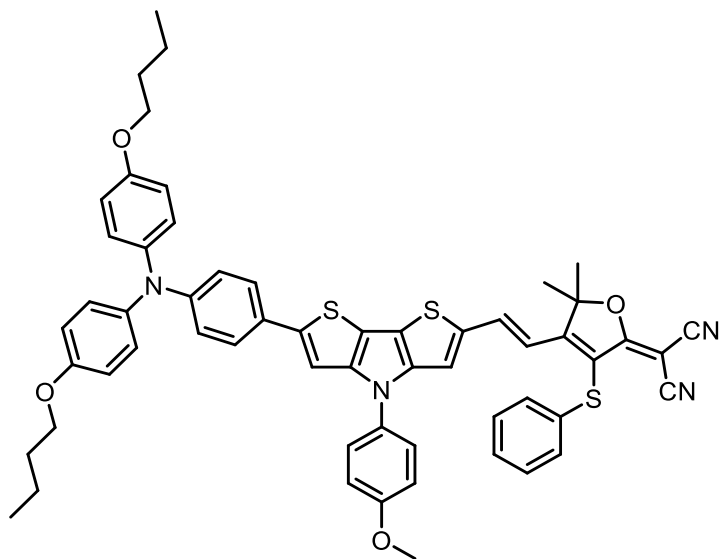
General procedure for Knoevenagel condensation. Synthesis of EBTN2-EBTN5.

In 10 mL microwave tubes, **12** (100 mg, 0.14 mmol) and the corresponding acceptors **h**, **a**, **d** and **b** (0.28 mmol) were dissolved in anhydrous DMF (5 mL), followed by addition of one drop of piperidine. The tubes were sealed and heated at 130°C by microwave irradiation. After cooling down to room temperature, the mixtures were transferred into round-bottom flasks and evaporated under reduced pressure. Then the crude products obtained were purified by column chromatography on silica.



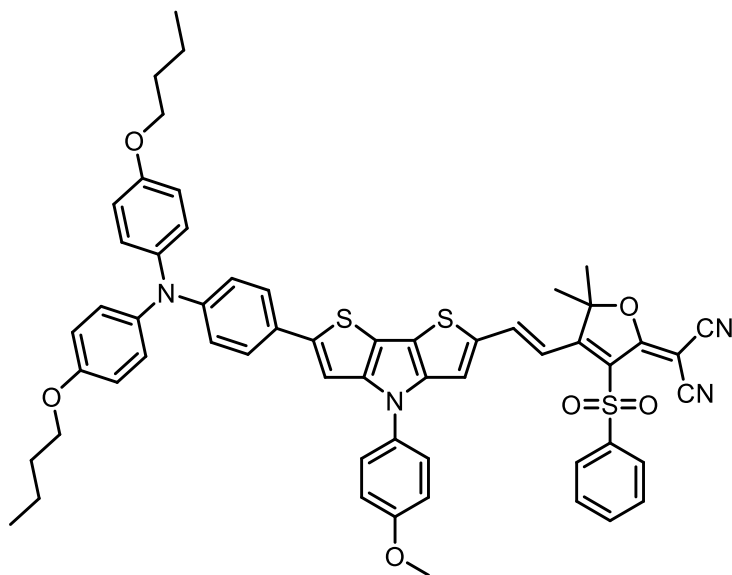
2-((6-(4-(bis(4-butoxyphenyl)amino)phenyl)-4-(4-methoxyphenyl)-4H-dithieno[3,2-b:2',3'-d]pyrrol-2-yl)methylene)-1H-indene-1,3(2H)-dione (EBTN2)

Black solid (66 mg, yield: 57 %), eluent DCM:PE=3:1, v/v. ^1H NMR (400 MHz, CD_2Cl_2 , ppm): δ 8.26 (s, 1H), 7.91 (m, 3H), 7.72 (m, 2H), 7.54 (d, $J = 8.7$ Hz, 2H), 7.43 (d, $J = 8.7$ Hz, 2H), 7.14 (m, 3H), 7.09 (d, $J = 8.9$ Hz, 4H), 6.92 (d, $J = 8.7$ Hz, 2H), 6.86 (d, $J = 8.9$ Hz, 4H), 3.97 (t, $J = 6.5$ Hz, 4H), 3.92 (s, 3H), 1.87-1.72 (m, 4H), 1.52 (m, 4H), 1.01 (t, $J = 7.4$ Hz, 6H). ^{13}C NMR (101 MHz, CDCl_3 , ppm): δ 190.8, 189.7, 158.6, 156.0, 150.9, 150.5, 149.3, 142.0, 140.3, 139.9, 137.4, 135.5, 134.4, 134.1, 131.7, 127.0, 126.5, 126.0, 124.7, 122.5, 122.4, 119.6, 115.4, 115.3, 114.8, 105.6, 68.0, 55.7, 31.4, 19.3, 13.9. HR-MS (ESI-QTOF): m/z $[\text{M}]^+$ calcd for $\text{C}_{51}\text{H}_{44}\text{N}_2\text{O}_5\text{S}_2$, 828.2692; found, 828.2688.



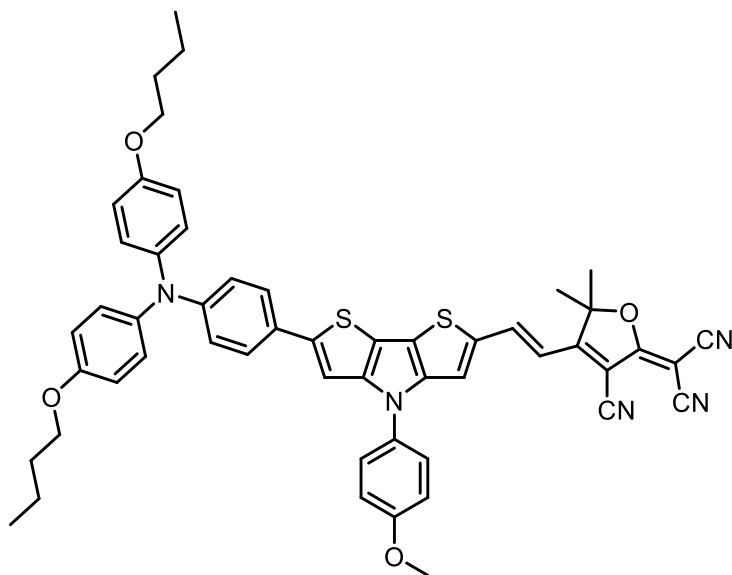
(*E*)-2-(4-(2-(6-(4-(bis(4-butoxyphenyl)amino)phenyl)-4-(4-methoxyphenyl)-4*H*-dithieno[3,2-*b*:2',3'-*d*]pyrrol-2-yl)vinyl)-5,5-dimethyl-3-(phenylthio)furan-2(5*H*)-ylidene)malononitrile (EBTN3)

Black solid (73 mg, 53%), eluent DCM. ^1H NMR (400 MHz, CDCl_3 , ppm) δ 7.53-7.45 (m, 3H), 7.42 (d, $J = 8.7$ Hz, 2H), 7.39-7.31 (m, 2H), 7.28-7.22 (m, 4H), 7.15-6.99 (m, 7H), 7.03 (d, $J = 16.2$ Hz, 1H), 6.92 (d, $J = 8.7$ Hz, 2H), 6.86 (d, $J = 8.9$ Hz, 4H), 3.97 (t, $J = 6.5$ Hz, 4H), 3.92 (s, 3H), 1.81 (s, 6H), 1.80-1.72 (m, 4H), 1.52 (m, 4H), 1.01 (t, $J = 7.4$ Hz, 6H). ^{13}C NMR (101 MHz, CDCl_3 , ppm) δ 180.5, 170.1, 158.6, 155.9, 149.1, 148.6, 147.9, 144.5, 140.0, 138.3, 136.7, 134.5, 131.7, 129.6, 127.8, 127.0, 126.9, 126.3, 126.2, 124.8, 122.0, 120.0, 116.8, 116.3, 115.4, 115.2, 114.8, 114.1, 113.0, 112.8, 105.8, 95.1, 68.0, 56.0, 55.1, 31.4, 27.0, 19.3, 14.0. HR-MS (ESI-QTOF): m/z $[\text{M}]^+$ calcd for $\text{C}_{58}\text{H}_{52}\text{N}_4\text{O}_4\text{S}_3$, 964.3145; found, 964.3151.



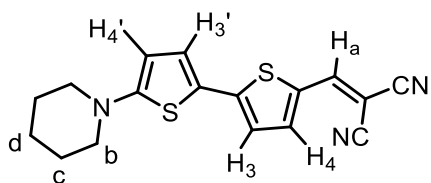
(E)-2-(4-(2-(6-(4-(bis(4-butoxyphenyl)amino)phenyl)-4-(4-methoxyphenyl)-4H-dithieno[3,2-b:2',3'-d]pyrrol-2-yl)vinyl)-5,5-dimethyl-3-(phenylsulfonyl)furan-2(5H)-ylidene)malononitrile (EBTN4)

Black solid (64 mg, 45%), eluent DCM. ¹H NMR (400 MHz, CDCl₃, ppm) δ 8.12-7.98 (m, 2H), 8.03 (d, *J* = 15.8 Hz, 1H), 7.65 (m, 3H), 7.51 (m, 3H), 7.43 (d, *J* = 8.8 Hz, 2H), 7.37 (s, 1H), 7.10 (m, 7H), 6.92 (d, *J* = 8.8 Hz, 2H), 6.87 (d, *J* = 9.0 Hz, 4H), 3.97 (t, *J* = 6.5 Hz, 4H), 3.92 (s, 3H), 1.89-1.72 (m, 10H), 1.52 (m, 4H), 1.01 (t, *J* = 7.4 Hz, 6H). ¹³C NMR (101 MHz, CDCl₃, ppm) δ 174.0, 169.7, 158.9, 156.1, 150.6, 150.6, 149.5, 145.5, 141.1, 140.8, 139.8, 138.5, 134.0, 131.3, 129.6, 127.6, 127.1, 126.5, 125.7, 125.6, 125.0, 120.7, 119.5, 115.4, 115.3, 115.2, 114.3, 113.3, 111.0, 105.5, 93.5, 68.0, 56.5, 55.7, 31.4, 27.9, 25.6, 19.3, 13.9. HR-MS (ESI-QTOF) *m/z*: [M]⁺ Calcd for C₅₈H₅₂N₄O₆S₃, 996.3043; found, 996.3061.



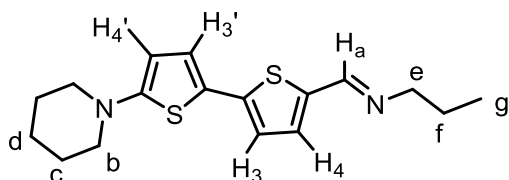
(E)-2-(4-(2-(6-(4-(bis(4-butoxyphenyl)amino)phenyl)-4-(4-methoxyphenyl)-4H-dithieno[3,2-b:2',3'-d]pyrrol-2-yl)vinyl)-3-cyano-5,5-dimethylfuran-2(5H)-ylidene)malononitrile (EBTN5)

Black solid (63 mg, 50%), eluent DCM ¹H NMR (400 MHz, CDCl₃, ppm) δ 8.17 (d, *J* = 15.6 Hz, 1H), 7.90 (s, 1H), 7.61 (d, *J* = 8.7 Hz, 2H), 7.56 (d, *J* = 8.2 Hz, 2H), 7.44 (s, 1H), 7.04 (m, d, *J* = 8.7 Hz, 4H), 6.92 (d, *J* = 8.7 Hz, 4H), 6.74 (d, *J* = 8.4 Hz, 1H), 6.64 (d, *J* = 15.6 Hz, 1H), 3.95 (t, *J* = 6.5 Hz, 4H), 3.86 (s, 3H), 1.76 (s, 6H), 1.72-1.61 (m, 4H), 1.53-1.37 (m, 4H), 0.94 (t, *J* = 7.4 Hz, 6H). ¹³C NMR (101 MHz, CDCl₃, ppm) δ 176.2, 172.3, 158.9, 156.1, 151.0, 150.9, 149.6, 145.5, 141.2, 139.7, 137.4, 131.1, 127.1, 126.5, 125.9, 125.5, 124.9, 119.4, 115.4, 115.3, 115.1, 112.7, 111.9 (2C) 109.2, 105.5, 96.6, 93.2, 68.0, 55.7, 55.4, 31.4, 26.5, 19.3, 13.9. HR-MS (ESI-QTOF) *m/z*: [M]⁺ Calcd for C₅₃H₄₇N₄O₆S₂, 881.3064; found, 881.3058.



2-((5'-(piperidin-1-yl)-[2,2'-bithiophen]-5-yl)methylene)malononitrile (PTTCN)

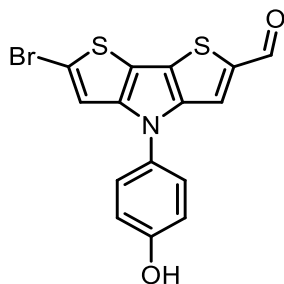
In a 5 mL microwave tube, **PTTAld** (300 mg, 1.08 mmol) and malononitrile (65 mg, 0.98 mmol) were dissolved in anhydrous EtOH (2 mL), followed by addition of one drop of piperidine. The tube was sealed and heated at 100°C by microwave irradiation for 1h. After cooling down to room temperature, the solid was filtrated and purified by column chromatography on silica (eluent: DCM/PE = 1.5/1, v/v) to afford a dark purple solid (244 mg, yield: 69%). ¹H NMR (400 MHz, DMSO-*d*₆, ppm) δ 8.39 (s, 1H, H_a), 7.76 (d, ³J = 4.3 Hz, 1H, H₄), 7.49 (d, ³J = 4.3 Hz, 1H, H₃'), 7.27 (d, ³J = 4.3 Hz, 1H, H₃), 6.25 (d, ³J = 4.3 Hz, 1H, H₄'), 3.29 (m, 4H, H_b), 1.61 (m, 4H, H_c), 1.57 (m, 2H, H_d). ¹³C NMR (101 MHz, DMSO-*d*₆, ppm) δ 162.7 (C₅'), 151.2 (C₂), 143.4 (C₄), 130.7 (C₃'), 121.2 (C₃), 129.6 (C₅), 117.2 (C₂'), 114.2 (C≡N), 115.4 (C≡N), 105.3 (C₄'), 68.4 (C^{IV}(CN)₂), 50.6 (C_b), 24.3 (C_c), 22.8 (C_d). HR-MS (ESI-QTOF) m/z: [M+H]⁺ calcd for C₁₇H₁₆N₃S₂, 326.0786; found, 326.0770.



(E)-1-(5'-(piperidin-1-yl)-[2,2'-bithiophen]-5-yl)-N-propylmethanimine (PTT-imine)

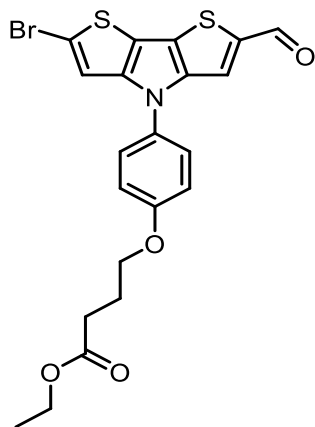
In a 5 mL microwave tube, bithiophene aldehyde (50 mg, 0.18 mmol) was dissolved in 2 mL DCM, propylamine (12 mg, 0.20 mmol), piperidine (8 mg, 0.09 mmol) and 4Å molecular sieves were added. The tube was sealed and stir at 60°C for 2h. Then the MS was filtered off, followed by evaporation under reduced pressure and vacuum to remove solvent and excess propylamine. A yellow solid was obtained, sufficiently pure to be used without further purification. (57 mg, yield: 99%). ¹H NMR (400 MHz, DMSO-*d*₆, ppm) δ 8.22 (s, 1H, H_a), 7.29 (d, J = 3.8 Hz, 1H, H₄), 7.06 (d, J = 4.0 Hz, 1H, H₃'), 6.98 (d, J = 3.8 Hz, 1H, H₃), 6.09 (d, J = 4.0 Hz, 1H, H₄'), 3.45 (t, J = 6.7 Hz, 2H, H_e), 3.14 (m, 4H, H_b), 1.61 (m, 4H, H_c), 1.58 (m, 2H, H_f), 1.53 (m, 2H, H_d), 0.89 (t, J = 6.7 Hz, 3H, H_g). ¹³C NMR (101 MHz, DMSO-*d*₆, ppm) δ 159.5 (C₅'), 154.1 (C_a), 140.8 (C₂), 138.4 (C₃), 132.1 (C₄), 125.3 (C₃'), 120.6 (C₃), 120.5 (C₂'), 104.7 (C₄'), 61.8 (C_e),

51.4 (C_b), 24.6 (C_c), 23.7 (C_f), 23.2 (C_d), 11.5 (C_g). HR-MS (ESI-QTOF) m/z: [M+H]⁺ calcd for C₁₇H₂₂N₂S₂, 319,1297; found, 319,1295.



6-bromo-4-(4-hydroxyphenyl)-4H-dithieno[3,2-b:2',3'-d]pyrrole-2-carbaldehyde (**13**)

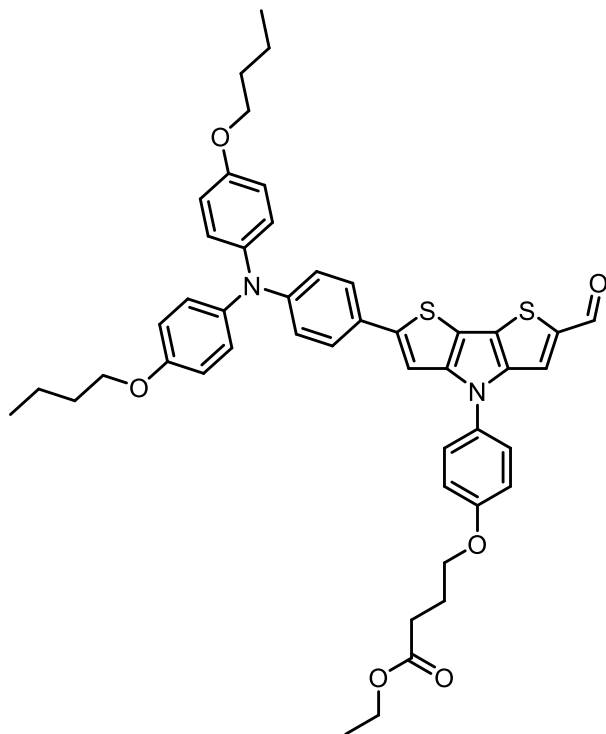
Under argon atmosphere, BBr₃ (10.2 mmol) was added dropwise to a solution of **9** (1.0 g, 2.55 mmol) in anhydrous DCM (200 mL) at 0°C. After stirring at room temperature for 6h, water (10 mL) was added to quench the reaction. Then the mixture was filtered. The filtrate was separated. The solid was washed with 1M HCl (250 mL) and extracted by DCM. Evaporation of the collected organic solvents, and purification of the crude by column chromatography on silica (eluent: DCM:EA=10:1, v/v) gave compound **13** as a yellow solid (895 mg, yield: 93%). ¹H NMR (400 MHz, DMSO-*d*₆, ppm) δ 9.88 (s, 1H), 9.83 (s, 1H), 8.11 (s, 1H), 7.49 (d, *J* = 8.8 Hz, 2H), 7.46 (s, 1H), 6.98 (d, *J* = 8.8 Hz, 2H). ¹³C NMR (101 MHz, DMSO-*d*₆, ppm) δ 185.0, 157.2, 145.8, 142.8, 141.2, 129.6, 125.2, 123.4, 116.9, 116.3, 116.2, 116.2. HR-MS (ESI-QTOF) m/z: [M+H]⁺ Calcd for C₁₅H₉BrNO₂S₂, 377.9258; found, 377.9252.



Ethyl 4-(4-(2-bromo-6-formyl-4H-dithieno[3,2-b:2',3'-d]pyrrol-4-yl)phenoxy)butanoate (**14**)

To a mixture of **13** (960 mg, 2.55 mmol) and K₂CO₃ (1.1 g, 7.65 mmol) in DMF (250 mL) was added dropwise ethyl 4-bromobutyrate (0.60 g, 3.06 mmol). The mixture was stirred overnight at 60°C. Evaporation under reduced pressure to remove most of the solvent, then the mixture was washed with water and extracted by EA. The organic phases were dried over MgSO₄, filtered, and evaporated under reduced

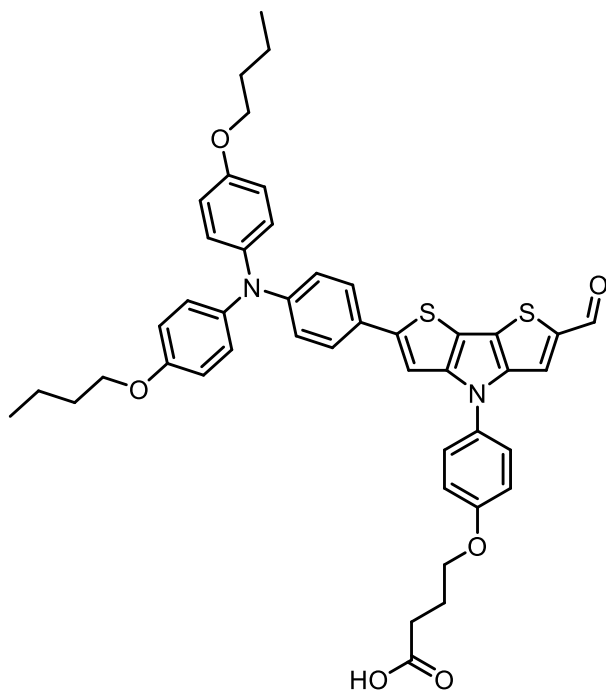
pressure to afford the crude product. Further purification by column chromatography on silica gel using DCM as eluent gave **14** as a yellow solid (1.20 g, yield: 96 %). ¹H NMR (400 MHz, CDCl₃, ppm) δ 9.87 (s, 1H), 7.69 (s, 1H), 7.44 (d, *J* = 8.9 Hz, 2H), 7.15 (s, 1H), 7.08 (d, *J* = 8.9 Hz, 2H), 4.20 (q, *J* = 7.1 Hz, 2H), 4.12 (t, *J* = 6.1 Hz, 2H), 2.58 (t, *J* = 7.2 Hz, 2H), 2.27 – 2.13 (m, 2H), 1.31 (t, *J* = 7.1 Hz, 3H). ¹³C NMR (101 MHz, CDCl₃, ppm) δ 183.0, 173.1, 158.1, 146.1, 143.0, 140.9, 131.3, 124.8, 124.0, 120.4, 116.2, 115.8, 115.2, 67.3, 60.6, 30.7, 24.6, 14.3. HR-MS (ESI-QTOF) *m/z*: [M+H]⁺ Calcd for C₂₁H₁₉BrNO₄S₂, 491.9939; found, 491.9929.



Ethyl 4-(4-(2-(4-(bis(4-butoxyphenyl)amino)phenyl)-6-formyl-4H-dithieno[3,2-b:2',3'-d]pyrrol-4-yl)phenoxy)butanoate (15**)**

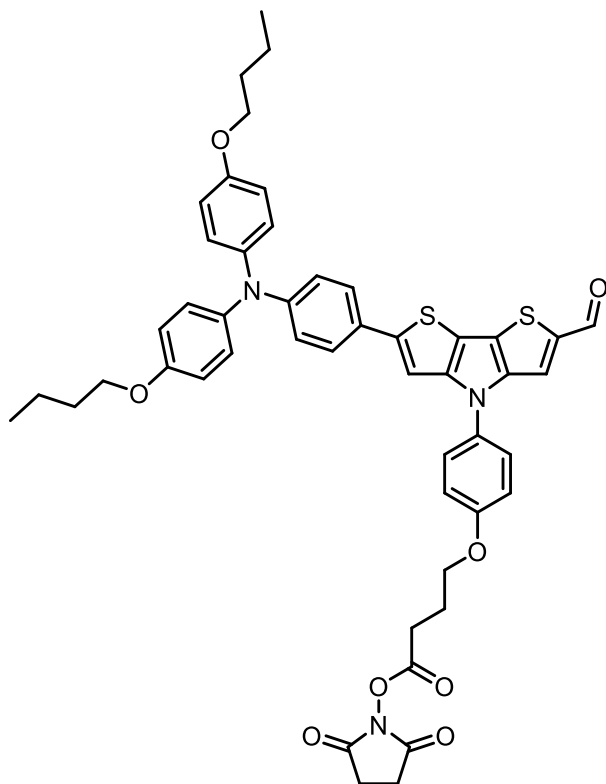
Under argon atmosphere, Pd(PPh₃)₄ (35 mg, 0.03 mmol) and 1M K₂CO₃ solution (0.2 mL) were added to a solution of **14** (38 mg, 0.07 mmol) and **5** (30 mg, 0.06 mmol) in THF (2 mL). The mixture was refluxed overnight. After cooling down to room temperature, DCM was added. Then the solution was filtered on celite to remove the Pd catalyst. The organic phase was washed three times with water then dried over MgSO₄. The solvent was evaporated under reduced pressure to give a crude solid which was purified by column chromatography on silica (eluent: DCM:PE=1:1, v/v). **15** was obtained as an orange solid (45 mg, yield: 76%). ¹H NMR (400 MHz, CDCl₃, ppm) δ 9.81 (s, 1H), 7.65 (s, 1H), 7.48 (d, *J* = 8.9 Hz, 2H), 7.42 (d, *J* = 8.8 Hz, 2H), 7.14 (s, 1H), 7.08 (d, *J* = 8.9 Hz, 6H), 6.92 (d, *J* = 8.8 Hz, 2H), 6.86 (d, *J* = 8.9 Hz, 4H), 4.20 (q, *J* = 7.1 Hz, 2H), 4.12 (t, *J* = 6.1 Hz, 2H), 3.97 (t, *J* = 6.5 Hz, 4H), 2.59 (t, *J* = 7.2 Hz, 2H), 2.28-

2.13 (m, 2H), 1.79 (m, 4H), 1.60-1.45 (m, 4H), 1.31 (t, $J = 7.1$ Hz, 3H), 1.01 (t, $J = 7.4$ Hz, 6H). ^{13}C NMR (101 MHz, CDCl_3 , ppm) δ 182.7, 173.1, 157.8, 155.9, 149.2, 149.1, 148.5, 143.3, 140.1, 139.9, 131.8, 126.9, 126.4, 126.2, 125.0, 124.8, 120.3, 119.8, 115.7, 115.4, 114.4, 105.8, 68.0, 67.2, 60.5, 31.4, 30.8, 24.6, 19.3, 14.3, 13.9. HR-MS (ESI-QTOF) m/z : $[\text{M}]^+$ Calcd for $\text{C}_{47}\text{H}_{48}\text{N}_2\text{O}_6\text{S}_2$, 800.2948; found, 800.2942.



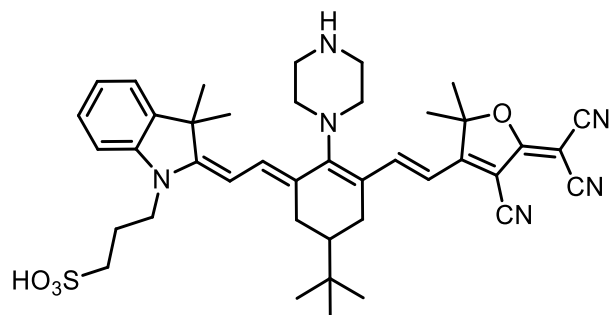
4-(4-(2-(4-(bis(4-butoxyphenyl)amino)phenyl)-6-formyl-4H-dithieno[3,2-b:2',3'-d]pyrrol-4-yl)phenoxy)butanoic acid (16)

In a 25 mL round-bottom flask, HCl (3 mL, 12M) was added to a solution of **15** (80 mg, 1.00 mmol) in THF (12 mL). After stirring at room temperature overnight, the mixture was extracted by DCM (50 mL \times 3). The organic phase was washed with water (100 mL), dried over MgSO_4 , filtered and evaporated under reduced pressure. The crude product was purified by column chromatography on silica (eluent: DCM:EA=2:3, v/v) to afford **16** as an orange solid (76 mg, yield: 97%). ^1H NMR (400 MHz, CDCl_3 , ppm) δ 9.83 (s, 1H), 7.67 (s, 1H), 7.48 (d, $J = 8.9$ Hz, 2H), 7.43 (d, $J = 8.8$ Hz, 2H), 7.15 (s, 1H), 7.08 (d, $J = 8.9$ Hz, 6H), 6.92 (d, $J = 8.9$ Hz, 2H), 6.86 (d, $J = 8.9$ Hz, 4H), 4.14 (t, $J = 6.0$ Hz, 2H), 3.97 (t, $J = 6.4$ Hz, 4H), 2.67 (t, $J = 7.2$ Hz, 2H), 2.22 (m, 2H), 1.79 (m, 4H), 1.52 (m, 4H), 1.01 (t, $J = 7.4$ Hz, 6H). ^{13}C NMR (101 MHz, CDCl_3 , ppm) δ 182.8, 177.3, 157.7, 155.9, 149.2, 149.1, 148.5, 143.3, 140.1, 139.9, 131.9, 126.9, 126.4, 126.1, 125.1, 124.2, 120.2, 119.8, 115.7, 115.4, 114.4, 105.8, 68.0, 67.0, 31.4, 30.2, 24.4, 19.3, 13.9. HR-MS (ESI-QTOF) m/z : $[\text{M}]^+$ Calcd for $\text{C}_{45}\text{H}_{44}\text{N}_2\text{O}_6\text{S}_2$, 772.2635; found, 772.2623.



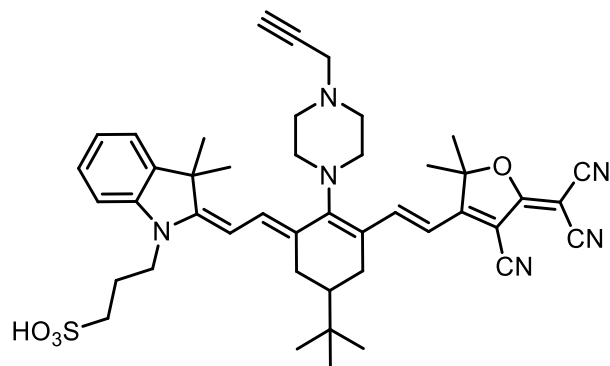
2,5-dioxopyrrolidin-1-yl-4-(4-(2-(4-(bis(4-butoxyphenyl)amino)phenyl)-6-formyl-4*H*-dithieno[3,2-*b*:2',3'-*d*]pyrrol-4-yl)phenoxy)butanoate (17)

Under argon atmosphere, *N*-hydroxysuccinimide (23 mg, 0.20 mmol) and EDC·HCl (38 mg, 0.20 mmol) were added into a solution of **16** (77 mg, 0.10 mmol) in anhydrous DMF (5 mL). After stirring at room temperature overnight, DCM was added. The mixture was washed with water, saturated NaHCO₃ then water, using DCM to extract. The organic phase was collected, dried over MgSO₄, filtered and evaporated under reduced pressure. Finally, the crude product was purified by column chromatography on silica (eluent: DCM:PE=1:1, v/v) to afford **17** as an orange solid (71 mg, yield: 82%). ¹H NMR (400 MHz, CDCl₃, ppm) δ 9.84 (s, 1H), 7.69 (s, 1H), 7.51 (d, *J* = 8.9 Hz, 2H), 7.44 (d, *J* = 8.8 Hz, 2H), 7.17 (s, 1H), 7.12 (d, *J* = 8.9 Hz, 2H), 7.09 (d, *J* = 9.0 Hz, 4H), 6.92 (d, *J* = 8.9 Hz, 2H), 6.86 (d, *J* = 9.0 Hz, 4H), 4.19 (t, *J* = 6.0 Hz, 2H), 3.97 (t, *J* = 6.4 Hz, 4H), 2.91 (m, 6H), 2.32 (m, 2H), 1.79 (m, 4H), 1.52 (m, 4H), 1.01 (t, *J* = 7.4 Hz, 6H). ¹³C NMR (101 MHz, CDCl₃, ppm) δ 182.7, 169.1, 168.3, 157.6, 155.9, 149.2, 149.1, 148.5, 143.3, 140.1, 139.9, 132.0, 126.9, 126.4, 126.2, 125.0, 124.8, 120.3, 119.9, 115.8, 115.3, 114.4, 105.8, 68.0, 66.4, 31.4, 27.8, 25.6, 24.4, 19.3, 13.9. HR-MS (ESI-QTOF) *m/z*: [M+H]⁺ Calcd for C₄₉H₄₈N₃O₈S₂, 870.2877; found, 870.2892.



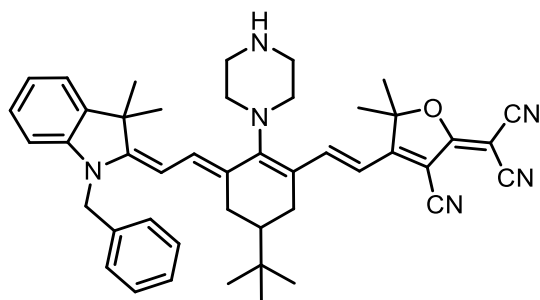
3-((*E*)-2-((*E*)-2-(5-(*tert*-butyl)-3-((*E*)-2-(4-cyano-5-(dicyanomethylene)-2,2-dimethyl-2,5-dihydrofuran-3-yl)vinyl)-2-(piperazin-1-ium-1-yl)cyclohex-2-en-1-ylidene)ethylidene)-3,3-dimethylindolin-1-yl)propane-1-sulfonate (COP-SO₃)

To a solution of **15** (150 mg 0.22 mmol) in EtOH (2 mL) was added a solution of piperazine (116.3 mg, 1.35mmol) in DMF (1 mL) under argon atmosphere. The mixture was stirred at room temperature overnight. Then the solvent was evaporated under reduced pressure, and the obtained crude product was purified by column chromatography on silica (eluent: MeCN:MeOH:H₂O=90:9:1, v/v/v) to afford **COP-SO₃** as a dark blue solid (130 mg, yield: 81%). ¹H NMR (400 MHz, DMSO-*d*₆, ppm) δ 7.91 (s, 1H), 7.65-7.52 (m, 2H), 7.47-7.34 (m, 2H), 7.21 (t, *J* = 7.4 Hz, 1H), 6.20 (d, *J* = 6.8 Hz, 1H), 5.83 (d, *J* = 6.8 Hz, 1H), 4.31 (t, *J* = 7.0 Hz, 2H), 3.88-3.64 (m, 4H), 3.28-3.06 (m, 4H), 2.75-2.65(m, 2H) 2.11-1.95 (m, 3H), 1.83 (t, *J* = 12.4 Hz, 1H), 1.63 (d, *J* = 6.8 Hz, 6H), 1.52 (d, *J* = 8.5 Hz, 6H), 1.39-1.21 (m, 2H), 0.99 (s, 9H). ¹³C NMR (101 MHz, DMSO-*d*₆, ppm) δ 177.0, 172.2, 170.4, 162.8, 144.5, 142.7, 141.4, 137.4, 129.1, 128.7, 125.1, 124.7, 122.9, 118.6, 117.2, 116.3, 111.8, 103.4, 99.6, 94.6, 51.4, 49.2, 48.5, 44.9, 44.0, 43.5, 33.0, 29.1, 28.3, 27.5, 27.3, 26.7, 23.8. HR-MS (ESI-QTOF) *m/z*: [M+H]⁺ Calcd for C₄₁H₅₀N₆O₄S, 723.3687; found, 723.3651. In DMF: λ_{abs} (706 nm), ε (53400 L/mol/cm), λ_{em} (856 nm), Φ (7%).



3-((E)-2-((E)-2-(5-(tert-butyl)-3-((E)-2-(4-cyano-5-(dicyanomethylene)-2,2-dimethyl-2,5-dihydrofuran-3-yl)vinyl)-2-(4-(prop-2-yn-1-yl)piperazin-1-yl)cyclohex-2-en-1-ylidene)ethylidene)-3,3-dimethylindolin-1-yl)propane-1-sulfonic acid (CPO-SO₃-alkyne)

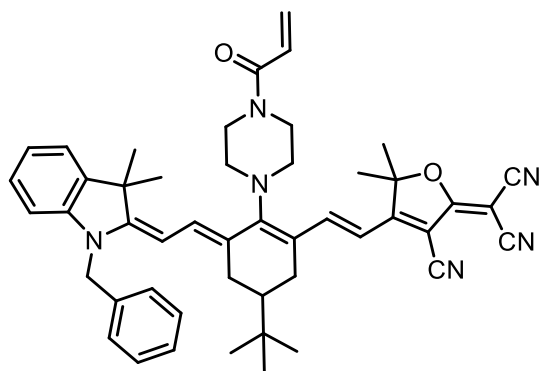
To a solution of **COP-SO₃** (20 mg 0.028 mmol) in DMF (2 mL) were added one drop of triethylamine and propargyl bromide (7.2 mg, 0.060 mmol) at 0°C. The mixture was stirred at room temperature overnight. Then diethyl ether (20 mL) was added. The precipitate was filtrated and purified by column chromatography on silica (eluent: MeOH:DCM=1:20, v/v) to afford **CPO-SO₃-alkyne** as a dark blue solid. (18 mg, yield: 86%). ¹H NMR (400 MHz, CDCl₃, ppm) δ 8.05 (s, 1H), 7.44 (d, *J* = 13.0 Hz, 1H), 7.28-7.21 (m, 2H), 7.10-7.01 (m, 2H), 5.83 (d, *J* = 12.0 Hz, 1H), 5.71-5.51 (m, 1H), 4.21-3.99 (m, 2H), 3.75 (s, 4H), 3.58-3.46 (m, 2H), 2.98 (s, 1H), 2.90 (s, 4H), 2.75-2.66 (m, 1H), 2.58-2.46 (m, 1H), 2.39 (s, 1H), 2.33-2.22 (m, 2H), 2.02-1.83 (m, 2H) 1.65-1.54 (m, 12H), 1.28 (s, 1H), 1.00 (s, 9H). Compound was too insoluble to record a proper ¹³C NMR spectrum. HR-MS (ESI-QTOF) *m/z*: [M+H]⁺ Calcd for C₄₄H₅₃N₆O₄S, 761.3844; found, 761.3826. In DMF: λ_{abs} (734 nm), ε (79400 L/mol/cm), λ_{em} (860 nm), Φ (9%).



4-((E)-6-(2-((E)-1-benzyl-3,3-dimethylindolin-2-ylidene)ethylidene)-4-(tert-butyl)-2-((E)-2-(4-cyano-5-(dicyanomethylene)-2,2-dimethyl-2,5-dihydrofuran-3-yl)vinyl)cyclohex-1-en-1-yl)piperazin-1-ium (CPOP1)

In a 50 mL round-bottom flask, piperazine (67.2 mg, 0.78 mmol) was added into a solution of **CPO1** (100 mg, 0.16 mmol) in DMF (30 mL). The mixture was stirred at 100°C for 3h. After cooling down to room temperature, DCM (50 mL) was added. Then the mixture was washed with saturated NH₄Cl (50 mL), extracted by DCM (50 mL×3). The collected organic phase was further wash with water (100mL), then dried over MgSO₄, filtered and evaporated under reduced pressure. The formed dark purple solid was re-dissolved into a small amount of MeOH and precipitated by dropwise addition into a large volume of diethyl ether. **CPOP1** was afforded by filtration as a dark blue solid (110 mg, yield 95%). ¹H NMR (400 MHz, DMSO-*d*₆, ppm) δ 7.74 (s, 1H), 7.54 (d, *J* = 7.2 Hz, 1H), 7.44 (d, *J* = 13.0 Hz, 1H), 7.39-7.18 (m, 7H), 7.12 (t, *J* = 7.2 Hz, 1H), 5.81 (d, *J* = 13.1 Hz, 1H), 5.56 (d, *J* = 13.1 Hz, 1H), 5.41-5.16 (m, 2H), 3.68 (s, 4H),

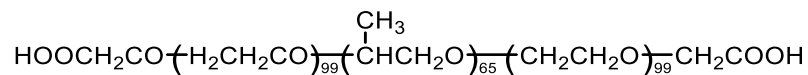
3.00 (s, 4H), 2.47-2.26 (m, 2H), 1.63 (d, $J = 9.8$ Hz, 6H), 1.51 (d, $J = 5.6$ Hz, 6H), 1.25 (s, 1H), 0.85 (s, 9H). ^{13}C NMR (101 MHz, DMSO- d_6 , ppm) δ 176.9, 174.9, 168.1, 167.9, 163.2, 146.0, 143.9, 140.2, 139.2, 136.2, 129.4, 128.9, 128.0, 127.0, 125.5, 124.3, 123.4, 123.2, 122.8, 122.6, 117.3, 116.3, 109.9, 101.5, 96.2, 94.2, 56.8, 47.7, 47.0, 46.5, 44.7, 33.1, 29.0, 28.9, 27.5, 27.2, 26.4. HR-MS (ESI-QTOF) m/z : $[\text{M}+\text{H}]^+$ Calcd for $\text{C}_{45}\text{H}_{50}\text{N}_6\text{O}$: 694.4119, found 694.4111. In DMF: λ_{abs} (701 nm), ϵ (50400 L/mol/cm), λ_{em} (856 nm), Φ (6%).



2-(4-((*E*)-2-((*E*)-2-(4-acryloylpiperazin-1-yl)-3-(2-((*E*)-1-benzyl-3,3-dimethylindolin-2-ylidene)ethylidene)-5-(*tert*-butyl)cyclohex-1-en-1-yl)vinyl)-3-cyano-5,5-dimethylfuran-2(5*H*)-ylidene)malononitrile (CPOP2)

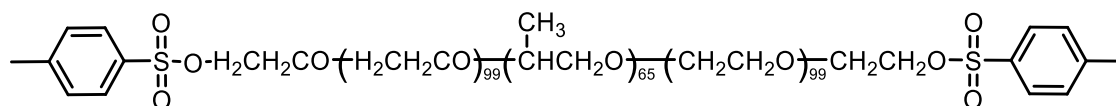
Under argon atmosphere, DIEA (0.18 mL) was added into a solution of **CPOP1** (70 mg, 0.10 mmol) in anhydrous DCM (15 mL) at 0°C. After 5 min, acryloyl chloride (46 mg, 0.51 mmol) was added. The mixture was stirred at 0°C for 2h, then was washed with saturated NH_4Cl (50 mL \times 3), extracted by DCM. The organic phase was collected, dried over MgSO_4 , filtered and evaporated under reduced pressure. Then the obtained crude product was purified by column chromatography on silica (eluent: MeOH:DCM=1:19, v/v) to afford **CPOP2** as a blue solid. (58 mg, yield: 77%) ^1H NMR (400 MHz, DMSO- d_6 , ppm) δ 7.96-7.76 (m, 1H), 7.55 (d, $J = 7.6$ Hz, 1H), 7.46 (d, $J = 12.8$ Hz, 1H), 7.39-7.21 (m, 7H), 7.15 (t, $J = 6.8$ Hz, 1H), 6.94-6.79 (m, 1H), 6.21 (dd, $J = 16.6$ Hz, 1H), 5.94-5.71 (m, 3H), (m, 2H), 3.81 (s, 4H), 3.63 (m, 4H), 2.69-2.52 (m, 2H), 1.86-1.68 (m, 2H), 1.62 (d, $J = 8.8$ Hz, 6H), 1.51 (d, $J = 7.8$ Hz, 6H), 1.23 (s, 1H), 0.87 (s, 9H). ^{13}C NMR (101 MHz, DMSO- d_6 , ppm) δ 208.9, 177.0, 173.4, 169.0, 164.8, 164.1, 143.7, 141.2, 140.5, 139.6, 136.0, 129.4, 128.9, 128.5, 128.3, 128.0, 126.9, 126.5, 123.8(2C), 122.9, 117.8, 117.0, 116.0, 110.3, 102.5, 97.2, 94.6, 56.3, 48.1, 44.6, 41.6, 33.0, 29.1, 28.9, 27.3, 27.2, 26.5. HR-MS (ESI-QTOF) m/z : $[\text{M}+\text{H}]^+$ Calcd for $\text{C}_{48}\text{H}_{52}\text{N}_6\text{O}_2$, 745.4225; found 745.4221. In DMF: λ_{abs} (731 nm) ϵ (79200 L/mol/cm), λ_{em} (862 nm) Φ (7%).

1.3. Synthesis and Characterization of Modified F127



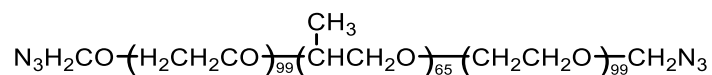
(F127-COOH)

F127 (2.0 g, 0.16 mmol) was dissolved in H₂O (50 mL), TEMPO (1.0 mg, 6.4 μmol), KBr (38.0 mg, 0.32 mmol) and NaClO (10 mL, 4.8%) were then added at 0°C. The mixture was stirred for 1h at 0°C then 6h at room temperature, and the pH of the mixture was controlled around 10 by addition of 0.5 N NaOH in this period of time. After quenching by EtOH (1mL), 4N HCl was added to adjust the pH of the mixture to 3. The mixture was then extracted by DCM, washed with water (250 mL×2) and concentrated by evaporation under reduced pressure. Followed by precipitation with diethyl ether and filtration, 1.2 g of **F127-COOH** as white powder was afforded. (Yield: 60%)



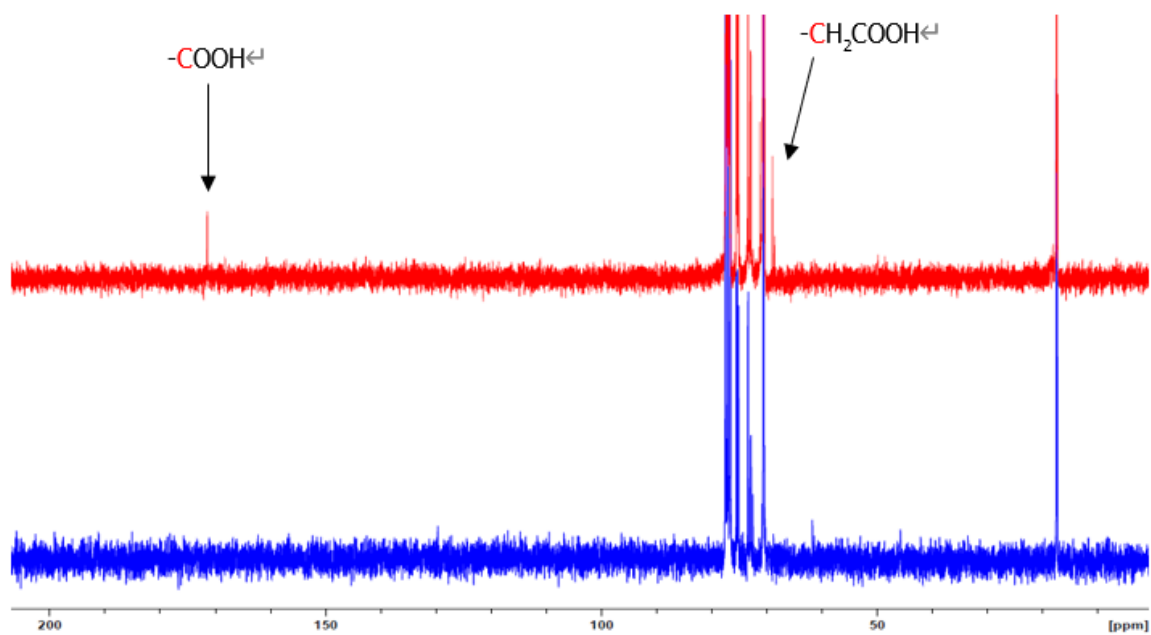
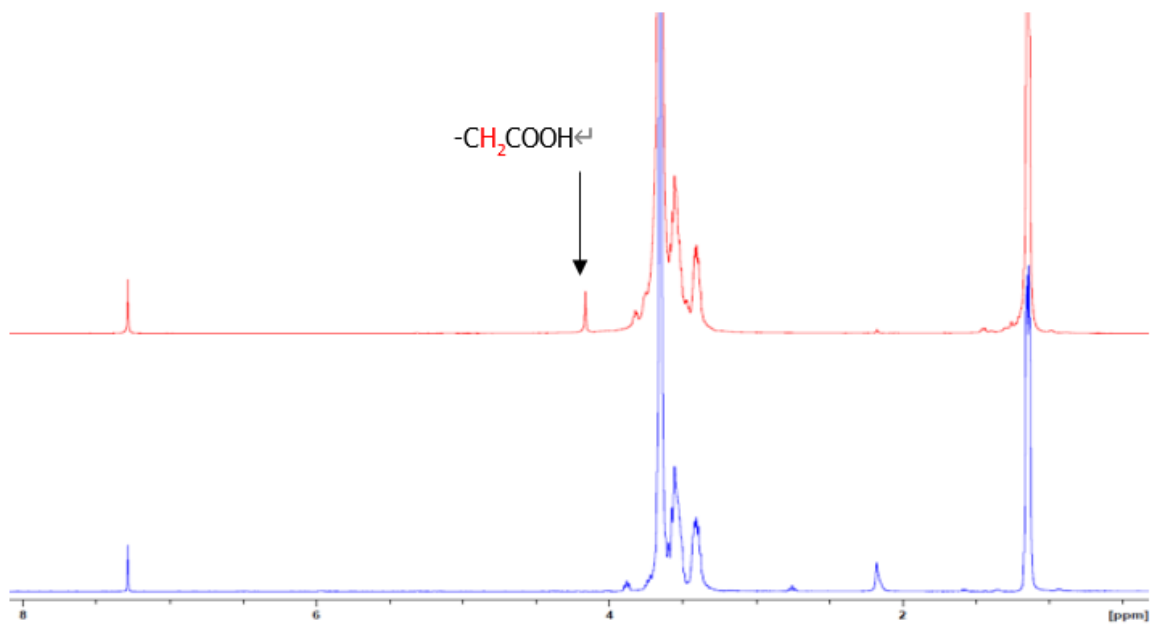
(F127-OTs)

F127 (5.0 g, 0.4 mmol) was dissolved in DCM (25 mL), TsCl (305 mg, 1.6 mmol) and TEA (5 mL) were then added. The mixture was stirred for 16h at room temperature. Then the organic solvent was evaporated under reduced pressure. 1M HCl (50 mL) was added, followed by extraction using DCM and washing twice with water (250 mL×2). The organic phase was collected and concentrated. After precipitation with diethyl ether and filtration, 4.35 g of **F127-OTs** was obtained as white powder. (Yield: 86%)



(F127-N₃)

F127-OTs (1.5 g, 0.12 mmol) and NaN₃ (46 mg, 0.71 mmol) were dissolved in DMF (20 mL). After stirring at 80°C for 6h, DCM (50 mL) was added. The mixture was washed with water (100 mL×3) and extracted by DCM. The organic phase was collected and concentrated, followed by precipitation with diethyl ether and filtration to form 1.40 g **F127-N₃** as white powder. (Yield: 94%).



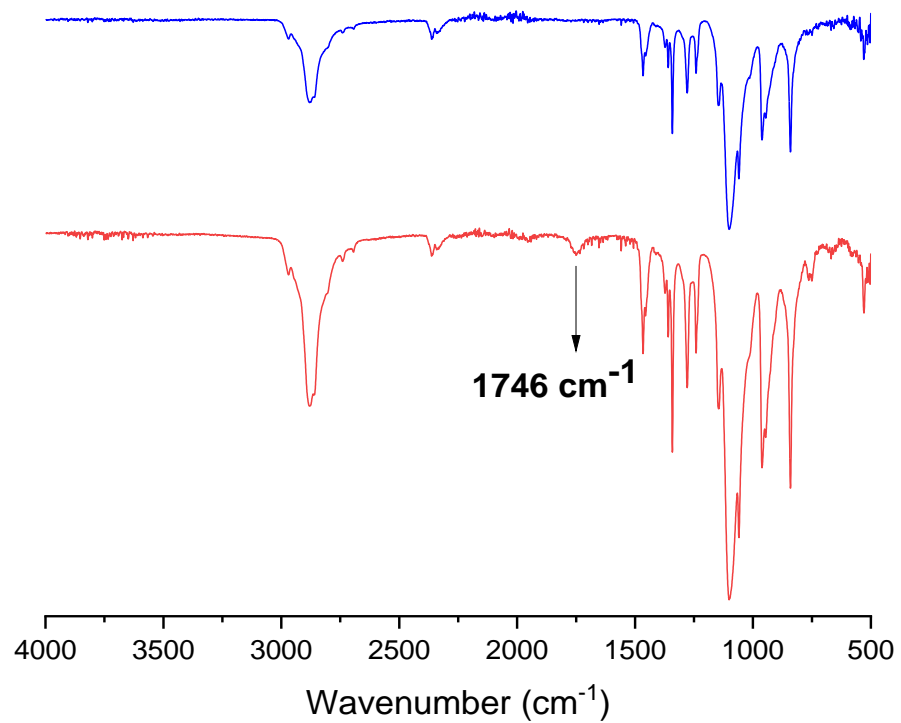


Figure 6 - 1 Characterization and comparison of **FI27-COOH** (red) with **FI27** (green).

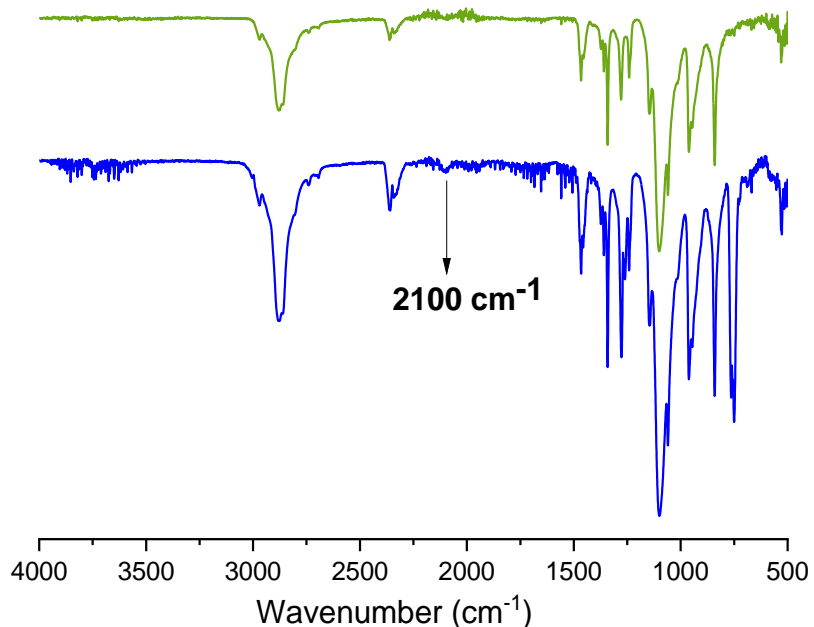


Figure 6 - 2 Characterization and comparison of *F127-OTs* (red) and *F127-N₃* (blue) with *F127* (green).

2. Preparation of Dye-loaded F127-SiO₂ NPs

General procedure of preparation of dye-encapsulated F127-SiO₂

In a 5 mL round bottom flask, **F127** and dye were dissolved in 1-2 mL of DCM, followed by evaporation of DCM by a gentle flow of argon at room temperature to form a film. NaCl (65 mg) and 0.85 N hydrochloric acid solution (3.1 mL) were added to the F127/dye mixture, not until an optical solution was generated, TEOS (360 μ L) was added to start the silica cross-linking. After stirring for 105 min, the suspension was added DEDMS (30 μ L) to terminate the silica growth, and was further stirred at room temperature for 24h. The mixture was transferred into a dialysis bag (cut-off 14,000 g/mol) to remove acid, free F127 and unreacted additives through dialysis against distilled water for 3 days. Finally, the F127-SiO₂ NPs solution was passed through a 0.2 μ m filter (regenerated cellulose).

TCBZ5@F127-SiO₂, TCBZ5@F127-COOH-SiO₂, TCBZ5@F127-N₃-SiO₂ and TCBZ5@F127-X-SiO₂ NPs

TCBZ5@F127-SiO₂ and **TCBZ5@F127-COOH-SiO₂** NPs were synthesized following the general procedure of making dye-encapsulated F127-SiO₂ NPs. For **TCBZ5@F127-X-SiO₂** and **TCBZ5@F127-TPP-SiO₂** NPs, a **TCBZ5@F127-N₃-SiO₂** NPs solution was firstly prepared by doubling the amount of all the reagents used in the general procedure. After passing through a 0.2 μm filter (regenerated cellulose), the **TCBZ5@F127-N₃-SiO₂** NPs was obtained with volume around 8.4 mL. Then the solution was diluted into 9 mL and separated into two parts with every part of 4.5 mL (particle concentration around 50 μM). Then, CuSO₄ (7.5 μmol), sodium ascorbate (2.5 μmol) and THPTA (12.5 μmol) were added to the mixtures followed by addition of the functional moieties (2.5 μmol). After gentle stirring for 3h, the mixtures were purified by dialysis for 3 days.

Sample	m_{Dye} (mg)	F127 (mg)	F127-COOH (mg)	F127-N₃ (mg)
TCBZ5@F127-SiO₂	1.0	200	0	0
TCBZ5@F127-COOH-SiO₂	1.0	190	10	--
TCBZ5@F127-X-SiO₂	1.0	100	--	100
TCBZ5@F127-TPP-SiO₂	1.0	100	--	100

EBTN1-EBTN5@F127-SiO₂ NPs

Sample	Dye (mg)	F127 (mg)
EBTN1@F127-SiO₂ NPs	EBTN1 (0.04 mg)	200
EBTN2@F127-SiO₂ NPs	EBTN2 (0.04 mg)	200
EBTN3@F127-SiO₂ NPs	EBTN3 (0.04 mg)	200
EBTN4@F127-SiO₂ NPs	EBTN4 (0.04mg)	200
EBTN5@F127-SiO₂ NPs	EBTN5 (0.04 mg)	200

Preparation of F127-CPO-SO₃-SiO₂ NPs

To a solution of **F127-N₃-SiO₂** NPs (4.2 mL, particle concentration around 50 μ M) was added CuSO₄ (3.25 μ mol), sodium ascorbate (1.25 μ mol), tris(3-hydroxypropyltriazolymethyl)amine (THPTA) (6.25 μ mol) then **CPO-SO₃-alkyne** (2.1 mg, 0.05 wt%) to volume around 4.5 mL (particle concentration around 50 μ M). After gentle stirring for 3h, the mixture was purified by dialysis for 3 days to afford the **F127-CPO-SO₃-SiO₂** NPs solution with volume around 5 mL.

3. *In vivo* Microscopy

3.1. *Two-Photon imaging*

Animal model: In accordance with the policy of the French legislation, experiments were done in compliance with the European Parliament and the Council Directive of September 22, 2010 (2010/63/EU) on the protection of animals used for scientific purposes. The research involving animals was authorized by the Direction Départementale des Services Vétérinaires de l'Isère – Ministère de l'Agriculture et de la Pêche, and the Ministère de l'Enseignement Supérieur et de la Recherche, France permit number: 2015051914157522_v1 (PI: Boudewijn van der Sanden, PhD, permit number 38 09 40 for animal experiments). All efforts were made to minimize the number of mice used and their suffering during the experimental procedure. Mice were housed in ventilated cages with food and water ad libitum in a 12 h light/dark cycle at 22 ± 1 °C. Mice were used directly for two-photon experiments of samples **TCBZ5@F127-SiO₂** and **TCBZ5@F127-X-SiO₂** NPs.

Two-photon microscopy was performed using a Trimscope II (LaVision BioTec, Bielefeld, Germany) equipped with a 16x water-immersion objective (NA 0.8, Nikon, France) and Inspector 2015 software. The excitation wavelengths of the pulsed infrared laser (Insight DeepSea, Spectra-Physics, Evry, France) were 900 nm for both NPs.

3.2. *PA imaging*

The experimental setup is shown in Figure 3 - 1. The beams of two CW laser diodes ($\lambda_1 = 415$ nm and $\lambda_2 = 660$ nm or 808 nm) are combined with a dichroic mirror. The laser diodes intensities are sinus modulated at $f_1 = 5$ MHz and $f_2 = 5.3$ MHz respectively. The beams are then expanded to fill the entrance pupil of the microscope objective (Zeiss LD Epiplan 20X/0.4). At the output of the objective, the beam waists are about 1 μ m and the mean optical powers are given as below. A two-axis galvanometric mirror scanner makes it possible to move the beams on the surface of the target to build an image, with a pixel

dwelt time of 150 μ s. The position of the target is set by a motorized three-axis translation stage. The PA signal is collected through an ultrasound transmission gel by a focused piezoelectric transducer (NDT Systems, IBMF054). The electric signal of the transducer is finally amplified and demodulated by two lock-in amplifiers respectively running around f_1 and f_2 to recover both the amplitudes of the PA signals generated at λ_1 and λ_2 .

Diode\laser power	10%	20%	30%	40%	50%	60%	70%	80%	90%	100%
415nm	0,7	1,5	2,3	3	3,7	4,2	4,7	5,2	5,7	6,1
660nm	0,8	1,7	2,7	3,6	4,2	5	6,2	7	7,8	7,2

Animal model. PA experiments were performed on the ears of white CD-1 IGS mice (Charles River, Écully, France). All efforts were made to minimize their number. They were housed in ventilated cages with food and water ad libitum in a 12 h light/dark cycle at $22 \pm 1^\circ\text{C}$. For the experience, mice were anesthetized using a gas mixture of 1% isoflurane in air/30% O_2 . Their body temperature was maintained at $36\text{-}37^\circ\text{C}$ using an electric heating pad with a feedback system. In experiments with dye infusion, mice were cannulated in a caudal vein (BD NeoflonTM, 16GA 0.6 x 19mm, Becton Dickinson, Helsingborg Sweden) and connected to a 1 ml syringe with a target volume of 200 μL of **CPO-SO₃** PNP. Before positioning the ear on the lid of a petri dish ($\varnothing=10\text{mm}$) in the focal plane of the objective with ultrasound gel, ears were cleaned with a hair-removing cream (VEET, France) and rinsed with 70% ethanol.

In accordance with the French legislation, experiments were done in compliance with the European Parliament and the Council Directive of September 22, 2010 (2010/63/EU). The research involving animals was authorized by the Direction Départementale des Services Vétérinaires de l'Isère-Ministère de l'Agriculture et de la Pêche, and the Ministère de l'Enseignement Supérieur et de la Recherche, France permit number: 2015051914157522_v1 (PI: B. van der Sanden, permit number 38 09 40 for animal experiences).

Image processing was performed with the NIH ImageJ software. Acquisitions were averaged or summed to give the images (sums gave a better image brightness). Background was subtracted (rolling ball radius of 20 pixels). Finally, the signal of **CPO-SO₃** PNP was (660 nm) colorized in green and in red for hemoglobin and melanin (415 nm).

4. Preparation of Solid Device for Primary Amine Vapor Detection

PTTCN sol-gel and PTTCN-PMMA film

Firstly, the solutions of **PTTCN** (2.0 mg) in THF (1mL) and DCM (1mL) were prepared. Followed addition of MTEOS&TEOS (2g, 54 wt% in THF) and PMMA (1.5 g, 10 wt% in DCM) to the **PTTCN** solutions formed the **PTTCN sol-gel** and **PTTCN-PMMA** mixtures. Then by spin-coating at speed of 2000 rpm, the mixtures were spread homogeneously on a glass surface. After heating at 90°C for 1h, the films were cooled down and protected from light.

EBTN1-glass

Glass slides were firstly cleaned by detergent, water, acetone and methanol in sequence using ultrasonication for 15 min, respectively, then, they were placed in the solution of APTES (5% in methanol) to stand at room temperature for 45-60 min. After being washed with methanol and dried at 120°C for 30min the slides were immersed into the solution of **EBTNAld** (100 μM) at 45°C overnight. Followed by rinsing with methanol and natural drying, the **EBTNAld**-loaded glass slides were immersed in malononitrile solution (10 mM) at room temperature for 6h. By rinsing with methanol the EBTN1-glass was finally formed.

5. Other Experiments

TCBZ1-TCBZ8 nanoaggregates

TCBZ1-TCBZ8 stock solutions (1 mM) were prepared using acetone as a good solvent. In a volumetric flask (5 mL) was added dye solution (250 μL, 2.5×10^{-4} mmol). Followed addition of water/acetone mixture (water fraction f_w % from 0 to 90) to the volume of the flask gave the final dye concentration (5×10^{-5} mol L⁻¹).

NMR titration

To a normal NMR tube was added **PTTCN** (6.0 mg, 18.4 μmol) or **EBTN1** (6.0 mg, 8.0 μmol) and deuterated DMSO (0.45 mL). N-propylamine (400 μL) or n-octylamine (100 μL) was diluted using deuterated DMSO to form a 2 mL amine solution (N-propylamine: 2.4 M; n-octylamine: 1.34 M). Then the

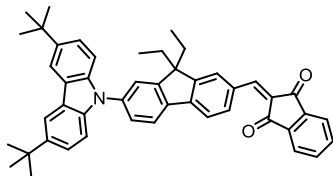
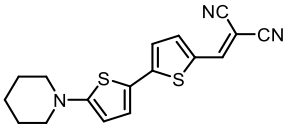
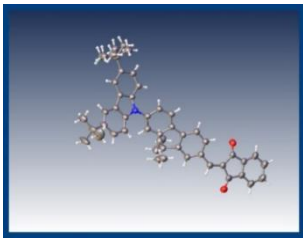
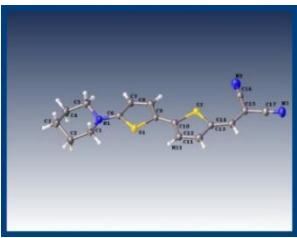
¹H NMR spectra were performed after every addition of n-propylamine (7.6 μL, 18.4 μmol) or n-octylamine solution (6 μL, 8.0 μmol) for 30 s.

UV/vis and fluorescence titration

Stock solution of **PTTCN** (1.0 mM) or **EBTN1** (0.5 mM) was prepared by dissolving **PTTCN** (1.63, 5.0 μmol) or **EBTN1** (1.87 mg, 2.5 μmol) into DMSO in a volumetric flask (5 mL). N-octylamine (8.2 μL) was dissolved in DMSO in a volumetric flask (50 mL) to form the n-octylamine stock solution (1.0 mM). In 11 volumetric flasks (5 mL) was added the same amount of stock solution of **PTTCN** (50 μL) or **EBTN1** (20 μL). Then, different and increased volume of amine stock solution was added into each flask (0, 50, 100 μL, and so on). The mixtures were diluted to volume of flask with DMSO, and preserved in dark place for 14 h. The UV/vis and fluorescence spectra were measured all at once.

6. X-ray Crystallography

Single crystals of **TCBZ8** and **PTTCN** were prepared by diffusion of a non-solvent (pentane or EtOH) in a concentrated solution of dye (in CHCl₃) at room temperature. The crystallographic data and refinement details are summarized in the following table.

Compound	TCBZ8	PTTCN
Chemical structure		
Crystal structure		
Crystal growth	CHCl ₃ /Pentane (diffusion)	CHCl ₃ /EtOH (diffusion)
Empirical formula	C ₄₇ H ₄₅ NO ₂	C ₁₇ H ₁₅ N ₃ S ₂
Formula weight	655.84	325.44

$D_{\text{calc.}}/\text{g cm}^{-3}$	1.206	1.366
Crystal system	Monoclinic	Monoclinic
Colour	Orange	Dark violate
μ [mm^{-1}]	0.072	0.336
T [K]	150.00 (10)	150.01 (10)
Space group	$P2_1/c$	$P2_1/c$
a [Å]	34.383 (5)	16.4065 (16)
b [Å]	12.0537 (12)	6.4682 (6)
c [Å]	17.729 (3)	15.0664 (17)
α [°]	90	90
β [°]	100.401 (13)	98.286 (9)
γ [°]	90	90
V [Å ³]	7226.8 (17)	1582.2 (3)
Z	8	4
Z'	1	1
Wavelength/Å	0.71073	0.71073
θ range (°)	2.838-29.716	3.031-26.620
total no. data	23036	21500
no. unique data	8501	4126
no. params refined	5166	3829
R_1	0.1778	0.0537
wR_2	0.2509	0.1270
GOF	0.940	1.073

References

- [1] Carbon nanotubes and mesenchymal stem cells: biocompatibility, proliferation and differentiation. Mooney, E.; Dockery, P.; Greiser, U.; Murphy, M.; Barron, V. *Nano Letters* **2008**, *8* (8), 2137-2143.
- [2] Intravital imaging of tumor apoptosis with FRET probes during tumor therapy. Zhou, F.; Xing, D.; Wu, S.; Chen, W. R. *Molecular Imaging and Biology* **2010**, *12* (1), 63-70.
- [3] Green fluorescent protein as a marker for gene expression. Chalfie, M.; Tu, Y.; Euskirchen, G.; Ward, W. W.; Prasher, D. C. *Science* **1994**, *263* (5148), 802.
- [4] Use of reporter genes for optical measurements of neoplastic disease in vivo. Contag, C. H.; Jenkins, D.; Contag, P. R.; Negrin, R. S. *Neoplasia* **2000**, *2* (1-2), 41-52.
- [5] Bioluminescent indicators in living mammals. Contag, P. R.; Olomu, I. N.; Stevenson, D. K.; Contag, C. H. *Nature Medicine* **1998**, *4* (2), 245-247.
- [6] High-sensitivity *in vivo* imaging for tumors using a spectral up-conversion nanoparticle NaYF₄: Yb³⁺, Er³⁺ in cooperation with a microtubulin inhibitor. Wei, Y.; Chen, Q.; Wu, B.; Zhou, A.; Xing, D. *Nanoscale* **2012**, *4* (13), 3901-3909.
- [7] Nerve-highlighting fluorescent contrast agents for image-guided surgery. Gibbs-Strauss, S. L.; Nasr, K. A.; Fish, K. M.; Khullar, O.; Ashitate, Y.; Siclovan, T. M.; Johnson, B. F.; Barnhardt, N. E.; Tan Hehir, C. A.; Frangioni, J. V. *Molecular Imaging* **2011**, *10* (2), 91-101.
- [8] New strategies for fluorescent probe design in medical diagnostic imaging. Kobayashi, H.; Ogawa, M.; Alford, R.; Choyke, P. L.; Urano, Y. *Chemical Reviews* **2010**, *110* (5), 2620-2640.
- [9] Exploiting the biological windows: current perspectives on fluorescent bioprobes emitting above 1000 nm. Hemmer, E.; Benayas, A.; Légaré, F.; Vetrone, F. *Nanoscale Horizons* **2016**, *1* (3), 168-184.
- [10] *In vivo* near-infrared fluorescence imaging. Frangioni, J. *Current Opinion in Chemical Biology* **2003**, *7* (5), 626-634.
- [11] Optical imaging in drug discovery and diagnostic applications. Licha, K.; Olbrich, C. *Advanced Drug Delivery Reviews* **2005**, *57* (8), 1087-1108.
- [12] Fluorescence-enhanced, near infrared diagnostic imaging with contrast agents. Sevick-Muraca, E. M.; Houston, J. P.; Gurfinkel, M. *Current Opinion in Chemical Biology* **2002**, *6* (5), 642-650.
- [13] Fluorescence molecular imaging of small animal tumor models. Graves, E. E.; Weissleder, R.; Ntziachristos, V. *Current Molecular Medicine* **2004**, *4* (4), 419-430.
- [14] Fluorescence imaging with near-infrared light: new technological advances that enable *in vivo* molecular imaging. Ntziachristos, V.; Bremer, C.; Weissleder, R. *European Radiology* **2003**, *13* (1), 195-208.
- [15] Review of long-wavelength optical and NIR imaging materials: contrast agents, fluorophores, and multifunctional nano carriers. Pansare, V. J.; Hejazi, S.; Faenza, W. J.; Prud'homme, R. K. *Chemistry of Materials* **2012**, *24* (5), 812-827.
- [16] Rhodamine-inspired far-red to near-infrared dyes and their application as fluorescence probes. Sun, Y.-Q.; Liu, J.; Lv, X.; Liu, Y.; Zhao, Y.; Guo, W. *Angewandte Chemie International Edition* **2012**, *51* (31), 7634-7636.
- [17] Silicon-substituted xanthene dyes and their unique photophysical properties for fluorescent probes. Ikeno, T.; Nagano, T.; Hanaoka, K. *Chemistry – An Asian Journal* **2017**, *12* (13), 1435-1446.

-
- [18] A versatile route to red-emitting carbopyronine dyes for optical microscopy and nanoscopy. Kolmakov, K.; Belov, V. N.; Wurm, C. A.; Harke, B.; Leutenegger, M.; Eggeling, C.; Hell, S. W. *European Journal of Organic Chemistry* **2010**, 2010 (19), 3593-3610.
- [19] A design concept of long-wavelength fluorescent analogs of rhodamine dyes: replacement of oxygen with silicon atom. Fu, M.; Xiao, Y.; Qian, X.; Zhao, D.; Xu, Y. *Chemical Communications* **2008**, (15), 1780-1782.
- [20] Development of an Si-rhodamine-based far-red to near-infrared fluorescence probe selective for hypochlorous acid and its applications for biological imaging. Koide, Y.; Urano, Y.; Hanaoka, K.; Terai, T.; Nagano, T. *Journal of the American Chemical Society* **2011**, 133 (15), 5680-5682.
- [21] Robust synthesis of NIR-emissive P-rhodamine fluorophores. Sauer, M.; Nasufovic, V.; Arndt, H.-D.; Vilotijevic, I. *Organic & Biomolecular Chemistry* **2020**, 18 (8), 1567-1571.
- [22] Nebraska Red: a phosphinate-based near-infrared fluorophore scaffold for chemical biology applications. Zhou, X.; Lai, R.; Beck, J. R.; Li, H.; Stains, C. I. *Chemical Communications* **2016**, 52 (83), 12290-12293.
- [23] Sulfone-rhodamines: a new class of near-infrared fluorescent dyes for bioimaging. Liu, J.; Sun, Y.-Q.; Zhang, H.; Shi, H.; Shi, Y.; Guo, W. *ACS Applied Materials & Interfaces* **2016**, 8 (35), 22953-22962.
- [24] Selenium- and Tellurium-containing fluorescent molecular probes for the detection of biologically important analytes. Manjare, S. T.; Kim, Y.; Churchill, D. G. *Accounts of Chemical Research* **2014**, 47 (10), 2985-2998.
- [25] Heteroatom-substituted rhodamine dyes: Structure and spectroscopic properties. Deng, F.; Xu, Z. *Chinese Chemical Letters* **2019**, 30 (10), 1667-1681.
- [26] Bismuth-rhodamine: a new red light-excitable photosensitizer. Hirayama, T.; Mukaimine, A.; Nishigaki, K.; Tsuboi, H.; Hirose, S.; Okuda, K.; Ebihara, M.; Nagasawa, H. *Dalton Transactions* **2017**, 46 (46), 15991-15995.
- [27] A reversible near-infrared fluorescence probe for reactive oxygen species based on Te-rhodamine. Koide, Y.; Kawaguchi, M.; Urano, Y.; Hanaoka, K.; Komatsu, T.; Abo, M.; Terai, T.; Nagano, T. *Chemical Communications* **2012**, 48 (25), 3091-3093.
- [28] Development of NIR fluorescent dyes based on Si-rhodamine for *in vivo* imaging. Koide, Y.; Urano, Y.; Hanaoka, K.; Piao, W.; Kusakabe, M.; Saito, N.; Terai, T.; Okabe, T.; Nagano, T. *Journal of the American Chemical Society* **2012**, 134 (11), 5029-5031.
- [29] Evolution of group 14 rhodamines as platforms for near-infrared fluorescence probes utilizing photoinduced electron transfer. Koide, Y.; Urano, Y.; Hanaoka, K.; Terai, T.; Nagano, T. *ACS Chemical Biology* **2011**, 6 (6), 600-608.
- [30] Bright, stable, and biocompatible organic fluorophores absorbing/emitting in the deep near-infrared spectral region. Lei, Z.; Li, X.; Luo, X.; He, H.; Zheng, J.; Qian, X.; Yang, Y. *Angewandte Chemie International Edition* **2017**, 56 (11), 2979-2983.
- [31] A unique rectilinearly π -extended rhodamine dye with large Stokes shift and near-infrared fluorescence for bioimaging. Liu, C.; Jiao, X.; Wang, Q.; Huang, K.; He, S.; Zhao, L.; Zeng, X. *Chemical Communications* **2017**, 53 (77), 10727-10730.
- [32] New near-infrared-absorbing non-symmetric and symmetric trimethinecyanine dyes containing a 7-dialkylamino-1-benzopyrylium end group. Czerney, P.; Grummt, U. W. *Journal of Chemical Research - Part S* **1996**, (4), 173.

-
- [33] A unique class of near-infrared functional fluorescent dyes with carboxylic-acid-modulated fluorescence ON/OFF switching: rational design, synthesis, optical properties, theoretical calculations, and applications for fluorescence imaging in living animals. Yuan, L.; Lin, W.; Yang, Y.; Chen, H. *Journal of the American Chemical Society* **2012**, *134* (2), 1200-1211.
- [34] De novo synthesis of phenolic dihydroxanthene near-infrared emitting fluorophores. Richard, J.-A. *Organic & Biomolecular Chemistry* **2015**, *13* (30), 8169-8172.
- [35] A unique “integration” strategy for the rational design of optically tunable near-infrared fluorophores. Chen, H.; Dong, B.; Tang, Y.; Lin, W. *Accounts of Chemical Research* **2017**, *50* (6), 1410-1422.
- [36] Hybrid rhodamine fluorophores in the visible/NIR region for biological imaging. Wang, L.; Du, W.; Hu, Z.; Uvdal, K.; Li, L.; Huang, W. *Angewandte Chemie International Edition* **2019**, *58* (40), 14026-14043.
- [37] Analogs of Changsha near-infrared dyes with large Stokes shifts for bioimaging. Yuan, L.; Lin, W.; Chen, H. *Biomaterials* **2013**, *34* (37), 9566-9571.
- [38] Donor–acceptor–donor NIR emissive rhodindolizine dye synthesized by C–H bond functionalization. Rathnamalala, C. S. L.; Gayton, J. N.; Dorris, A. L.; Autry, S. A.; Meador, W.; Hammer, N. I.; Delcamp, J. H.; Scott, C. N. *The Journal of Organic Chemistry* **2019**, *84* (20), 13186-13193.
- [39] Postfunctionalization of the BODIPY core: synthesis and spectroscopy. Boens, N.; Verbelen, B.; Dehaen, W. *European Journal of Organic Chemistry* **2015**, *2015* (30), 6577-6595.
- [40] BODIPY dyes and their derivatives: syntheses and spectroscopic properties. Loudet, A.; Burgess, K. *Chemical Reviews* **2007**, *107* (11), 4891-4932.
- [41] The triplet excited state of Bodipy: formation, modulation and application. Zhao, J.; Xu, K.; Yang, W.; Wang, Z.; Zhong, F. *Chemical Society Reviews* **2015**, *44* (24), 8904-8939.
- [42] Tetraaryl-BODIPY dyes: convenient synthesis and characterization of elusive near IR fluorophores. Buyukcakil, O.; Bozdemir, O. A.; Kolemen, S.; Erbas, S.; Akkaya, E. U. *Organic Letters* **2009**, *11* (20), 4644-4647.
- [43] π -Fused bis-BODIPY as a candidate for NIR dyes. Nakamura, M.; Tahara, H.; Takahashi, K.; Nagata, T.; Uoyama, H.; Kuzuhara, D.; Mori, S.; Okujima, T.; Yamada, H.; Uno, H. *Organic & Biomolecular Chemistry* **2012**, *10* (34), 6840-6849.
- [44] Monofunctionalized 1,3,5,7-tetraarylazaBODIPYs and their application in the synthesis of azaBODIPY based conjugates. Koch, A.; Ravikanth, M. *The Journal of Organic Chemistry* **2019**, *84* (17), 10775-10784.
- [45] [a]-Phenanthrene-fused BF₂ azadipyromethene (azaBODIPY) dyes as bright near-infrared fluorophores. Sheng, W.; Cui, J.; Ruan, Z.; Yan, L.; Wu, Q.; Yu, C.; Wei, Y.; Hao, E.; Jiao, L. *The Journal of Organic Chemistry* **2017**, *82* (19), 10341-10349.
- [46] Synthesis, crystal structure, and the deep near-infrared absorption/emission of bright azaBODIPY-based organic fluorophores. Sheng, W.; Wu, Y.; Yu, C.; Bobadova-Parvanova, P.; Hao, E.; Jiao, L. *Organic Letters* **2018**, *20* (9), 2620-2623.
- [47] Water-soluble aza-BODIPYs: biocompatible organic dyes for high contrast *in vivo* NIR-II imaging. Godard, A.; Kalot, G.; Pliquett, J.; Busser, B.; Le Guével, X.; Wegner, K. D.; Resch-Genger, U.; Rousselin, Y.; Coll, J.-L.; Denat, F.; Bodio, E.; Goze, C.; Sancey, L. *Bioconjugate Chemistry* **2020**, *31* (4), 1088-1092.

-
- [48] Beyond the cyanine limit: Peierls distortion and symmetry collapse in a polymethine dye. Tolbert, L. M.; Zhao, X. *Journal of the American Chemical Society* **1997**, *119* (14), 3253-3258.
- [49] Detection of sentinel node in gastric cancer surgery by indocyanine green fluorescence imaging: comparison with infrared imaging. Miyashiro, I.; Miyoshi, N.; Hiratsuka, M.; Kishi, K.; Yamada, T.; Ohue, M.; Ohigashi, H.; Yano, M.; Ishikawa, O.; Imaoka, S. *Annals of Surgical Oncology* **2008**, *15* (6), 1640-1643.
- [50] Fluorescence navigation with indocyanine green for detecting sentinel lymph nodes in breast cancer. Kitai, T.; Inomoto, T.; Miwa, M.; Shikayama, T. *Breast Cancer* **2005**, *12* (3), 211-215.
- [51] Quantitative lymph imaging for assessment of lymph function using indocyanine green fluorescence lymphography. Unno, N.; Nishiyama, M.; Suzuki, M.; Yamamoto, N.; Inuzuka, K.; Sagara, D.; Tanaka, H.; Konno, H. *European Journal of Vascular and Endovascular Surgery* **2008**, *36* (2), 230-236.
- [52] Lymphatic imaging in humans with near-infrared fluorescence. Rasmussen, J. C.; Tan, I. C.; Marshall, M. V.; Fife, C. E.; Sevick-Muraca, E. M. *Current Opinion in Biotechnology* **2009**, *20* (1), 74-82.
- [53] Intraoperative evaluation of skin-flap viability using laser-induced fluorescence of indocyanine green. Holm, C.; Mayr, M.; Höfter, E.; Becker, A.; Pfeiffer, U. J.; Mühlbauer, W. *British Journal of Plastic Surgery* **2002**, *55* (8), 635-644.
- [54] Perfusion zones of the DIEP flap revisited: a clinical study. Holm, C.; Mayr, M.; Höfter, E.; Ninkovic, M. *Plastic and Reconstructive Surgery* **2006**, *117* (1), 37-43.
- [55] Monitoring free flaps using laser-induced fluorescence of indocyanine green: a preliminary experience. Holm, C.; Tegeler, J.; Mayr, M.; Becker, A.; Pfeiffer, U. J.; Mühlbauer, W. *Microsurgery* **2002**, *22* (7), 278-287.
- [56] Fluorescent cholangiography using indocyanine green for laparoscopic cholecystectomy: an initial experience. Ishizawa, T.; Bandai, Y.; Kokudo, N. *Archives of Surgery* **2009**, *144* (4), 381-382.
- [57] Pharmacokinetic-rate images of indocyanine green for breast tumors using near-infrared optical methods. Alacam, B.; Yazici, B.; Intes, X.; Nioka, S.; Chance, B. *Physics in Medicine and Biology* **2008**, *53* (4), 837-859.
- [58] Expanding the polymethine paradigm: evidence for the contribution of a bis-dipolar electronic structure. Pascal, S.; Haefele, A.; Monnereau, C.; Charaf-Eddin, A.; Jacquemin, D.; Le Guennic, B.; Andraud, C.; Maury, O. *The Journal of Physical Chemistry A* **2014**, *118* (23), 4038-4047.
- [59] Review on near-infrared heptamethine cyanine dyes as theranostic agents for tumor imaging, targeting, and photodynamic therapy. Changhong, S.; Jason, B. W.; Dongfeng, P. *Journal of Biomedical Optics* **2016**, *21* (5), 1-11.
- [60] Near-infrared fluorescent pH responsive probe for targeted photodynamic cancer therapy. Siriwibool, S.; Kaekratoke, N.; Chansaenpak, K.; Siwawannapong, K.; Panajapo, P.; Sagarik, K.; Noisa, P.; Lai, R.-Y.; Kamkaew, A. *Scientific Reports* **2020**, *10* (1), 1283.
- [61] Single-dose intravenous toxicity study of IR-dye 800CW in Sprague-Dawley rats. Marshall, M. V.; Draney, D.; Sevick-Muraca, E. M.; Olive, D. M. *Molecular Imaging and Biology* **2010**, *12* (6), 583-594.
- [62] Dual-labeled trastuzumab-based imaging agent for the detection of human epidermal growth factor receptor 2 overexpression in breast cancer. Sampath, L.; Kwon, S.; Ke, S.; Wang, W.; Schiff, R.; Mawad, M.; Sevick, E. *Journal of nuclear medicine : official publication, Society of Nuclear Medicine* **2007**, *48*, 1501-1510.

-
- [63] Quality analysis of *in vivo* near-infrared fluorescence and conventional gamma images acquired using a dual-labeled tumor-targeting probe. Houston, J. P.; Ke, S.; Wang, W.; Li, C.; Sevick-Muraca, E. M. *Journal of Biomedical Optics* **2005**, *10* (5), 054010.
- [64] Molecular design of near infrared polymethine dyes: a review. Bricks, J. L.; Kachkovskii, A. D.; Slominskii, Y. L.; Gerasov, A. O.; Popov, S. V. *Dyes and Pigments* **2015**, *121*, 238-255.
- [65] Fluorescence quantum yields of a series of red and near-infrared dyes emitting at 600–1000 nm. Rurack, K.; Spieles, M. *Analytical Chemistry* **2011**, *83* (4), 1232-1242.
- [66] An efficient 1064 nm NIR-II excitation fluorescent molecular dye for deep-tissue high-resolution dynamic bioimaging. Li, B.; Lu, L.; Zhao, M.; Lei, Z.; Zhang, F. *Angewandte Chemie International Edition* **2018**, *57* (25), 7483-7487.
- [67] Lifetime, photostability, and chemical structure of IR heptamethine cyanine dyes absorbing beyond 1 μm . Kopainsky, B.; Qiu, P.; Kaiser, W.; Sens, B.; Drexhage, K. H. *Applied Physics B* **1982**, *29* (1), 15-18.
- [68] Flavylium polymethine fluorophores for near- and shortwave infrared imaging. Cosco, E. D.; Caram, J. R.; Bruns, O. T.; Franke, D.; Day, R. A.; Farr, E. P.; Bawendi, M. G.; Sletten, E. M. *Angewandte Chemie International Edition* **2017**, *56* (42), 13126-13129.
- [69] Indolizine-cyanine dyes: near infrared emissive cyanine dyes with increased Stokes shifts. Gayton, J.; Autry, S. A.; Meador, W.; Parkin, S. R.; Hill, G. A.; Hammer, N. I.; Delcamp, J. H. *The Journal of Organic Chemistry* **2019**, *84* (2), 687-697.
- [70] Simple and efficient near-infrared organic chromophores for light-emitting diodes with single electroluminescent emission above 1000 nm. Qian, G.; Zhong, Z.; Luo, M.; Yu, D.; Zhang, Z.; Wang, Z. Y.; Ma, D. *Advanced Materials* **2009**, *21* (1), 111-116.
- [71] Theoretical exploitation of acceptors based on benzobis(thiadiazole) and derivatives for organic NIR-II fluorophores. Zhou, B.; Hu, Z.; Jiang, Y.; Zhong, C.; Sun, Z.; Sun, H. *Physical Chemistry Chemical Physics* **2018**, *20* (30), 19759-19767.
- [72] A small-molecule dye for NIR-II imaging. Antaris, A. L.; Chen, H.; Cheng, K.; Sun, Y.; Hong, G.; Qu, C.; Diao, S.; Deng, Z.; Hu, X.; Zhang, B.; Zhang, X.; Yaghi, O. K.; Alamparambil, Z. R.; Hong, X.; Cheng, Z.; Dai, H. *Nature Materials* **2016**, *15* (2), 235-242.
- [73] Novel bright-emission small-molecule NIR-II fluorophores for *in vivo* tumor imaging and image-guided surgery. Sun, Y.; Ding, M.; Zeng, X.; Xiao, Y.; Wu, H.; Zhou, H.; Ding, B.; Qu, C.; Hou, W.; Er-bu, A. G. A.; Zhang, Y.; Cheng, Z.; Hong, X. *Chemical Science* **2017**, *8* (5), 3489-3493.
- [74] Rational design of molecular fluorophores for biological imaging in the NIR-II window. Yang, Q.; Ma, Z.; Wang, H.; Zhou, B.; Zhu, S.; Zhong, Y.; Wang, J.; Wan, H.; Antaris, A.; Ma, R.; Zhang, X.; Yang, J.; Zhang, X.; Sun, H.; Liu, W.; Liang, Y.; Dai, H. *Advanced Materials* **2017**, *29* (12), 1605497.
- [75] Electric field poled organic electro-optic materials: state of the art and future prospects. Dalton, L. R.; Sullivan, P. A.; Bale, D. H. *Chemical Reviews* **2010**, *110* (1), 25-55.
- [76] Recent progress in second-order nonlinear optical polymers and dendrimers. Cho, M. J.; Choi, D. H.; Sullivan, P. A.; Akelaitis, A. J. P.; Dalton, L. R. *Progress in Polymer Science* **2008**, *33* (11), 1013-1058.
- [77] Nonlinear optical polymeric materials: from chromophore design to commercial applications. Dalton, L. (2002) In: Lee, K. S. (eds) *Polymers for Photonics Applications I. Advances in Polymer Science, vol 158*. Springer, Berlin, Heidelberg.

-
- [78] Fundamental aspects of property tuning in push–pull molecules. Bureš, F. *RSC Advances* **2014**, *4* (102), 58826-58851.
- [79] Dual-use chromophores for photorefractive and irreversible photochromic applications. Harris, K. D.; Ayachitula, R.; Strutz, S. J.; Hayden, L. M.; Twieg, R. J. *Applied Optics* **2001**, *40* (17), 2895-2901.
- [80] Solvent effect on color, band shape, and charge-density distribution for merocyanine dyes close to the cyanine limit. Würthner, F.; Archetti, G.; Schmidt, R.; Kuball, H.-G. *Angewandte Chemie International Edition* **2008**, *47* (24), 4529-4532.
- [81] Recent progresses in fluorescent probes for detection of polarity. Xiao, H.; Li, P.; Tang, B. *Coordination Chemistry Reviews* **2021**, *427*, 213582.
- [82] A NIR fluorescent probe for detection of viscosity and lysosome imaging in live cells. Chen, T.; Chen, Z.; Liu, R.; Zheng, S. *Organic & Biomolecular Chemistry* **2019**, *17* (26), 6398-6403.
- [83] Bright and photostable push-pull pyrene dye visualizes lipid order variation between plasma and intracellular membranes. Niko, Y.; Didier, P.; Mely, Y.; Konishi, G.-i.; Klymchenko, A. S. *Scientific Reports* **2016**, *6* (1), 18870.
- [84] A fluorescent membrane tension probe. Colom, A.; Derivery, E.; Soleimanpour, S.; Tomba, C.; Molin, M. D.; Sakai, N.; González-Gaitán, M.; Matile, S.; Roux, A. *Nature Chemistry* **2018**, *10* (11), 1118-1125.
- [85] Potentiometric dyes: imaging electrical activity of cell membranes. Loew, L. M. *Pure and Applied Chemistry* **1996**, *68* (7), 1405-1409.
- [86] Imaging membrane potential with voltage-sensitive dyes. Zochowski, M.; Wachowiak, M.; Falk, C.; Cohen, L.; Lam, Y.; Antic, S.; Zecevic, D. *The Biological bulletin* **2000**, *198*, 1-21.
- [87] Novel naphthylstyryl-pyridinium potentiometric dyes offer advantages for neural network analysis. Obaid, A. L.; Loew, L. M.; Wuskell, J. P.; Salzberg, B. M. *Journal of Neuroscience Methods* **2004**, *134* (2), 179-190.
- [88] Synthesis, spectra, delivery and potentiometric responses of new styryl dyes with extended spectral ranges. Wuskell, J. P.; Boudreau, D.; Wei, M.-d.; Jin, L.; Engl, R.; Chebolu, R.; Bullen, A.; Hoffacker, K. D.; Kerimo, J.; Cohen, L. B.; Zochowski, M. R.; Loew, L. M. *Journal of Neuroscience Methods* **2006**, *151* (2), 200-215.
- [89] Dyes for biological second harmonic generation imaging. Reeve, J. E.; Anderson, H. L.; Clays, K. *Physical Chemistry Chemical Physics* **2010**, *12* (41), 13484-13498.
- [90] Red emitting neutral fluorescent glycoconjugates for membrane optical imaging. Redon, S.; Massin, J.; Pouvreau, S.; De Meulenaere, E.; Clays, K.; Queneau, Y.; Andraud, C.; Girard-Egrot, A.; Bretonnière, Y.; Chambert, S. *Bioconjugate Chemistry* **2014**, *25* (4), 773-787.
- [91] DCDHF fluorophores for single-molecule imaging in cells. Lord, S. J.; Conley, N. R.; Lee, H.-L. D.; Nishimura, S. Y.; Pomerantz, A. K.; Willets, K. A.; Lu, Z.; Wang, H.; Liu, N.; Samuel, R.; Weber, R.; Semyonov, A.; He, M.; Twieg, R. J.; Moerner, W. E. *Chemphyschem* **2009**, *10* (1), 55-65.
- [92] A photoactivatable push–pull fluorophore for single-molecule imaging in live cells. Lord, S. J.; Conley, N. R.; Lee, H.-l. D.; Samuel, R.; Liu, N.; Twieg, R. J.; Moerner, W. E. *Journal of the American Chemical Society* **2008**, *130* (29), 9204-9205.
- [93] Donor–acceptor–donor thienopyrazines via Pd-catalyzed C–H activation as NIR fluorescent materials. McNamara, L. E.; Liyanage, N.; Peddapuram, A.; Murphy, J. S.; Delcamp, J. H.; Hammer, N. I. *The Journal of Organic Chemistry* **2016**, *81* (1), 32-42.

-
- [94] Fumaronitrile-based fluorogen: red to near-infrared fluorescence, aggregation-induced emission, solvatochromism, and twisted intramolecular charge transfer. Shen, X. Y.; Yuan, W. Z.; Liu, Y.; Zhao, Q.; Lu, P.; Ma, Y.; Williams, I. D.; Qin, A.; Sun, J. Z.; Tang, B. Z. *The Journal of Physical Chemistry C* **2012**, *116* (19), 10541-10547.
- [95] Facile synthesis of red/NIR AIE luminogens with simple structures, bright emissions, and high photostabilities, and their applications for specific imaging of lipid droplets and image-guided photodynamic therapy. Wang, D.; Su, H.; Kwok, R. T. K.; Shan, G.; Leung, A. C. S.; Lee, M. M. S.; Sung, H. H. Y.; Williams, I. D.; Lam, J. W. Y.; Tang, B. Z. *Advanced Functional Materials* **2017**, *27* (46), 1704039.
- [96] A photostable AIE luminogen with near infrared emission for monitoring morphological change of plasma membrane. Zhang, W.; Yu, C. Y. Y.; Kwok, R. T. K.; Lam, J. W. Y.; Tang, B. Z. *Journal of Materials Chemistry B* **2018**, *6* (10), 1501-1507.
- [97] Highly efficient photosensitizers with far-red/near-infrared aggregation-induced emission for *in vitro* and *in vivo* cancer theranostics. Wang, D.; Lee, M. M. S.; Shan, G.; Kwok, R. T. K.; Lam, J. W. Y.; Su, H.; Cai, Y.; Tang, B. Z. *Advanced Materials* **2018**, *30* (39), 1802105.
- [98] Far-red and near-IR AIE-active fluorescent organic nanoprobe with enhanced tumor-targeting efficacy: shape-specific effects. Shao, A.; Xie, Y.; Zhu, S.; Guo, Z.; Zhu, S.; Guo, J.; Shi, P.; James, T. D.; Tian, H.; Zhu, W.-H. *Angewandte Chemie International Edition* **2015**, *54* (25), 7275-7280.
- [99] Amplified two-photon brightness in organic multicomponent nanoparticles. Campioli, E.; Nikolaidou, D. M.; Hugues, V.; Campanini, M.; Nasi, L.; Blanchard-Desce, M.; Terenziani, F. *Journal of Materials Chemistry C* **2015**, *3* (28), 7483-7491.
- [100] Molecular-based fluorescent nanoparticles built from dedicated dipolar thienothiophene dyes as ultra-bright green to NIR nanoemitters. Mastrodonato, C.; Pagano, P.; Daniel, J.; Vaultier, M.; Blanchard-Desce, M. *Molecules* **2016**, *21* (9), 1227.
- [101] Tuning solid-state fluorescence to the near-infrared: a combinatorial approach to discovering molecular nanoprobe for biomedical imaging. Singh, A.; Lim, C.-K.; Lee, Y.-D.; Maeng, J.-h.; Lee, S.; Koh, J.; Kim, S. *ACS Applied Materials & Interfaces* **2013**, *5* (18), 8881-8888.
- [102] Aggregation induced emissive carbazole-based push pull NLOphores: synthesis, photophysical properties and DFT studies. Lanke, S. K.; Sekar, N. *Dyes and Pigments* **2016**, *124*, 82-92.
- [103] Boron difluoride hemicurcuminoid as an efficient far red to near-infrared emitter: toward OLEDs and laser dyes. D'Aléo, A.; Sazzad, M. H.; Kim, D. H.; Choi, E. Y.; Wu, J. W.; Canard, G.; Fages, F.; Ribierre, J. C.; Adachi, C. *Chemical Communications* **2017**, *53* (52), 7003-7006.
- [104] Near-infrared solid-state emitters based on isophorone: synthesis, crystal structure and spectroscopic properties. Massin, J.; Dayoub, W.; Mulatier, J.-C.; Aronica, C.; Bretonnière, Y.; Andraud, C. *Chemistry of Materials* **2011**, *23* (3), 862-873.
- [105] Solid state red biphotonic excited emission from small dipolar fluorophores. Ipuy, M.; Liao, Y.-Y.; Jeanneau, E.; Baldeck, P. L.; Bretonnière, Y.; Andraud, C. *Journal of Materials Chemistry C* **2016**, *4* (4), 766-779.
- [106] Tuning the solid-state emission of small push-pull dipolar dyes to the far-red through variation of the electron-acceptor group. Redon, S.; Eucat, G.; Ipuy, M.; Jeanneau, E.; Gautier-Luneau, I.; Ibanez, A.; Andraud, C.; Bretonnière, Y. *Dyes and Pigments* **2018**, *156*, 116-132.
- [107] Development of far-red / near-Infrared luminescent chromophores and nanoparticles for *in vivo* biphotonic applications. Zheng, Z. (2016) Thèse de l'Université de Lyon - École Normale Supérieure de Lyon. N° national de thèse : 2016LYSEN024.

-
- [108] Photostable far-red emitting pluronic silicate nanoparticles: perfect blood pool fluorophores for biphotonic in vivo imaging of the leaky tumour vasculature. Zheng, Z.; Caraguel, F.; Liao, Y.-Y.; Andraud, C.; van der Sanden, B.; Bretonnière, Y. *RSC Advances* **2016**, 6 (96), 94200-94205.
- [109] 4,5,5-trimethyl-2,5-dihydrofuran-based electron-withdrawing groups for NIR-emitting push-pull dipolar fluorophores. Rémond, M.; Zheng, Z.; Jeanneau, E.; Andraud, C.; Bretonnière, Y.; Redon, S. *The Journal of Organic Chemistry* **2019**, 84 (16), 9965-9974.
- [110] Développement de nouveaux chromophores dipolaires pour l'imagerie de fluorescence et l'imagerie photoacoustique. Maxime, R. (2018) Thèse de l'Université de Lyon - École Normale Supérieure de Lyon. N° national de thèse : 2018LYSEN062.
- [111] Développement de nouveaux chromophores dipolaires pour l'imagerie de fluorescence et l'imagerie photoacoustique. Rémond, M. (2018) Thèse de l'Université de Lyon - École Normale Supérieure de Lyon. N° national de thèse : 2018LYSEN062.
- [112] A practical guide to photoacoustic tomography in the life sciences. Wang, L. V.; Yao, J. *Nature Methods* **2016**, 13 (8), 627-638.
- [113] Deeply penetrating photoacoustic tomography in biological tissues enhanced with an optical contrast agent. Ku, G.; Wang, L. V. *Optics Letters* **2005**, 30 (5), 507-509.
- [114] Sensitivity of laser opto-acoustic imaging in detection of small deeply embedded tumors. Esenaliev, R. O.; Karabutov, A. A.; Oraevsky, A. A. *IEEE Journal of Selected Topics in Quantum Electronics* **1999**, 5 (4), 981-988.
- [115] Biomedical applications of photoacoustic imaging with exogenous contrast agents. Luke, G. P.; Yeager, D.; Emelianov, S. Y. *Ann Biomed Eng* **2012**, 40 (2), 422-437.
- [116] Contrast agents for molecular photoacoustic imaging. Weber, J.; Beard, P. C.; Bohndiek, S. E. *Nature Methods* **2016**, 13 (8), 639-650.
- [117] Inorganic nanoparticles for cancer imaging and therapy. Huang, H. C.; Barua, S.; Sharma, G.; Dey, S. K.; Rege, K. *Journal of Controlled Release* **2011**, 155 (3), 344-357.
- [118] Light in and sound out: emerging translational strategies for photoacoustic imaging. Zackrisson, S.; van de Ven, S. M. W. Y.; Gambhir, S. S. *Cancer Research* **2014**, 74 (4), 979.
- [119] Structural and functional photoacoustic molecular tomography aided by emerging contrast agents. Nie, L.; Chen, X. *Chemical Society Reviews* **2014**, 43 (20), 7132-7170.
- [120] Photoacoustic microscopy using Evans Blue dye as a contrast agent. Junjie, Y.; Konstantin, I. M.; Song, H.; Lihong, V. W. (2010) *Proceedings of SPIE*, 7564.
- [121] Local determination of hemoglobin concentration and degree of oxygenation in tissue by pulsed photoacoustic spectroscopy. Raul, F.; Basil, J. S.; John, C. M.; David, A. W.; Daniel, F. H. (2000) *Proceedings of SPIE*, 3916.
- [122] Photoacoustic tomography with novel optical contrast agents based on gold nanocages or nanoparticles containing near-infrared dyes. Xinmai, Y.; Sara, S.; Erich, S.; Bin, W.; Xunbin, W.; Younan, X.; Lihong, V. W. (2008) *Proceedings of SPIE*, 6856.
- [123] Photoacoustic imaging of integrin-overexpressing tumors using a novel ICG-based contrast agent in mice. Capozza, M.; Blasi, F.; Valbusa, G.; Oliva, P.; Cabella, C.; Buonsanti, F.; Cordaro, A.; Pizzuto, L.; Maiocchi, A.; Poggi, L. *Photoacoustics* **2018**, 11, 36-45.

-
- [124] Indocyanine green-labeled polysarcosine for *in vivo* photoacoustic tumor imaging. Sano, K.; Ohashi, M.; Kanazaki, K.; Makino, A.; Ding, N.; Deguchi, J.; Kanada, Y.; Ono, M.; Saji, H. *Bioconjugate Chemistry* **2017**, *28* (4), 1024-1030.
- [125] Photoacoustic and fluorescence imaging of cutaneous squamous cell carcinoma in living subjects using a probe targeting integrin $\alpha\text{v}\beta\text{6}$. Zhang, C.; Zhang, Y.; Hong, K.; Zhu, S.; Wan, J. *Scientific Reports* **2017**, *7* (1), 42442.
- [126] *In vivo* photoacoustic imaging of cancer using indocyanine green-labeled monoclonal antibody targeting the epidermal growth factor receptor. Sano, K.; Ohashi, M.; Kanazaki, K.; Ding, N.; Deguchi, J.; Kanada, Y.; Ono, M.; Saji, H. *Biochemical and Biophysical Research Communications* **2015**, *464* (3), 820-825.
- [127] Intraoperative resection guidance with photoacoustic and fluorescence molecular imaging using an anti-B7-H3 antibody-indocyanine green dual contrast agent. Wilson, K. E.; Bachawal, S. V.; Willmann, J. K. *Clinical Cancer Research* **2018**, *24* (15), 3572.
- [128] Spectroscopic photoacoustic molecular imaging of breast cancer using a B7-H3-targeted ICG contrast agent. Wilson, K. E.; Bachawal, S. V.; Abou-Elkacem, L.; Jensen, K.; Machtaler, S.; Tian, L.; Willmann, J. K. *Theranostics* **2017**, *7* (6), 1463-1476.
- [129] Photoacoustic imaging for transvascular drug delivery to the rat brain. Ryota, W.; Shunichi, S.; Yasuyuki, T.; Satoko, K.; Toshiya, T.; Mitsuhiro, T. (2015) *Proceedings of SPIE*, 9305.
- [130] Sentinel lymph nodes and lymphatic vessels: noninvasive dual-modality *in vivo* mapping by using indocyanine green in Rats — volumetric spectroscopic photoacoustic imaging and planar fluorescence imaging. Kim, C.; Song, K. H.; Gao, F.; Wang, L. V. *Radiology* **2010**, *255* (2), 442-450.
- [131] Photoacoustic microscopy. Yao, J.; Wang, L. V. *Laser & Photonics Reviews* **2013**, *7* (5), 758-778.
- [132] Preclinical evaluation of a novel cyanine dye for tumor imaging with *in vivo* photoacoustic imaging. Takashi, T.; Satoru, O.; Kengo, K.; Masahiro, O.; Hideo, S. *Journal of Biomedical Optics* **2014**, *19* (9), 1-3.
- [133] Development of photostabilized asymmetrical cyanine dyes for *in vivo* photoacoustic imaging of tumors. Satoru, O.; Takashi, T.; Kengo, K.; Masahiro, O.; Hideo, S. *Journal of Biomedical Optics* **2015**, *20* (9), 1-9.
- [134] Towards highly fluorescent and water-soluble perylene dyes. Kohl, C.; Weil, T.; Qu, J.; Müllen, K. *Chemistry – A European Journal* **2004**, *10* (21), 5297-5310.
- [135] Synthesis and application of water-soluble, photoswitchable cyanine dyes for bioorthogonal labeling of cell-surface carbohydrates. Alexander, M.; Sebastian, L.; Elisabeth, M.; Markus, S.; Jürgen, S. *Zeitschrift für Naturforschung C* **2016**, *71* (9-10), 347-354.
- [136] Perylene polyether hybrids: highly soluble, luminescent, redox-active dyes. Williams, M. E.; Murray, R. W. *Chemistry of Materials* **1998**, *10* (11), 3603-3610.
- [137] Jetting performance of polyethylene glycol and reactive dye solutions. Tang, Z.; Fang, K.; Song, Y.; Sun, F. *Polymers* **2019**, *11* (4), 739.
- [138] Highly water-soluble, near-infrared emissive BODIPY polymeric dye bearing RGD peptide residues for cancer imaging. Zhu, S.; Zhang, J.; Janjanam, J.; Bi, J.; Vegesna, G.; Tiwari, A.; Luo, F.-T.; Wei, J.; Liu, H. *Analytica Chimica Acta* **2013**, *758*, 138-144.
- [139] Highly fluorescent and water-soluble diketopyrrolopyrrole dyes for bioconjugation. Heyer, E.; Lory, P.; Leprince, J.; Moreau, M.; Romieu, A.; Guardigli, M.; Roda, A.; Ziessel, R. *Angewandte Chemie International Edition* **2015**, *127*.

-
- [140] Targeting dyes for biology. Saurabh, S.; Bruchez, M. (2014) In: Cambi, A.; Lidke, D. S. (eds) *Cell Membrane Nanodomains: From Biochemistry to Nanoscopy, 1st Edition*. CRC Press.
- [141] Nanochemistry and nanomedicine for nanoparticle-based diagnostics and therapy. Chen, G.; Roy, I.; Yang, C.; Prasad, P. N. *Chemical Reviews* **2016**, *116* (5), 2826-2885.
- [142] Nanotechnology in cancer therapeutics: bioconjugated nanoparticles for drug delivery. Sinha, R.; Kim, G. J.; Nie, S.; Shin, D. M. *Molecular Cancer Therapeutics* **2006**, *5* (8), 1909-1917.
- [143] Iridium doped silica-PEG nanoparticles: enabling electrochemiluminescence of neutral complexes in aqueous media. Zanarini, S.; Rampazzo, E.; Bonacchi, S.; Juris, R.; Marcaccio, M.; Montalti, M.; Paolucci, F.; Prodi, L. *Journal of the American Chemical Society* **2009**, *131* (40), 4208-4209.
- [144] A new class of silica cross-linked micellar core-shell nanoparticles. Huo, Q.; Liu, J.; Wang, L.-Q.; Jiang, Y.; Lambert, T. N.; Fang, E. *Journal of the American Chemical Society* **2006**, *128* (19), 6447-6453.
- [145] Energy transfer from silica core-surfactant shell nanoparticles to hosted molecular fluorophores. Rampazzo, E.; Bonacchi, S.; Juris, R.; Montalti, M.; Genovese, D.; Zaccheroni, N.; Prodi, L.; Rambaldi, D. C.; Zattoni, A.; Reschiglian, P. *The Journal of Physical Chemistry B* **2010**, *114* (45), 14605-14613.
- [146] A versatile strategy for tuning the color of electrochemiluminescence using silica nanoparticles. Valenti, G.; Rampazzo, E.; Bonacchi, S.; Khajvand, T.; Juris, R.; Montalti, M.; Marcaccio, M.; Paolucci, F.; Prodi, L. *Chemical Communications* **2012**, *48* (35), 4187-4189.
- [147] Multiple dye-doped NIR-emitting silica nanoparticles for both flow cytometry and *in vivo* imaging. Biffi, S.; Petrizza, L.; Rampazzo, E.; Voltan, R.; Sgarzi, M.; Garrovo, C.; Prodi, L.; Andolfi, L.; Agnoletto, C.; Zauli, G.; Secchiero, P. *RSC Advances* **2014**, *4* (35), 18278-18285.
- [148] Targeted dual-color silica nanoparticles provide univocal identification of micrometastases in preclinical models of colorectal cancer. Soster, M.; Juris, R.; Bonacchi, S.; Genovese, D.; Montalti, M.; Rampazzo, E.; Zaccheroni, N.; Garagnani, P.; Bussolino, F.; Prodi, L.; Marchiò, S. *International Journal of Nanomedicine* **2012**, *7*, 4797-4807.
- [149] Polymer-encapsulated organic nanoparticles for fluorescence and photoacoustic imaging. Li, K.; Liu, B. *Chemical Society Reviews* **2014**, *43* (18), 6570-6597.
- [150] Biocompatible polypyrrole nanoparticles as a novel organic photoacoustic contrast agent for deep tissue imaging. Zha, Z.; Deng, Z.; Li, Y.; Li, C.; Wang, J.; Wang, S.; Qu, E.; Dai, Z. *Nanoscale* **2013**, *5* (10), 4462-4467.
- [151] Semiconducting polymer nanoparticles as photoacoustic molecular imaging probes in living mice. Pu, K.; Shuhendler, A. J.; Jokerst, J. V.; Mei, J.; Gambhir, S. S.; Bao, Z.; Rao, J. *Nature Nanotechnology* **2014**, *9* (3), 233-239.
- [152] Conjugated polymer nanoparticles for photoacoustic vascular imaging. Liu, J.; Geng, J.; Liao, L.-D.; Thakor, N.; Gao, X.; Liu, B. *Polymer Chemistry* **2014**, *5* (8), 2854-2862.
- [153] Highly absorbing multispectral near-infrared polymer nanoparticles from one conjugated backbone for photoacoustic imaging and photothermal therapy. Chen, H.; Zhang, J.; Chang, K.; Men, X.; Fang, X.; Zhou, L.; Li, D.; Gao, D.; Yin, S.; Zhang, X.; Yuan, Z.; Wu, C. *Biomaterials* **2017**, *144*, 42-52.
- [154] D-A polymers for fluorescence/photoacoustic imaging and characterization of their photothermal properties. Zhu, Y.; Gu, C.; Miao, Y.; Yu, B.; Shen, Y.; Cong, H. *Journal of Materials Chemistry B* **2019**, *7* (42), 6576-6584.

-
- [155] Fluorescent nanoparticles from PEGylated polyfluorenes. Behrendt, J. M.; Wang, Y.; Willcock, H.; Wall, L.; McCairn, M. C.; O'Reilly, R. K.; Turner, M. L. *Polymer Chemistry* **2013**, *4* (5), 1333-1336.
- [156] Fluorescent organic nanocrystals and non-doped nanoparticles for biological applications. Fery-Forgues, S. *Nanoscale* **2013**, *5* (18), 8428-8442.
- [157] Incorporating functionalized polyethylene glycol lipids into reprecipitated conjugated polymer nanoparticles for bioconjugation and targeted labeling of cells. Kandel, P. K.; Fernando, L. P.; Ackroyd, P. C.; Christensen, K. A. *Nanoscale* **2011**, *3* (3), 1037-1045.
- [158] Near-infrared phosphorescent polymeric nanomicelles: efficient optical probes for tumor imaging and detection. Kumar, R.; Ohulchanskyy, T. Y.; Roy, I.; Gupta, S. K.; Borek, C.; Thompson, M. E.; Prasad, P. N. *ACS Applied Materials & Interfaces* **2009**, *1* (7), 1474-1481.
- [159] Facile synthesis of fluorescent polymer nanoparticles by covalent modification–nanoprecipitation of amine-reactive ester polymers. Lee, Y.; Hanif, S.; Theato, P.; Zentel, R.; Lim, J.; Char, K. *Macromolecular Rapid Communications* **2015**, *36* (11), 1089-1095.
- [160] Highly emissive PEG-encapsulated conjugated polymer nanoparticles. Li, Y.; Liu, J.; Liu, B.; Tomczak, N. *Nanoscale* **2012**, *4* (18), 5694-5702.
- [161] Red-emitting DPSB-based conjugated polymer nanoparticles with high two-photon brightness for cell membrane imaging. Liu, P.; Li, S.; Jin, Y.; Qian, L.; Gao, N.; Yao, S. Q.; Huang, F.; Xu, Q.-H.; Cao, Y. *ACS Applied Materials & Interfaces* **2015**, *7* (12), 6754-6763.
- [162] Fluorescent polymer nanoparticles based on dyes: seeking brighter tools for bioimaging. Reisch, A.; Klymchenko, A. S. *Small* **2016**, *12* (15), 1968-1992.
- [163] Multicolor conjugated polymer dots for biological fluorescence imaging. Wu, C.; Bull, B.; Szymanski, C.; Christensen, K.; McNeill, J. *ACS nano* **2008**, *2* (11), 2415-2423.
- [164] Design of highly emissive polymer dot bioconjugates for *in vivo* tumor targeting. Wu, C.; Hansen, S. J.; Hou, Q.; Yu, J.; Zeigler, M.; Jin, Y.; Burnham, D. R.; McNeill, J. D.; Olson, J. M.; Chiu, D. T. *Angewandte Chemie International Edition* **2011**, *50* (15), 3430-3434.
- [165] Long-circulating near-infrared fluorescence core-cross-linked polymeric micelles: synthesis, characterization, and dual nuclear/optical imaging. Yang, Z.; Zheng, S.; Harrison, W. J.; Harder, J.; Wen, X.; Gelovani, J. G.; Qiao, A.; Li, C. *Biomacromolecules* **2007**, *8* (11), 3422-3428.
- [166] Fabrication of aggregation induced emission dye-based fluorescent organic nanoparticles *via* emulsion polymerization and their cell imaging applications. Zhang, X.; Zhang, X.; Yang, B.; Liu, M.; Liu, W.; Chen, Y.; Wei, Y. *Polymer Chemistry* **2014**, *5* (2), 399-404.
- [167] Turning double hydrophilic into amphiphilic: IR825-conjugated polymeric nanomicelles for near-infrared fluorescence imaging-guided photothermal cancer therapy. Pan, G.-Y.; Jia, H.-R.; Zhu, Y.-X.; Wu, F.-G. *Nanoscale* **2018**, *10* (4), 2115-2127.
- [168] Engineering of multifunctional nano-micelles for combined photothermal and photodynamic therapy under the guidance of multimodal imaging. Gong, H.; Dong, Z.; Liu, Y.; Yin, S.; Cheng, L.; Xi, W.; Xiang, J.; Liu, K.; Li, Y.; Liu, Z. *Advanced Functional Materials* **2014**, *24* (41), 6492-6502.
- [169] Light-responsive AIE nanoparticles with cytosolic drug release to overcome drug resistance in cancer cells. Yuan, Y.; Xu, S.; Zhang, C.-J.; Liu, B. *Polymer Chemistry* **2016**, *7* (21), 3530-3539.
- [170] Appendix: characteristics of fluorescent organic compounds. Valeur, B.; Berberan-Santos, M. N. (2012) In: Valeur, B.; Berberan-Santos, M. N. (eds) *Molecular Fluorescence: Principles and Applications*, 2nd Edition. Wiley-VCH.

-
- [171] TEMPO-oxidized cellulose with high degree of oxidation. Tang, Z.; Li, W.; Lin, X.; Xiao, H.; Miao, Q.; Huang, L.; Chen, L.; Wu, H. *Polymers* **2017**, *9* (9), 421.
- [172] Surface chemistry architecture of silica nanoparticles determine the efficiency of *in vivo* fluorescence lymph node mapping. Helle, M.; Rampazzo, E.; Monchanin, M.; Marchal, F.; Guillemin, F.; Bonacchi, S.; Salis, F.; Prodi, L.; Bezdetnaya, L. *ACS Nano* **2013**, *7* (10), 8645-8657.
- [173] Large Two-photon Absorption of Highly Conjugated Porphyrin Arrays and Their *in vivo* Applications. Park, J. K. (2015) Dissertation submitted for the degree of Doctor of Philosophy of Duke University.
- [174] Rhodamine 800 as reference substance for fluorescence quantum yield measurements in deep red emission range. Alessi, A.; Salvalaggio, M.; Ruzzon, G. *Journal of Luminescence* **2013**, *134*, 385-389.
- [175] Absolute luminescence yield of cresyl violet. A standard for the red. Magde, D.; Brannon, J. H.; Cremers, T. L.; Olmsted, J. *The Journal of Physical Chemistry* **1979**, *83* (6), 696-699.
- [176] Biocompatible nanoparticles based on diketo-pyrrolo-pyrrole (DPP) with aggregation-induced red/NIR emission for *in vivo* two-photon fluorescence imaging. Gao, Y.; Feng, G.; Jiang, T.; Goh, C.; Ng, L.; Liu, B.; Li, B.; Yang, L.; Hua, J.; Tian, H. *Advanced Functional Materials* **2015**, *25* (19), 2857-2866.
- [177] Two-photon excited fluorescence of BF₂ complexes of curcumin analogues: toward NIR-to-NIR fluorescent organic nanoparticles. D'Aléo, A.; Felouat, A.; Heresanu, V.; Ranguis, A.; Chaudanson, D.; Karapetyan, A.; Giorgi, M.; Fages, F. *Journal of Materials Chemistry C* **2014**, *2* (26), 5208-5215.
- [178] Concise multigram-scale synthesis of push-pull tricyanofuran-based hemicyanines with giant second-order nonlinearity: an alternative for electro-optic materials. Bentoumi, W.; Mulatier, J.-C.; Bouit, P.-A.; Maury, O.; Barsella, A.; Vola, J.-P.; Chastaing, E.; Divay, L.; Soyer, F.; Le Barny, P.; Bretonnière, Y.; Andraud, C. *Chemistry – A European Journal* **2014**, *20* (29), 8909-8913.
- [179] Fluorescent RAFT polymers bearing a nitrilotriacetic acid (NTA) ligand at the α -chain-end for the site-specific labeling of histidine-tagged proteins. Duret, D.; Haftek-Terreau, Z.; Carretier, M.; Ladavière, C.; Charreyre, M.-T.; Favier, A. *Polymer Chemistry* **2017**, *8* (10), 1611-1615.
- [180] Millisecond lifetime imaging with a europium complex using a commercial confocal microscope under one or two-photon excitation. Grichine, A.; Haeefele, A.; Pascal, S.; Duperray, A.; Michel, R.; Andraud, C.; Maury, O. *Chemical Science* **2014**, *5* (9), 3475-3485.
- [181] Highly sensitive built-in strain sensors for polymer composites: fluorescence turn-on response through mechanochemical activation. Li, Z. a.; Toivola, R.; Ding, F.; Yang, J.; Lai, P.-N.; Howie, T.; Georgeson, G.; Jang, S.-H.; Li, X.; Flinn, B. D.; Jen, A. K. Y. *Advanced Materials* **2016**, *28* (31), 6592-6597.
- [182] A mild and catalyst-free conversion of solid phase benzylidenemalononitrile/benzylidenemalonate to N-benzylidene-amine and its application for fluorescence detection of primary alkyl amine vapor. Shi, L.; Fu, Y.; He, C.; Zhu, D.; Gao, Y.; Wang, Y.; He, Q.; Cao, H.; Cheng, J. *Chemical Communications* **2014**, *50* (7), 872-874.
- [183] A colorimetric and ratiometric fluorescent sensor for biogenic primary amines based on dicyanovinyl substituted phenanthridine conjugated probe. Saravanakumar, M.; Umamahesh, B.; Selvakumar, R.; Dhanapal, J.; Ashok kumar, S. K.; Sathiyarayanan, K. I. *Dyes and Pigments* **2020**, *178*, 108346.
- [184] A ratiometric fluorescent probe for specific detection of cysteine over homocysteine and glutathione based on the drastic distinction in the kinetic profiles. Yuan, L.; Lin, W.; Yang, Y. *Chemical Communications* **2011**, *47* (22), 6275-6277.

-
- [185] Coumarin-based thiol chemosensor: synthesis, turn-on mechanism, and its biological application. Jung, H. S.; Ko, K. C.; Kim, G.-H.; Lee, A.-R.; Na, Y.-C.; Kang, C.; Lee, J. Y.; Kim, J. S. *Organic Letters* **2011**, *13* (6), 1498-1501.
- [186] Synthesis of dicyanovinyl-substituted 1-(2-pyridyl)pyrazoles: design of a fluorescent chemosensor for selective recognition of cyanide. Orrego-Hernández, J.; Portilla, J. *The Journal of Organic Chemistry* **2017**, *82* (24), 13376-13385.
- [187] Michael addition-based colorimetric and fluorescence chemodosimeters for the nanomolar-level tracking of cyanide ions in aqueous-organic media. Jeong, J. w.; Angupillai, S.; Kim, I. J.; Jeong, J.; Kim, H.-S.; So, H.-S.; Son, Y.-A. *Sensors and Actuators B: Chemical* **2016**, *237*, 341-349.
- [188] Turn-on fluorescent sensor for the detection of cyanide based on a novel dicyanovinyl phenylacetylene. Thanayupong, E.; Suttisintong, K.; Sukwattanasinitt, M.; Niamnont, N. *New Journal of Chemistry* **2017**, *41* (10), 4058-4064.
- [189] Recent progress in the development of fluorescent probes for the detection of hydrazine (N₂H₄). Yan, L.; Zhang, S.; Xie, Y.; Mu, X.; Zhu, J. *Critical Reviews in Analytical Chemistry* **2020**, 1-20.
- [190] Chapter 9. Chemical tests for functional groups. Shriner, R. L.; Hermann, C. K. F.; Morrill, T. C.; Curtin, D. Y.; Fuson, R. C. (2003) In: Shriner, R. L.; Hermann, C. K. F. (eds) *Comprehensive organic name reactions and reagents, 8th Edition*. Wiley & Sons Ltd.
- [191] Environmental impact of amines. Eide-Haugmo, I.; Brakstad, O. G.; Hoff, K. A.; Sørheim, K. R.; da Silva, E. F.; Svendsen, H. F. *Energy Procedia* **2009**, *1* (1), 1297-1304.
- [192] Biogenic amines: their importance in foods. Santos, M. H. S. *International Journal of Food Microbiology* **1996**, *29* (2), 213-231.
- [193] Biogenic amines and polyamines: similar biochemistry for different physiological missions and biomedical applications. Medina, M. Á.; Urdiales, J. L.; Rodríguez-Caso, C.; Ramírez, F. J.; Sánchez-Jiménez, F. *Critical Reviews in Biochemistry and Molecular Biology* **2003**, *38* (1), 23-59.
- [194] A review of the liquid chromatographic methods for the determination of biogenic amines in foods. Önal, A.; Tekkeli, S. E. K.; Önal, C. *Food Chemistry* **2013**, *138* (1), 509-515.
- [195] Capillary electrophoretic separation of biologically active amines and acids using nanoparticle-coated capillaries. Huang, Y.-F.; Chiang, C.-K.; Lin, Y.-W.; Liu, K.; Hu, C.-C.; Bair, M.-J.; Chang, H.-T. *Electrophoresis* **2008**, *29* (9), 1942-1951.
- [196] A molecular probe for the optical detection of biogenic amines. Lee, B.; Scopelliti, R.; Severin, K. *Chemical Communications* **2011**, *47* (34), 9639-9641.
- [197] Montmorillonite-supramolecular hydrogel hybrid for fluorocolorimetric sensing of polyamines. Ikeda, M.; Yoshii, T.; Matsui, T.; Tanida, T.; Komatsu, H.; Hamachi, I. *Journal of the American Chemical Society* **2011**, *133* (6), 1670-1673.
- [198] Selective fluorescence detection of histamine based on ligand exchange mechanism and its application to biomonitoring. Seto, D.; Soh, N.; Nakano, K.; Imato, T. *Analytical biochemistry* **2010**, *404* (2), 135-139.
- [199] Amine-responsive cellulose-based ratiometric fluorescent materials for real-time and visual detection of shrimp and crab freshness. Jia, R.; Tian, W.; Bai, H.; Zhang, J.; Wang, S.; Zhang, J. *Nature Communications* **2019**, *10* (1), 795.
- [200] Fluorescent sensors for amines. Klockow, J.; Hettie, K. S.; Glass, T. (2017) In: Atwood, J. L. (eds) *Comprehensive Supramolecular Chemistry II. 2nd Edition, Fluorescence sensors and imaging agents*. Elsevier BV

-
- [201] Fluorescent light-up detection of amine vapors based on aggregation-induced emission. Gao, M.; Li, S.; Lin, Y.; Geng, Y.; Ling, X.; Wang, L.; Qin, A.; Tang, B. Z. *ACS Sensors* **2016**, *1* (2), 179-184.
- [202] Selective amine recognition: development of a chemosensor for dopamine and norepinephrine. Secor, K. E.; Glass, T. E. *Organic Letters* **2004**, *6* (21), 3727-3730.
- [203] Fluorescent sensors for diamines. Secor, K.; Plante, J.; Avetta, C.; Glass, T. *Journal of Materials Chemistry* **2005**, *15* (37), 4073-4077.
- [204] Aldehyde cruciforms: dosimeters for primary and secondary amines. Patze, C.; Broedner, K.; Rominger, F.; Trapp, O.; Bunz, U. H. F. *Chemistry – A European Journal* **2011**, *17* (49), 13720-13725.
- [205] Tunable molecular logic gates designed for imaging released neurotransmitters. Klockow, J. L.; Hettie, K. S.; Secor, K. E.; Barman, D. N.; Glass, T. E. *Chemistry – A European Journal* **2015**, *21* (32), 11446-11451.
- [206] Detection of amines and unprotected amino acids in aqueous conditions by formation of highly fluorescent iminium ions. Feuster, E. K.; Glass, T. E. *Journal of the American Chemical Society* **2003**, *125* (52), 16174-16175.
- [207] Light-activated sensitive probes for amine detection. Valderrey, V.; Bonasera, A.; Fredrich, S.; Hecht, S. *Angewandte Chemie International Edition* **2017**, *56* (7), 1914-1918.
- [208] Development of chromogenic reactands for optical sensing of alcohols. Mohr, G. J.; Citterio, D.; Spichiger-Keller, U. E. *Sensors and Actuators B: Chemical* **1998**, *49* (3), 226-234.
- [209] Reversible chemical reactions as the basis for optical sensors used to detect amines, alcohols and humidity. J. Mohr, G.; Citterio, D.; Demuth, C.; Fehlmann, M.; Jenny, L.; Lohse, C.; Moradian, A.; Nezel, T.; Rothmaier, M.; E. Spichiger, U. *Journal of Materials Chemistry* **1999**, *9* (9), 2259-2264.
- [210] Chromo- and fluororeactands: indicators for detection of neutral analytes by using reversible covalent-bond chemistry. Mohr, G. J. *Chemistry – A European Journal* **2004**, *10* (5), 1082-1090.
- [211] A reaction-based sensing scheme for volatile organic amine reagents with the chromophoric-fluorogenic dual mode. Yang, X.; Zhou, J.; Li, Y.; Yan, M.; Cui, Y.; Sun, G. *Spectrochimica Acta Part A* **2020**, *240*, 118539.
- [212] Design and characterization of dicyanovinyl reactive dyes for the colorimetric detection of thiols and biogenic amines. Mastnak, T.; Lobnik, A.; Mohr, G. J.; Turel, M. *Sensors* **2018**, *18*, 814.
- [213] Indicator layers based on ethylene-vinyl acetate copolymer (EVA) and dicyanovinyl azobenzene dyes for fast and selective evaluation of vaporous biogenic amines. Mastnak, T.; Lobnik, A.; Mohr, G. J.; Finsgar, M. *Sensors* **2018**, *18*, 4361.
- [214] A turn-on fluorogenic probe for detection of MDMA from ecstasy tablets. Moreno, D.; Greñu, B. D. d.; García, B.; Ibeas, S.; Torroba, T. *Chemical Communications* **2012**, *48* (24), 2994-2996.
- [215] Dual-mode photonic sensor array for detecting and discriminating hydrazine and aliphatic amines. Liu, T.; Yang, L.; Feng, W.; Liu, K.; Ran, Q.; Wang, W.; Liu, Q.; Peng, H.; Ding, L.; Fang, Y. *ACS Applied Materials & Interfaces* **2020**, *12* (9), 11084-11093.
- [216] A sensitive TICT probe exhibiting ratiometric fluorescence response to detect hydrazine in solution and gas phase. Gupta, R.; Dwivedi, S.; Ali, R.; Razi, S.; Tiwari, R.; Krishnamoorthi, S.; Misra, A. *Spectrochimica Acta Part A* **2020**, 118153.
- [217] Use of Lawesson's reagent in organic syntheses. Ozturk, T.; Ertas, E.; Mert, O. *Chemical Reviews* **2007**, *107* (11), 5210-5278.

-
- [218] Limit of detection. A closer look at the IUPAC definition. Long, G. L.; Winefordner, J. D. *Analytical Chemistry* **1983**, *55*, (07), 712A–724A.
- [219] A ratiometric fluorescent probe for detection of biogenic primary amines with nanomolar sensitivity. Mallick, S.; Chandra, F.; Koner, A. L. *Analyst* **2016**, *141* (3), 827-831.
- [220] Ylidenemalonitrile Enamines as Fluorescent “Turn-On” Indicators for Primary Amines. Longstreet, A. R.; Jo, M.; Chandler, R. R.; Hanson, K.; Zhan, N.; Hrudka, J. J.; Mattoussi, H.; Shatruk, M.; McQuade, D. T. *Journal of the American Chemical Society* **2014**, *136* (44), 15493-15496.
- [221] Reaction-based colorimetric cyanide chemosensors: rapid naked-eye detection and high selectivity. Cheng, X.; Zhou, Y.; Qin, J.; Li, Z. *ACS Applied Materials & Interfaces* **2012**, *4* (4), 2133-2138.
- [222] Fluorescent light-up detection of amine vapors based on aggregation-induced emission. Gao, M.; Li, S.; Lin, Y.; Geng, Y.; Ling, X.; Wang, L.; Qin, A.; Tang, B. Z. *ACS Sensors* **2015**, *1* (2), 179-184.
- [223] A highly sensitive bimodal detection of amine vapours based on aggregation induced emission of 1,2-dihydroquinoxaline derivatives. Alam, P.; Leung, N. L. C.; Su, H.; Qiu, Z.; Kwok, R. T. K.; Lam, J. W. Y.; Tang, B. Z. *Chemistry – A European Journal* **2017**, *23* (59), 14911-14917.
- [224] Synthesis and Investigation of Solar-Cell Photosensitizers Having a Fluorazone Backbone. Mátravölgyi, B.; Hergert, T.; Thurner, A.; Varga, B.; Sangiorgi, N.; Bondoni, R.; Zani, L.; Reginato, G.; Calamante, M.; Sinicropi, A.; Sanson, A.; Faigl, F.; Mordini, A. *European Journal of Organic Chemistry* **2017**, *2017* (14), 1843-1854.
- [225] Energy levels, charge injection, charge recombination and dye regeneration dynamics for donor–acceptor π -conjugated organic dyes in mesoscopic TiO₂ sensitized solar cells. Planells, M.; Pellejà, L.; Clifford, J. N.; Pastore, M.; De Angelis, F.; López, N.; Marder, S. R.; Palomares, E. *Energy & Environmental Science* **2011**, *4* (5), 1820-1829.